Laser Induced Selective Activation For Subsequent Autocatalytic Electroless Plating

Zhang, Yang

Publication date:
2010

Document Version
Publisher's PDF, also known as Version of record

Laser Induced Selective Activation For Subsequent Autocatalytic Electroless Plating

By

Yang Zhang

For fullfilment of degree

Doctor of Philosophy

Department of Mechanical Engineering

Technical University of Denmark

October 2010

Title
Laser Induced Selective Activation For Subsequent Autocatalytic Electroless Plating
Manuscript by
Yang Zhang

Examining committee
Prof. Leonardo De Chiffre
Department of Mechanical Engineering
Technical University of Denmark (DTU)
Kgs. Lyngby
Denmark

Dr. Peter Leisner
Adjunct professor
Head of the Electronics Department
SP Technical Research Institute of Sweden, Borås,
School of Engineering, Jönköping University
Sweden

Dr. Wolfgang Eberhardt
Head of technology department
HSG-IMAT
Stuttgart
Germany

DTU Mechanical Engineering
Section of Manufacturing Engineering
Dtechnical University of Denmark

Produktionstorvet
Bygning 427S
DK2800 Kgs.Lyngby
Denmark

www.me.mek.dtu.dk
Tel: 0045 4525 4763
Fax: 0045 4593 0190

Category: PhD dissertation

Version: 1. Edition

ISBN 978-87-90416-39-3

Printed: 2011

庄子与惠子游于濠梁之上。

庄子曰：“儵鱼出游从容，是鱼之乐也？”

惠子曰：“子非鱼，安知鱼之乐？”

庄子曰：“子非我，安知我不知鱼之乐？”

--------庄子 (375B.C. – 295B.C.) · 秋水

Zhuangzi and Huizi were strolling along the dam of the Hao Waterfall.

Zhuangzi said, "See how the minnows swim leisurely! That's what fish really enjoy!"

Huizi said, "You're not a fish — how do you know what fish enjoy?"

Zhuangzi said, "You're not me, so how do you know I don't know what fish enjoy?"

--------Zhuangzi (375B.C. – 295B.C.) · Autumn waterfall

Preface

This thesis is made for the Ph.D. project "Laser Induced Selective Activation for Subsequent autocatalytic Electroless Plating" at the Department of Mechanical Engineering (MEK), Technical University of Denmark (DTU).

It represents all the experiments and analysis made in the project, which was carried out at the Department of Mechanical Engineering, DTU, and HSG-IMAT in Stuttgart, Germany.

All the work has been carried out during the period from the 1st October, 2007 to the 30th September, 2010. The work was supervised by Professor Hans Nørgaard Hansen, DTU, Dr. Peter Torben Tang, IPU, Associate Professor Arnaud De Grave, DTU, and laboratory engineer Jacob Skov Nielsen, DTU.

It has been a great experience to work as a PhD student at DTU MEK. The last three years have been fantastic, second only to my innocent and joyous childhood. Being employed has been a much better experience than the previous 18 years of schooling, where studying has been the sole purpose. I have enjoyed the research work I have done and look forward to all my future research.

Looking back with a more philosophical view, these years have taught me how to study, communicate, and work. I have obtained a new way of thought, which is to set up a hypothesis first, followed by the best effort to prove or disprove it, and it is finally concluded with an analysis of the experimental outcomes.

To become an engineer, one has to devote many years reading books to acquire an in-depth knowledge in the field. In turn, this traps thinking within a box formed by all those books. It takes a creative mind to break through that boundary to form a new idea, much like how the idea of LISA came about.

The only thing that I am disappointed about these three years is that my eyesight went from -7 to -8.5 during that span. I try not to blame all the different types of microscopes that I have stared down, because it was also my own fault that I did not use the correct physical posture when I sat in front of them.. On a positive note, I was very happy and satisfied whenever I took a very clear image, even if it meant more time needes to be spent in front of a computer screen. I believe that I am more patient and careful than I ever was.

Attitude is everything, to learn, to live, and to love.

Yang Zhang · 张阳

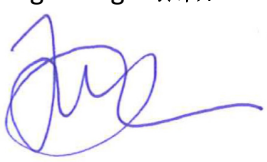

September, 2010

Lyngby, Denmark

Acknowledgement

Firstly I owe my deepest gratitude to my supervisors, Dr. Hans Nørgaard Hansen, Dr. Peter Torben Tang, Dr. Arnaud De Grave, and Jacob Skov Nielsen, for their valuable and experimental suggestions for the project all the time. All words are pale here to describe how helpful they are and how grateful I am. It is my honor and good fortune to work with them.

Also I would like to thank to all my students for the excellent work they have done. They are Monika Butrimaite, Tobias Maduro Nørbo, Fan Cheng, Christian Dela, Robert K. Fraser, Peter Andreas Jørgensen, Patrcik Westergaard, Freja N. Jespersen, Manuel E. P. Korell, and Huma Malik.

There are a lot nice DTU colleagues who helped me a lot, for example, Professor Jesper Hattel, Dr. Cem Celal Tutum, Professor Georgios Kontogeorgis, Professor Alexander Shapiro, Dr. Jingdong Zhang, etc. I'd like to say thanks to them all.

I appreciate the help from all the technicians. They are Reinholdt Koch, Kim Chi Szabo, Laila leth Steffen S. Munch, Rusmus Knud Pedersen who are from DTU; and Allan Stojko, Christian Ravn and Klaus Schütt Hansen from IPU.

It's a pleasure to thank HSG-IMAT in Stuttgart, Germany. It is a nice collaboration on LISA project. Also, to all the companies, which are interested in LISA technology, their joint work makes me feel confident and positive for the project.

I am indebted to many of my colleagues who supported me, Pia Holst Nielsen, David Bue Pedersen, Stefania Gasparin, Guido Tosello, Aminul Islam, Finn Paaske Christensen, Flemming Jørgensen, Giuliano Bissacco and Matteo Calaon.

All my friends, in Denmark and all over the world, who always support me, are the best.

Here I have very special thanks to my Fan, thanks for the lovely home you gave me, which is wht I always dreamed of. The 3 years PhD becomes a true-life experience because of you, and I'd like to celebrate this PhD thesis by spending the rest of my life with you.

Last but not least, my thanks go to my mum, sister, dad, my mother in law and other families who supported me endlessly. Their love spread over the whole Eurasian continent from both ends and I'm right in the middle.

Abstract (English)

The subject of this PhD thesis is "Laser induced selective activation for subsequent autocatalytic electroless plating." The objective of the project is to investigate the process chains for micro structuring of polymer surfaces for selective micro metallization. Laser induced selective activation (LISA) is introduced and studied as a new technique for producing 3D moulded interconnect devices (3D-MIDs). This technique enables the metallization of polymer surface modified by laser and subsequently activated by a $PdCl_2/SnCl_2$ system.

Various technologies exist on an industrial level for manufacturing MIDS, e.g. LDS®, 2-shot injection moulding, *etc.* Compared with them, LISA shows economic and environmental advantages. First, the range of available polymers is wide, and no pretreatment such as filler premix is need. Commercial polymer such as polyethylene and polystyrene, polycarbonate, ABS, *etc.* can be directly used in the LISA process. Second, in the wet steps, no chromic acid or other similar toxic compounds are used.

The principle of the $PdCl_2/SnCl_2$ activation system is explained based on previous researchers' studies. Investigations were conducted as to how the laser tracks keep the activation colloids based on three hypotheses. The first hypothesis is that laser machining leads to chemical changes of the polymer, which results in chemical bonding with the activation colloids. Chemical changes on the laser track were investigated by XPS or FTIR spectroscopy, but no evidence shows that chemical bonds exist. However, it is still not excluded that chemical bonding is part of the mechanism. The second hypothesis is that the laser track has a stronger attraction work to the activation solution. This is proved by a calculation using van Oss *et al*., theory based on contact angle measurement. The third hypothesis is that the activation and rinsing process can be described by diffusion. This hypothesis is proved using Fick's diffusion laws combined with the short-time-plating experiment.

The influence of laser parameters on the surface structure is investigated for Nd: YAG, UV, and fiber lasers. The mechanism of the surface structure formation reason is discussed and the Nd: YAG laser parameters' effect on the structure of the laser track is investigated. There is a trend showing that the height of the laser track increases with the laser energy output. A characterization method for the porous surface based on the bearing area curve and its parameters is propsed.

Comparison of two activation methods based on plating velocity was performed. It was found that the plating velocity is independent of the height of the laser track, as long as the structure is sponge-like and continuous. The adhesive strength of the copper coating is related to the laser structure. High laser energy input will lead to high laser track, on which the copper coating has a stronger adhesion than on the track made by lower energy, even though the coatings have similar thickness.

The LISA method was tested in the case of an antenna. Two simple antenna shapes, planar dipole, and planar loop were studied, as well as a co-planar stripline. The antennas made by LISA exhibited impedance characteristics expected from the respective antenna shapes and comparable to antennas made by PCB technology.

Resume (Dansk)

Temaet for denne PhD afhandling er "Laser induceret selektiv aktivering til efterfølgende auto-katalytisk kemisk plettering". Formålet med projektet er at undersøge proceskæder til mikrostrukturering af plastoverflader for efterfølgende selektiv metallisering. "Laser induceret selektiv aktivering" (LISA) er en ny teknologi, der introduceres i projektet som en metode til fremstilling af såkaldte 3D moulded interconnect devices (3D-MID). Metoden muliggør metallisering af en plastoverflade, der er modificeret ved hjælp af en laser og aktiveret med en $PdCl_2/SnCl_2$ opløsning.

Der eksisterer forskellige industrielle metoder til fremstilling af MID, f.eks. LDS® eller to-komponent sprøjtestøbning. LISA har økonomiske og miljømæssige fordele i forhold til disse teknologier. LISA kan bruges på mange forskellige plasttyper, uden at der blandes fyldstoffer i selve plasten. Projektet viser at bl.a. polyethylene, polystyrene, polycarbonate og ABS kan bruges i LISA processen. Derudover er brugen af meget giftige kemikalier som f.eks. kromsyre elimineret i LISA.

$PdCl_2/SnCl_2$ aktiveringssystemet er baseret på andre forskeres arbejde. Undersøgelserne i projektet er fokuseret mod at forstå hvorfor de laseraktiverede områder fastholder aktiveringspartiklerne bedre end de andre dele af overfladen. Den første hypotese bygger på antagelsen om at der sker en kemisk ændring af polymeren ved laserstruktureringen, således at aktiveringspartiklerne bindes kemisk til plastoverfladen. Eksperimentelle undersøgelser med XPS og FTIR spektroskopi kunne hverken bekræfte eller afkræfte denne hypotese. Den anden hypotese bygger på antagelsen om, at den laserstrukturerede overflade har en større affinitet i forhold til aktiveringspartiklerne. Denne hypotese blev bekræftet ved hjælp af undersøgelser af overfladespændinger. Tredje hypotese bygger på diffusion af aktiveringspartikler ind i den laserstrukturerede overflade. Denne hypotese blev bekræftet af korttids-metalliseringsforsøg kombineret med en modellering baseret på Fick's diffusionslove.

Indflydelsen af laserparametre på den dannede overfladestruktur er blevet undersøgt for Nd:YAG, UV og fiber-lasere. Mekanismen i overfladedannelsen er diskuteret og Nd:YAG procesparametrenes indflydelse på overfladestrukturen blevet undersøgt. Der er en tendens til at højden af den laserstrukturerede del af plastoverfladen stiger med laserstrålens energi. Der er blevet udviklet en karakteriseringsmetode til de porøse overflader baseret på bærekurven for overfladen.

To metalliseringsmetoder er blevet sammenlignet ved observation af hastigheden af metalliseringen. Det blev konstateret, at metalliseringshastigheden er uafhængig af lasersporets højde, under forudsætning af at lasersporet har en porøs struktur. Vedhæftningen af kobberlaget er afhængig af lasersporets struktur. En høj laserenergi resulterer i et højt voluminøst laserspor, der sikrer en bedre vedhæftning af kobberet til plastoverfladen.

LISA metoden er blevet testet til fremstilling af en række antennestrukturer. To simple former (planar dipole og planar loop) og en såkaldt co-planar stripline blev undersøgt. Antennestrukturerne fremstillet med LISA teknologien viser impedans karakteristika som forventet og er sammenlignelige med standard PCB teknologi.

Table of Contents

Chapter 1. Introduction and project definition

1.1 Project background

Molded interconnect devices (MIDs) integrate electrical and mechanical functions in a single construction unit, as illustrated by Figure 1.1. Compared to conventional printed circuit boards technology, the injection molded substrate for MIDs can be in 3 dimensions. MIDs can integrate electrical and mechanical elements into almost any shape of interconnected device allowing entirely new functions to be created. The advantanges of 3D-MID technology include [1]:

- Reduction of the number of components and space saving.
- Minimization of the product size.
- Flexibility of design and development.
- Improvement of the functionality and reliability.
- Increase of the quality of a given system and the logistics of production.
- Reduction of the production cost.
- *Etc.*

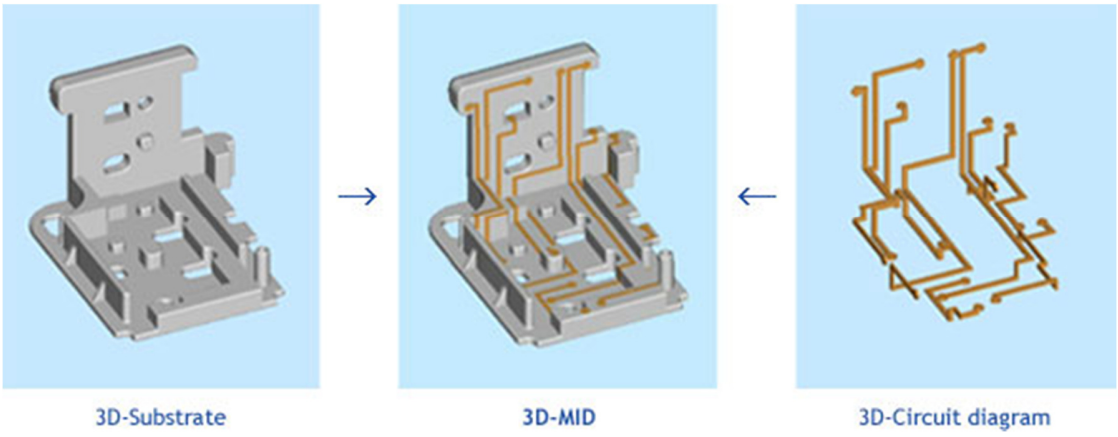

Figure 1.1 Illustration of the MID technology [2]

Key markets for the MID technology are automotive electronics and telecommunications. Besides those, MIDs are also suitable for computers, household appliances or medical technology (e.g. hearing aids). It is most often used in three basic ways: electro-mechanical (signal or current carrying traces), RF technology (antennas), and for shielding applications [3].

For instance, in the automotive industry, MIDs are commonly used in the interior locations of vehicles as adaptive cruise control, headlight sensors, windshield wiper sensors and door/window switches, or other applications including pressure and flow sensors for engine management, air conditioning, crash detection and exterior lighting fixtures [4].

Another example of an MID application is the Microsoft Joystick Switch mount, as illustrate by picture (a) in Figure 1.2 [5]. It used multi-planar 3D circuit geometry to minimize the used space and reduce the components count. The problem of needing to mount and interconnect eight

switches and eight diodes over four planes was overcome. The MID solution provided electrical pathways and mounting pads over multiple planes, eliminating 16 separate wires and four circuit boards, as well as providing significant labor reduction. This component was manufactured in mass production with more than 2.5 million parts.

The MID market is currently showing an annual growth rate of about 20% [2]. Two antennas manufactured by MID technologies are shown in Figure 1.2 [3]. The relevant technologies, LDS® and 2-shot injection moulding will be introduced in the next chapter.

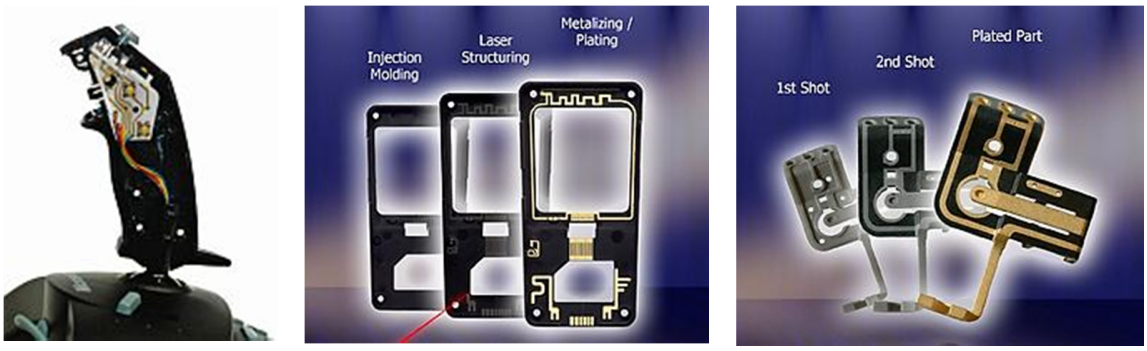

(a) (b) (c)

Figure 1.2 Electroni components utilizing MID technologies (a) Microsoft Joy Stick (b) antenna manufactured by LDS® (c) antenna manufactured by 2-shot moulding [3]

Laser induced selective activation (LISA) is a new technique for selective metallization on polymers for 3D MIDs. A patent application was filed in 2007 including the author as a co-inventor [6].

The process chain of LISA is illustrated in Figure 1.3 [7]. In step 1 the laser 'draws' the desired pattern on the polymer substrate in a medium of water; the surface of the laser-machined area becomes as porous as a sponge. Step 2 (in Figure 1.3) is the activation of the laser-machined area, where the workpiece is submerged in an activation solution composed mainly of $PdCl_2$ and $SnCl_2$. In this step, the activation colloids adhere to the laser machined area due to one or more mechanisms. Finally, in step 3 (in Figure 1.3) the metallization of the laser track is accomplished by a commercial auto-catalytic electroless copper bath (or nickel, or palladium bath), and the activation colloids play a role as the seeds for copper deposition**.** Optionally, subsequent metal layers such as nickel and gold can be deposited on top of copper.

The work needing to be done for LISA includes:

- Exploring the mechanism of LISA, e.g. how the special structure forms during the laser machining, why LISA, etc can realize the selective plating.
- Investigating the process parameters, so that the product quality can be controlled by all the input parameters, e.g. laser setup, plating time, etc.

- Optimizing the process chain, so that the product made by LISA can meet industrial standards and requirements.

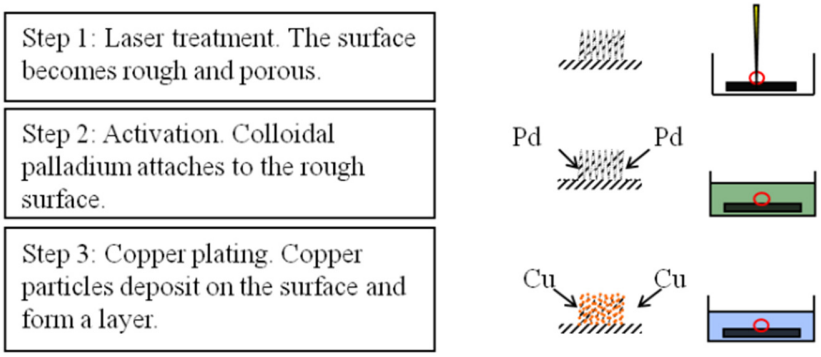

Figure 1.3 Process chain of LISA in brief [7]

1.2 Project definition

It is the overall objective of the PhD project to develop process chains for establishing micro structured polymer surfaces with a specific functionality, i.e. the ability to be plated in an autocatalytic electroless plating bath. This is done by applying a systematic approach to surface engineering comprising surface specification and design based on functionality, surface generation based on complex process chains and surface characterization (as indicated in Figure 1.4).

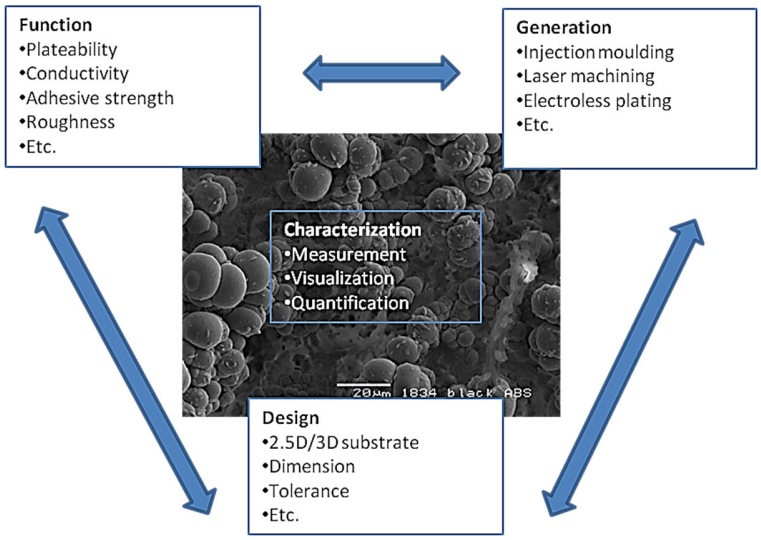

Figure 1.4 Surface engineering approach [8]

Available laser technologies are investigated theoretically and experimentally and their capability in terms of achievable surface structure, overall precision, coating quality, *etc.* will be

identified. The process referring to Nd: YAG laser is the subject of intense investigations. The mechanism of the activation process is another subject.

The work is based on experimental as well as theoretical approaches. The characteristic properties of process chains and obtainable surfaces will be described using a variety of analysis instrumentation available at DTU MEK or collaborating institutes (microscope, profilometry, SEM, *etc*.). The investigations will use materials typical for micro-products and industry, for example polycarbonate, polystyrene, *etc.* Antennas will be produced as demonstrators and evaluated on the basis of functional tests.

1.3 Project and thesis plan

The reseach plan of this project is illustrated by the flowchart in Figure 1.5. Based on the primary process chain (in red boxes) of LISA, optimization of the process or mechanism exploring work is carried on. The main methods to accomplish the study are set in purple boxes.

This thesis presents 3 years of research work. First, the state of the art of 3D-MIDs technology is introduced. Several leading technologies in the industrial market also among the popular research are compared with LISA. The main experimental laboratory set-up is the following discussion, and the involved parameters of intensively used Nd: YAG laser is explained. Then the working principle of LISA is explained. The mechanism of the activation and subsequent copper growth is analyzed from several possible aspects. The next chapters state the process in detail. The laser track is observed by optical and scanning electron microscopes, and the structure is analyzed using several methods. The velocity and the quality of the plating are studied. The goal is to find out an optimized laser setup which can result in plating with the best quality, fast plating velocity, and also minimize the energy consumption. Finally demonstrators on 2.5D substrates are displayed. Also antenna manufactured using LISA technology is shown and compared with antennas using PCB technology.

Additionally, in this thesis:

- The term “laser track” refers to an area or line machined by laser.
- The term “LISA surface” refers to the area machined by laser, which can be activated and then successfully plated by an auto-catalytic electroless copper bath.

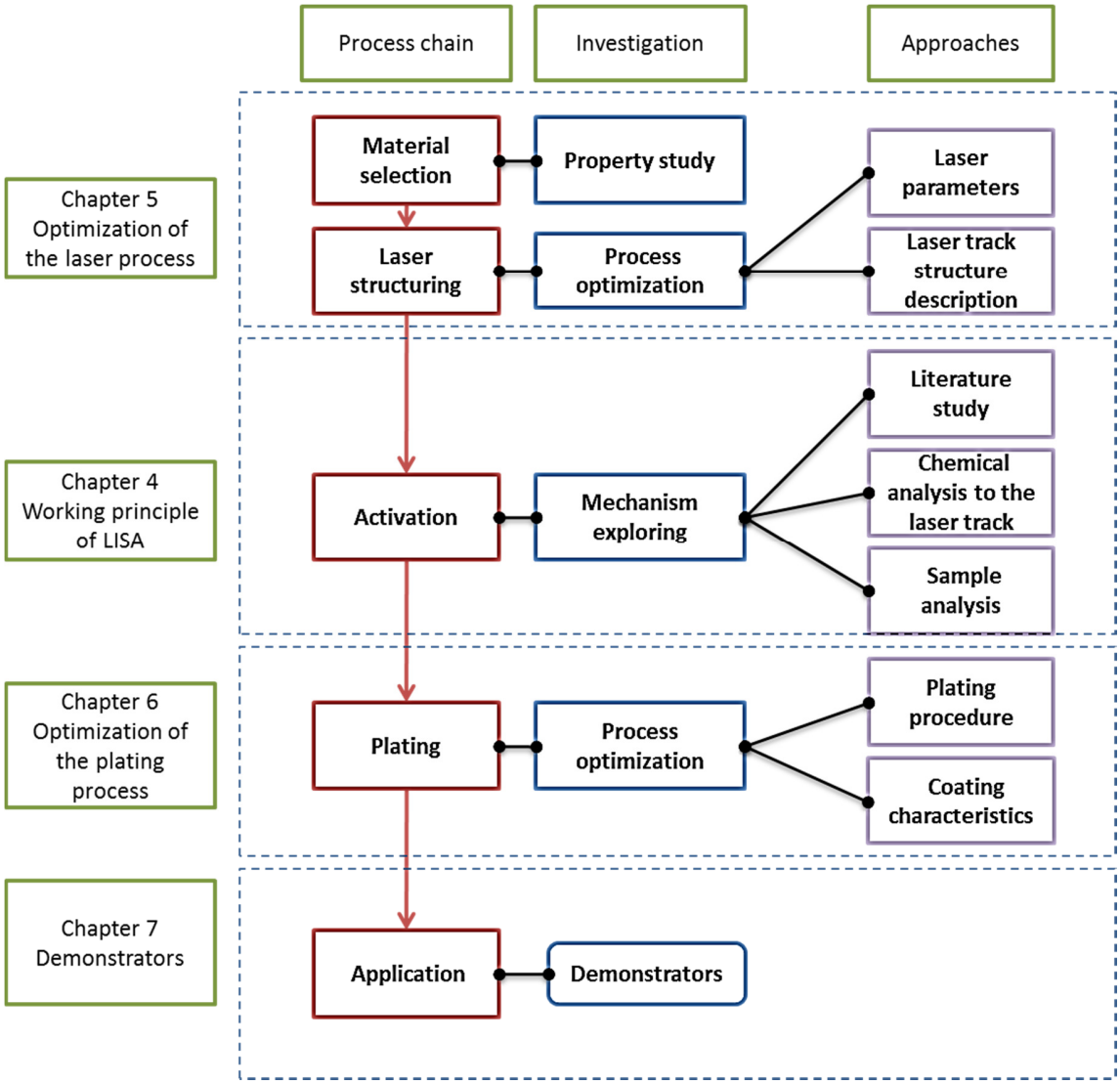

Figure 1.5 Scheme of the project plan

1.4 Acronyms and abbreviations

The following list of acronyms and abbreviations will be used frequently and without additional explanation. Furthermore the chemical symbols for all elements (and alloys) will be used consistently (e.g. Pd for palladium, Cl for chloride, *etc.*).

3D-MIDs	3 dimensional - molded interconnect devices
ABS	Copolymer of acrylonitrile, butadiene and styrene
AFM	Atomic Force Microscopy

CNC	Computer numerically controlled
COV	Coefficient of variance
CVD	Chemical Vapour Deposition
CW	Continuous wave
DOE	Design of experiments
EDAX	Energy Dispersive Analysis by X-rays (commercial name for EDX)
EDX	Energy Dispersive X-ray analysis (=EDAX)
FTIR	Fourier Transferred Infrared Spectroscopy
LDS®	Laser direct structuring
LISA	Laser induced selective activation
Nd: YAG	Neodymium-doped Yttrium Aluminium garnet
OSP	Organic solderability preservative
PE	Polyethylene
PBT/PET	Blend of polybutylene terephthalate and polyethylene terephthalate
PC	Polycarbonate
PCB	Printed circuit board
PS	Polystyrene
PVD	Physical Vapour Deposition
SAN	Copolymer of styrene and acrylonitrile
SEM	Scanning Electron Microscopy
SHE	Standard Hydrogen Electrode
UV	Ultraviolet

XPS	X-ray Photoelectron Spectroscopy

Reference

[1] G. van Alst, P. van Dijk and F. van Meijl, “MID interconnection considerations”, Circuit World, Vol. 22, No.1, 1996, pp. 14-17.

[2] Internet source: http://www.3d-mid.de/cms/front_content.php?idcat=10, accessed: 01-10-2010.

[3] Internet source: http://www.tycoelectronics.com/catalog/html/en/Presentations/AntennaManufacturingCapabilities_embeddedantennas.html, accessed: 07-10-10.

[4] Internet source: http://www.tycoelectronics.com/mid/automotive.asp, accessed: 07-10-10.

[5] Internet source: http://www.tycoelectronics.com/mid/electronics.asp, accessed: 07-10-10.

[6] P. T. Tang, P.C. Nielsen, J. S. Nielsen, H. N. Hansen, Y. Zhang, “Preparation of a Polymer Article for Selective Metallisation”, Patent application filed March 30, 2007, published as WO2008/119359 A1.

[7] Y. Zhang, P.T. Tang, H.N. Hansen, J.S. Nielsen, “Electroless Plating on Plastic Induced by Selective Laser Activation”, Plating and Surface Finishing, Vol. 97, pp. 43, 2010.

[8] L. De Chiffre, P. M. Lonardo, H. Trumpold, D. A. Lucca, G. Goch, C. A. Brown, J. Raja, H. N. Hansen, “quantitative characterization of surface texture”, Annals of CIRP, Vol49/2/2000, pp.635, 2000.

Chapter 2. State of the art

2.1 Plating on plastic

Plating on non-conductive materials has a long history already. At the beginning the purpose was mainly for decoration. Since the 1960s, plating on plastic became a commercial process, and industries like automotive, plumbing, appliance and electronics started to utilize the technologies [1]. Plastics plating was develop for industrial interests because of the low cost, the ability to mold large and complex parts, the weight reduction, *etc*. In the early 1970s, when the gasoline crises occurred, weight reduction became a very important benefit to the automotive industry.

Until today, many plastic materials are plated, including ABS, polypropylene, polysulfone, polyethersulfone polyetherimide, teflon, polyarylether, polycarbonate, polyphenylene oxide, polyacetal and so on [1]. They are applied in the fields of decoration, shielding of electronics against radio frequency, electromagnetic interference, printed circuits, *etc.* [2].

2.1.1 Chemical plating method

The chemical plating method is well developed, and very little has changed in the last twenty or thirty years [3]. The process includes cleaning, etching, neutralization, activation, acceleration and finally electroless plating. Etchants are usually strong oxidizing solutions that eat away the plastic surface to varying degrees. For ABS, commonly etchants are chromium trioxide or/and sulphuric acid. By etching, the surface area is greatly increased, and the microscopic holes left in the surface provide mechanical anchoring sites for the deposited metal. Neutralizers aim at eliminating excessive etchants. Activators provide the seed for the subsequent electroless-plating, and they usually contain some precious metals such as Pd, Pt, or Au. The $PdCl_2/SnCl_2$ system is mostly used. An accelerator is used after rinsing following the activator, and it is used to remove the excess Sn while leaving the Pd sites intact for the electroless deposition. Then after rinsing, the parts are ready to be plated in an electroless-plating bath.

However the hexavalent chromium contained in the etchant is extremely toxic and is closely regulated in water emission. The minimum use of chromium or even chromium free plating is a popular research area these years, e.g. [3] and [4]. The new method claimed in [4] is chosen to be described in this chapter, because the basic process chain is similar to the conventional method; however the chemical components are changed.

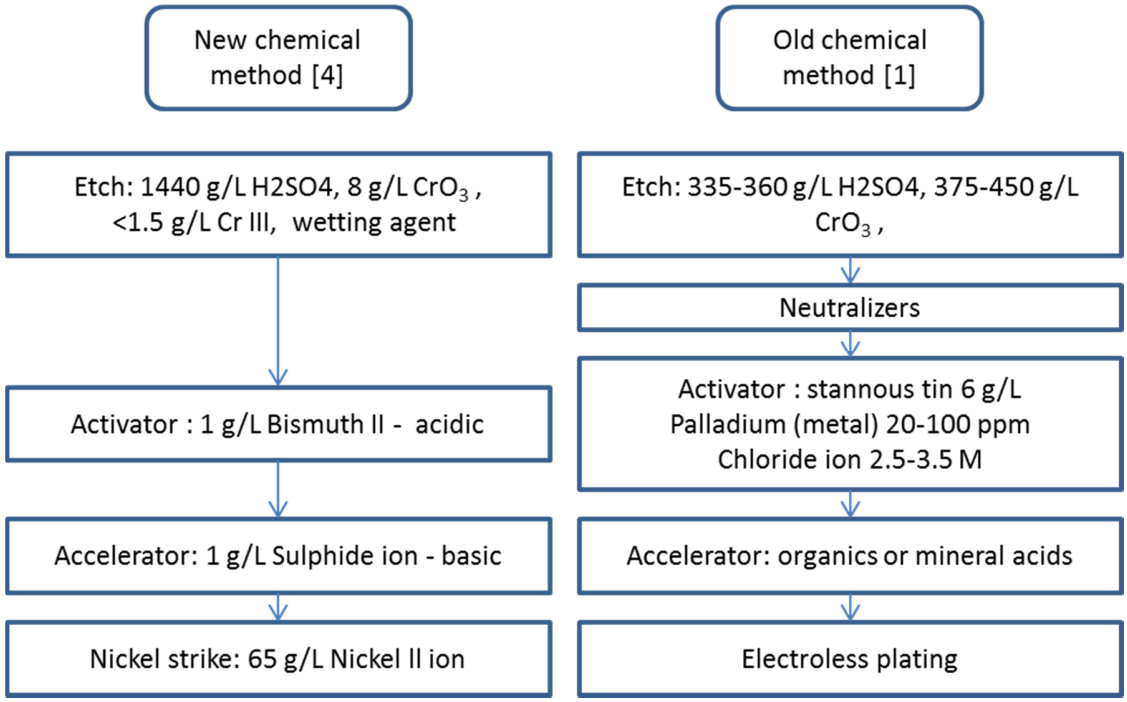

Figure 2.1 Comparison between the new [4] and conventional [1] process chains of the plating method on ABS

The new etch solution contains a content of 6-10 g/L CrO_3, which is 50 times less than in the conventional method [4]. A certain amount of hexavalent chromium is needed to ensure the adhesion of the coating to the substrate. The mechanism of the reduced chromium etch is entirely different from the conventional method. In the conventional way, mixture of chromatic and sulphuric acid attack the butadiene part in the polymer blend and create voids on the surface as explained previously. When chromatic acid is reduced, the principle is that the surface becomes highly polarity due to chemical reactions of SO_3 with the functional groups on the polymer. It is claimed by [4] that when using this new solution, brighter and smoother coatings can be obtained than using the conventional method. Furthermore the adhesion strengths of the coating using those two methods are not significantly different. Some representative products using this new method are shown in Figure 2.2.

Figure 2.2 Representative products using the ultra low chromium plating method [4]

2.1.2 Other techniques for plating on plastic

Alternatively, polymer metallization can be carried out by physical vapour deposition, thermal evaporation, ion beam or magnetron sputtering, and chemical vapour deposition and so on [5]. Compared to wet chemical methods, plasma assisted processes for etching and metallization by physical/chemical vapour deposition or sputtering have advantages such as, low environmental pollution and high gloss finishing [6]. The workpiece is placed in a vacuum chamber in which a metallic vapour is created physically or chemically, and deposited on the product. A protective clear topcoat is then applied over the thin metal layer for abrasion and environmental resistance. The vacuum metallizing process can also be based on an electron beam to vaporize the metal. The sputter plating process uses plasma to produce the metallic vapour [7]. However, to achieve thick metal layer (tens of micrometres), electroplating is always required afterwards.

2.2 Selective plating on polymer

Selective metallization, just as the name implies, can be defined as depositing metal layers only on the area where it is required and without a detrimental side effect. It can be accomplished by masking, local area of heating, nucleation sites, or local application of electrolyte solutions [8].

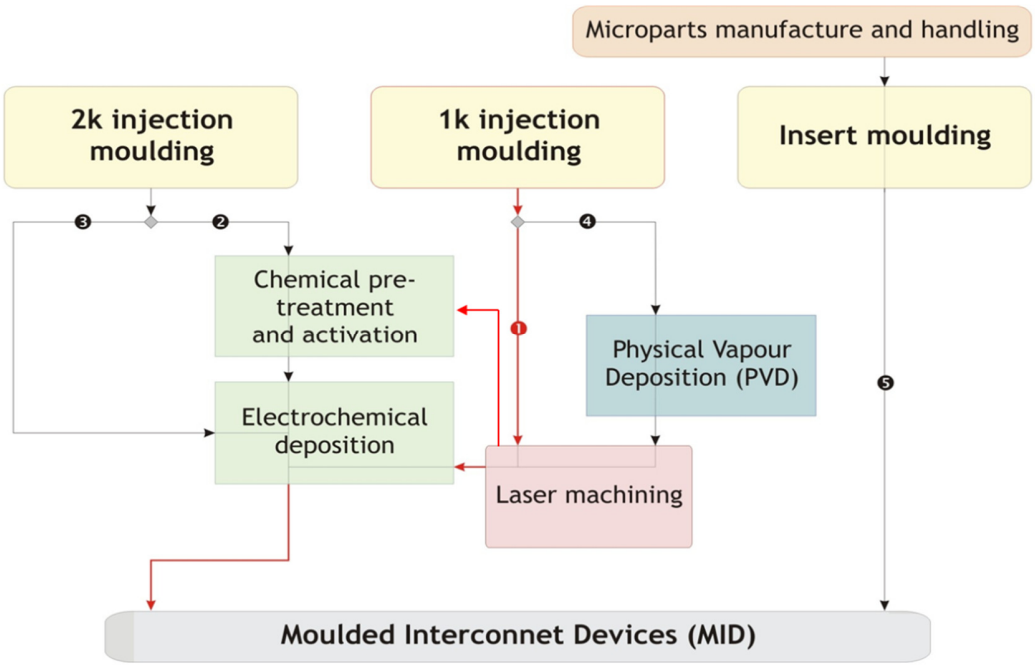

Figure 2.3 Process chains of MID technologies [9]

MIDs are manufactured using a large variety of processes but what is common to all process chains is the use of injection molding. Figure 2.3 shows several process chains for MID production [9]. For workpieces made by conventional one-shot (or 1k) injection molding, laser machining is a good way to prepare the circuit pattern. The 1st chain displays a “positive”

process, i.e. the laser machined area will be plated and kept as the circuits, such as in LDS® and LISA. Otherwise, laser ablation is used, as illustrated by the 4th chain. In the first place PVD or another method is used to deposit a thin layer of metal on the entire surface, and then laser ablation removes the unwanted part. Electroplating and electroless plating are always used to obtain the needed metal coating. Alternatively, two-shot (2k) injection molding can be used, as shown by the 2nd and 3rd chains. The workpiece is composed of two types of polymer, and only the polymer for the future circuits part can be plated. Based on the used polymer, chemical treatment and activation may be needed or not. To avoid wet steps, insert molding can be used, as shown by the 5th chain.

The following contents present several MID techniques and PCB technology, in order to give an overview of the leading technologies and compare with LISA.

2.2.1 PCB and other printing technology

A printed circuit board is an insulating substrate material, e.g. Teflon, FR-4, CEM-1, *etc.* [10], upon which circuits is either etched or plated. If semiconductor devices are applied to the circuit pattern, the circuit is called a hybrid microcircuit [1]. This technology is famous for the low cost and high reliability for mass production [11]. It is also referred to as printed wiring board (PWB) or etched wiring board.

The process can be subtractive or additive. The basic principle for a subtractive process is that etching makes electronic components from copper sheets laminated onto a non-conductive substrate. There are quite a few different dielectrics that can be chosen to provide different insulating values depending on the requirements of the circuit. These materials can also be assembled in a variety of different ways potentially using multiple laminates, different materials and different plated through-hole structures. Copper is plated on the substrate by electroplating or rolling [12]. A mask is used to protect the desired traces; exposing a photo resist to UV-light through a photo mask creates the mask. Then subsequently etching removes the unwanted copper. It's also possible without a mask, like PCB milling, which uses a mechanical milling system to mill away the copper foil from the substrate [13].

Regarding the additive process, a reverse mask, which exposes the desired part, is applied to the substrate with a thin layer of copper on top. Additional copper as well as other metal layers like nickel and gold is then plated onto the board in the exposed areas; then the mask is stripped away and a soft etching step removes the original copper laminate from the board, so only the desired traces are left. The additive process is commonly used for multi-layer boards due to the capability to plate through holes in the circuit board [10].

2.2.2 MID technologies: 2K injection molding and insert injection molding

2k-injection molding (or 2-shot injection molding, 2-component injection molding) is a mature MID technique. The method is tied to product-specific tools to create a circuit on the

component. However, increasing the miniaturization of the circuits on MID components leads to a considerable rise in tooling-up time and expense [14].

In two-component molding, two different polymer materials are sequentially or simultaneously injected into a mold to make products with a layered structure [14]. In order to achieve selective plating, a catalyzed "plateable" resin is molded in conjunction with a standard non-plateable resin to define the desired area to be plated. This area is metallized initially with copper, followed by nickel and, optionally, gold plating. The plated area has the benefit of accurate tolerance and registration due to the fact that it is created by mold steel [15].

In insert molding, metallic circuit structures or flexible polymer foils with printed circuit pattern are used as inserts [14]. Figure 2.4 displays examples made by those two technologies.

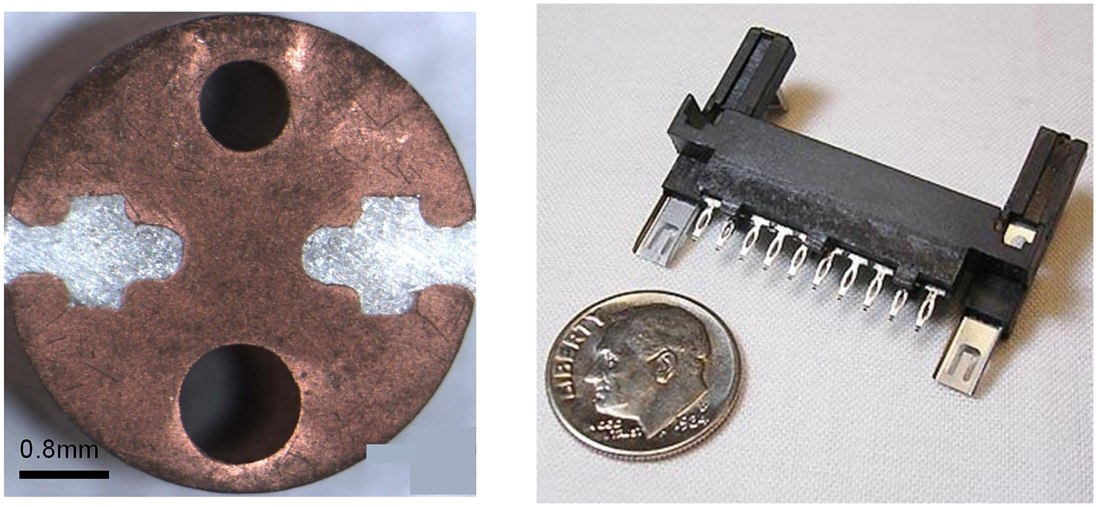

(a) (b)

Figure 2.4 (a) 2k injection molding sample [14] (b) Insert molding sample [16].

The main limitation of those two technologies is the complicated mold design, which increases the cost and makes the process not as flexible as laser based processes. Also, the available material range is still limited and usually a large amount of toxic chemicals has to be used.

2.2.3 MID technology: MIPTEC process developed by Panasonic®

Microscopic integrated processing technology (MIPTEC) is developed by Panasonic® [17]. Laser ablation is used to make a pattern on a full plated surface. It is claimed that fine and accurate (±30 µm) structures can be achieved by this technology. Besides, internal surface can also be machined.

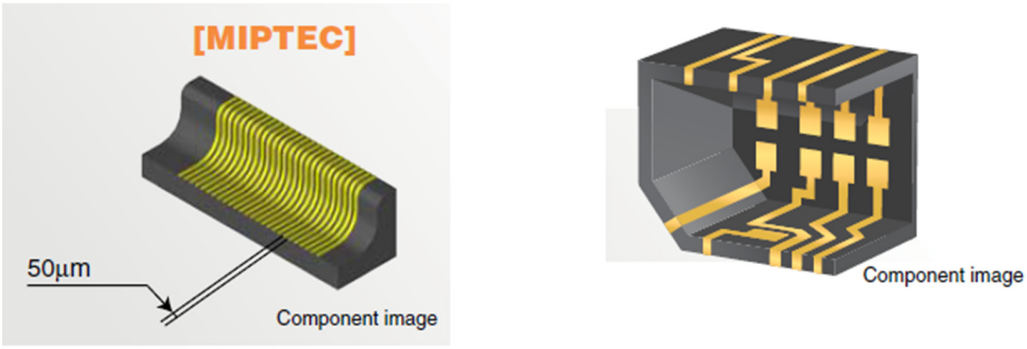

(a) (b)

Figure 2.5 MIPTEC samples [17]. (a) MIPTEC is able to form a pattern of line/space=50µm/50µm on a side wall. (b) Sample of internal pattern.

Many polymers, such as polyphthalamide (PPA) and liquid crystal polymer (LCP), and ceramics like alumina and aluminum nitride are available to this process.

Surface activation processing and original material development provide extra pattern surface smoothness and strong adhesion of the circuit pattern – enabling stable flip-chip mounting and wire bonding of bare chips. Figure 2.6 displays the comparison of the smoothness between the surface made by MIPTEC and a conventional method.

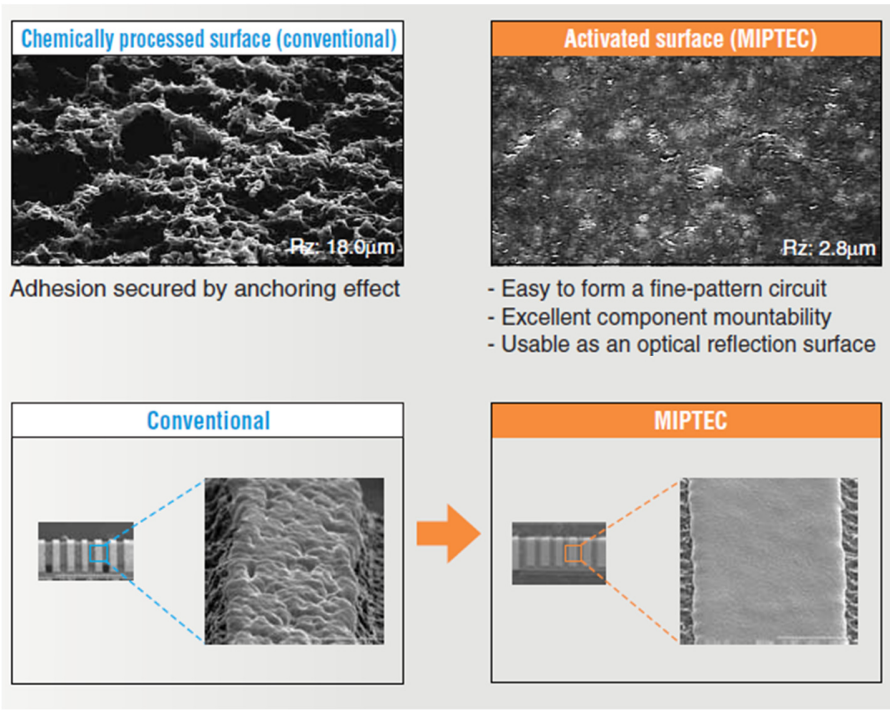

Figure 2.6 the pattern smoothness comparison between MIPTEC and conventional method [17]

Figure 2.7 illustrates the process chain of MIPTEC. Firstly the molded parts are processed by plasma, and a thin film of copper is formed by physical vapour deposition (PVD) all over the surface. A laser beam is utilized to remove the copper layer surrounding the desired pattern, then the desired pattern is connected to a circuit and electroplating is applied, so the thickness of copper layer is increased. Afterwards, soft etching removes the unwanted metal part. Lastly, on top of the copper layer, nickel and gold layers are electroplated. Now the parts are ready for dicing and assembling.

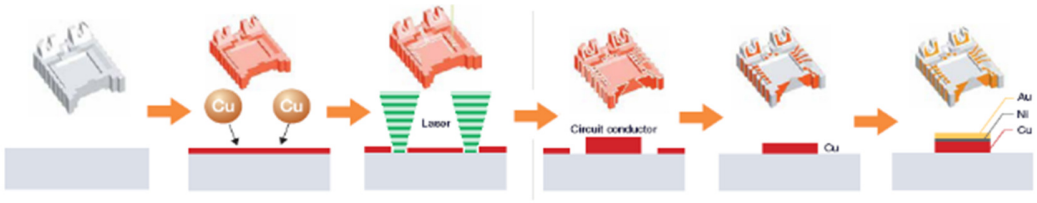

Figure 2.7 The process chain of MIPTEC [18]

This technology, as mentioned before, has a high accuracy and ability to make fine structures, which contributes to high performance and high reliability of the products and modules. Also the freedom of making pattern on 3D parts is increased. The pattern is controlled by laser programming, which can be rewritten in the middle of the design. So the development speed is increased and the cost is reduced.

However there are certain disadvantages, which limit the application:

- Extra equipment such as plasma and PVD increase the cost.
- It is a line of sight process.
- Full plating means that a relative large part of the metal layer is removed. This is a waste of material, and it increases the cost.
- The available polymer range is limited.

2.2.4 MID technology: Laser direct structuring (LDS®)

Since 1997, LPKF has developed LDS technology as a laser-based procedure for the production of MID: laser direct structuring, i.e. LPKF-LDS® [18]. And now it is a commercial available industrial process, which has lots of successful cases.

The LDS® process chain includes:

1. Injection molding

Special fillers are mixed to the thermoplastic granules, and there are several types of plastic available for this process. One shot injection molding is used to produce the parts to be laser structured.

2. Laser structuring

The laser beam draws patterns on the surface of the parts. The special fillers release metallic nuclei since the laser beam activates a physical-chemical reaction. The released nuclei act as a catalyst for reductive copper plating. Moreover, a rough surface forms in the laser structuring process, so copper particles can entangle with the plastic thus providing strong adhesion between the copper layer and the substrate. Figure 2.8 illustrates this process.

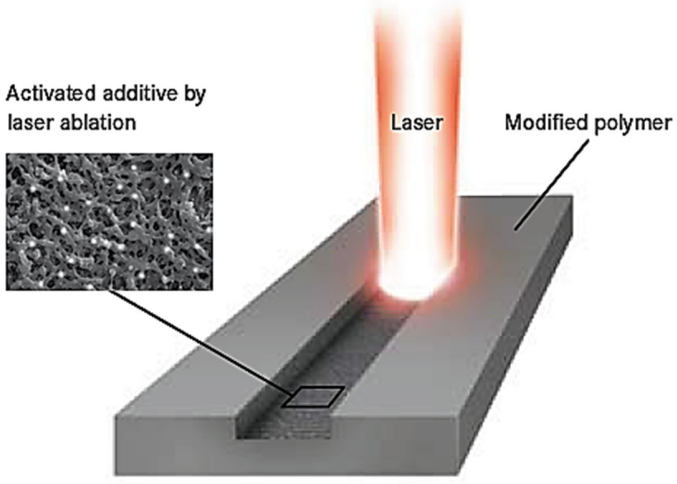

Figure 2.8 Illustration of the laser treated surface for LDS® [18]

3. Metallization

Electroless copper plating bath is used for the metallization process. Subsequently nickel and gold plating is performed on top of the copper layer. A cleaning step is required before the copper plating. Specific coatings such as Sn, Ag, Pd/Au, OSP, *etc*. can also be created.

Now the parts are ready to be assembled.

LDS® is a stable and promising process [19]. Free design of the needed pattern is realized, and no complicated mold is needed. However, the process is quite expensive due to the delicate laser equipment and the special polymers. The limited range of available material is another challenge. In addition, the process-working window is quite narrow.

2.3 Comparison between LISA and other laser involved technologies

Compared to MID using 2k injection molding or insert injection molding process, LISA uses laser to draw the pattern on the substrate, which makes the pattern design much more free. It can be modified conveniently, which is not limited by the mold production. LISA also has several economic and environmental advantages over other laser involved technologies [20]. Table 2.1 makes a comparison between LISA and some of the mentioned technologies. Firstly, the range of available polymers is wide, and no pretreatment such as filler premix is need. Commercial polymer such as PE, PS, PC, and ABS *etc.* can be used in LISA process directly, which decreases

the production cost significantly. Meanwhile no extra equipment except laser is needed. Second, in the wet steps, no chromic acid or other similar toxic compounds are used, which is environment friendly.

Table 2.1 Comparison between LISA and some other typical technologies

	LDS®[18]	MIPTEC®[17]	Chemical plating	LISA
Materials	Special grades of PSU, LCP, PPA, PA6/6T, PET, PBT, PC, ABS, *etc*.	PPA, LCP, alumina, aluminum nitride, etc.	ABS, PP, Teflon, PC, PA, PPO, LCP, polysulfone, PES, PEI, *etc*.	PE, PP, PS, PC, ABS, PBT/PET, PEI, PA66, *etc.*
Main pretreatment	Mixing special filler in substrate	Plasma and PVD	Etching, predip, neutralization	The material should be able to absorb the laser energy
Circuits pattern	Laser structuring	Laser ablation	Laser ablation or 2k molding	Laser structuring
Laser type	Special wavelength to crack chemical bonds, special laser head to improve the adhesion	Special wavelength to remove the metal layer	Special laser wavelength to remove the metal layer	Standard industrial lasers e.g. UV laser and Nd: YAG laser *etc*.
Plating	Electroless plating	Electroplating	Activation and electroless plating	Activation and electroless plating

Reference

[1] G. O. Mallory, J. B. Hajdu, "Electroless Plating - Fundamentals and Applications", William Andrew Publishing/Noyes, 1990.

[2] W. G. Simpson, "Plastics: surface and finish", The Royal Society of Chemistry, 1995.

[3] R. Hamilton, C. Buehler, S. Brown, "A New Plating-on-Plastic Process for Chrome Plating non-ABS Substrates", Conference Proceeding, Sur/Fin 2009, Kentucky, US, 2009.

[4] A. Fath, J. McCaskie, "Metallizing of Plastics with Virtually Hexavalent Chromium Free Etch Solutions", Conference Proceeding, Sur/Fin 2009, Kentucky, US, 2009.

[5] G. Wypych, "PVC Degradation & Stabilization", ChemTec Publishing, 2nd Ed. 2008.

[6] H. Kupfer, R. Ostwald, "Physical and chemical surface preconditioning and metallization of thermalplastics for electronic components", Metallized plastic 5&6, Fundamental and applied aspects, pp.85-96, K.L. Mittal [Ed.], 1998.

[7] Dominick V. Rosato, Donald V. Rosato, M. G. Rosato, "Plastics Design Handbook", Springer - Verlag, 2001.

[8] D.M. Mattox, "Handbook of Physical Vapor Deposition (PVD) Processing", William Andrew Publishing/Noyes, 1998.
[9] H. N. Hansen, P. T. Tang, A. Islam, and G. Tosello, "Selected process chains for manufacturing of moulded interconnect devices (MID)", Conference Proceeding, 7th euspen International conference, Bremen, 2007.
[10] Internet source, http://en.wikipedia.org/wiki/Printed_circuit_board, accessed: 01-10-2010.
[11] C. F. Coombs, "Printed Circuits Handbook", 6th Ed, McGraw-Hill Professional, 2007.
[12] Internet source, http://www.ieee.li/pdf/viewgraphs_pwb_design.pdf, accessed: 01-10-2010.
[13] W. C. Bosshart, "Printed circuit boards: design and technology", Tata McGraw-Hill, 1983.
[14] M. A. Islam, "Two component micro injection molding for molded interconnect devices", Ph.D. thesis ISBN: 978-87-89502-75-5. 2008.
[15] Internet source, http://www.tycoelectronics.com/mid/2shot.asp, accessed: 07-10-2010.
[16] Internet source, http://www.threerplastics.com, accessed: 01-10-2010.
[17] Technical Brochure, "MIPTEC, Micro Integrated Processing Technology", Panasonic Electric Works 3D Packaging Devices, Panasonic Electric works Co., Ltd, 2009.
[18] Technical Brochure, "3-Dimensional Circuits, Laser Direct Structuring Technology (LPKF-LDS™) for Molded Interconnect Devices", LPKF Laser & Electronics AG, 2009.
[19] Internet source, http://www.molex.com/molex/products/family?key=laser_direct_structuring_lds_technology&channel=products&chanName=family&pageTitle=Introduction, accessed: 17-01-2011.
[20] Y. Zhang, P. T. Tang, H. N. Hansen, J. S. Nielsen, "Electroless Plating on Plastic Induced by Selective Laser Activation", Plating and Surface Finishing. Vol. 97, pp. 43, 2010.

Chapter 3. Main Lab set-up of LISA

This PhD project aims at building up special surface structure, which can be metalized in the subsequent steps. It is necessary to introduce the experimental set-ups at the beginning. The toolbox includes the main studied laser equipment, the substrate fixture, and the liquid used as medium for laser treatment. All the other equipments, for example, the analytical instruments, are attached in Appendix 2.

The set-up in activation and plating steps are also introduced in this chapter.

All the studied polymers in this project are commercial grades. Their commercial names are attached in Appendix 1, as well as datasheets for the most used grades in this project, PC and PBT/PET.

The following conctents introduce the tools and relavant set-ups, sequenced by the step in the LISA process.

3.1 Step 1: laser structuring on substrate

3.1.1 An Nd: YAG laser

An Nd: YAG laser is the main studied equipment for the laser process, as shown in Figure 3.1. It is from BAASEL Lasertech® and made in Germany in the beginning of 1990's.

Figure 3.1 The studied Nd: YAG laser (BAASEL Lasertech®), located in DTU.

There is a monitor on the laser. A clear image can be obtained when the laser beam is focused on the substrate. The height of the platform for placing the sample can be set manually, however, it cannot move horizontally. The movement of the beam is realized through a laser beam scanner, which will be explained in the following section. The laser beam focus range is around 1mm; there are several platforms available in the lab, and their Z direction movement resolutions are all fine enough to find the focus.

3.1.2 Laser parameters for the studied Nd: YAG laser

As shown in Figure 3.2, there are three major parts in a typical Nd: YAG laser: the flash lamp which is the pump source (in the studied laser it is an arc lamp instead), a pair of mirrors which make up the optical resonator, and the Nd: YAG crystal which is the laser medium [1].

The Neodymium-doped Yttrium Aluminium Garnet (Nd: YAG) crystal is the heart of the laser, called gain medium or active laser medium, which acts as a light amplifier at the specific wavelength 1064 nm. It transfers external energy into laser beam. This wavelength is in the band of near infrared, so it can be absorbed by most of opaque materials [1].

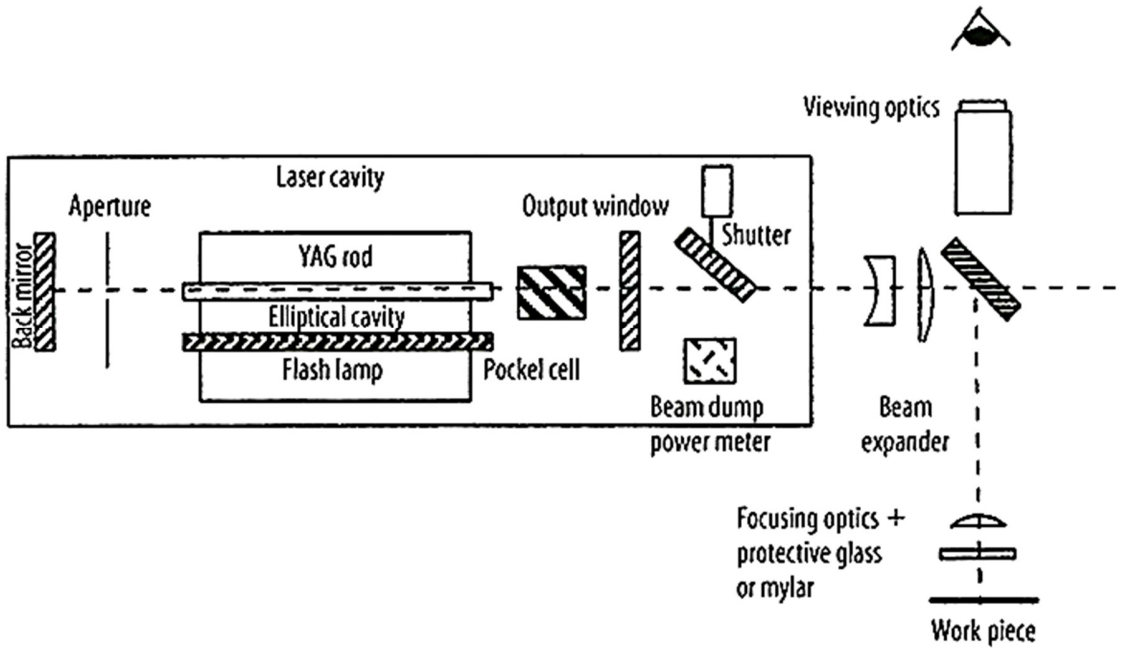

Figure 3.2 Construction of an Nd: YAG laser with Q-switch shutter [1]. The laser studied in this project is with an arc lamp instead of a flash lamp.

When light provided by the arc lamp is transmitted into the rod through its cylindrical surface, the laser rod is excited, or pumped. So the external light is also called pump source. The light is amplified when population inversion is achieved, which refers to the state with more members in an excited energy state than in lower energy states, and the emission amount is larger than

the absorption amount [1]. For the studied laser, setting the lamp current can control the light intensity of the arc lamp.

A pair of mirrors forms an optical cavity, which is a type of resonator cavity [1]. The coherent beam inside the cavity oscillates between the two mirrors before it is emitted from output aperture, so the YAG rod is passed through more than once [2]. Diffraction or absorption inside the cavity can lead to loss. All photons passing through the rod will be amplified; but to be amplified significantly, they need to be aligned with the cavity, so they can pass through the rod more than once. If the amplification in the medium is stronger than the resonator losses, the power of the circulating light can rise exponentially. When the gain medium is saturated, a light emission is simulated, meanwhile high level state particles return to ground level. The gain saturation and cavity loss balance the pump power, which produce an equilibrium value of the laser power inside the cavity; if the pump power is set to be insufficient, the resonator losses may be larger than the gain and the laser will emit only very small light powers. Then part of the light passes through the partially transparent mirror (the output window as illustrated in Figure 3.2.) and appears as a beam of light. The window is partially reflecting and is selective transparent, e.g. for a YAG laser it has very low absorptions at the 1064μm wavelength. The beam is collimated out of the cavity to be parallel. However a strictly collimated beam cannot be achieved due to diffraction.

To enhance the output peak power and enable them to perform some very demanding tasks, a device called Q-switch (Q stands for quality) is used to break up the output into a series of pulses and at the same time increase the peak power. This technique can produce pulses with high peak power in a laser with a continuous excitation source. The peak power is much higher than produced by the continuous wave (CW) mode of laser, in which the wave amplitude and frequency is constant.

Q-switching is achieved by a type of variable attenuator inside the resonator. An attenuator is an electronic device to reduce the wave amplitude or power preserving its waveform. It can be a mechanical shutter, or other type of device based on various optoelectronic effects, illustrated in Figure 3.2 marked with “shutter”. In most industrial Nd: YAG lasers, an acousto-optic switch is used [3]. This attenuation inside the cavity corresponds to a decrease in the quality factor (or Q factor), which is the ratio of the energy stored to the energy lost per cycle in the optical resonator. When the shutter is closed, the Q-switch prevents laser action by inhibiting light feedback into the gain medium, producing an optical resonator with low Q, and during this closing time, excitation energy continues to be absorbed by the YAG rod, and more electrons jump to the upper laser energy level, which increases the population inversion. Since the rate of stimulated emission depends on the amount of light entering the medium, the energy stored in the gain medium increases as the medium is pumped until some maximum level called gain saturated state.

As the gain saturated state is reached, the Q-switch is quickly changed from low to high Q, and the shutter is opened. Then a large number of excited electrons become available for stimulated emission, producing a large burst of energy until the upper level is depleted [4]. The net result is a short pulse of light output from the laser, which may have very high peak intensity. Figure 3.3 shows two pulses produced by the studied Nd: YAG laser, when the Q-switch frequency (or Q-switch repitiation rate, referring to the number of pulses per second with unit of Hz) is 1200Hz and the lamp current is 18A; Figure 3.4 is the detail of one pulse at same condition. The average power of this pulse is approximately 3 watts, while the peak power reaches a thousand times more than this. The equipment for the pulse shape (PicoScope® 3000 series) and energy measurement (Scientech® Vector D200) is listed in Appendix 2.

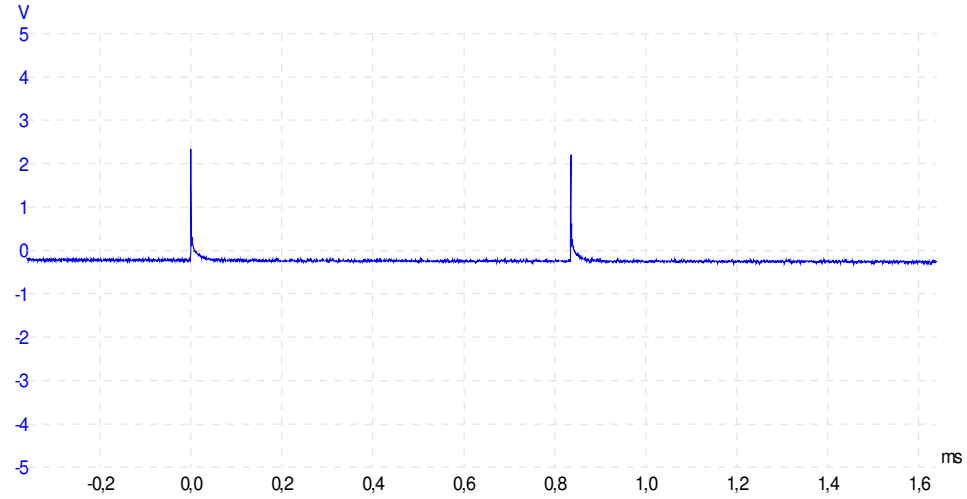

Figure 3.3 Two pulses generated by Q-switch shutter. The lamp current is 18A, Q-switch frequency is 1200Hz.

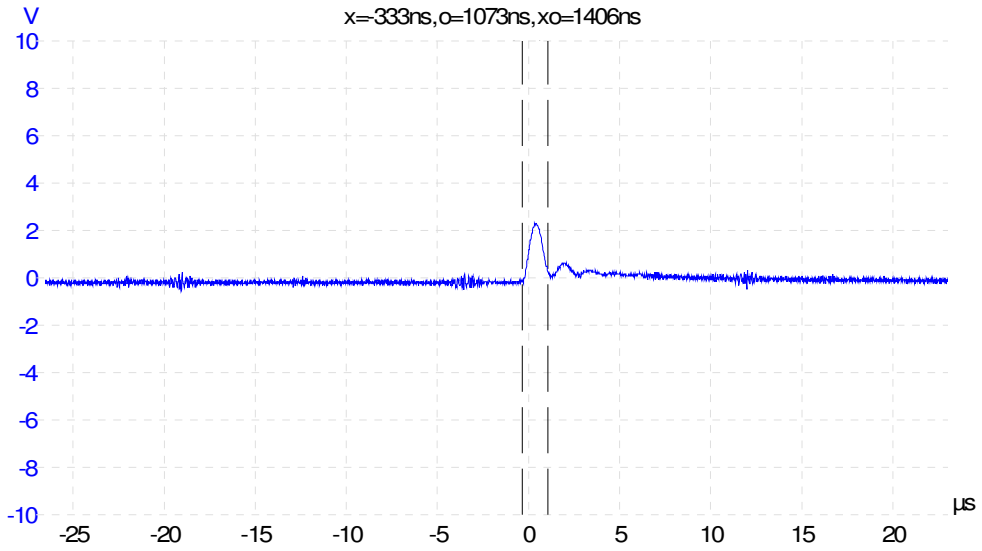

Figure 3.4 A pulse generated by Q-switch shutter. The lamp current is 18A, and the Q-switch frequency is 1200Hz

When the laser is utilized for material processing, the main involved parameters are: the arc lamp's current, and the Q-switch frequency. Besides, the velocity of the laser beam and the number of passes are also influencial.

For the studied laser, the movement of laser beam is realized using a galvanometer scanner. Some laser systems may have a fixed laser head and a movable sample holder such as a CNC (computer numerically controlled) platform.

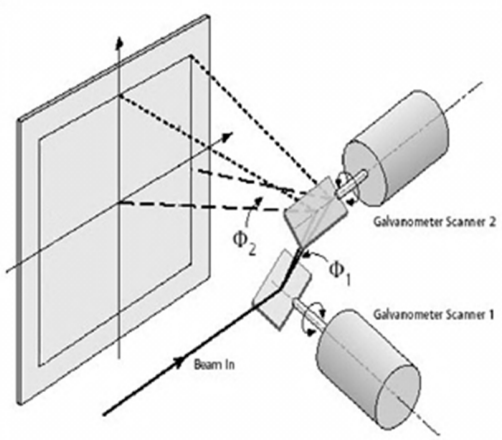

Figure 3.5 Schematic diagram of the laser beam scanner [5]

A scanner is a device that is able to move laser beam with two mirrors in two dimensions: first mirror moves the beam along the X-axis and the second along the Y-axis. The mirrors are fixed on the galvanometers, it means, mirrors are moved by a mechanical meter that senses electric current [6]. Figure 3.5 illustrates the scheme of the scanner system. The position of the galvanometer rotor is controlled by input voltage. Due to their lightness the rotor and the mirrors can move very fast. The control signals for the galvanometer scanners are transferred digitally from computer interface board to the scan head. The digital interface inside the scan head converts the data to analog values that are subsequently transmitted to analog regulator circuits that control the position of the deflection mirrors.

Regarding the studied laser, when the laser beam moves towards one direction, it simultaneously moves along a circle path, which is called wobbling and this movement is used to increase the width of a single line. The wobble size specifies the size of the circle path, e.g. wobble size 4 leads to a track with approximately 0.4mm width on aluminium foil. The speed of moving forward and the wobbling range determine the instant velocity of the laser beam movement. For example, picture (a) in Figure 3.6 shows a laser track made on an aluminium foil, the speed is 60 mm/s and the wobble size is 4. The pattern was not repeated, so the laser beam's movement can be traced. The total direction is from left to right as shown by the black arrow. It can be observed that at the beginning and the ends, the dots overlap more than in the middle range, because at the beginning, the laser beam need accelerate to the nominal speed

and at the end, it needs to decelerate to 0, which means the speed is actually lower than 60 mm/s. So the middle region (picture (b) in Figure 3.6) is used to illustrate how the laser beam moves along circle paths. Picture (c) in Figure 3.6 presents the sequence of laser spots, which intimates the wobbling movement. The wobbling effect can be illustrated more vividly when using another set of wobble size and speed. Figure 3.7 shows (plated) laser tracks on green ABS, and the used laser beam speed was 99mm/s and wobble size 3 for the track in picture (a), and speed 60 mm/s, wobble size 2 for the track in picture (b). The circles are isolated from each other on this track, because the speed was so fast that the distance between two circles is long enough to avoid overlapping.

In this project, wobbling is often used because it increases the width of the laser track. When characterizing the laser-machined surface, a certain area is usually required. For example, the easiest way to make a square is combining several strait lines closely. Wide lines are preferred to minimize the machining time. It is proven that lines made without wobbling can also be plated.

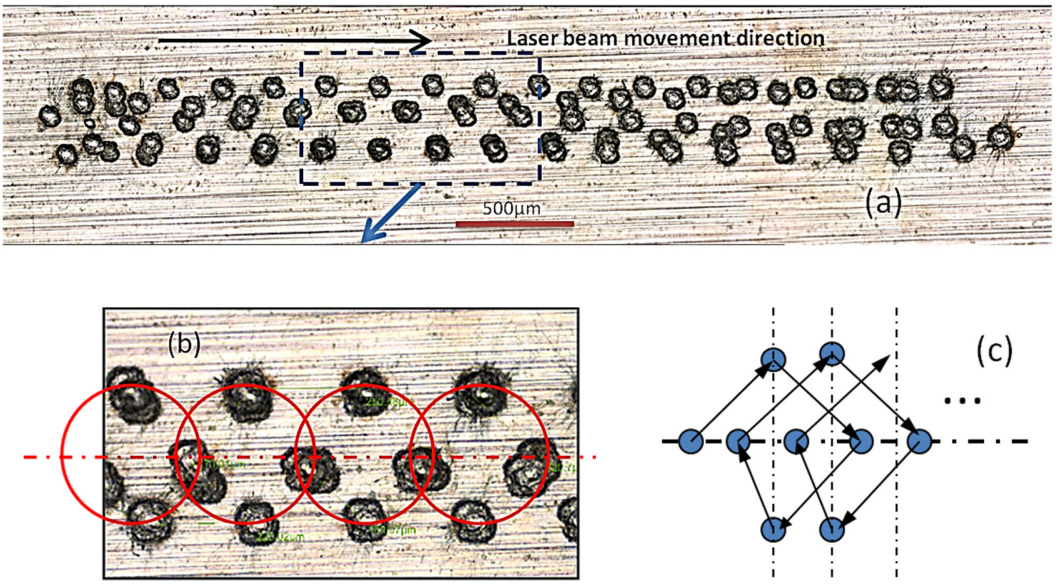

Figure 3.6 Illustration of wobbling by a laser track on an aluminum foil. The pattern was not repeated. The black arrow shows the direction of the movement. (a) the laser track from the beginning to the end, the hight light part is the middle region for picture (b); (b) the middle region, where the dots overlap is less than the two ends; (c) illustration of the wobbling movement

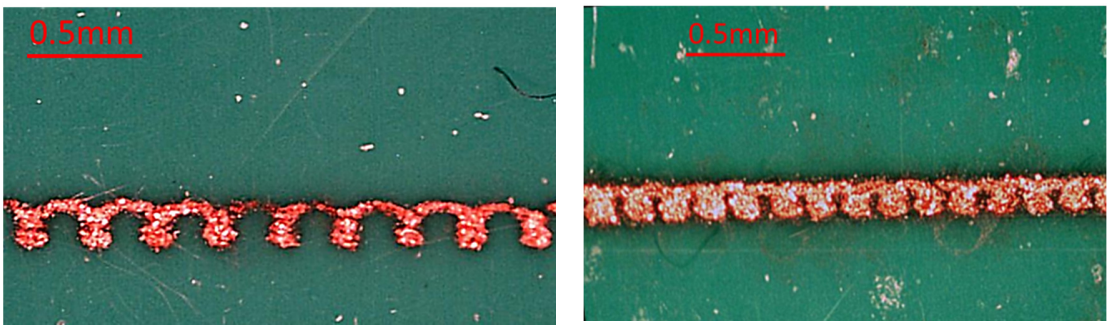

(a) (b)

Figure 3.7 Illustration of wobbling. When the laser beam speed is high enough, the circles can be isolated. (a) a plated laser track made at wobble size 3, speed 99 mm/s (b) a plated laser track made at wobble size 2, speed 60 mm/s

To conclude, for the studied Nd: YAG laser, the involved parameters are: the lamp current, the Q-switch frequency, the laser beam speed, and the wobble size.

3.1.3 Medium liquid

In the previous experiments before LISA research, the workpiece was machined in an open-air environment. However, plating could not occur on those laser tracks. The polymer workpiece can be easily burnt by laser beam. It is found that a cooling medium is required.

Water is used as the cooling medium during the laser treatment. Water is almost transparent to the laser beam (1064 nm wavelength. Distilled water is easy, safe, and cheap to obtain, and reduces the possibility of unknown reactions. Other types of liquids such as alcohol, acetone and soap water (sodium lauryl sulphate solution) were also checked, but no significant difference on the list process was discovered.

3.1.4 Sample holders for laser machining

To hold a polymer plate in water, a shallow glass beaker is the easiest way, as illustrated by Figure 3.8. Two metal blocks are used to weigh down the sample, preventing it from floating.

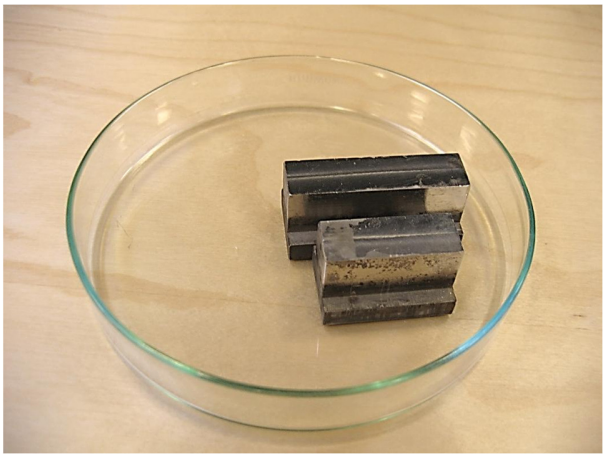

Figure 3.8 A shallow glass beaker is used to hold sample in water. The two metal blocks are used to prevent the samples from floating by weighing them down.

In some cases, the desired laser pattern requires a better alignment with the sample, or water cycle is needed to keep the water clean, so a chamber with a fixture is designed for the YAG laser setup. The chamber is used to hold water, and the fixture aims at preventing samples from floating in water. Based on experiences, constraints are put forward, based on which the conceptive design was performed, and finally the product was made combining the practical conditions.

The constraints to design the chamber include:

1. It should be easy and convenient to change sample.
2. The material should withstand water or acid corrosion.
3. There are specific dimension requirements, e.g. limitation from the laser box size, price, *etc.*
4. If on a moving XY table, water waves should be avoided.
5. Laser could not destroy the bottom of the chamber. The material should be transparent to the laser beam.
6. The chamber should be mechanically strong enough to hold water or other liquids.
7. The chamber might be water or vapour tight in the connection part of the lid and the body. Apparently the box is not allowed to leak.
8. A lid with a laser transparent window may be required, used to prevent damage to the laser lens. Beam divergence and energy lost should be minimized when laser beam goes through. During the laser process, avoid water vapour condensing on the window
9. A water circuit can be generated, e.g. using pump and filter.

The constraints to design the fixture include:

1. The material should withstand water or acid corrosion.
2. There are specific dimension requirement, eg. Limitation from the chamber, the focus distance, *etc.*
3. It should be possible to adjust the depth of water over the sample.
4. The fixture should be available to samples of different size

5. The production of the fixture is supposed to be easy and fast.

Transparent polymer is selected to be the chamber material. A polymer box is easy and cheap to produce. When needed, the materials constrained by liquid used in a laser process could be changed to another type. In the case of wear or other damage, a new one could simply be made for substitution. And lots of transparent plastic such as PMMA or PC are mechanically strong enough. The final product is a cubic box made of PC, as illustrated by (b) in Figure 3.9. The walls and the bottom of the box are glued together. They were cut from a whole 10mm thick PC plate. Boltholes were made on the upside of each wall to fasten the lid by screw. On two of walls, larger size boltholes were left for inlet and outlet water pipe. The position of the inlet hole is higher than the outlet. On the bottom, a 0.5mm deep square mark, which has the same size as the metal fixture part, is located in the centre. So when putting the metal fixture inside, there will be a position reference. The size of the chamber is constrained by the space in the laser box and the scanning range of the laser beam.

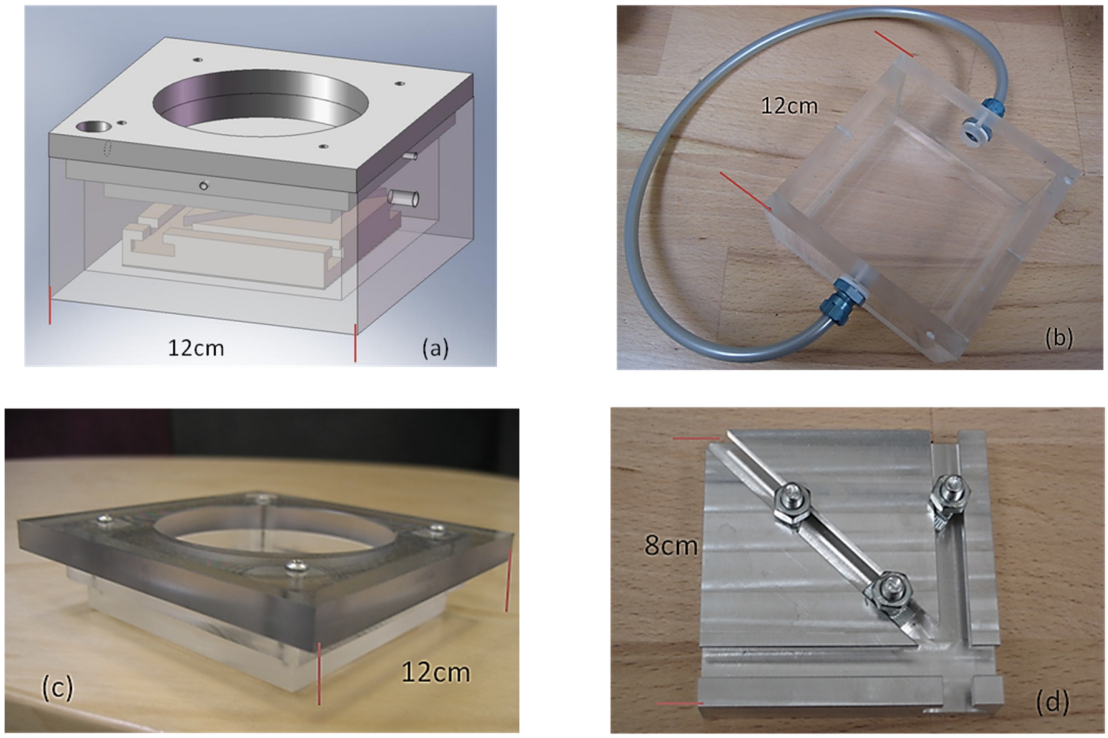

Figure 3.9 The chamber with a fixture to hold samples during laser machining. (a) Assembly of the chamber, fixture, and lid (b) chamber made by PC, the pipe can be used to connect other components such as pump or filter (c) the lid, on the bottom later a special glass window is installed (d) the aluminum fixture, the three screw head are used to fix polymer plates

A pump can be used to generate a water cycle. Another option, which is often used in the study, is to utilize the syphonage phenomenon, as illustrated by picture (a) in Figure 3.10. A soft rubber pipe with inner diameter 2mm is used. In this way, no extra power supply is needed and

the flow rate is enough to remove the floating debris and most of the air bubbles on the substrate.

An aluminium square block is used to fix sample, as illustrated by (d) in Figure 3.9. So the plastic sample will not float in water or move during machining. Instead of several holes, grooves are milled for screws, which make the fixing position more flexible. And the height of the fixture can be increased by a 'height adjuster' when needed, as illustrated by picture (b) in Figure 3.10.

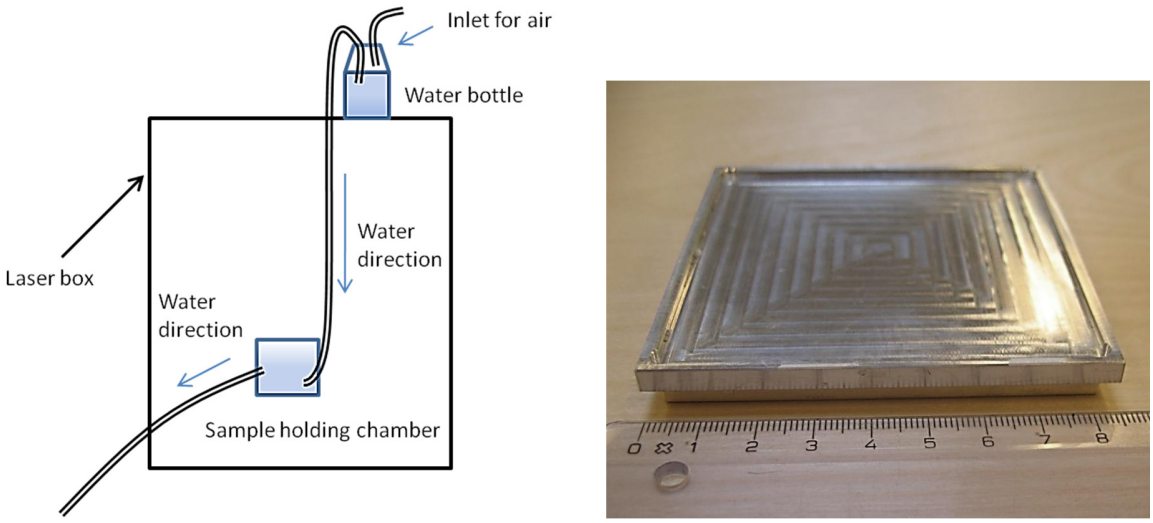

Figure 3.10 (a) Schematic diagram of water flow system utilizing syphonage phenomenon, for the YAG laser box. (b) "Height adjuster" for the fixture. It should be put under the fixture when needed.

The lid is made up of three layers of PC plates, which are screwed together, as illustrated by (c) in Figure 3.9. They were cut from the same PC plate as the body part, for the sake of easy production. It is an easy way for the workshop to produce and to change the window in case of damage. To minimize the laser path in the window, circular holes are made in the center of all the three layers, and on the last layer a Ø75mm BK7 glass window is mounted. The advantages of the three-layer window are: (1) the laser beam only has to pass the glass window; (2) The window layer protrudes into the chamber body and during the machining process, water will be added until it reaches the window. So water waves and vapour coagulation on the window can be avoided. The second layer can be screwed to the walls, so that the lid is fixed with the chamber body. An air hole is left on the top, in case there is air generated in the laser treatment, otherwise a screw could shut it. Picture (a) in Figure 3.9 illustrates the assembly of the lid, the box and the aluminium fixture. However, during the laser treatment, air bubbles generated from the surface of the substrate are stuck on the window and cannot be removed even though there is water flow inside. This problem has not been solved yet, so the lid is not often used.

3.2 Step 2 and 3: activation and plating

Except the experiments carried on in in the laboratory of Hahn-Schickard-Gesellschaft (HSG-IMAT), Stuttgart, Germany, all the other plating work was made in the galvano laboratory, DTU. Beakers were used as containers for electroless copper bath, activation bath, acid rinsing bath *etc*. The copper bath is Circuposit 3350 from Rohm and Haas. For the copper bath, an electromagnet oven with glass thermometer is used to keep the temperature at 45 ℃, and a magnet bar is used to stir the bath. Figure 3.11 illustrates the lab set up for the activation and plating process.

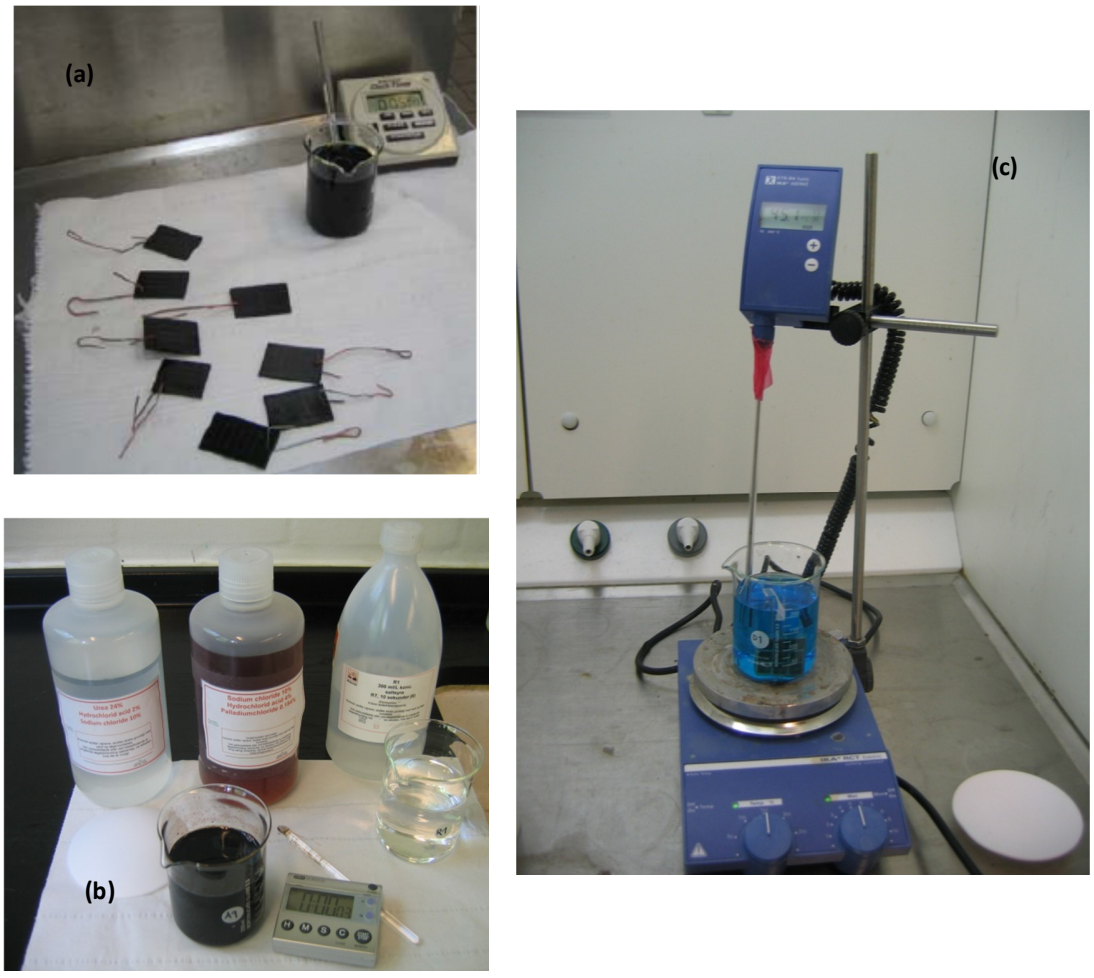

Figure 3.11 DTU lab set up for the plating process. (a)The old activation bath. (b) the new activation bath. (c) Copper bath is heated by magnetic oven

Reference

[1] W.M. Steen, "Laser Material Processing", 3rd ed. Springer-Verlag London Limited 2005.
[2] Internet source: http://en.wikipedia.org/wiki/Laser, accessed: 01-10-2010.

[3] Y. Feng, Z. Q. Liu, X. S. Yi, 2000, "Co-occurrence of photochemical and thermal effects during laser polymer ablation via a 248-nm excimer laser", Applied Surface Science, vol. 156 issue 1-4.
[4] Internet source: http://en.wikipedia.org/wiki/Q-switching, accessed: 01-10-2010.
[5] Internet source: http://www.zamisel.com/SSpostavka2.html, accessed: 01-10-2010.
[6] Internet source: http://en.wikipedia.org/wiki/Mirror_galvanomete, accessed: 01-10-2010.

Chapter 4. Working principles for LISA

In the alternative techniques, one or several pretreatments of the substrate are always needed to realize the plateability. For example, in LDS®, spinels are mixed in the plastic. During the laser treatment, metal particles are released as the seeds for the copper autocatalytic electroless plating. Or in the chemical etching method, on ABS, butadiene parts are removed so the surface is activated by the left active bonds, and the deposited metal has a certain chemical bond with the surface. This chapter discusses why a LISA surface can be metalized. Firstly, the working principle of the electroless plating bath and activation bath is explained based on a written study. Then three hypotheses are proposed, aiming at finding out how the laser track keeps the activation colloids, and they are investigated by experiments and theoretical analysis.

4.1 Working principle of the $PdCl_2/SnCl_2$ initiated electroless copper plating

4.1.1 Electroless copper plating bath

When an iron substrate is immersed in a solution of copper sulfate ($CuSO_4$), the iron dissolves while the copper deposits onto the substrate surface [1]. This is called immersion plating. It can be explained by Equation 4-1 and Equation 4-2, which are two half-reactions for a typical electrochemical reaction. When two redox systems with different redox potential are brought into contact, the most electropositive redox system will be reduced (e.g. copper is reduced and deposits), while the most electronegative will be oxidized (e.g. iron is oxidized and dissolved). From Table 4.1, it is clear that the redox potential for the reducing agent must be more negative than that for the metal being plated.

$$\text{Cathodic: } Cu^{2+} + 2e^- \rightleftarrows Cu^0 \quad E^0 = +0.337V \text{ vs. SHE} \qquad \textbf{Equation 4-1}$$

$$\text{Anodic: } \quad Fe^0 \rightleftharpoons Fe^{2+} + 2e^- \quad E^0 = -0.44V \quad \text{vs. SHE} \qquad \textbf{Equation 4-2}$$

When the entire substrate is covered with copper, the anodic oxidation virtually ceases [1]; therefore, plating is stopped. The important limitations imposed in this type of reaction include: (1). The film thickness is with average values of only 1 µm. (2). The coating doesn't have a good adhesion to the substrate. (3). The coating is usually porous. (4). The process is only applicable to deposit noble metals. (5). The plating bath quickly becomes contaminated with ions of the substrate metal.

Table 4.1 Standard redox pair and their potential at 25 ℃ [1]

Reaction	Potential V vs. SHE
$Ag^+ + e^- \rightleftarrows Ag^0$	+0.799
$Cu^{2+} + e^- \rightleftarrows Cu^+$	+0.158
$Ni^{2+} + 2e^- \rightleftarrows Ni^0$	+0.230
$Fe^{2+} + 2e^- \rightleftarrows Fe^0$	-0.440
$HCOOH + 2H^{2+} + 2e^- \rightleftarrows HCHO + H_2O$ (pH=0)	+0.056
$H_3PO_3 + 2H^{2+} + 2e^- \rightleftarrows H_3PO_2 + H_2O$ (pH=0)	-0.500
$HCOO^- + 2H^{2+} + 2e^- \rightleftarrows HCHO + 3OH^-$ $(pH = 14)$	-1.070
$HPO_3^{2-} + 2H_2O + 2e^- \rightleftarrows H_2PO_2^- + 3OH^-$ $(pH = 14)$	-1.650

Table 4.2 Common chemicals, which can be chosen as components of electroless copper plating bath [1]

Reducing agent	**Complexant**	**Stabilizer**	**Exaltant**
Fomaldehyde	Sodium Potassium tartrate (Rochelle salt)	Oxygen	Cyanide
Dimethylamine (DMAB)	Ethylenediamine tetraacetic acid (EDTA)	Thiourea	Proprionitrile
Sodium Hypophosphite	Glycolic acid	2-mercaptobenzothiazole	O-phenanthroline
	Triethanol amine	Diethyldithicarbamate	
		Vanadium pentoxide	

Further limitation for electroless plating is that the electrochemical reactions should only occur on the substrate, and not lead to a homogeneous reaction of the plating bath, which is decomposition and called collapse of the bath. To achieve thicker deposits, the reaction must occur initially on a metallic substrate or activated non-conductive substrate and subsequently on the deposit itself. An example of solution decomposition is the addition of formaldehyde (E =

+0.056V vs. SHE at pH = 0) to silver nitrite solution, which causes spontaneous precipitation of metallic silver [1].

Theoretical conditions for the electroless plating of a metal may be determined from the Pourbaix diagrams [2]. Pourbaix diagrams show the ranges of potential and pH over which various ions, oxides, pure metals, *etc.* are thermodynamically stable. To illustrate this theoretical region where copper plating is possible, a combined diagram for pH, the copper-water system, and the carbon-water system is shown in Figure 4.1. The overlap area of copper reduction and formaldehyde oxidation zones is shaded to show the possibility. At potentials greater than +0.337 V vs. SHE, in acid solution, the copper ion is thermodynamically stable. For metal deposition, the potential of the substrate must be lowered below this value, into the region where metallic copper is stable. In the carbon-water system, oxidation of formaldehyde to formic acid or formate anion occurs at potentials below +0.377 V vs. SHE over the entire range of pH. Thus the electrochemical processes that could theoretically occur on the metal surface in acid solutions are:

$$\text{Cathodic}\ \ Cu^{2+} + 2e^- \rightleftarrows Cu^0\ E^0 = +0.340v \qquad \textbf{Equation 4-3}$$

$$\text{Anodic}\ \ HCOOH + 2H^{2+} + 2e^- \rightleftarrows HCHO + H_2O\ \ E^0 = +0.056v \qquad \textbf{Equation 4-4}$$

However, successful electroless plating cannot be guaranteed by simply adding a solution of the reducing agent to one containing metal ions. Oxidation of the reducing agents involves the formation of either hydrogen (H^+) or hydroxyl (OH^-) ions, as a result, the pH value changes in the bath, which can lead to precipitation of the metal in bulk solution. To overcome this difficulty, first, buffers are added to stabilize the pH. These include carboxylic acids in acid media and organic amines in alkaline solutions. Secondly, complexants are added to the plating bath to depress the free metal ion concentration, in order to stop the dissociation of the metal complex, therefore the metal ions are maintained in the solution [1]. Table 4.2 shows some common complexants, and they can be chosen according to other components.

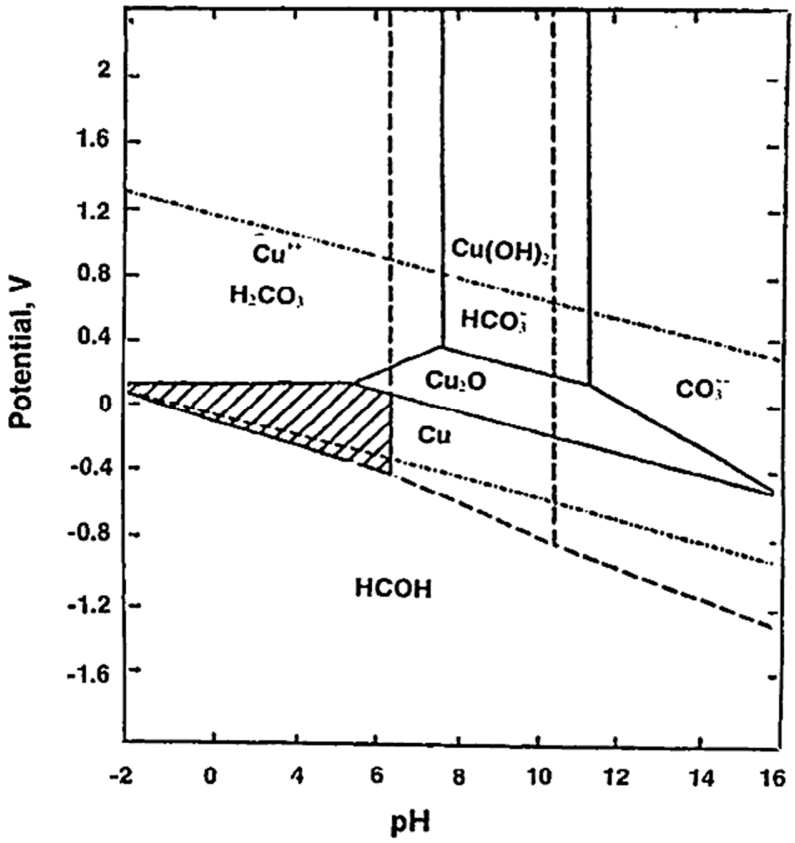

Figure 4.1 Combined potential-pH diagram for copper-water system and carbon-water system, indicating the range of value within which metal deposition is possible [1]

Besides, the complexant also makes higher pH values to be available for the plating. It is indicated from Figure 4.1 that when the pH increases, the potential difference, which is the thermodynamic driving force for copper deposition, becomes greater. Therefore, copper deposition is thermodynamically more favorable in alkaline solutions. Meanwhile, to prevent copper precipitating at elevated pH values, a complexant such as sodium potassium tartrate is added to the plating formulation. Some common complexants used in commercial electroless copper processes are also listed in Table 4.2. Nevertheless, if the metal is complexed excessively, there will be insufficient free metal ions available for deposition.

In addition, stabilizers are added to the bath in small concentration. This is to prevent homogeneous decomposition of the plating bath due to the presence of active nuclei such as dust or metallic particles in the bath. The active nucleuses can be completely absorbed by the stabilizers, and they will be shielded from the reducing agent. However, if stabilizers are used in excess, metal deposition may be completely prevented, even on the substrate itself.

Last but not least, to increase the plating rate, accelerators or so-called exaltants are added, because sometimes complexants lower the plating rate inordinately. These additives are generally anions, such as CN, which are capable of making the anodic oxidation process easier.

In summary, typical electroless plating formulations contain (a) a source of metal ions, (b) a reducing agent, (c) a complexant, (d) a buffer, (e) exaltants and (f) stabilizers. A summary of common agents that can be chosen for electroless copper plating is given in Table 4.2.

4.1.2 $PdCl_2/SnCl_2$ activation system

Electroless plating to metalize non-conductive substrates usually needs a preliminary treatment of the surface to make it catalytic, (also called “active” or “sensitive”) to initiate the deposition of metal from the electroless bath [1]. $PdCl_2$ and $SnCl_2$ mixture is the most commonly utilized catalysts for autocatalytic electroless plating. It was a two steps process in the past, which consists of sensitization ($SnCl_2$ solution) and activation ($PdCl_2$ solution), then it was developed to be a single-step mixed $PdCl_2/SnCl_2$ catalyst system, which was first described by Shipley [3]. Several research groups study the activation mechanism. In this section, the core-shell theory reported by Cohen *et al.* [4] is quoted.

In the activation solution, HCl is usually used as diluting agent. Pd-Sn nanocolloids form in the acid suspension. On one side, the affinity of Pd and Sn is indicated by the relatively large mixing enthalpy; the Pd-Sn phase diagram shows a large number of crystalline alloying phases: Pd_3Sn, Pd_2Sn, Pd_3Sn_2, PdSn, $PdSn_2$, $PdSn_3$, and $PdSn_4$ [5]. On the other side, it is expected that Sn will segregate on the surface of Pd-Sn nanocolloids because of the surface energy difference, since tin has a surface tension about 3 times less than that of palladium [6]. The activity and stability of the solution always depend on the concentration of the Cl^- and Sn^{4+} [7].

Cohen and West have established that Pd and Sn form a metallic core at the center of the nanocolloids [4]. (On the contrary, Rantell and Holtzman and other groups believed that Pd and Sn existed in the form of solute or deposited complexes) And they used further experiments to show that the shell of the nanocolloids consists of $(SnCl_3)^-$ complexes, which stabilize the surface, stoped the growth of the particle, and also prevent the agglomeration in the suspension [2].

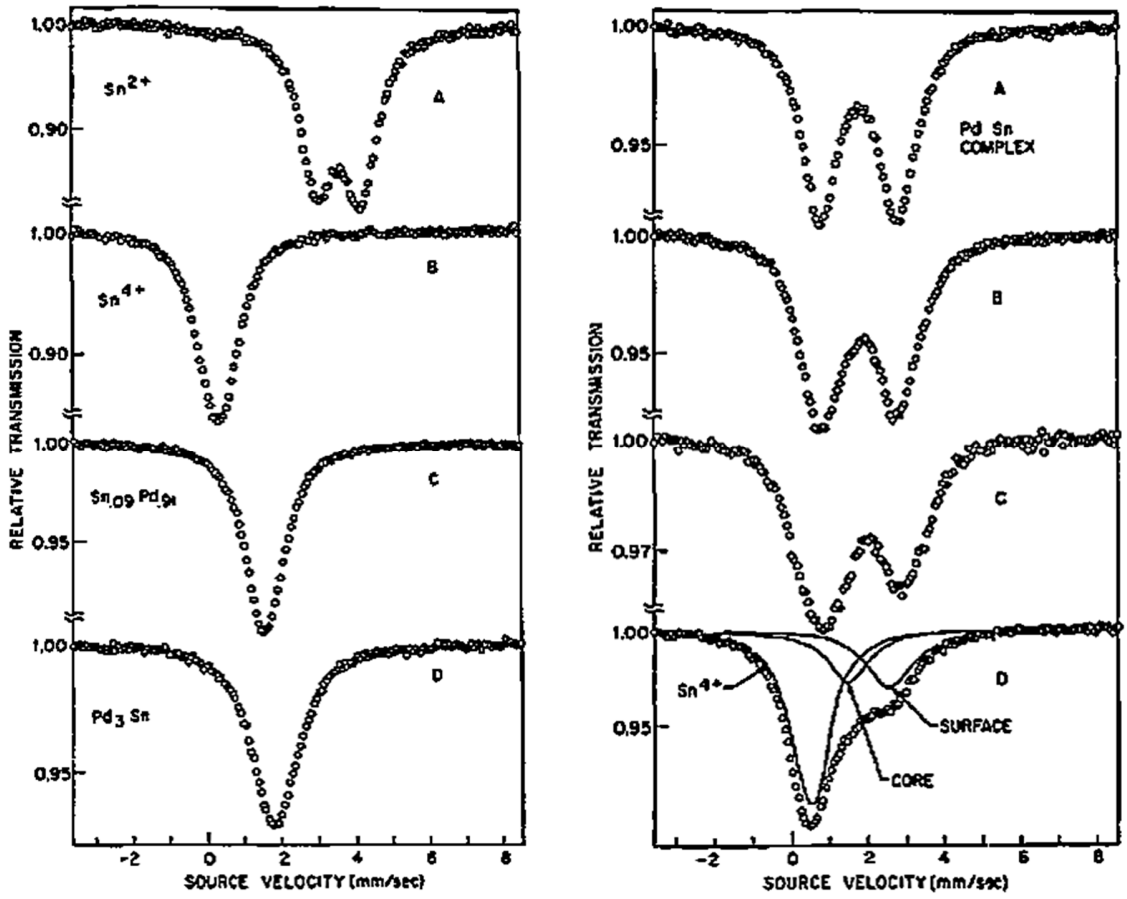

(i) (ii)

Figure 4.2 Mössbauer spectra of (i) Tin and (ii) Sn-Pd solutions [4]. (i) Mössbauer spectra of pure phases of some tin species encountered in the solutions studied; A, spectrum of Sn^{2+} complexed with Cl^- or OH^-. B, spectrum of Sn^{4+}, bare or complexed ions. C and D are the spectra of $Sn_{0.09}Pd_{0.91}$ and Pd_3Sn (ii) Spectra of Sn-Pd complex solutions (Sn/Pd ratio 2:1) at A: 0.2 min B: 6 min C: 30 min D: 120 min after mixing.

According to Cohen *et al.* 's work [4], when combining $PdCl_2$ and $SnCl_2$ together, in the first place, a complex of Pd-Sn is formed, they also concluded that the stoichiometry of the Pd-Sn complex is Pd (II)·3Sn(II). Figure 4.2 (ii) illustrates the colloid forming process by Mössbauer spectra. The Pd-Sn colloid forms immediately after the complex is made, so the $PdCl_2/SnCl_2$ solution was frozen to slow down the process. Figure 4.2 (i) shows the pure phase of tin, and the spectra are used to be compared with the mixture's spectra in Figure 4.2(ii). It is clear that the doublet of SnCl complexes (A in (i)) disappeared; it has been replaced by another doublet, which is believed to be Pd-Sn complex in HCl, shown by A in (ii). It decomposes with time, producing complexed Sn^{4+} due to the redox reaction, Sn-Pd alloy, a small amount of dissolved Sn^{2+}, and a line which is believed to the protective Sn^{2+} layer surrounding the Pd-Sn particles, as showed in B, C and D in (ii). During this decomposition process, the red-brown color of the

solution changes to a grayish-brown, and then eventually to dark green. The process can be described by Equation 4-5, in which the dissolved complex is expressed as $(Pd\text{-}Sn)_c$. To be supplemental, J. Horkan proposed that the Sn metal in the core forms due to under-potential deposition on the growing [8], as illustrated by Equation 4-6. Other researchers group also suggested that the ratio of Pd and Tin in the alloy could be $PdSn_2$, Pd_3Sn or other different structures [9].

$$(\mathrm{Pd-Sn})_c \rightarrow \mathrm{Pd_{metal}} + \mathrm{Sn^{4+}} + 2\mathrm{Sn^{2+}} \qquad \textbf{Equation 4-5}$$

$$\mathrm{Sn^{2+}/Sn^{4+}} \xrightarrow{\text{underpotential deposition}} \mathrm{Sn_{metal}} \qquad \textbf{Equation 4-6}$$

If the solution gets in contact with air, coagulation tends to take place, due to the oxidation of Sn^{2+} to Sn^{4+}, so the $(SnCl_3)^-$ layer works as a protector to the core. A likely configuration for such a layer is believed to be bonded to the Pd-Sn alloy core via Sn-Pd bonds, with the Cl^- ions on the outside.

The activity of the single-step $PdCl_2/SnCl_2$ system can be enhanced by using an acceleration step. Typical accelerators are fluoborate, ammonium bifluoride, fluoboric acid, sulphuric acid, or sodium hydroxide. They are applied after the activation step and rinsed by water [9]. Usually a short time like 10 seconds is needed. It is believed that the accelerator removes the $(SnCl_3)^-$ layer, so it's easier for Cu^{2+} ions to reach the Pd-Sn alloy core; also, they accelerate the coagulation of small activation colloids to form high-density particles [10].

J. Kim *et al*. showed that the catalytic particle was 1-2nm in diameter in the activation solution, and when absorbed by a substrate, they were clustered into 20-50nm in diameter [11]. It was also observed that the clusters were uniformly distributed over the substrate surface independent of the surface topography. If the hydration effect is considered, the size of the particles can be in the order of a magnitude more. (The particle size distribution of the new activation bath in this project is illustrated in the Figure 4.14.)

4.1.3 Initial stage of copper deposition

J. Kim *et al*. studied the microstructure of copper crystal evolution during the deposition [11].

In the very early stage of the copper deposition on Pd/Sn catalysts, the process is believed to be copper substitutes tin and Cu-Pd alloy forms, instead of separate copper and palladium grains. J. Kim *et al*. used EDAX measurements showing that the surface is composed primarily of copper and palladium rather than Cu, Pd and Sn [11]. The EDX measurement showed that the lattice constant of the formed Cu/Pd alloy is intermediate between that of Cu and Pd; hence it is an alloy of Cu and Pd without Sn in the lattice. This is also supported by the observation that Pd/Sn catalysts are intrinsically more active than Pd. In addition, the replacement starts after approximately 5 seconds in the plating bath and finishes in another 5 seconds, according to

EDAX measurement by J. Kim *et al.* The deposition speed varies with the activity of the activation bath and the temperature.

After around 1 minute of plating, Cu grains grow to 10-50nm in diameter with a spherical shape. As plating progresses, some of the grains have grown to a much larger size than others. Facets of grain boundaries start to occur, and the deposit connects better laterally. As the grains grew further they form a structure with larger grains with facets. There are local variations in grain size and the thickness of the deposition, as well as many twins and dislocations observed inside the grains and at their boundaries. After several minutes of plating, the random orientation of each grain is observed.

J. Kim *et al.* believed that the Cu forms nucleuses on the substrate randomly, and the grains subsequently coalesce, re-crystallize, and grow laterally, impinging on each other before spreading over the whole substrate. In the following stage, Cu deposits epitaxial on the existing grains rather than by the nucleation, growth, and coalescence of addition Cu grains as it did in the earlier stage.

4.2 How can a laser treated surface keep Pd

In electroless Cu plating, Cu only deposits on active sites or copper. In the traditional techniques, strong oxidizing solution (usually containing Cr^{6+}) is always used as an etchant to eat away the surface material to a certain degree. As a result, the surface area is greatly increased, which is in favour of the activation particle's absorption, meanwhile, microscopic holes are left on the surface, so the deposited metal can be locked inside to have a mechanical bond with the surface. In the LPKF-LDS technique, polymers with metal complex filler are used as the substrate and a laser with a special wavelength is used to crack the chemical bonds, which releases metal seeds for subsequent copper deposition. In LISA, neither poisonous chemicals nor "pre-seeding" for the substrate are used. After laser treatment, the surface becomes as porous as a sponge, which is believed to be the main reason for keeping the activation particles.

Above all, it must be emphasized that the rinsing after activation is necessary and cannot be skipped. Because there will be some remaining activation drops on the non-treated part, which can also be plated in the plating step. The metal layer deposited on these remaining activation drops has a weak adhesion to the substrate and can be removed easily, but the risk is that, if metal deposition happens in an excessive area, it may cause collapse of the plating bath. So the remaining drops must be removed by rinsing the working pieces in distilled water.

The question that needs to be answered is that, after rinsing, why activation particles still exist on the laser-machined area, but not on the non-machined area. The mechanism may be multiple. Hypotheses to explain this are: (1) The laser machining leads to chemical changes to the substrate, then there is one or several types of chemical bonds between the activation colloids and the laser machined surface. (2) The laser-machined area may have a different wetting property with the non-machined part, due to the porous structure formed in the laser

machining process. So when in contact with the activation bath, the laser machined area tends to attract the solution more than the non-machined area. (3) The activation and rinsing is controlled by diffusion. When rinsing, the Pd/Sn colloid need a longer time to diffuse out of the porous structure formed in the laser process than those out of the laser track. The following sections attempt to prove the hypotheses.

4.2.1 Hypothesis (1): there are chemical changes on the laser track in favor of bonding with palladium

XPS (X-ray Photoelectron Spectroscopy) and FTIR (Fourier Transferred Infrared Spectroscopy) spectra were used to detect the chemical changes of the substrate after laser treatment. Principles for both instruments are explained in Appendix 2. XPS spectra mainly show the elemental composition difference before and after laser treatment. FTIR spectra are used to find out whether there is polymer groups loss or new groups generation.

A green ABS piece with a laser track was analyzed by XPS. N1s scan (nitrogen 1s electron scan) was used to check the nitrogen loss.

Spectra (b) and (c) in Figure 4.3 illustrate the nitrogen amount before and after the laser treatment. It is clear that there is a more than 50% loss of organic nitrogen, indicating the loss of nitrile group (-CN) in ABS. The C1s scan (carbon 1s electron scan) results (Figure 4.4) also prove this conclusion. Besides, other groups such as C-O and C-H are also lost. It corresponds to the phenomena in the laser process, i.e. a burning smell exists even though the laser track does not look burnt. Figure 4.5 is an area map displaying the normalized elements amount of distribution, on which the O1s scan (oxygen 1s scan) shows that at the surrounding area of the laser track, oxygen is richer than on the track or the other non-machined area. It shows an oxidation reaction has occurred during the laser process.

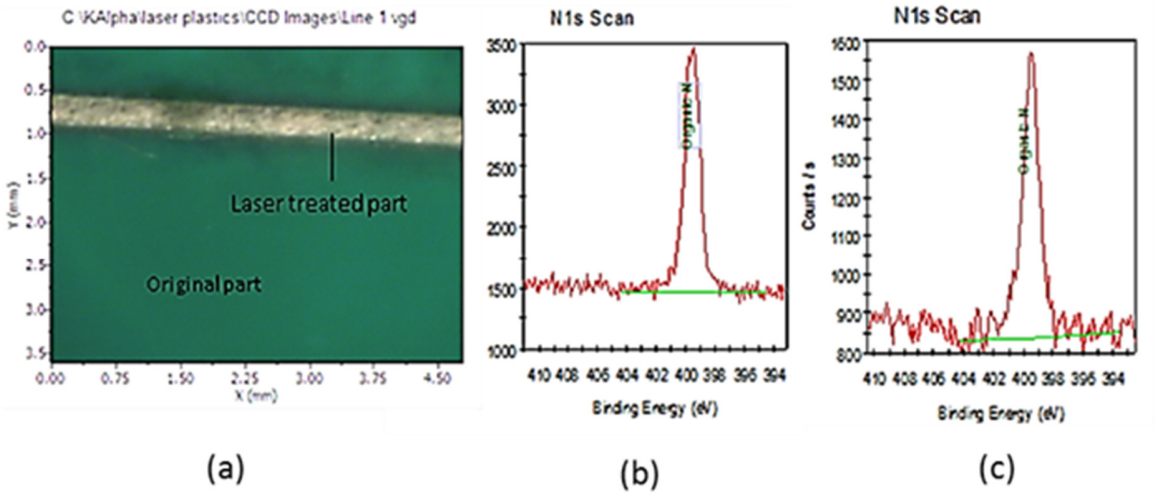

Figure 4.3 XPS spectroscopy. Picture (a) is the tested piece; N1 scan was made separately on the original part (b) and on the laser treated part (c). N1s scan chart indicates the amount of nitrogen.

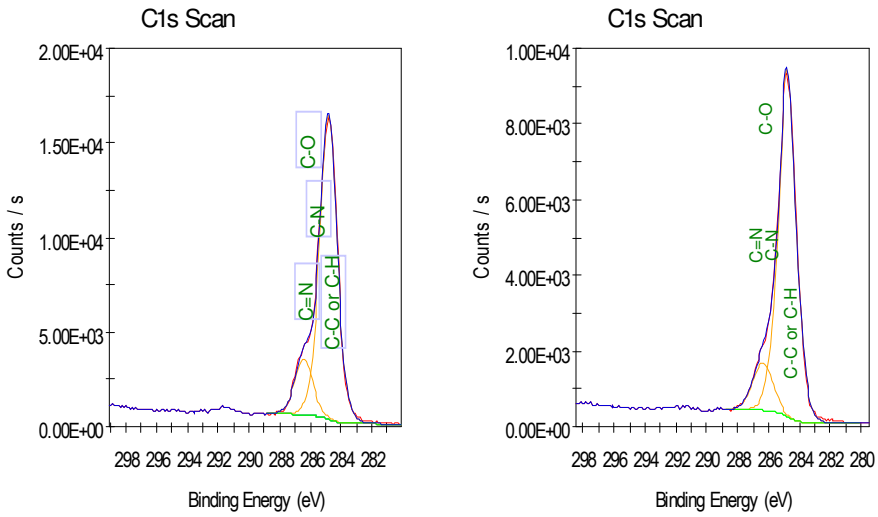

Figure 4.4 XPS spectroscopy. C1s scan on both original ABS surface (a) and laser treated part (b), which can indicate the amount of carbon.

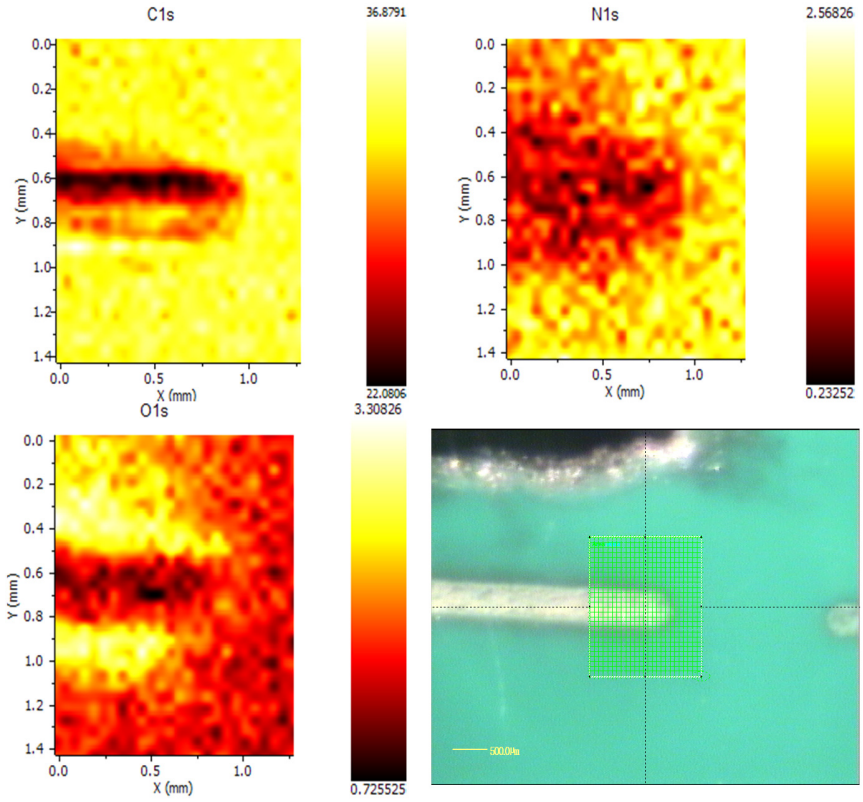

Figure 4.5 XPS spectroscopy. Normalized area map illustrates a certain element amount distribution on the substrate

The XPS spectra indicate that the laser machining process results in chemical changes on the surface. The most significant one is the nitrile group (-CN) loss, which may leave positive charges on the surface, so the shell of the colloid bonds with the surface.

Based on the XPS analysis of ABS, SAN (copolymer of styrene and acrylonitrile), PS (polystyrene), PB (polybutadiene), and ABS (copolymer of styrene, butadiene, and acrylonitrile) were chosen to be analyzed by FTIR. Their monomers are showed in Table 4.3. In this way, functional group loss can be compared. Moreover, on the ABS substrate, laser tracks made by a series laser lamp current and a piece treated by plasma were compared.

Figure 4.6 illustrates how to perform an ATR-FTIR test. The sample surface is intimately pressed into the top surface of the crystal window. The infrared radiation from the spectrometer enters the crystal. It then reflects through the crystal and penetrates "into" the sample a finite amount with each reflection along the top surface via the so-called "evanescent" wave. At the output end of the crystal, the beam is directed out of the crystal and back into the normal beam path of the spectrometer [12].

Table 4.3 Polymers used of FTIR test and their monomers

Polymers	Monomer
PS	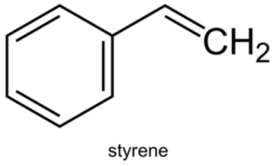 styrene
Polybutadiene	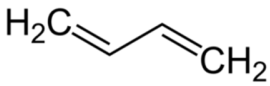 1,3-butadiene
SAN	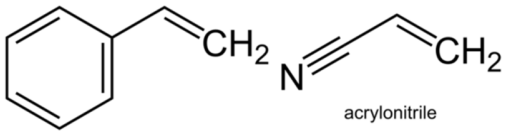 styrene acrylonitrile
ABS	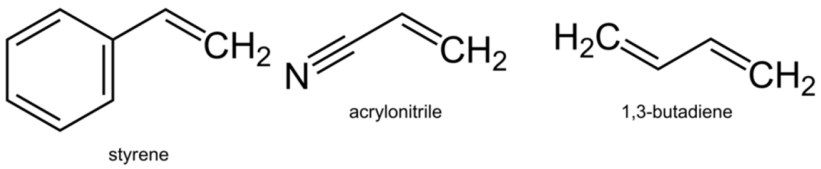 styrene acrylonitrile 1,3-butadiene

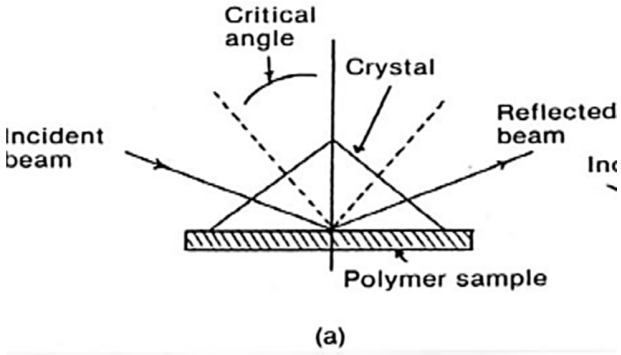

Figure 4.6 How a polymer sample is put on the window of ATR-FTIR equipment [12]

The utilized instrument is ATR-FTIR spectrometer from the Department of Chemical Engineering, DTU. The crystal window is 1mm in diameter and made of diamond. The samples to be tested were prepared in two methods. The first method was to directly put a laser track towards the window; the laser treated area must be large enough to cover the window. The tested laser tracks were 2mm wide and long enough to make 3 to 4 tests on each piece. To improve the contact between the window and the laser-machined surface, thin plastic foil (30-50μm) pressed from a small injection molded piece by hot embossing equipment was used. The pressed foil is half transparent which leads to a thinner laser-affected layer. The hot embossing equipment is illustrated in Appendix 2. FTIR test shows that no chemical change happens during the hot embossing process. Then the foil was machined by (a) YAG laser using the same parameters as the non-pressed pieces. The laser-machined area on foils could be plated as common injection molded pieces.

The second method was to collect the laser machined material by scraping the laser track; then the obtained powder would be put on the detecting window compactly for the analysis. However, it is not easy to collect the desired powder without any substrate material, since the thickness of the laser modified layer is only 80-100μm.

The used laser parameters for the tested laser tracks are shown in Table 4.4. For ABS, the tested lamp currents were varied from 14A to 22A to vary the power output.

Table 4.4 The Laser parameters to prepare the laser track for FTIR test

Lamp current	Q-frequency	Speed	Wobble
18A	1200Hz	60mm/s	4

When making IR spectrum, firstly a background test was run on blank window. The 32 scans mode was employed to lead to a stronger spectrum. All the functional groups have characteristic peaks (single or multiple peaks) in the spectrum.

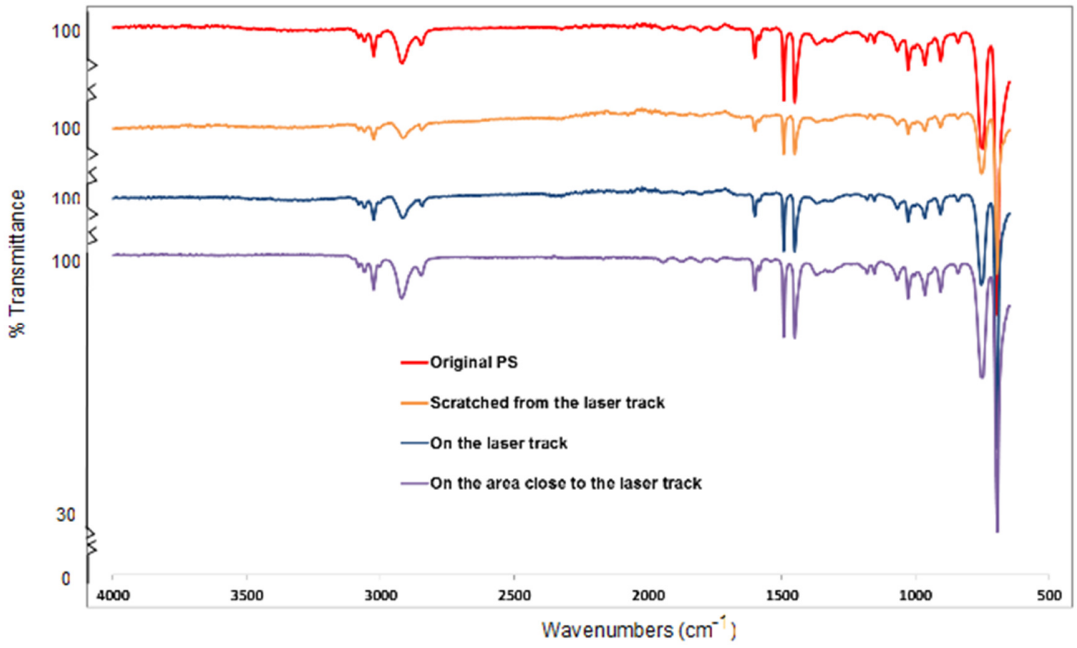

Figure 4.7 FTIR spectra overlay of PS. Spectrum made from original injection molded piece is "PS original". The sample made by scraping the track of the surface is called "Scratched from the laser track". The spectrum directly made on the laser track is named as "On the laser track". The area near the track was also measured, and the spectrum is called "on the area close to the laser track".

A piece of rubber from bicycle inner tyre was studied instead of PB for the similarity of the monomer structure. However no change was shown by the FTIR spectrum before and after laser treatment.

Figure 4.7 displays the spectrum from measurements on PS substrates. Comparison is made among the original injection molded plastic and the surface after laser treatment; the laser treated samples were not thin foils. The area near the laser treated part was also analyzed. First of all, all the peaks are not as strong as in the monomer's spectrum, because the concentration of the functional group is much smaller in polymers than in monomers. Figure 4.8 shows the styrene's spectrum, which can be used to compare with the PS's. For example, regarding the peaks at 700 and 800 cm^{-1} for a mono-substituted benzene ring, styrene has much stronger peaks than PS. It is shown that on the laser track, the peaks (2000-1800cm^{-1} and 800-700 cm^{-1}) for the benzene ring mono-substitution are weaker than the original PS. The spectrum from the scratched powder is even weaker than from the laser track. No new peaks are generated after laser treatment.

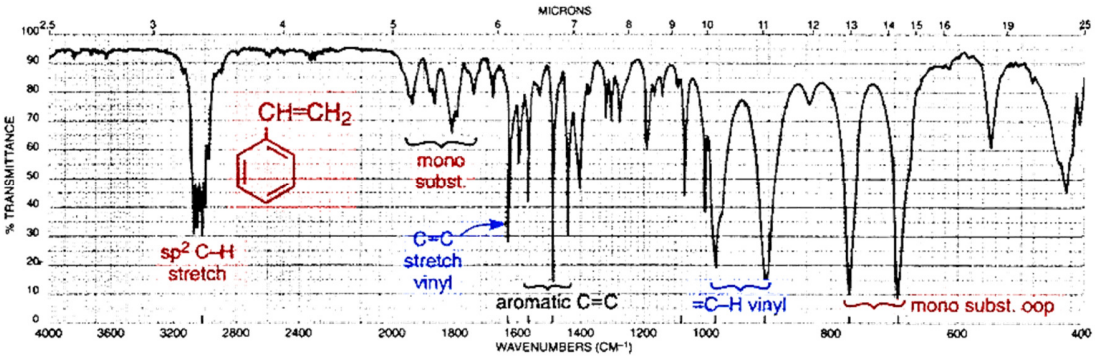

Figure 4.8 FTIR spectrum of styrene (neat liquid, KBr Plates) [13]

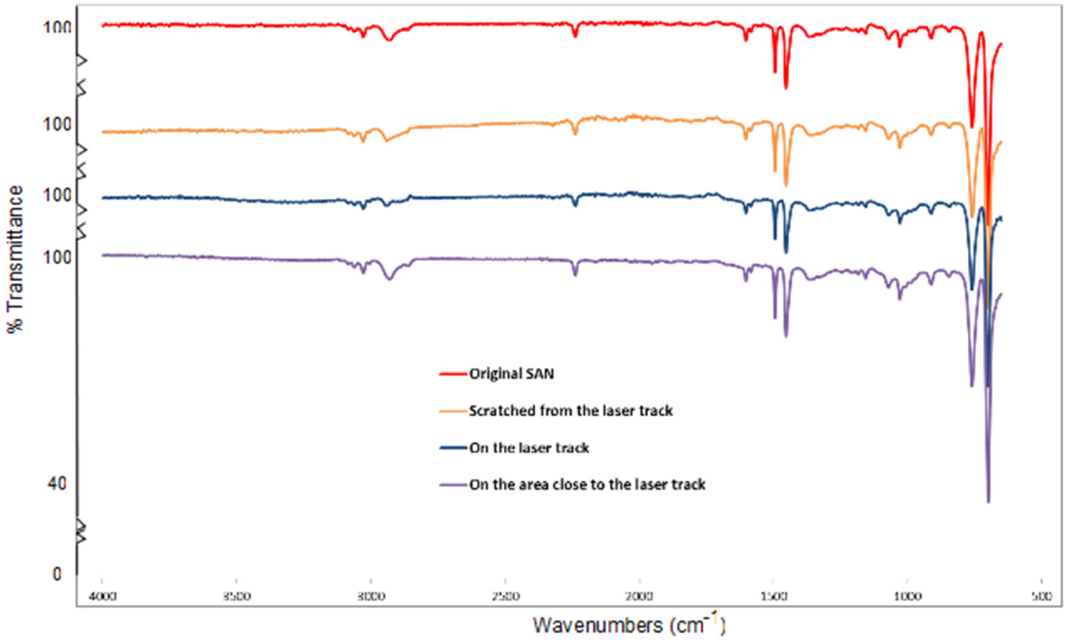

Figure 4.9 FTIR spectra overlay of SAN. The nomination of each spectrum is similar to PS's

SAN is copolymer of styrene and acrylonitrile, and Figure 4.10. shows the structure. The spectra of PS and SAN are quite similar; the small peak at 2200cm^{-1} on SAN's spectrum contributes to the nitrile group. In the XPS study of ABS, a nitrile group loss was indicated, which may be proved in Figure 4.11, on the spectrum "on laser track", the nitrile's peak is weaker than the other, but the nitrile group loss didn't happen to SAN. On PS's spectrum, the scraped sample has smaller peaks at the band 900cm^{-1}, which is a sign of loss of the aromatic group. But at the same band, no clear change happens to SAN.

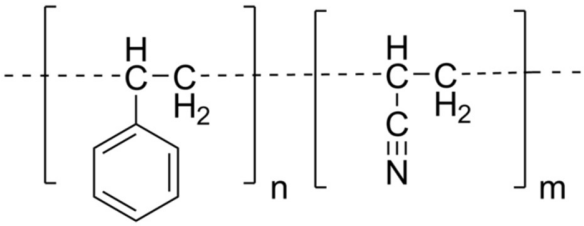

Figure 4.10 polymer chain structure of SAN

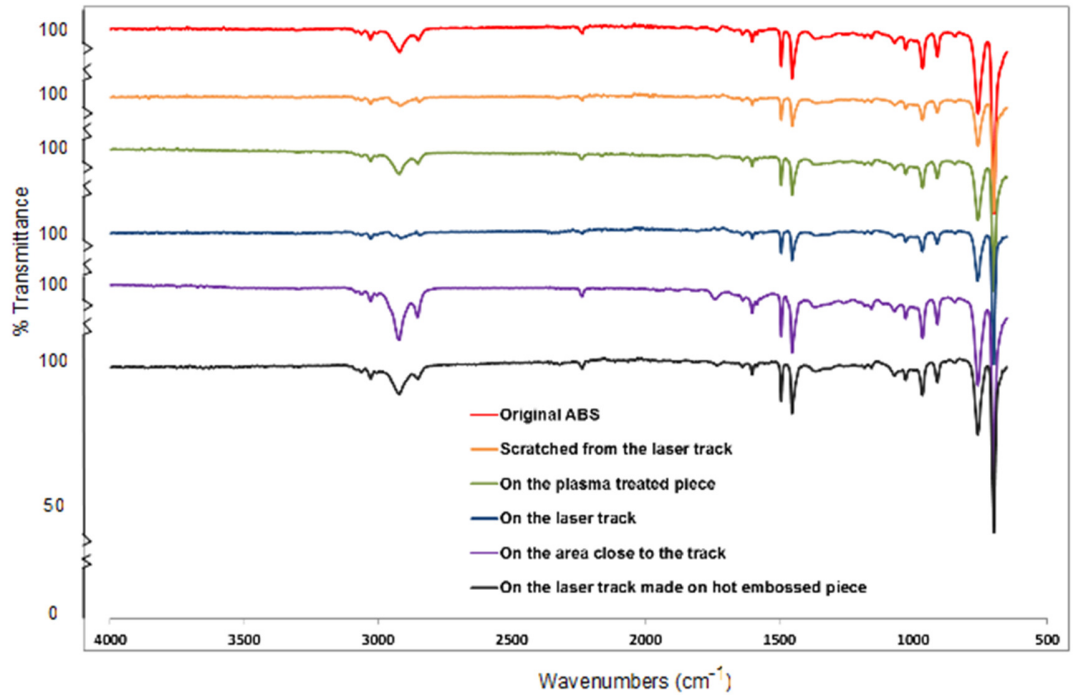

Figure 4.11 FTIR spectra overlay of ABS. The surface treated by 2 minutes Ar plasma was also tested, and the spectrum is called 'on the plasma treated piece'. "On the laser track made on hot embossed piece" shows the spectra from laser track on thin foil. And other nominations is the same as in figures above

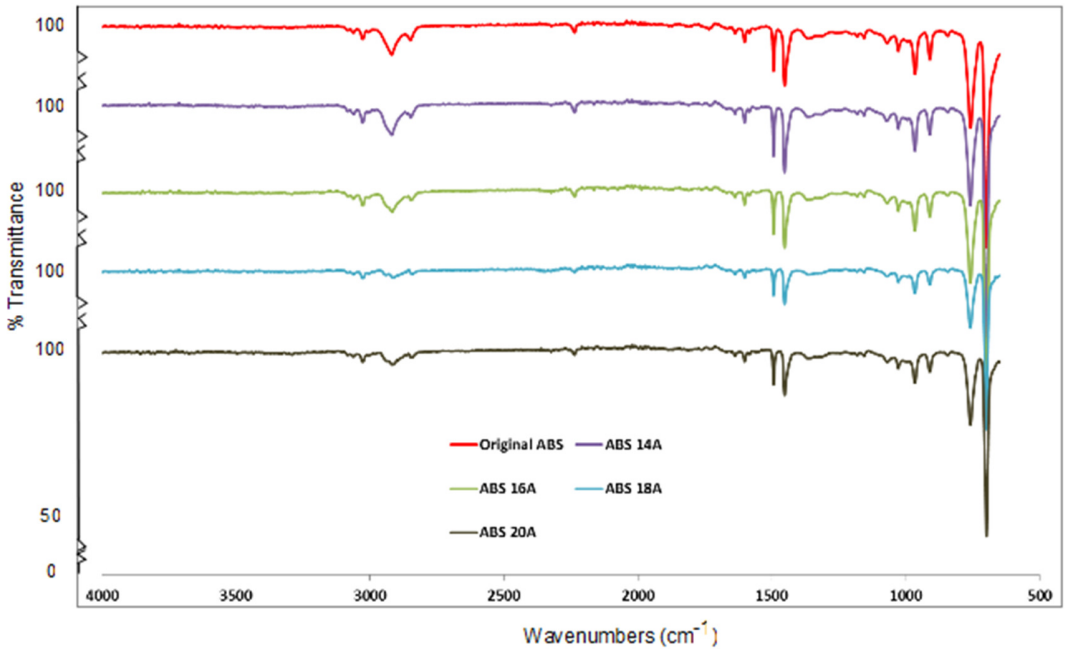

Figure 4.12 FTIR spectra overlay of ABS. The lamp current is varied for each laser track. The test method is using laser track directly.

For ABS, besides the thin foil sample, a plasma treated sample is also analyzed by FTIR spectroscopy and put in the over lay. The plasma was provided by PVD equipment, the plasma setting is mainly used to clean the surface before sputtering deposition. During the laser treatment, plasma generation is quite strong showing sound and sparks. So the same substrates of ABS were treated only by plasma, to check whether plasma can change the chemical structure. Also, according to the XPS test, the area close to the laser track shows a different chemical composition, a richness of oxygen. So this area was also tested. Figure 4.11 illustrates the comparison. Figure 4.12 is a comparison of ABS machined using different lamp current, i.e. the other laser parameters are the same, and only the lamp current is varied. High lamp current will lead to high laser energy output.

The plasma treated sample didn't show a different spectrum compared to the original one, except a slightly smaller 2200cm^{-1} peak. The spectrum of the area close to the laser track showed a small peak at ~1680cm^{-1}, which may contribute to the C=O bonds formed in the oxidation process. Figure 4.12 shows that samples made under high laser power have a weak band in the 3100cm^{-1} to 2850cm^{-1} range, which corresponds to a sp2 C-H stretch, i.e. the activity of the aromatic ring or double bonds in the butadiene group. The same trend can be seen in PS and SAN spectrums (both of them using LS 180 as the laser parameter), so the main reason should be the oxidation or the loss of the aromatic ring.

To conclude, on one side, both XPS and FTIR spectroscopes confirm the chemical changes on the laser treated area; mainly oxidation happens to the substrate. In fact, the Nd: YAG laser's

energy is not high enough to break covalence bonds in the polymer. All the possible reactions happen under the condition of high temperature and participation of water. Perhaps a slight decomposition happens due to local high temperature. However, to find out how the surface is bonded to the activator particles chemically, more analysis is needed. On the other side, almost all those changes happen to the aromatic group or nitrile group. Then what will happen to a simpler structure polymer such as polyethylene and polypropylene, both of which are proved to be available for LISA? Even if the structure of those materials is modified by a laser, then in the subsequent step, the chemical bonding with the Pd/Sn particle can hardly be the same. So to reveal the mechanism of activator adsorption in a way, which can be applied to all different materials, another aspect has to be investigated. The following two sections aim to look into this problem.

4.2.2 Hypothesis (2): The laser machined surface has a larger adhesion work to the activation solution than the non-machined surface

The second hypothesis is that, from the surface energy point of view, the work of adhesion between the activation solution and the laser-machined area is larger than the corresponding work of the non-machined area. It is because after laser machining, the laser treated area has different wetting characteristics than the non-machined part [15].

The reason why this aspect was chosen to be studied, originates from the contact angle measurements. PC, PS, *etc*. were used as substrate. Originally, it was expected that the laser treated area was more "activation-solution-philic" than the non-machined surface. The contact angle measurements, however, seemed to result in different conclusions. The employed equipment was a Dataphysics® contact angle system with related software OCA20, from the Department of Chemical Engineering, DTU. All the tested substrates were cleaned by 96% alcohol and then dried in a fume hood. For each wetting liquid, water and activation solution, 3 or 4 drops were measured on a given surface. The advancing contact angle measurements were made on both sides of the drop and then the data were averaged.

Table 4.5 lists the average advancing contact angle values. In most of the cases, the laser track has a significantly larger contact angle than the non-machined surface, for both water and the activation solution. The results mean that on a dry laser machined polymer surface, the activation solution is actually easier to be removed than water.

Table 4.5 Advancing contact angle measurement results on the laser machined and non-machined plastic surface using activation solution and de-ionized water. Typical standard deviation of 4.3% is observed.

Material	Condition			
	Water on original plastic	Water on laser machined surface	Activation solution on original plastic	Activation solution on laser machined surface
PC	86.0	145.8	92.0	148.4
ABS	92.5	141.3	99.0	144.0
PE	106.0	143.8	114.0	138.0
PS	68.0	146.0	103.5	153.2
SAN	70.5	98.7	102.0	111.0

Table 4.6 presents the images from contact angle measurement on polycarbonate and its laser tracks; including water drops on both laser machined and non-machined polycarbonate surface, and the activation drops on these two types of surfaces [14]. Clearly, the laser track on PC leads to a larger contact angle.

The contact angle measurement result is also proved practically in the activation step. A completely dry working piece takes a very long time to become wet by the activation solution. Experiments show that completely dry samples need at least 2 hours to become wet by the activation solution, so that plating can take place afterwards. Usually the workpiece is washed by alcohol before the activation, which helps removing the organic contamination. Meanwhile, alcohol can wet the surface, so it is easy for the surface to become soaked by water and then by the activation solution.

The conclusion from the contact angle measurement seems to be that the laser treated surface "likes" the activation bath less than the non-treated surface, which resulted in uncertainties of the process of exploring the mechanism. However, another possibility, still by studying the wetting characteristics, is via the assessment of the interaction between the liquid and solid surface. In this work the acid-base theory for interfacial tensions proposed by van Oss *et al.* [16] will be used for calculating the work of adhesion and for characterizing the surfaces from a wetting point of view.

Table 4.6 Picture from the contact angle measurements. De-ionized water and activation solution on original polycarbonate surface and the laser-machined area (on polycarbonate) are shown. [14].

	Distilled water	Activation solution
On injection molded plastic surface (so-called non-machined surface)	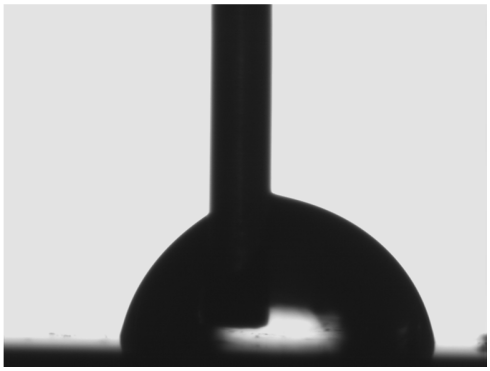	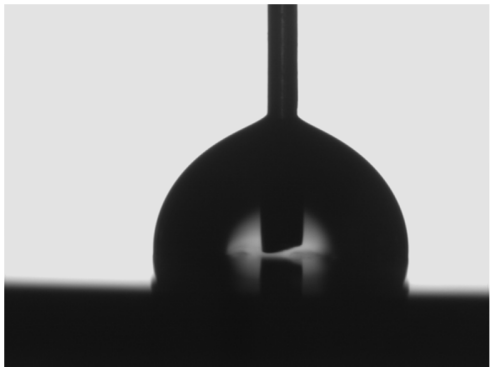
On the laser machined surface	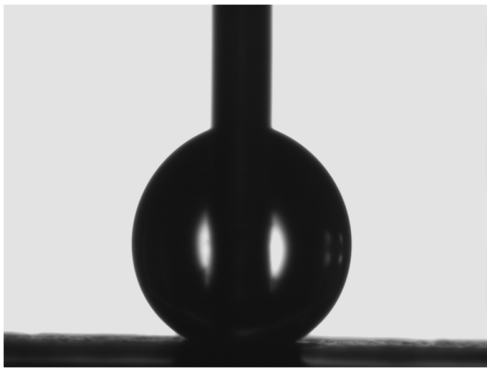	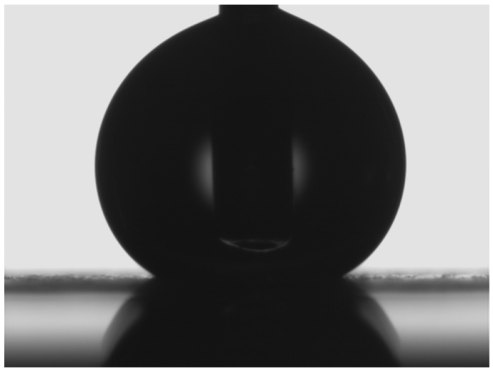

The theory proposed by van Oss *et al.* is not the only one available for estimating the interfacial tension. There are many more theories, and a common characteristic is that they can be used to estimate the theoretical work of adhesion and in combination with the Young equation for the contact angle, the solid components and solid surface tensions, which cannot be directly measured. Thus, theories for interfacial tension can be used in understanding wetting and adhesion phenomena and for characterizing solid surfaces e.g. helping us determine the desired modification of solid surfaces for tailor-made applications. Although most available interfacial theories can in principle be applied to all types of various interfaces (liquid-liquid, solid-liquid, even solid-solid ones), it is difficult to select a priori, the best theory, for a specific application. As shown by several researchers e.g. Balkenende *et al.* [17], all theories have advantages and shortcomings, but based on numerous investigations e.g. [18] the van Oss et al. is possibly the best tool to-date. It has been used extensively for describing interfacial phenomena (interactions) involving polymers, paints, proteins and other complex systems (polymer surface

characterization, CMC determination of surfactants, protein adsorption, cell adhesion, enzyme-substrate interactions). Several publications e.g. [19]-[25] discuss these applications.

According to the van Oss *et al.* acid–base theory, the interfacial tension between two surfaces includes contributions from both the polar and apolar components, i.e. the Lifshitz-van der Waals (LW), the electron acceptor or acidic (LA or "+") and electron donor or basic (LB or "-") parts. The expression for the surface tension is [25]:

$$\gamma = \gamma^{LW} + \gamma^{AB} = \gamma^{LW} + 2\sqrt{\gamma^{+}\gamma^{-}} \qquad \textbf{Equation 4-7}$$

The expression for the interfacial tension between two surfaces denoted as 1 and 2 is expressed as:

$$\gamma_{12} = \left(\sqrt{\gamma_1^{LW}} - \sqrt{\gamma_2^{LW}}\right)^2 + 2\left(\sqrt{\gamma_1^{+}} - \sqrt{\gamma_2^{-}}\right)\left(\sqrt{\gamma_1^{-}} - \sqrt{\gamma_2^{+}}\right) \qquad \textbf{Equation 4-8}$$

The free energy of interaction between two molecules or particles when 1 is immerged in liquid 2 is expressed as

$$\Delta G_{121} = -2\gamma_{12} \qquad \textbf{Equation 4-9}$$

Obviously, when γ_{12} >0, there is an attraction between the two surfaces. In water-based systems, the work due to LW force is negligible, and the major driving force for the interaction between a-polar particles is the strong acidic and basic energy [16]. So the energy between two surfaces under these assumptions could be approximately expressed as:

$$\gamma_{12} \approx 2(\sqrt{\gamma_1^{+}} - \sqrt{\gamma_2^{+}})(\sqrt{\gamma_1^{-}} - \sqrt{\gamma_2^{-}}) \qquad \textbf{Equation 4-10}$$

In the case of LISA, two types of surfaces are submerged in the same type of liquid, i.e. the laser machined surface, and the non-machined surface. What is needed in order to compare the work of adhesion are γ^{-}, γ^{+} and γ^{LW} values for each type of surface. The attraction work between the liquid and the two solid surfaces can be compared based on the contact angle measurements.

Upon combining the Young equation for the contact angle, the Dupré equation, for the work of adhesion and the van Oss *et al*. theory, the following equation for the work of adhesion of solid-liquid interfaces can be derived [16]:

$$W_{Sl}^{adh} = \gamma_L(1 + \cos\theta) = 2(\sqrt{\gamma_S^{LW}\gamma_L^{LW}} + \sqrt{\gamma_S^{+}\gamma_L^{-}} + \sqrt{\gamma_S^{-}\gamma_L^{+}}) \qquad \textbf{Equation 4-11}$$

Where γ_L is the surface tension of the liquid and γ_L^-, γ_L^+ and γ_L^{LW} are liquid basic, acidic and van der Waals components. Similarly γ_S^+, γ_S^- and γ_S^{LW} are the acidic, basic and van der Waals components of the surface tension of the solid surface. θ is the contact angle of the liquid on the solid surface. Several researchers have presented the surface tension parameters for various liquids for the Van Oss et al. theory, as shown in Table 4.8.

According to Equation 4-11, in order to characterize a solid surface, which means obtaining the LW and LA-LB components of the solid, the contact angles and the LW/LA-LB components of three types of liquid on the surface under investigation need to be known. Two of the liquids must be polar such as water and ethylene glycol, and the other one must be non-polar (or a-polar i.e. with zero Lewis AB components such as methylene iodide).

Besides water, two other liquids, ethylene glycol and methylene iodide's contact angles on PC and laser treated PC were measured by the same instrument. Table 4.7 shows the measured average contact angles for the investigated liquids on both injection moulding PC surface and laser machined PC surface. Table 4.8

Once contact angle data are available for the liquids, there are various methods for obtaining the acid/base parameters for the solid surface, including graphical approaches, as shown by McCafferty [25]. Of course, the parameters can be obtained by solving a system of three equations with three unknowns (the surface components of the solid).

Table 4.7 Contact angle results for three liquids on the PC and the laser machined PC surfaces. The observed standard deviation for measurement of ethylene glycol and methylene iodide was 12% in average.

Advancing CA (degree)	Ethylene glycol	Methylene iodide	Water
On PC original	41.8	34.7	86.0
On Laser machined PC surface	6.0	19.0	145.8

Table 4.8 Surface tension components values for standard liquids used in the van Oss et al. method published by two groups of researchers [25]

(1)	Van Oss and Good [16], [23]- [25]			
mJ/m2	γ_L	γ_L^{LW}	γ_L^-	γ_L^+
Methylene iodide	50.8	50.8	0	0
Water	72.8	21.8	25.5	25.5
Ethylene glycol	48.0	29.0	47.0	1.92

(2)	Della Volpe and Siboni (1997) [16], [25], [26]			
mJ/m2	γ_L	γ_L^{LW}	γ_L^-	γ_L^+
Methylene iodide	50.8	50.8	0	0
Water	72.8	21.8	10.0	65.0
Ethylene glycol	48.0	31.4	42.5	1.58

(3)	Della Volpe and Siboni (2000) [16], [25], [27]			
mJ/m2	γ_L	γ_L^{LW}	γ_L^-	γ_L^+
Methylene iodide	50.8	50.8	0	0
Water	72.8	26.2	11.2	48.5
Ethylene glycol	48.0	33.9	51.6	0.966

Equation 4-11 can be written as a set of three simultaneous equations and expressed in matrix form:

$$\begin{bmatrix} (\gamma_{L1}^{LW})^{1/2} & (\gamma_{L1}^-)^{1/2} & (\gamma_{L1}^+)^{1/2} \\ (\gamma_{L2}^{LW})^{1/2} & (\gamma_{L2}^-)^{1/2} & (\gamma_{L2}^+)^{1/2} \\ (\gamma_{L3}^{LW})^{1/2} & (\gamma_{L3}^-)^{1/2} & (\gamma_{L3}^+)^{1/2} \end{bmatrix} \begin{bmatrix} (\gamma_S^{LW})^{1/2} \\ (\gamma_S^+)^{1/2} \\ (\gamma_S^-)^{1/2} \end{bmatrix} = \frac{1}{2} \begin{bmatrix} \gamma_{L1}(1+\cos\theta_1) \\ \gamma_{L2}(1+\cos\theta_2) \\ \gamma_{L3}(1+\cos\theta_3) \end{bmatrix} \quad \textbf{Equation 4-12}$$

Where the numerical subscripts refer to the wetting liquid. The surface tension components for all the three liquids are shown in Table 4.8, and the contact angle for each liquid on the studied surface are obtained from experiments results shown above.

The calculated surface tension components for the two surfaces are shown in Table 4.9. The polar part is calculated by:

$$\gamma_S^{AB} = 2\sqrt{\gamma_S^+ \gamma_S^-} \qquad \textbf{Equation 4-13}$$

And the total surface tension is:

$$\gamma_S^{Total} = \gamma_S^{LW} + \gamma_S^{AB} \qquad \textbf{Equation 4-14}$$

Despite the many successful application stories, the van Oss *et al.* method has been criticized because the convention of equal acid/base parameters for water (used by the authors) seems arbitrary. Moreover, in most cases large base values are obtained and different "triplets" of liquids may yield different surface parameters for solids. For this reason, we considered it necessary to carry out our investigation using not only the original parameters of van Oss *et al.* for the test liquids but also the revised parameters proposed in 1997 and 2000 by Della Volpe and Siboni [26][27]. Thus, three sets of the solid surfaces' parameters are shown in Table 4.9, which correspond to the three sets of liquid acid/base parameters.

The results shown in Table 4.9 with all three sets are qualitatively similar for both the original and the laser machined PC surface. All three sets of calculated surface tension components for the studied surfaces show that the laser machined PC surface has larger polar components than the original surface, while the apolar (LW) parts are rather similar. This means that the laser machined surface has a large surface tension in total, and also according to Equation 4-11, a larger adhesion work can be obtained between the laser machined surface and the activation solution. For the activation solution, this result is not contradictory to the contact angle measurements, which showed a very large contact angle on the laser-machined area. This is because the measurement was operated on a dry surface, and the discussed case here is a completely wet one, which means that the liquid drop forms on actually a different surface "composite". The dry surface consists of air and plastic, and the wet surface consists of liquid and plastic.

It can be calculated from Equation 4-11 that the work of adhesion of the activation solution with laser-machined surface is much larger than with the non-treated surface. This means that, when rinsed by water, the activation solution may tend to stay more on the laser-machined surface than water does. However, on the original surface, it is easier for water to substitute the Pd solution. Moreover, as observed in Table 4.9, the laser-machined surface has a higher basic surface tension component, while the original surface has similar basic and acid parts. It is known that the activation solution is acidic (pH value is 1), i.e. compared to water the activation

solution can provide more protons. This observation provides additional confidence for the favourable adsorption (adhesion) of the activation solution on laser-machined areas. Similar enhanced adhesion due to acid/base interactions is often reported in literature [19][25].

Table 4.9 Van Oss et al theory's van der Waals (LW), acid (+) and base (-) components for the original (non-treated) PC surface and the laser treated PC surfaces, obtained based on the contact angle values shown in Table 4.7

(1)	Della et al.1997 [16], [25], [26]	
mJ/m^2	PC	PC laser
γ_S^{LW}	42.2	48.1
γ_S^+	0.5	4.7
γ_S^-	0.6	16.6
γ_S^{AB}	1.1	17.7
γ_S^{Total}	43.3	65.8

(2)	Della et al. 2000 [16], [25], [27]	
mJ/m^2	PC	PC laser
γ_S^{LW}	42.2	48.1
γ_S^+	0.2	3.0
γ_S^-	0.3	25.1
γ_S^{AB}	0.6	17.3
γ_S^{Total}	42.8	65.4

(3)	Van Oss et al. [16][25]	
mJ/m^2	PC	PC laser
γ_S^{LW}	42.2	48.1
γ_S^+	0.7	10.4
γ_S^-	0.8	70.1
γ_S^{AB}	1.5	54.0
γ_S^{Total}	43.7	102.1

In this section, the surface tension components of the van Oss et al. acid/base theory for the laser-machined and the non-machined surface were calculated based on contact angle measurements. From surface tension and interfacial work point of view, the laser-machined surface shows more attraction to the activation solution. So after rinsing by water, there are still activation drops on the laser-machined area but not on the original plastic surface, then subsequently plating only takes place on the laser-machined area. This is a plausible explanation when the chemical bonding mechanism is still not available. But it should be kept in mind that, the Young equation is based on perfectly flat surface; however the studied case is not perfectly flat. But if the porosity or roughness factor is considered, then other factors such as the interlock force contributing to the adhesion work should also be discussed, which increases the complexity.

4.2.3 Hypothesis (3): the activation and rinsing process can be described by diffusion

The third hypothesis is that the activation and rinsing process can be analyzed based on the diffusion behavior of the activation colloids. A mathematic model can be built according to Fick's diffusion law. The goal is to optimize the rinsing time by means of the diffusion model.

This opinion was hinted at initially from the so-called "short-time-plating" experiment, which was intended to illustrate where the copper starts to deposit on the laser track. Cross-section of laser tracks plated for 1, 2 and 3 minutes on both polyethylene and polycarbonate were observed, using a scanning electron microscope (SEM). Pictures (a) – (c) in Figure 4.13 show the cross sections of short-time-plated PE. PE is chosen to be displayed due to the clear layer structure; by contrast PC's cross-section only shows a cloud-like form because of the cross section moulding process. The bright dots in the pictures present heavy elements, which are copper particles in this figure. Figure 4.13 (a) shows that after 1 minute, copper particles appear

in the middle layers. In Figure 4.13 (b), the second minute, copper propagates along the top layer, while also starting to deposit at other sites in the middle layers. In Figure 4.13 (c), after a 3-minute plating, more copper deposits on the top layer. It can be seen that copper deposition does not happen simultaneously all over the surface structure.

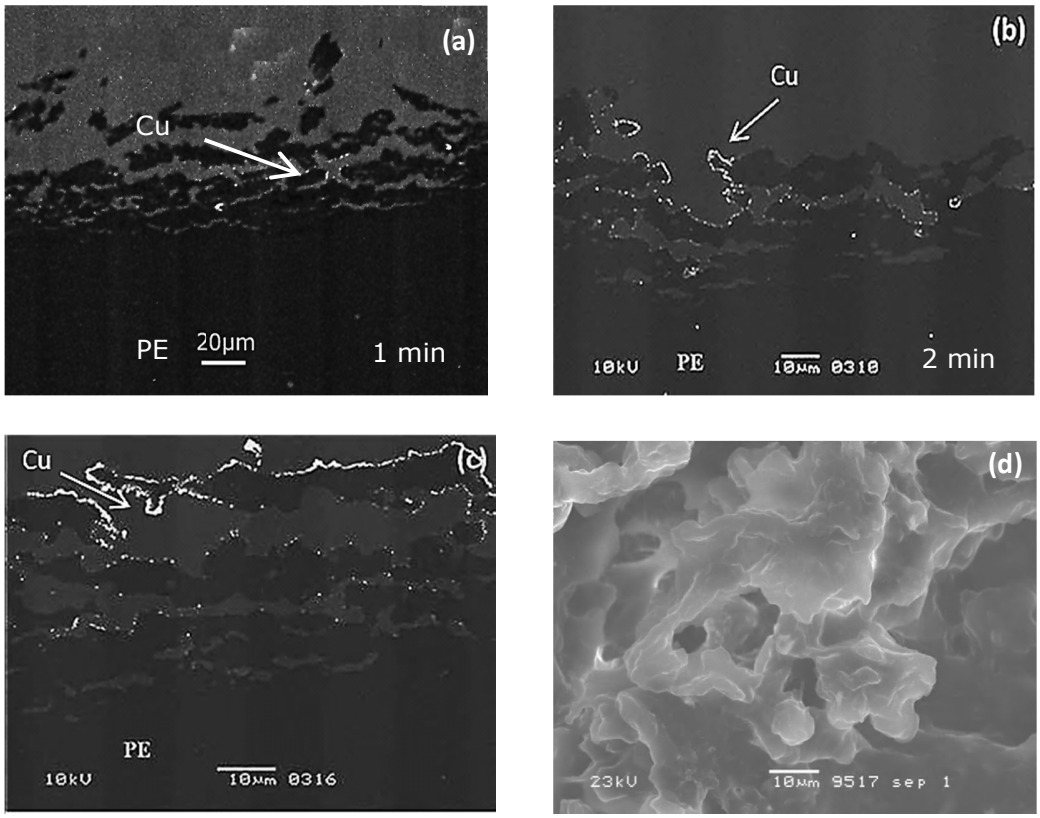

Figure 4.13 Cross-section of polyethylene (PE) plated for (a) 1.0 min and (b) 2.0 min (c) 3min (d) The sponge structure formed on PE surface by laser machining

Initially, this phenomena can be explained; on the top of the track, the activation colloid was rinsed away, while in the middle layers, the concentration of the activation colloids are the largest, that's why copper starts deposition from there, while in the deepest layer, the activation colloids didn't get enough time to diffuse there, so the concentration is low again.

Figure 4.13 (d) shows the size of the pores in the surface machined by an Nd: YAG laser and they are between 10 and 100µm in diameter. The pores size differs with material and laser setup. The porous structure creates a surface with a capillary effect for water or alcohol, i.e. water or alcohol tends to go into those pores. (But the activation solution will not go inside the porous structure if the surface is completely dry, because the contact angle on the plastic is larger than 90 degrees). In the rinsing afterwards, the activation solution in the laser machined area cannot be totally rinsed away. In other words, there is not sufficient time for all the palladium ions to diffuse out of the porous surface (into the rinsing water). Since all the activation drops on the

un-machined area are gone, during the plating, copper can only deposit on the laser treated area.

To apply Fick's diffusion laws, the diffusion is assumed to occur in only one dimension, i.e. activation colloids diffuse from the activation solution to water (or in the opposite direction) only at the direction vertical to the surface. In the first place, in order to ensure the research direction, estimation of diffusivity is performed using Equation 4-15, where D is the diffusivity or diffusion coefficient, in dimension of (m^2s^{-1}), l is the diffusion length and τ is the time needed for the diffusion. To activate the laser track, 5 minutes is sufficient for plating to take place, i.e. within 5 minutes, the concentration of activation colloids reaches a certain level and will not increase significantly. The structure's depth is used as the diffusion length. According to previous experiments, the average depth of the laser-machined structure is 60μm. In this method, D is approximately 2.13E-11 m^2s^{-1}, which is a reasonable value as a diffusion coefficient if estimated using the Einstein-stoke equation (Equation 4-18). It means diffusion theory can describe the plating and activation process.

$$D \approx \frac{l^2}{\tau}$$ **Equation 4-15**

$$\frac{\partial C}{\partial t} = \frac{\partial}{\partial x}\left[D_e \frac{\partial C}{\partial x} \right]$$ **Equation 4-16**

$$D_e = \frac{D \varepsilon_t \delta}{\tau}$$ **Equation 4-17**

The Fick's second diffusion law (Equation 4-16) predicts how particle concentration (C) changes with time (t) and distance (x). D_e is the effective diffusivity. When diffusion takes place in a porous media, the diffusivity can be corrected by Equation 4-17, where D is the diffusion coefficient in gas or liquid filling the pores (m^2s^{-1}), ε_t is the porosity available for the transport (dimensionless), δ is the constrictivity, which is a dimensionless parameter used to describe transport processes (often molecular diffusion) in porous media, viewed to depend on the ratio of the diameter of the diffusing particle to the pore diameter. τ is tortuosity (dimensionless), which is a property of the curve being twisted, estimated by the ratio of the curve's length to the distance between the ends of it.

To solve Equation 4-16, the value of D_e for specific particles (activation colloids or Cu^{2+} ions) is needed and relevant initialy and boundary conditions assumption must be made. Einstein-Stokes equation (Equation 4-18) provides a method to estimate the diffusivity for diffusion of spherical particles through liquids with a low Reynolds number.

$$D = \frac{K_B T}{6\pi\eta r}$$ **Equation 4-18**

In Equation 4-18, K_B is Boltzmann's constant, η is the liquid's viscosity, r is the radius of the spherical particle, and T is the absolute temperature. Water's viscosity and room temperature (293K) is used. The involved particles are activation colloids and Cu^{2+} ions. The particle radius is discussed in the following content.

Except by Equation 4-17, D_e can also be estimated by Equation 4-19, since it is not always easy to attain all the parameters in Equation 4-17. To be further simplified, the tortuosity can be estimated as $\sqrt{2}$ [28][28]-[30]. Combined Equation 4-16 with Equation 4-19, Equation 4-20 is arrived. Then the remaining difficulties are to estimate the particle size (to calculate D) and the porosity reasonably.

$$D_e = \frac{\varepsilon}{\tau^2} D = \frac{\varepsilon}{2} D$$ **Equation 4-19**

$$\frac{\partial C}{\partial t} = \frac{D}{2} \frac{\partial}{\partial x}\left[\varepsilon_x \frac{\partial C}{\partial x} \right]$$ **Equation 4-20**

The particles size in the activation solution was measured by equipment named Nanosight®. The working principle of this equipment is based on a conventional optical microscope, using a laser light source to illuminate the particles in solution, and then the diffusion behavior is analyzed so the particle diameter is obtained from Equation 4-18.

To accomplish this measurement, the activation solution was diluted by 10% HCl until the color of the solution disappeared (it was dark green before diluted). Figure 4.14 displays the measured particles size distribution in the activation solution, in which the x-axis is the size and the y-axis is the amount of the particles. However, unfortunately, the type of the particles cannot be distinguished in the measurement. So a reasonable inference drawn from the measured particle size distribution is necessary. The equipment can detect particles with a diameter within 10nm to 1000nm. Both sizes of single Pd^{2+} and Sn^{2+} ions are less than 1nm, according to the reported diffusion coefficient (1.17×10^{-9} and 2.5×10^{-10} $m^2 s^{-1}$) [31]. They are not visible to the equipment. Other components such as HCHO and related ions are also too small to be detected. The major peak in Figure 4.14 is from particles with size of 168nm in diameter. Larger particles exist due to agglomeration, meanwhile, smaller particles are also there because the final colloid structure is not formed yet or the shell is removed by excessive acid. So there are minor peaks at 370nm, 86nm and 37nm. 168nm is believed to be the size of the activation colloid. This value is much larger than the reported size, 1-2nm by J. Kim *et al.* [11]. The samples used by J. Kim *et al.* was made for TEM observation, which means the hydration layer was

removed; Besides, the samples were accelerated by HCl solution, which means the ($SnCl_3$) shell was also removed. When using Nanosight and operating the measurement in solution, It is believed to be reasonable that the obtained values are 2 orders of magnitudes larger. 460nm is believed to be the size of agglomerated particles, which is used in the diffusion calculation when rinsing the workpieces in water. It is also reasonable compared to the reported value 20-50nm. The size estimation will be verified by the diffusion curve.

Porosity is defined as the ratio of voids volume to the whole volume. In this case the concept effective porosity fits better, which is the fraction of the total volume in which fluid flow is effectively taking place (this excludes dead-end pores or non-connected cavities) [32].

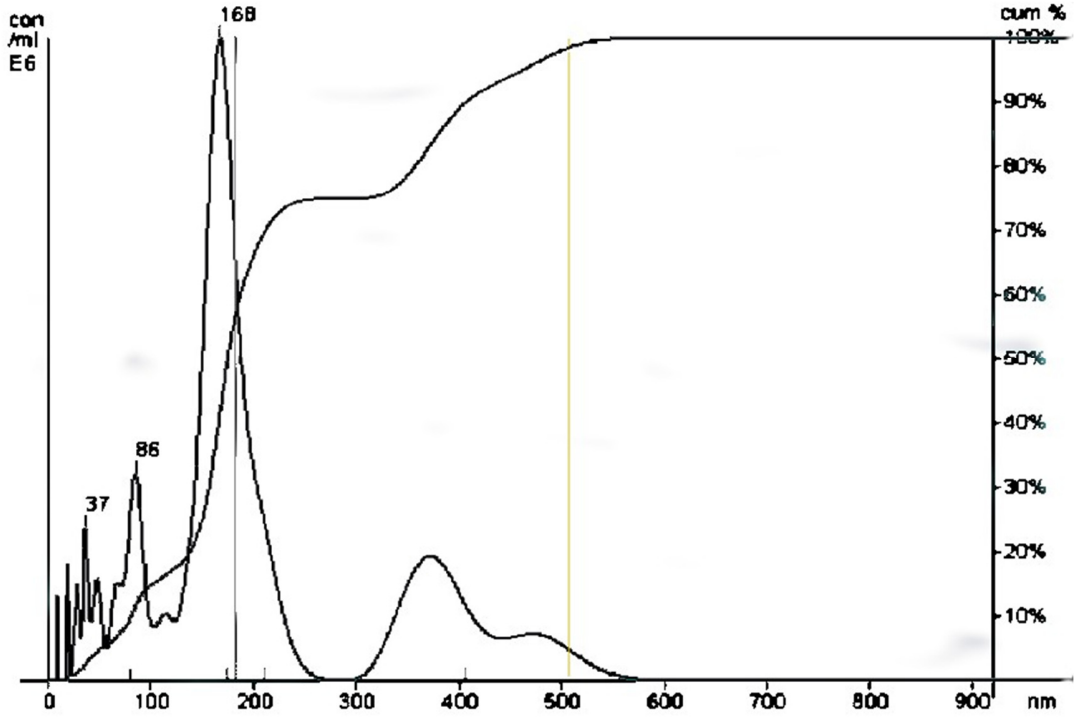

Figure 4.14 Particle size distribution in the new activation bath, obtained by Nanosight®

Obviously the porosity decreases with the depth. The porosity has to be analyzed layer by layer along the diffusion direction. It is assumed that in each layer, the pores are averagely distributed with the same size. The water saturation method or evaporation method cannot describe how the porosity changes. An Alicona InfiniteFocus® microscope is used to investigate the surface structure. It is able to take pictures layer by layer and then generate a 3D model. The relevant software provides access to make surface analysis. The porosity-depth curve can be obtained from the analysis. (This idea is generated from the bearing area curve method for the structure description, which is introduced in detail in Section 5.4). In Appendix 2, the technical specification and working principle of the instrument is attached.

It has to be mentioned that when Alicona InfiniteFocus® makes the scanning, the light shooting from above makes the focus, and the reflected light contains the topography information. As a

result, if one part is blocked by a structure lying above it, this part is lost in the final 3D model generated by Alicona InfiniteFocus® ®. Figure 4.15. Illustrates this. However, so far it is the best solution to characterize the structure formed by laser machining. The cross section may be an option, however the risk is that the porous structure may be dissolved by epoxy, which makes the image analysis difficult.

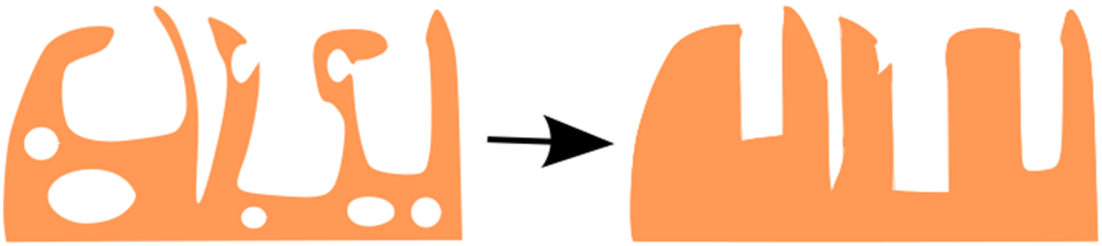

Figure 4.15 Structure information gets lost when Alicona InfiniteFocus® generates the 3 D model. If the real section of a workpiece has a feature of the left picture, then scanned by Alicona, the generated 3D model may have a cross section like the right picture.

To illustrate how porosity decreases with depth, the depth is used as y-axis; an example is shown in Figure 4.16, together with a cross section of a laser track on PE, which also explains how the depth is defined. (The laser parameters used to machine the track were: lamp current 18A, Q1200Hz, repeat 30 times speed 60mm/s, and wobble size 4.) The real porosity of the structure may change slower than shown by the curve because the obtained 3D model misses pores, which means the real porosity may be larger than the measured one.

To describe the curve mathematically, it is divided into three parts, 1st, the head, in which the porosity is close to 100%, i.e. the structure is almost open and barely has material, 2nd, the core part, where the porosity changes with depth almost linearly, 3rd, the tail, where the porosity is very close to 0, which means the structure is almost filled with material. To standardize the calculation, porosity 10% and 90% are used to define the head and tail. (10% and 90% are used in the volume parameters of the bearing area curve to define the peak part and the valley part). Figure 4.17 shows the modified curve from a porosity curve from a polycarbonate substrate. A trend line is made to the core part, and the equation describing the trend line is also displayed. Since the R-square value is quite high, the trend line equation is chosen to describe the porosity-depth trend of the core part. Furthermore the head part is considered as 100% open (porosity =1), and the tail part is 100% closed (porosity =0). Then the porosity is displayed as a function of depth (x) in a unit of µm, shown by Equation 4-21, where 32.3 µm and 74.2 µm presents the depth when the porosity is 10% and 90% respectively.

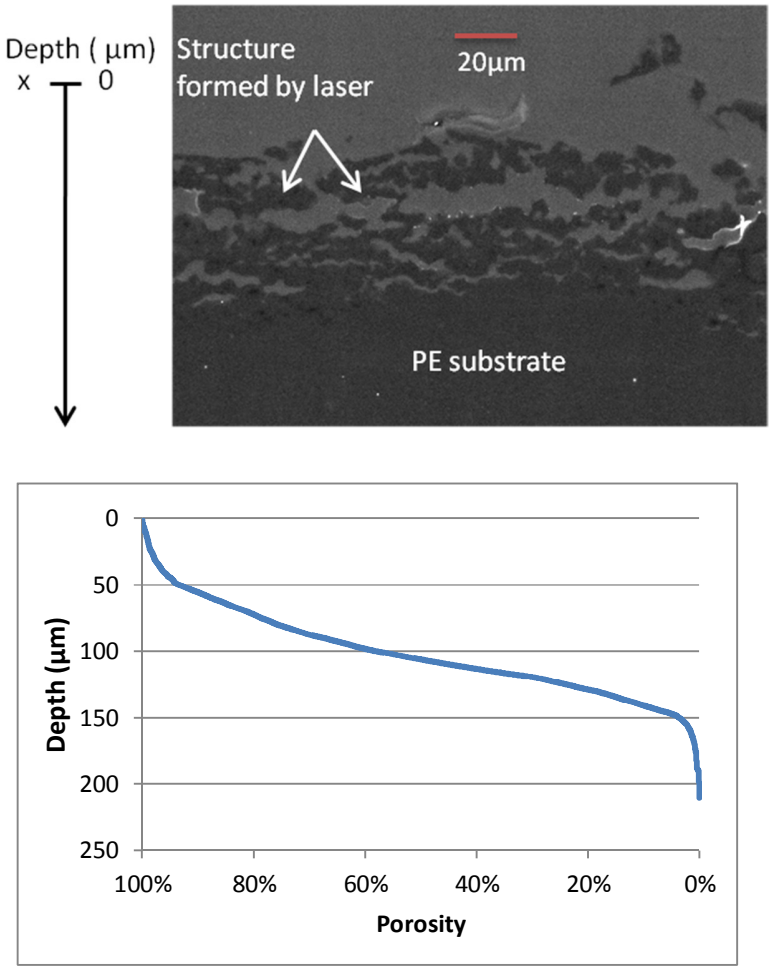

Figure 4.16 (a) is a SEM image which is a cross section of a laser track, and indicates how the "depth" is defined. (b) is a porosity curve made by Alicona InfiniteFocus® surface analysis.

$$\begin{cases} 0 \le x < 64.4, & \varepsilon = 1 \\ 64.4 \le x < 141, & \varepsilon = -0 - 0104x + 1.5695 \\ 141 \le x, & \varepsilon = 0 \end{cases}$$ **Equation 4-21**

According to Equation 4-19, the effective diffusion coefficient (D_e) is a function of the porosity. If combined with Equation 4-21, the effective diffusion coefficient (D_e) becomes a function of the depth, shown by Equation 4-22. In Equation 4-22, D_0 is the diffusion coefficient of particles in liquid filling the pores.

$$\begin{cases} 0 \le x < 64.4, & D_e = \frac{1}{2} D_0 \\ 64.4 \le x < 141, & D_e = \frac{1}{2}(-0.0104x + 1.5695) D_0 \\ 141 < x, & D_e = 0 \end{cases}$$

Equation 4-22

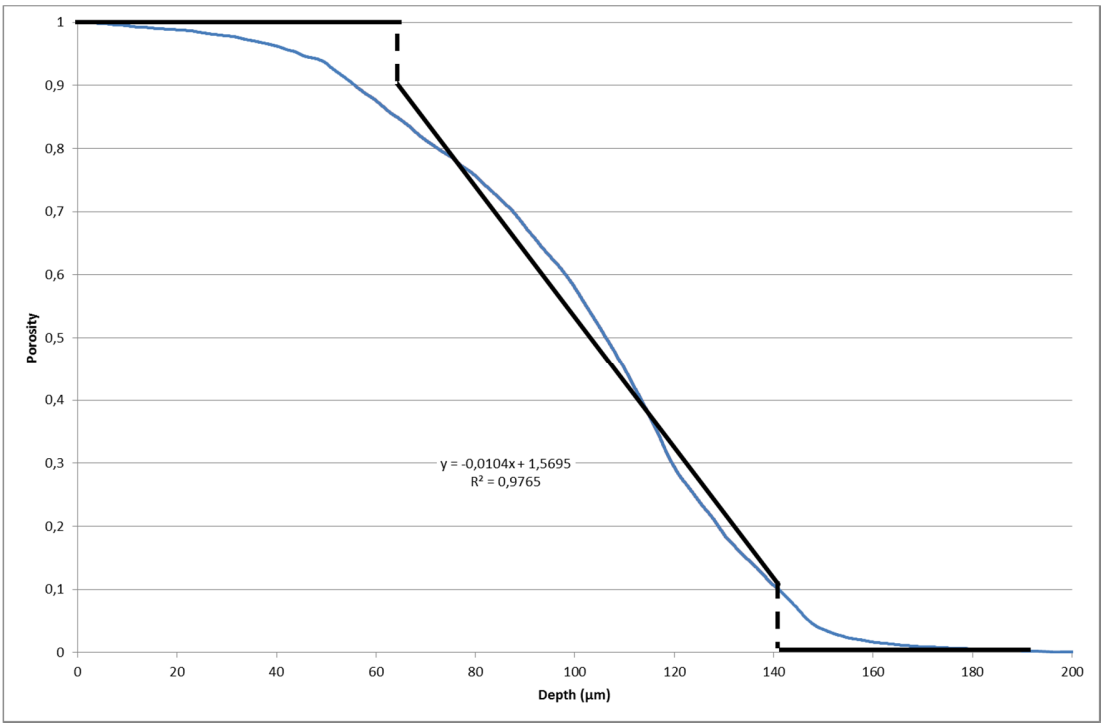

Figure 4.17 How the porosity curve is approximated for the diffusion calculation. The core part is approximated linearly. The head and tail parts are assumed as 100% and 0% porosity. The blue curve is the porosity curve and the black lines are the approximation.

If Equation 4-20 is combined to Equation 4-22, Equation 4-23 is obtained.

$$\begin{cases} 0 \le x < 64.4, & \dfrac{\partial C}{\partial t} = D_0 \dfrac{\partial}{\partial x} \dfrac{\partial C}{\partial x} \\ 64.4 \le x < 141, & \dfrac{\partial C}{\partial t} = D_0 \dfrac{\partial}{\partial x} \left[\dfrac{\partial C}{\partial x} (-0.0104x + 1.5695) \right] \\ 141 \le x, & \dfrac{\partial C}{\partial t} = 0 \end{cases}$$

Equation 4-23

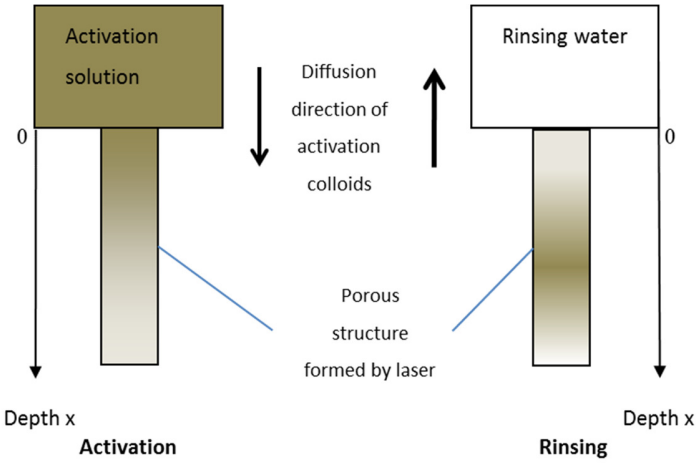

Figure 4.18 1D assumption for the diffusion behavior in activation and subsequent rinsing

The activation and plating process is divided into three steps according to the diffusion of activation colloids. 1st, the workpiece (which is fully wetted by water) is submerged in the activation solution, where the activation colloids diffuse from the activation solution to the water contained by the laser structure. The left side of Figure 4.18 illustrates the diffusion direction and the concentration change. This part needs 300 seconds. Compared to the volume in the laser structure, the activation solution is considered as infinitively large, which means at the boundry of the diffusion, the concentration of the activation solution is constant. And the initial concentration of the activation colloids in the laser structure is 0. Second, the workpiece is rinsed by distilled water for 30 seconds. In this step, the activation colloids obtained by the laser structure diffuse out of the track, as illustrated by the right side of Figure 4.18. Due to agglomeration, the particles size is one magnitude larger than when they diffused into the track. The rinsing water is considered as an infinitively large tank and with a concentration 0. So both the boundary and the initial concentration are 0. Third, when the rinsed workpiece is submerged in the electroless-plating bath, the activation colloids have a chance to diffuse out of the track again. However, as explained previously, the copper deposition happens in a very short time, so the diffusion of activation colloids will be ignored. Meanwhile, the components of the plating bath diffuse into the track in a similar rate due to the similar size.

$$\text{Concentration percentation} = \text{Final concentration} / \text{Original concentration} \times 100\% \qquad \textbf{Equation 4-24}$$

Combined with the initial and boundary conditions, Equation 4-23 is solved using the finite element method for the numerical solution of the partial differential equation in Matlab®. The final concentration result is given in the form of concentration percentage as shown by Equation 4-24. The concentration is plotted as a function of the depth of the laser track in Figure 4.19. After rinsing, the colloids concentration is 0 at the top of the laser track, and it increases to a peak value and decreases again. Approximately, from depth 10 µm to 45 µm, the

concentration of the activation colloids is relatively higher, which means more copper deposition can be triggered. A cross section of laser track on PE, plated for 1 minute (picture (a) in Figure 4.20), which illustrates where copper starts to deposit, shows that there are more visible copper particles in the depth of around 40µm. When the colloids concentration is too low, no copper deposition occurs or the copper particles are too small to be observed. In deeper area, not only the activation colloids concentration, the plating bath components are not sufficient either, especially at the beginning stage.

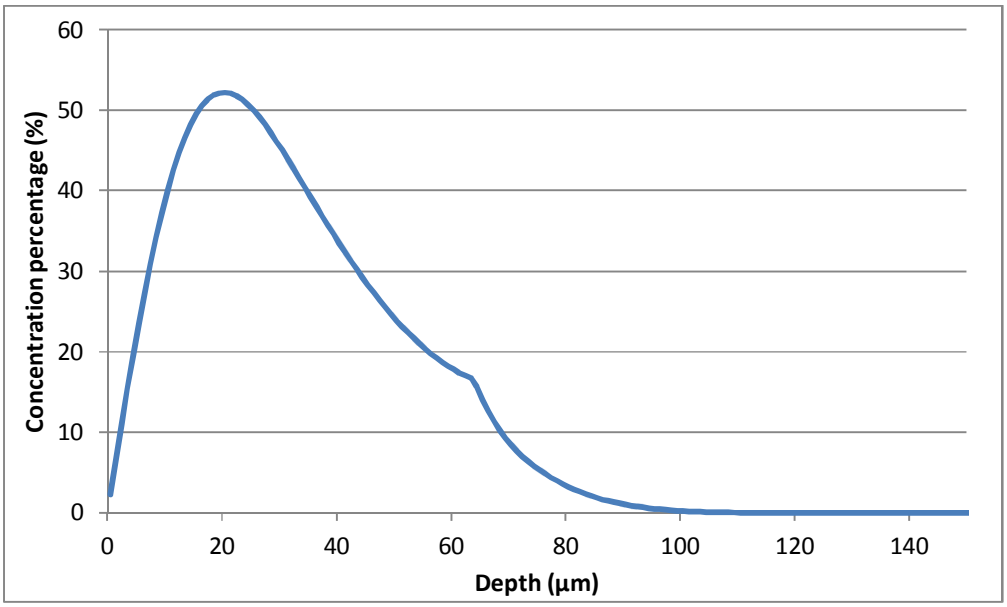

Figure 4.19 After 300s activation and 30s rinsing the concentration of the activation colloids is plotted against depth, in the form of percentage of the original concentration.

Since the true porosity is larger than the measured one, the concentration curve's peak position should appear at a deeper place than the current one at approximately 22µm. The laser track is not uniform even on the same plane with the same depth. This can be seen from the cross section pictures. As a result, the copper deposition on the laser track does not have the same rate of progress. Picture (a) in Figure 4.20 is a cross from a laser track plated for 1 minute. It is clear that the part with a big opening received more copper deposited, though the position is deeper.

How copper deposition propagates along the outer layer of the laser track is illustrated by Figure 4.20 (b) and (c). Though only few of the activation colloid should be there after rinsing, the main reason for the copper propagation is that copper deposition has a larger tendency on copper than on activation colloid, as J. Kim *et al* showed in their work [11]. Meanwhile the deposition in the middle layers continues, and more bright dots can be seen. Picture (d) in Figure 4.20 shows a laser track cross section on PC substrate, plated for 60 minutes. It is found that most of the copper deposition occurs on the top layers, and copper particles meet and a

layer tends to form. While in the deep part of the laser track, however some single copper particles can still be found.

It can be concluded that the diffusion model can be used to explain how the activation colloids are kept by the laser track, combined with the short-time-plating experiment. It reveals that the structure of the laser track and rinsing time have a significant effect on the process. Figure 4.21 shows how the peak position changes with the rinsing time.

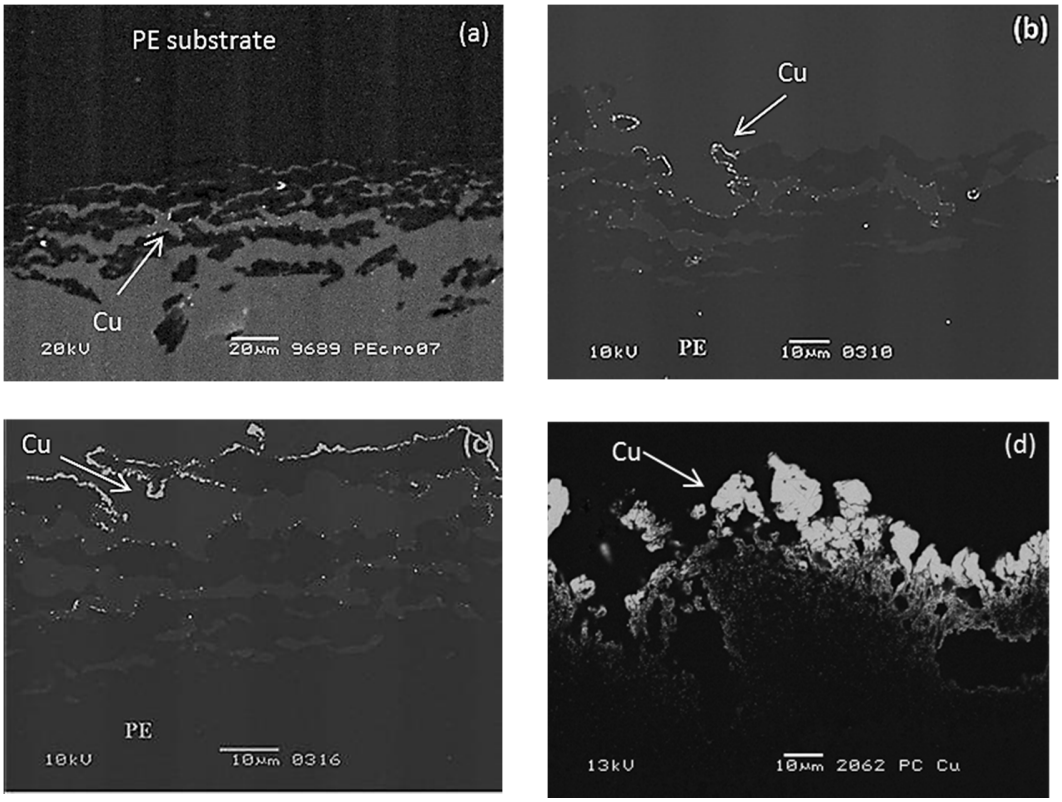

Figure 4.20 (a), (b) and (c) are SEM images of "short-time-plating" PE samples cross section. (a) Plated for 1 minute. (b) Plated for 2 minutes. (c) Plated for 3 min. (d) is a SEM image of PC sample cross section plated for 1 hour. In those pictures, bright color presents heave element, which is copper (the bight dots is proved to be copper by EDS).

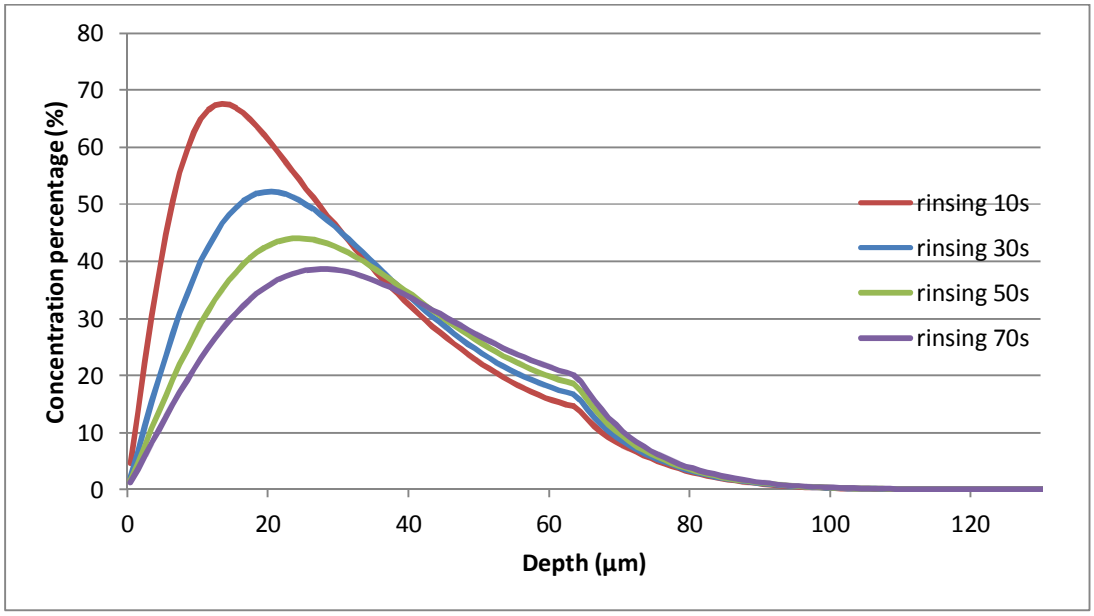

Figure 4.21 Rinsing time affects the concentration curve.

The essential premise in using the diffusion model is that, the structure formed by laser is foam-like or sponge-like. Figure 4.22 (a) and (b) show two types of cross sections, presenting two different surface structures, and they may have the same porosity vs. depth curve if measured using the method mentioned in this chapter. However, only the foam-like structure, shown by picture (b) in Figure 4.22, can be successfully plated, which means the coating can reach a certain depth and strongly bond to the substrate.

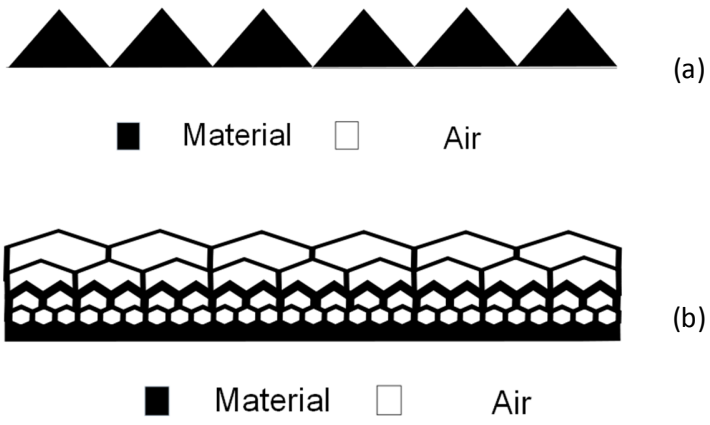

Figure 4.22 Two types of structure that may have the same porosity curve (a) cross section of a non-porous structure (b) cross section from a porous and foam-like structure

In addition, this diffusion model should be further optimized. For example, a better solution to acquire the porosity curve is needed. The sponge-like structure should be described in more detail, (so) that Equation 4-17 could be used to attain a better estimation of effective diffusivity.

And the diffusion model may be extended to 2 or 3 dimensions, not only in the direction of depth, but also the variance in the same plane can be considered. In addition, polymers machined by another type of laser, UV laser, show a similar sponge structure in a much smaller size, which can be studied to prove the conclusion, using the diffusion analysis and the short-time-plating experiment.

One of the goals of this diffusion model is that the rinsing time can be set according to the result. However, a necessary condition to solve this problem is that the lower limit of the activation colloids required to trigger the copper deposition, (As it is not found yet it will remain a task for future exploration.) This will be a task for the future.

4.3 Conclusion

In this chapter, the mechanism of the $PdCl_2/SnCl_2$ activation system is introduced mainly based on previous researchers' work. The activation colloids have a Pd-Sn alloy core and $(SnCl_3)^-$ shell. In the subsequent electroless copper plating, copper substitutes Sn in the core firstly, and the other copper ions can deposit on the existing copper.

How the laser tracks keep the activation colloids is studied. Three hypotheses were made. The first hypothesis is that laser machining leads to chemical changes to the polymer, which results in chemical bonding with the activation colloids. Chemical changes were investigated by XPS and FTIR spectroscopy, but no evidence shows that chemical bonds exist between the laser track and the activation colloids. However, it cannot be excluded that chemical bonding is part of the mechanism. The second hypothesis is that the laser track has a stronger attraction work to the activation solution. This is proven by the calculation using van Oss *et al*. theory based on contact angle measurement. PC was mainly studied. In the future work, more polymers should be tested to support the conclusion. The third hypothesis is that the activation and rinsing process can be described by diffusion. This is supported using Fick's diffusion law combined with the short-time-plating experiments.

Reference

[1] G. O. Mallory, J. B. Hajdu, "Electroless Plating - Fundamentals and Applications" William Andrew Publishing/Noyes, 1990.

[2] M. Pourbaix, "Atlas of Electrochemical Equilibria in Aqueous Solutions", Pergamon, Oxford, New York, 1966.

[3] C.R. Shipley Jr., "Method of Electroless Deposition on a Substrate and Catalyst Solution Therefor," U.S. Patent 3011920, 1961.

[4] R. L. Cohen, K. W. West, "Generative and stabilizing processes in Tin-palladium Sols and palladium sol sensitizers", Journal of Electrochemistry Society: Electrochemical Science and Technology, Vol. 120, pp.502, 1973.

[5] T. B. Massalski, J. L. Murray, L. H. Bennett, H. Baker, "Binary alloy Phase diagrams", American Society for Metals: Metals Park, OH, 1986.

[6] C. L. Yaws, "Chemical Properties Handbook: Physical, Thermodynamic, Environmental, Transport, Safety, and Health Related Properties for Organic and Inorganic Chemicals", Mcgraw-Hill: New York, 1999.

[7] O. Holderer, T. Epicier, C. Esnouf, G. Fuchs, "Direct Structural and Chemical Analysis of Individual Core-shell (Pd,Sn) Nanocolloids", The Journal of Physical Chemistry, Vol. 107, No. 8, Feberuary 27, 2003.

[8] J.Horkans, "A cyclic voltammetric study of Pd-Sn colloidal catalysts for electroless deposition", Journal of Electrochemistry Society, Vol 130,pp. 311, 1983.

[9] T. Osaka, H. Takematsu, "A Study on Activation and Acceleration by Mixed PdCl2/SnCl2 Catalysts for electroless Metal Deposition", Transactions of the Society for Advancement of Electrochemical Science and Technology, Vol.127, No. 5, pp.1021-1029, 1980.

[10] E.J. Fadgen, E.B.Saubestre, "Activator solutions, their preparation and use in electroless plating of surfaces" U.S. Patent 3767583, 1973.

[11] J. Kim, S. H. Wen, D. Y. Jung, R. W. Johnson, "Microstructure evolution during electroless copper deposition", IBM Journal of Research and Development archive, Vol. 28, No. 6, November 1984.

[12] Technical Brochure: Internet source. http://www.dpc.kt.dtu.dk/upload/centre/dpc/research/instruments/ftir.pdf, accessed: 01-10-2010.

[13] J. R. Dyer, "Applications of absorption spectroscopy of organic compounds", Prentice-hall, Englewood Cliffs, N.J. 1965.

[14] Y. Zhang, P. T. Tang, H.N. Hansen, J.S. Nielsen, "Electroless Plating on Plastic Induced by Selective Laser Activation", Plating and Surface Finishing, Vol. 97,pp. 43, 2010.

[15] Y. Zhang; G. M. Kontogeorgis; H. N. Hansen, "An explanation of the selectiveplating of laser machined surfaces using surface tension components", Journal of adhesion science and technology, submitted 03, August, 2010.

[16] C. J. van Oss, M. K. Chaudhury, R. J. Good, Monopolar Surfaces, "Advances in Colloid and Interface Science", Vol.28, pp.35, 1987.

[17] A. R. Balkenende, H.J.R.P. van de Boogaard, M. Scholten, N. P. Willard, "Evaluation of Different Approaches To Assess the Surface Tension of Low-Energy Solids by Means of Contact Angle Measurements", Langmuir, Vol.14, pp. 59071998.

[18] P. C. Hiemenz, R. Rajagopalan, "Principles of Colloid and Surface Science", 3rd edition. Marcel Dekker, 1997.

[19] J. R. Svendsen, G. M. Kontogeorgis, S. Kiil, C. Weinell, C. M. Grønlund, "Adhesion between coating layers based on epoxy and silicone", Journal of Colloid Interface Science, Vol. 316 pp.678, 2007.

[20] G.M. Kontogeorgis, G.K. Folas, "Thermodynamic models for industrial applications: From Classical and Advanced Mixing Rules to Association Theories", John Wiley & Sons: New York, 2010.

[21] M. Osterhold, K. Armbruster, "Correlation between surface tension and physical paint properties Progress in Organic Coating", Vol 33, pp. 197, 1998.

[22] J.H. Clint, "Adhesion and components of solid surface energies", Current Opinion in Colloid Interface Science, Vol.6, pp. 28-332001.

[23] R. J. Good and C. J. van Oss, "Modern Approaches to Wettability", Plenum Press, New York, 1992.

[24] R. J. Good, "Contact angle, wetting, and adhesion: a critical review", Journal of Adhesion Science and Technology. Vol 6, issue12, pp. 1269,1992.

[25] E. McCafferty, "Acid-base effects in polymer adhesion at metal surfaces", Journal of Adhesion Science and Technology, Vol. 16, No.3, pp.239-255, 2002.

[26] C. Della Volpe and S. Siboni, "Some Reflections on Acid–Base Solid Surface Free Energy Theories", Journal of Colloid Interface and Science, Vol. 195, pp. 121, 1997.

[27] C. Della Volpe and S. Siboni, "Acid-base surface free energies of solids and the definition of scales in the Good-van Oss-Chaudhury theory", Journal of Adhesion Science and Technology, Vol.14, pp. 235, 2000.

[28] P. V. Zhelezny, A. A. Shapiro, "Experimental investigation of the diffusion coefficients in porous media by application of X-ray computer tomography", Journal of Porous Media, vol.9, issue 4, , pp. 275-288, 2006.

[29] N. Bakhvalov, and G. Panasenko, "Homogenisation Averaging Processes in Periodic Media", Kluwer Academic Publishers, Dordrecht. 1989.

[30] A. A. Shapiro and E. H. Stenby, "Factorization of Transport Coefficients in Macroporous Media", Transport in porous media, Vol.41 pp.305 -323, 2000.

[31] M. Garcı´a-Gabaldo´n, V. Pe´rez-Herranz, J. Garcı´a-Antôn, J. L. Guinôn, "Electrochemical study of the activating solution for electroless plating of polymers", Journal of Applied Electrochemistry Vol 37, pp. 1145–1152, 2007.

[32] W. C. Lyons, G. J. Plisga, "Standard handbook of petroleum and natural gas engineering", 2nd Ed. Elsevier.

Chapter 5. Optimization of the laser process

The study of the laser process aims at: (1). Finding out a quantitative characterization method for the structure formed by laser machining, so that an identical structure description can be built for a different laser set-up (2). Finding out how a laser setup affects the structure of the laser track (3). Finding out a quantitative characterization method for the porous structure, where the characterization response will be used to predict whether the laser track can be plated or not.

In this chapter, first, the process of laser machining is introduced in detail. As explained in the previous chapter, it is believed that the porous structure formed in the laser process is the key factor to attract the activation colloids. How the laser structure forms will be discussed based on the laser beam property as well as a simple thermal effect simulation. Suitable porous surfaces are displayed and compared with failed surfaces.

The YAG laser's parameters are chosen to be studied due to the easy access of the equipment. Besides, laser tracks made by a fibre laser and a UV laser will be shown, and set-ups for these two lasers are recommended as well.

Finally, a normalized bearing area curve is proposed as a characterization method for the porous structure. For the LISA surfaces made by a UV laser and a YAG laser, very similar normalized bearing area curves can be achieved. This method is feasible to find out the common ground for all the LISA surfaces.

5.1 The process of laser machining to polymer surface

5.1.1 Procedure

The standard procedure for the laser machining process is described below [1]:

Step 1: design the pattern to be selectively metallized. The pattern design rule depends on the laser's mode and the software in service. Also the sample holder of the system limits the pattern and the substrate dimension. For example, a cylinder's surface may need to be machined on a rotating sample holder.

Step 2: clean the workpiece using distilled water. If it is necessary to remove grease, alcohol should be used.

Step 3: set up the laser, choose proper parameters for the laser power output, laser beam speed and so on.

Step 4: fix the workpiece in a chamber with water and adjust the alignment if necessary. The water cycle system or flowing water system may be used to keep the water clean.

Step 5: run the laser so the desired pattern is accomplished.

Step 6: store the workpiece properly. It is recommended to store the workpieces in water to be prepared for the subsequent activation and plating.

5.1.2 Structure forming mechanism hypothesis

The laser-induced modification on the surface can be attributed to a photochemical effect and a thermal effect. In both cases the reactions are caused by the energy provided from the photons. The photon energy depends on the wavelength of the laser (Equation 5-1):

$$E = \frac{hc}{\lambda}$$ **Equation 5-1**

Table 5.1 Comparison of photon energy from typical lasers and common covalent bonds strength [2]

		Energy or bond strength (KJ/mol)
Laser	Nd: YAG laser	112
	UV laser (340nm)	352
Common covalent bonds In polymer	C-C	348
	C=C	614
	C-H	413
	C-Cl	330
	C-N	308
	C-O	360
	H-O	366

The wavelength of the investigated Nd: YAG laser is 1064 nm. Table 5.1 compares the photon energy from an Nd: YAG laser with the strength of some typical covalent bond in polymers. Apparently the photon from an Nd: YAG laser is not enough to break any covalent bond in the table, and as a result almost all the photon energy is absorbed as heat. UV lasers have the possibility to break bonds because of the high energy photons, however, usually in commercial polymer grade, UV resistant are added, which can absorb UV energy and transfer the energy to heat almost 100% [3]. It is believed that all the absorbed energy by the workpiece surface is transferred to thermal effect; as a result a thin layer on the surface melts. The surrounding water then instantly cools it down, so the polymer solidifies quickly and maintains the structure when it melts. After several passes (15 - 30 passes) of the laser, the laser track will be full of

peaks and pores due to the random distribution of the pulses. However, it cannot be excluded that chemical reactions happen under high temperature due to the intense local heating. Usually, a burnt smell can be noticed during the laser machining process; it is also observed that air bubbles keep being generated from polymer surface, which is supposed to be due to the boiling of water.

To support this hypothesis, a transient thermal model is used to simulate the laser treatment on the substrate. Based on the dimension of the real workpiece, the size of the simulation substrate is 2x3x10mm^3, as shown in Figure 5.1. It is a half of a piece and the other half is symmetric, since in this way it is able to observe the cross section of the simulated laser spot. PC is used as the substrate, and the datasheet is attached in Appendix 1. Since Water is used as a medium, and (the) convective coefficient is assumed to be 500 W/(m^2·K) (no experimental data is available so this value has to be assumed, and for water the range of the convective coefficient is from 50 to 10000 W/(m^2·K) when external force exists).

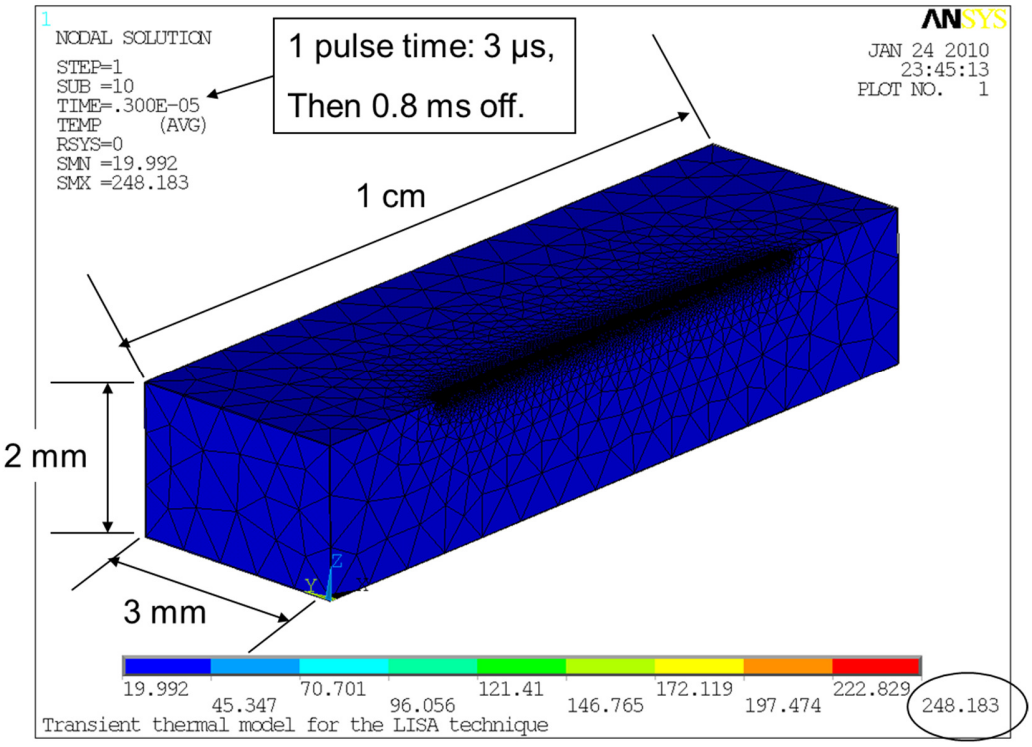

Figure 5.1 The substrate used in the thermal effect simulation. The dimension is set according to the injection molding workpiece. It is only a half of a piece, and the other half is supposed to be symmetric. Therefore the cross section can be observed.

As explained in the previous chapter, the Nd: YAG laser is Q-switch pulsed. When the Q-frequency is 1200Hz (which is a common setup for LISA surface), the pulse width is about 3μs and then the pulse is off for around 800μs until the next pulse comes. A nominal laser beam diameter of 80μm is used for the size of the heat source. The first step of the simulation work (Figure 5.2) shows the temperature distribution immediately after one pulse, i.e. the time span

is 3µs. It can be seen that the temperature of more than half of the spot is higher than 120°C, which is enough to soften the polymer. In the center area, a high temperature around 250°C is achieved, which may be able to cause morphological change or even remove parts of the polymer (the studied PC melts at 310°C). The heat-affected zone is less than 20 µm deep, which corresponds well to experimental observation, e.g. the cross section of laser tracks.

Then the next step of the simulation considers the wobbling effect. Figure 5.3 is a screen shot at 7227µs, when the 9th spot is just started. Arrows mark the sequence of all the spots. Obviously, when later spots are started, the temperature of the earlier ones goes down. It must be mentioned that the speed of the laser beam used in this part is only around 10mm/s in total, and the instant speed between dots is around 30mm/s. No overlap of heat-affected zones is shown yet from this figure. If the laser beam moves faster, there is less chance for overlap among heat-affected zones. Although the simulation work didn't go further due to the project time limitation, the obtained results effectively illustrate the cycle of material heating up and the rapid cooling down. It is believed that this approach is necessary in order to understand the formation of the sponge structure.

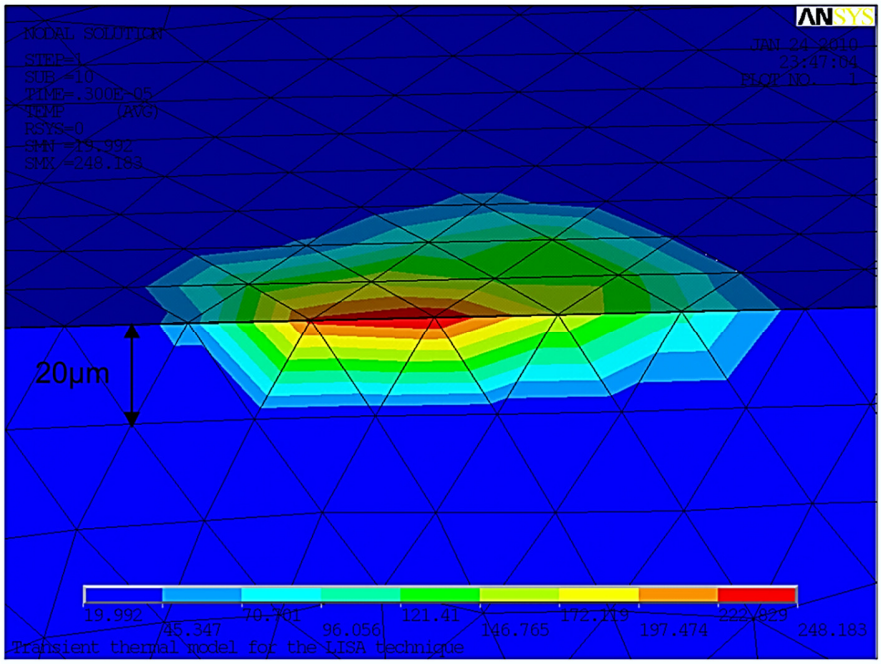

Figure 5.2 Temperature distribution after 3µs, which is the length of a pulse from YAG laser, the lower half of the figure shows the cross section part, and the depth is marked on the figure.

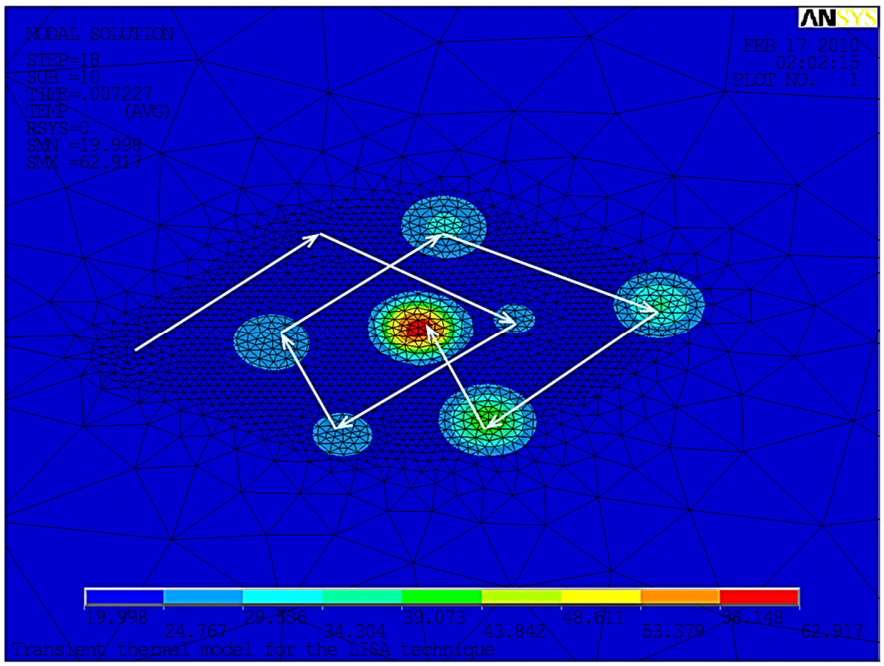

Figure 5.3 When time span is 7227µs, 9 spots can be made due to the wobbling effect. The pass of the beam movement, i.e. the sequence of the spots, is shown by the arrows.

5.1.3 Suitable surfaces for LISA

It is possible to use a microscope to check whether the obtained surface is suitable for LISA. This is a qualitative method.

After the YAG laser treatment with proper setup, the surface becomes porous and spongy. As shown by Figure 5.4 below. The surface roughness was measured by an optical profilometer (UBM), assisted by the image analysis software SPIP. A short introduction to the UBM equipment is attached in Appendix 2. Compared to the original surface of which the roughness (S_a) is approximately 0.6µm, the laser treated part is as rough as 5.7µm (S_a). Figure 5.5 shows the profile and the 3D image of a transition region from original area to the laser treated area. They also illustrate that material was lifted because of the porous structure formed on the laser treated area. When using other types of laser or material, the roughness may change, and the amount that the surface is lifted is changed as well.

A similar topograghy is seen in laser tracks made by LDS®. It is claimed that such a porous structure provides an anchoring force to the metal particles. However, this is not the reason for LDS® metal particles deposition, as explained in the previous chapter. No further data such as the structure thickness or the pores size are available for LDS® track to make a comparison.

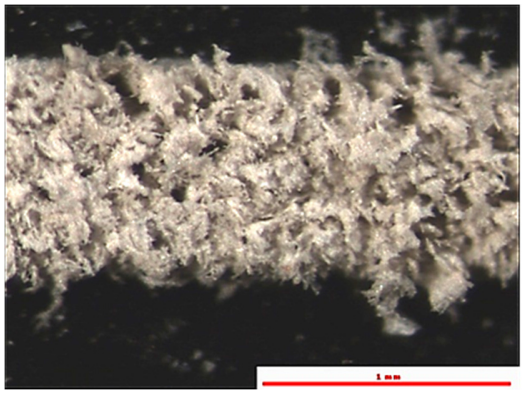

Figure 5.4 Structure formed after laser machining on PC surface, observed by optical microscope.

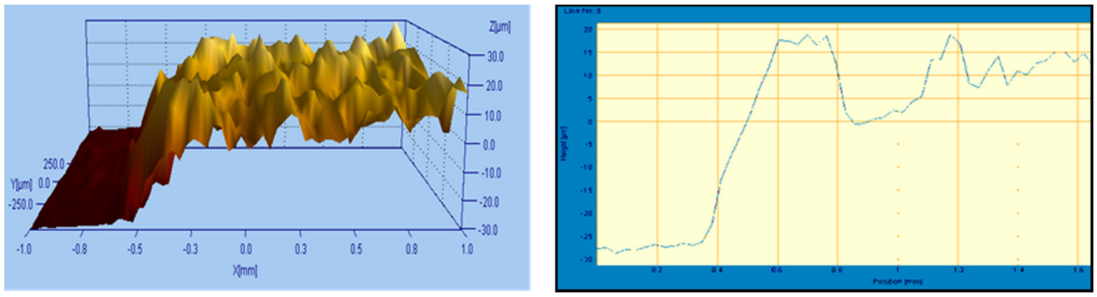

Figure 5.5 SPIP analyzed UBM picture displaying a transition from untreated to laser treated surface. The left picture is 3D view, and the right picture is a profile on the surface.

All of the displayed samples in Figure 5.4 and Figure 5.5 were made by the YAG laser parameters of lamp current 18A, Q 1200 Hz, speed 60mm/s and wobble size 4.

The main drawback of such a type of surface is that it is easy to scratch, i.e. the porous structure can be easily broken due to foreign forces.

5.1.4 Material

Thermoplastics with different melting temperature in a large range were tested, for example, PE (130 °C), ABS (250 °C), PC (310 °C), PEEK (340 °C), *etc*. High melt point materials are supposed to need more energy input, but the laser parameters, which are good for a material with low melting temperature can also be applied to others. For example, PE's melting temperature is almost 200 degree lower than PC, however, the working window of the laser parameters when using the Nd: YAG laser, i.e. the parameters range in which the resulted laser track can be plated, was observed to be the same for both PE and PC; the resulting laser tracks are slightly different when using same parameters on those two polymers, for example the thickness porous structure and the roughness, but the laser tracks on both polymers can be plated.

Not all material grades are suitable for LISA, even if they are the same polymer. For example, not all grades of PE can be used. Figure 5.6 shows laser tracks on two types of PE. The substrate for (a) is called "bad PE", because the laser track failed to be plated. Obviously, this type of laser track is made of smooth bumps, and the activation solution is easily rinsed away. The substrate

for (b) is called “good PE” and it can be used for LISA. However, the datasheet is not available for the so-called “good PE”. Since no comparison can be made between the material properties, the reason for the failure of “bad PE” has not found out yet.

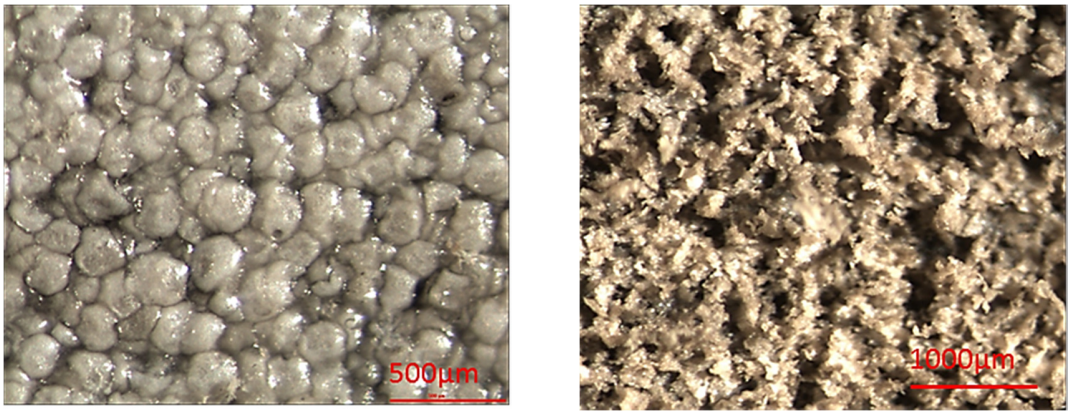

(a) (b)

Figure 5.6 Different grades of PE have different surface structure after laser machining. (a) is from the so-called “bad PE”, which cannot be plated; (b) is from the so-called “good PE”, which is also used other studies in this project

5.2 Study of YAG laser’s parameters

5.2.1 The incidence angle effect on the height of laser machined surface

It was observed that the incidence angle affects a single laser spot as illustrated by Figure 5.7. Efforts were put on the effect of incidence angle on LISA surface. The height of the track was used as a characteristic parameter of the surface.

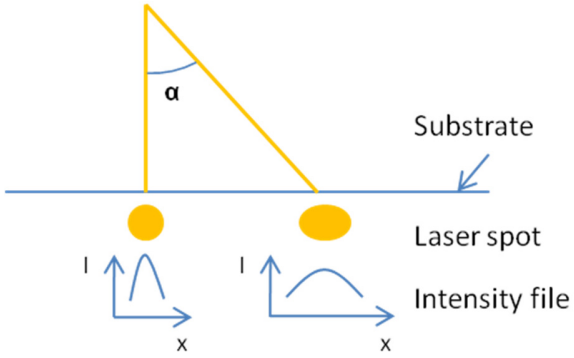

Figure 5.7 Illustration of the effect from incidence angle on the spot shape and the energy intensity profile.

7mm long and 2mm wide tracks were made for this measurement. The distance between two parallel tracks is 1.5mm, and 4 tracks were made on each piece. The incidence angle of the laser beam for each track varies from 0° to 4.8°. The samples are not reusable since the microscope

lens may touch the track and damage the surface. The illustration of the tracks and the incidence angle is shown in Figure 5.8.

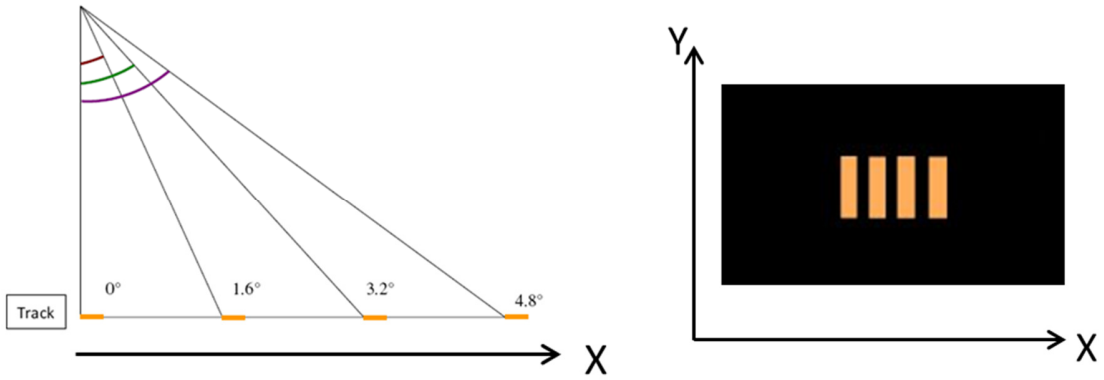

(a) (b)

Figure 5.8 Incidence angle for four tracks on one piece, only the angle at X direction is considered, the effect on the Y direction is ignored. (a) shows how the angle is calculated, the vertical distance is measured from the lens to the sample; (b) illustrates the workpiece with 4 laser tracks.

The laser track height was measured by a stereo microscope. On the stereo microscope, there are two separate optical paths with two objectives and two eyepieces to provide slightly different viewing angles to the left and right eyes. In this way it produces a three-dimensional visualization of the examined sample [4]. In the microscope lab of MPP, three objective lenses were available, 5x, 20x, and 50x. The calibration of the equipment was made by standard measuring bars. When using a higher magnification, a smaller depth of field and a narrower field of view can be obtained, which means, a smaller portion of the observed piece appears sharp in the image. From this point of view, to measure the distance at Z direction, the highest magnification is always preferred, so the top of the track can be distinguished from the bottom significantly. The 50X lens was used initially.

The height measuring procedure was as follows: firstly the substrate top surface is focused, and the position was set as zero; then the top surface of the laser track was focused, so the position value was the height of the laser track. The problem that followed was when using a magnification as high as 50X; the field of view was too small to give enough surface information. It's also due to the surface non-uniformity. A LISA surface is far from homogeneous, so at high magnification only a few peaks can be seen in the ocular lens, but the amount is too few to represent the whole workpiece's height level. For instance, if the observed peaks were actually much higher or lower than all the other parts, it is not fair to use the height of those peaks for the whole laser track. Otherwise quite a large amount of points need to be measured to get the average value, but it will increase the work amount significantly.

Finally a 20X lens was used in the height measurement. In this case, a relatively large area can be observed meanwhile the depth of the field is still small enough to observe the track height. Furthermore, as long as the same lens is applied to all the samples, the obtained data give a good indication to make a comparison.

The incidence angles from the first track to the fourth are 0°, 1.6°, 3.2°, and 4.8°. The height of each track was plotted against the incidence angles and shown in Figure 5.9 to Figure 5.11, i.e. the Y-axis is the height of track and the x-axis shows the incidence angle. The laser parameters effect is also observed here, so separately, the lamp current is 15A, 18A and 21A for the three charts. A slight trend is seen in that the tracks made with the highest laser incidence angle are lower than those made by the vertical beam (incidence angle 0 degree). But if the measurement deviation is considered, the difference between the four tracks on one workpiece is almost eliminated. As a result, within 5°, the incidence angle does not influence the laser track height significantly. (According to the samples made so far, the largest incidence angle we used is 14.35°, compared to LDS®'s limit 12.6° [5]). The average standard deviation and COV% of the height for each incidence angle are shown in Table 5.2. Moreover, it can be observed that a higher lamp current will lead to a higher laser track, which will be discussed further in section 5.2.5.

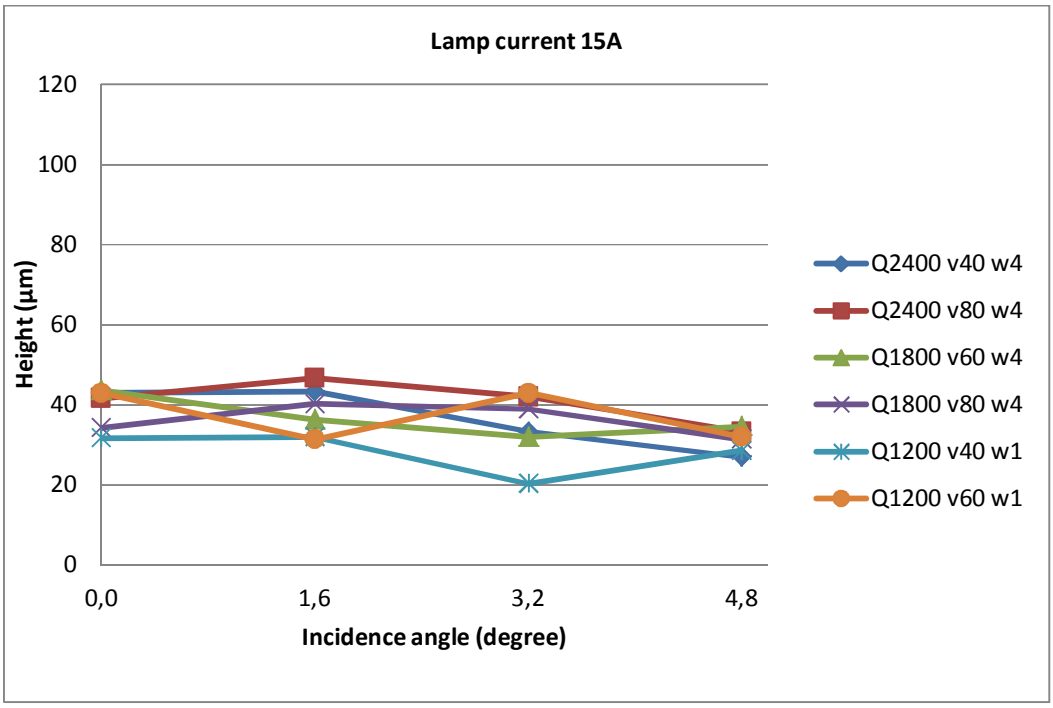

Figure 5.9 The effect of incidence angle of Nd: YAG laser when lamp current is 15A. Q is the Q-switch frequency. V is the laser beam velocity and W is the wobble size. The height is measured from the top of laser tracks to the substrate top surface.

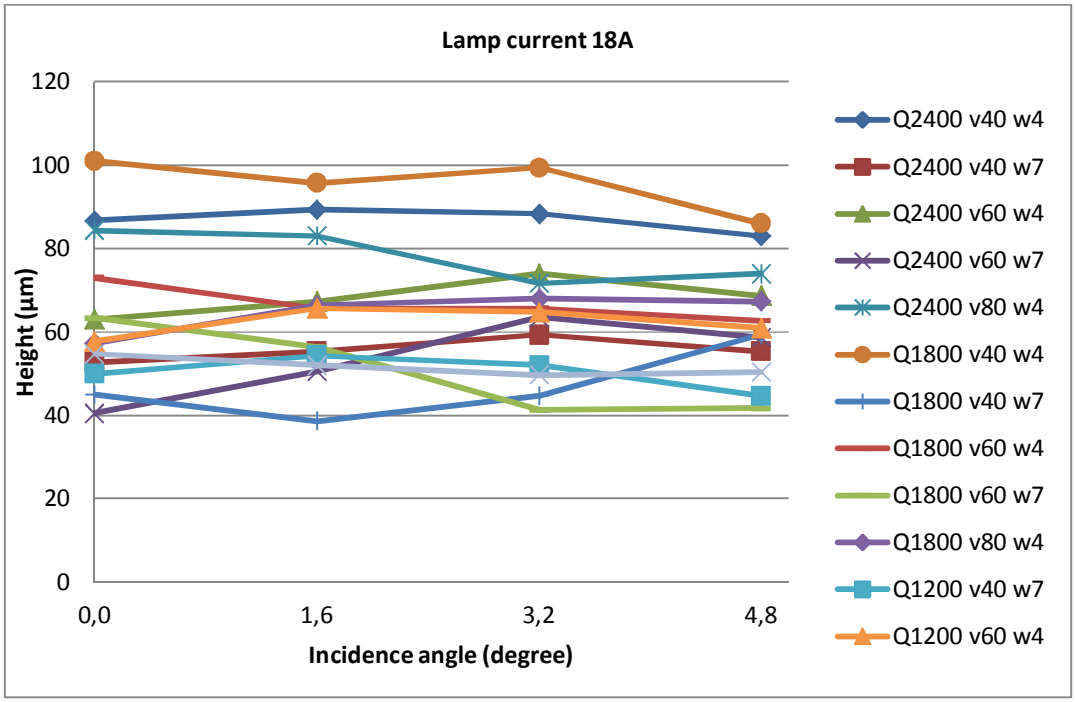

Figure 5.10 The effect of incidence angle of Nd: YAG laser when Lamp current is 18A. Q is the Q-switch frequency. V is the laser beam velocity and W is the wobble size. The height is measured from the top of laser tracks to the substrate top surface.

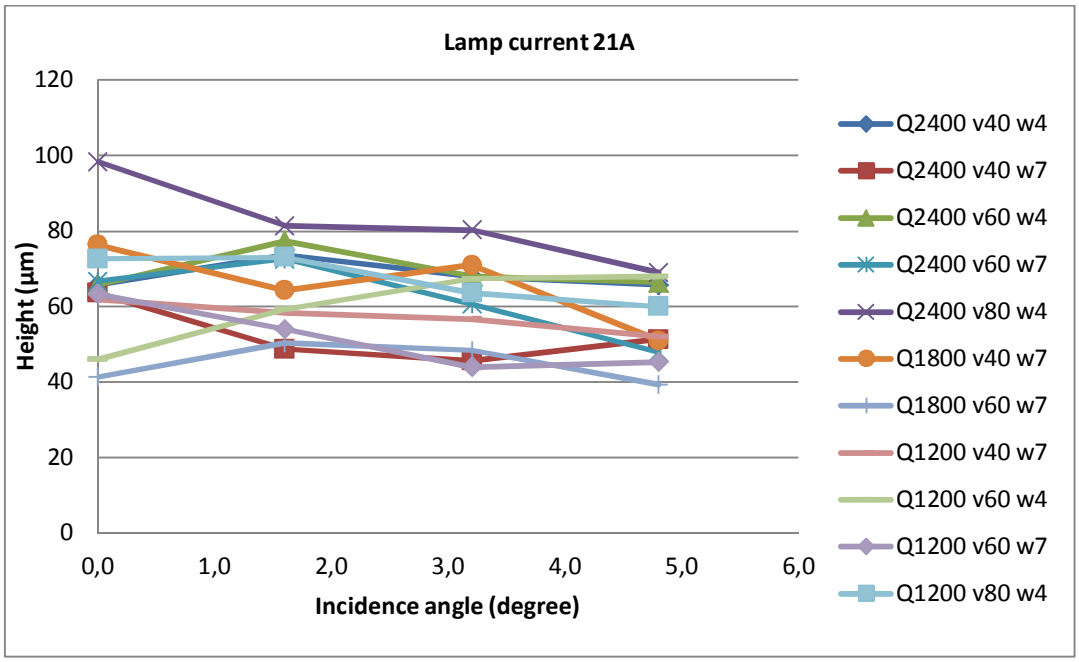

Figure 5.11 The effect of incidence angle of Nd: YAG laser when Lamp current is 21A. Q is the Q-switch frequency. V is the laser beam velocity and W is the wobble size. The height is measured from the top of laser tracks to the substrate top surface.

The mean standard deviation among the four tracks on one piece is 10 µm. As a result, if we make an area or a pattern by laser, the height of the laser-machined area varies due to the change of incidence angle. The surface of the laser-machined area is not homogeneous. It is an important reason that the plated laser track is not homogenous either.

Table 5.2 Standard deviation and COV in the height measurement of incidence angle effect, for Nd: YAG laser

Incidence angle	0	1.6	3.2	4.8
Standard Deviation (µm)	5	4	5	5
COV %	7.9%	6.3%	15.5%	10.4%

5.2.2 The DOE used to screen the most influential parameters

A design of experiments (DOE) was used to screen the most influential factors in the laser process. Two polymers were studied as the substrates, PE (melting point 120℃) and PC (melting point 310 ℃). It was a half factorial 2-level DOE, and the factors included lamp current, Q-Switch frequency, beam speed, wobble size, pass times, and also the melt point of the materials. The factors and levels are shown in Table 5.3. There are 32 runs in the DOE.

The "Main effects plot" is used to compare the effect from each parameter.

Table 5.3 The YAG laser parameters used for the 1st DOE

Lamp current (A)	Q-switch (Hz)	Beam speed (mm/s)	Wobble size	Pattern repetition number	Substrate melting temperature (℃)
22	3000	99	9	40	310
14	1100	40	1	10	120

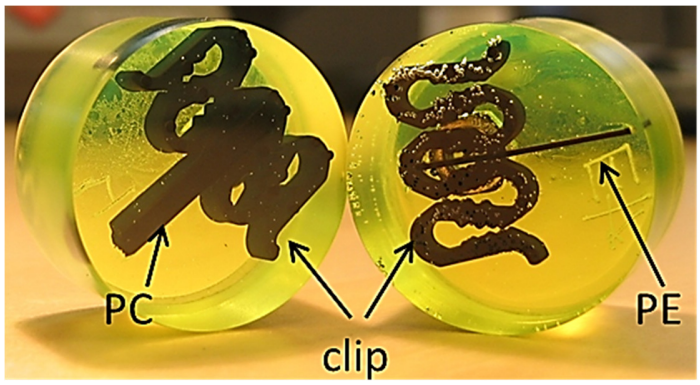

Figure 5.12 Epoxy mold for observation of cross sections. Polymer pieces are molded in epoxy.

One single straight track was made for each parameter group. Then the cross section of the track was observed by a microscope. Figure 5.12 displays how the samples are fixed to be observed for cross section. The valley's depth of the cross section was measured as a response for the main effects plots. Figure 5.13 illustrates how the "valley's depth" is measured, i.e. from the substrate top surface (not the top of the laser track) to the bottom of the heat affected zone.

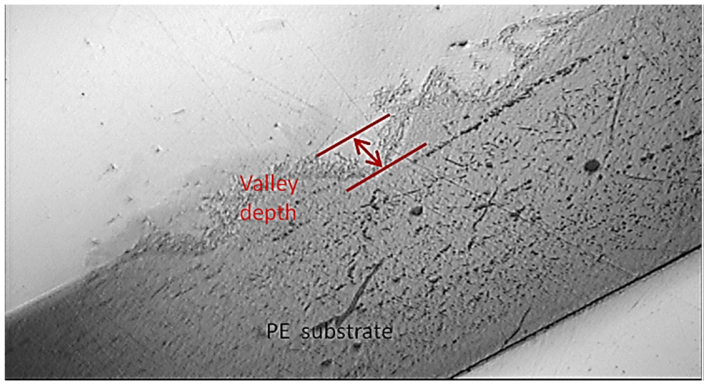

Figure 5.13 A sample of cross section observed by microscope. The valley's depth is used as a response for DOE test.

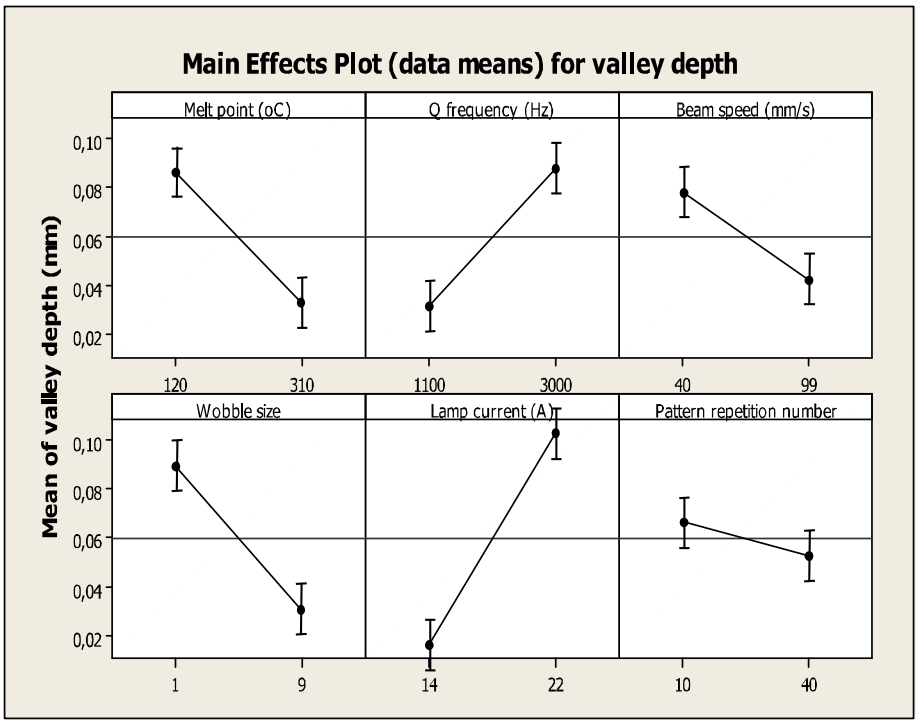

Figure 5.14 Main effect plot for the valley depth, to screen out the most influential laser parameters. Among the six parameters, pass time has the least influence.

In Figure 5.14 the main effect plots of each parameter were compared. An uncertainty of 10 µm should be considered based on the standard deviation in the measurement. The results show

that in the involved laser parameters set, the number of passes has the weakest influence among all the factors. This was also supported by the optical microscope observation; it was found that when the pass number is above 10 it only affects the density of the peak but has little effect on the height of the track. When the repetition number is below 10 the porous structure is not continuous. Obviously the lamp current has the most significantly influence on the valley depth. So in the following study of laser parameters, the lamp current is always chosen as varied. The melting point regarding the substrate material; it is more influential than the repetition number, however, to focus on the effect from the laser parameters, in the following study only one type of material is used. The beam speed and wobble size determine the time for the laser spot to stay on the substrate; the Q-frequency affects the energy in each pulse. These three parameters are investigated further.

5.2.3 Repetition number

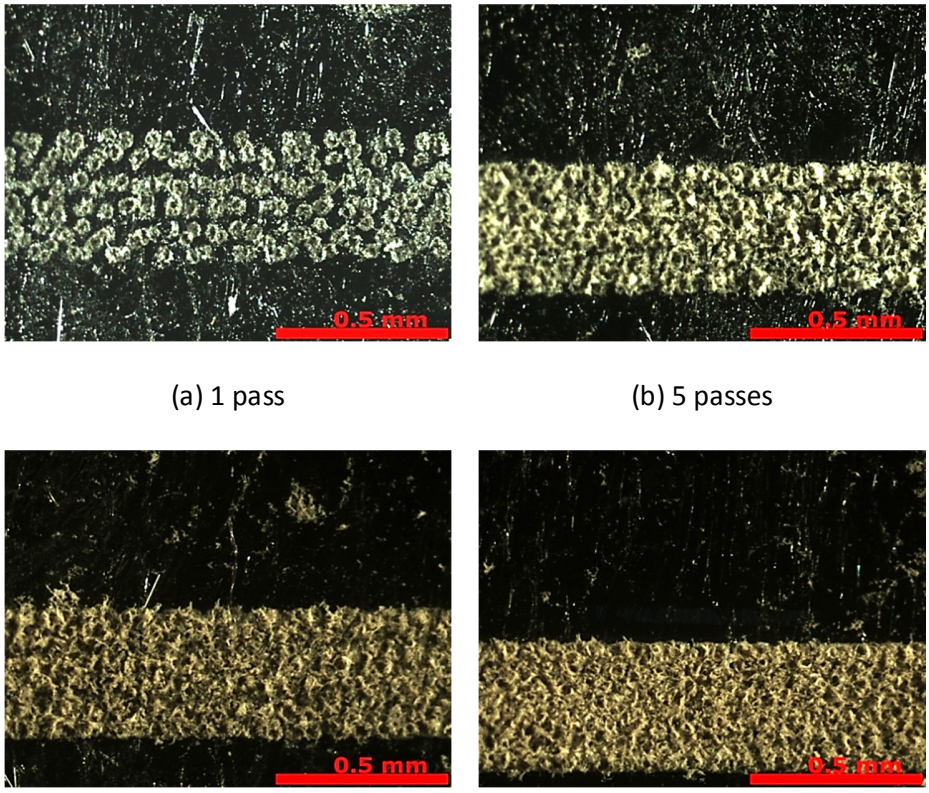

(a) 1 pass (b) 5 passes

(c)10 passes (d) 20passes

Figure 5.15 Topography of the surfaces after different numbers of pattern repetition. The substrate is PC and the used laser is Nd: YAG laser

As discussed in the previous section, the pattern repetition number has the least influence on the valley depth of a laser track. However, it must be sufficient to make the porous structure

continuous. When the laser repeats the pattern, there is an insignificant offset every time, then after a certain amount of repetition (15 -30 passes), the whole area is passed through.

Figure 5.15 shows typical laser tracks with repetition numbers from 1 pass to 20 passes. Obviously if no repetition is executed, only disconnected dots are made on the substrate. If the track is repeated for five times, all the dots are connected, also the porous structure starts to form. After 10 passes, the laser track is continuously porous and the appearance is similar if machined by 20 or even more passes. However, passes of more than 50 may destroy the porous structure, due to excess energy absorbed by the material; also it is a waste of time and energy.

5.2.4 Energy density

If the laser set-up leads to excessive energy output, there is a risk of burning the surface, shown by the picture (a) in Figure 5.16. If even more energy is absorbed by the surface, only a channel can form, for example, if the workpiece is machined barely in area, the absorbed heat cannot be conducted to the air as rapidly as by water; in most cases the polymer surface will be burnt and removed.

But if the laser energy is not high enough, the surface will have an appearance like picture (b) in Figure 5.16. It is believed that the absorbed energy is not sufficient to melt the surface, so no porous structure forms.

The laser-machined surface that can be plated in the future (the so-called LISA surface) is shown in picture (d) in Figure 5.16. In the microscope the laser track shows a clear porous structure. Meanwhile, the track is continuous, not like the picture (c) in Figure 5.16, which has a non-machined area along the track. This is due to the wobbling movement of the laser beam. The blank area cannot be covered by copper after the plating. Suitable speed should be selected for each wobbling dimension if an unbroken laser track is desired.

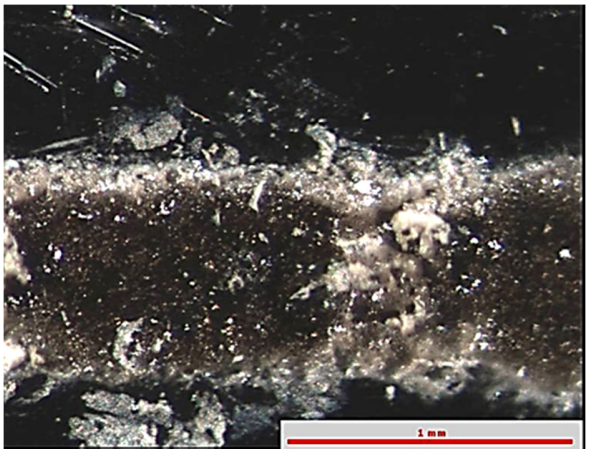

(a) Laser energy was too high. LC15A, Q2400Hz, W1, S40mm/s

(b) Laser energy was not high enough. LC15A, Q1200Hz, W7, S40mm/s

(c) Too much space is left on the laser track, but beside the blank area the other is good for the plating. LC18A, Q2400Hz, W7, S80mm/s

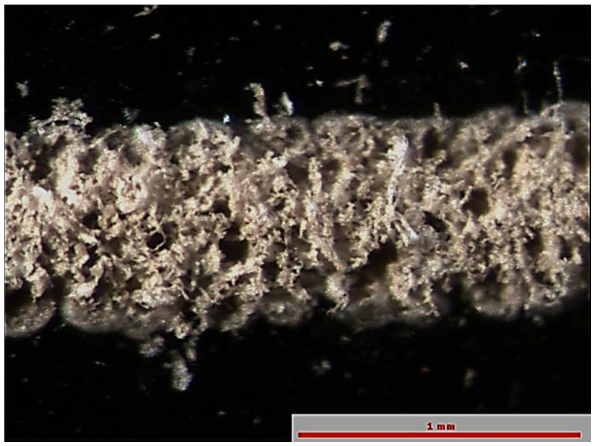

(d) Desired surface, the so-called LISA surface, LC15A, Q1200Hz, W1, S60mm/s

Figure 5.16 Topography of different surfaces machined by YAG laser. LC: lamp current, Q: Q-switch frequency, W: wobble size, S: speed

5.2.5 Output power of the YAG laser and the height of the track

For most of the polymers tested by the YAG laser so far, the laser machined area tends to be higher than the non-machined part. The height of the track refers to the distance measured from the top of the laser treated part to the substrate. In some applications a lower track is demanded. Because the laser-machined area is brittle and is easily scratched, a lower track can decrease the risk of damage. But for some other applications a higher track is preferred. So

effort was applied to build a relationship between the laser set-up, and the height of the laser machined area.

The investigated laser parameters and the chosen levels are shown in Table 5.4. The level is mainly based on the laser-working window. 81 samples were made, and after a microscope check, only 36 had the possibility to be plated, i.e. having the sponge-like structure. As a result, only 36 out of 81 samples were used for the height measurement.

Table 5.4 Laser parameters for the track height measurement

Lamp current (A)	Q frequency (HZ)	Speed (mm/s)	Wobble size
15	1200	40	1
18	1800	60	4
21	2400	80	7

The energy is calculated as the average power divided by the beam velocity and the spot size. The average power of a pulse is measured by a calorimeter while varying lamp current and Q-switch frequency. Unfortunately the calorimeter was a specific power detector for the CO2 laser, of which the wavelength is 10 times the Nd: YAG lasers. The power value detected by the calorimeter can only be used as an indication. In this case, no repeated experiments were performed. The calorimeter is introduced in Appendix 2 in detail. The spot area is calculated from nominal laser beam's diameter, 80μm.

$$energy\ density = \frac{average\ power}{Qfrequency \times spot\ area}$$ **Equation 5-2**

The structure formed after laser treatment is a result from the interaction between all parameters. In Figure 5.17, the height of the tracks is plotted as a function of energy input according to the specific laser parameters. The energy intensity is calculated by Equation 5-2. Figure 5.17 shows that there is a slight trend that the laser track height increases with the energy input. When more energy is absorbed, more material melts and after cooling down, a higher structure with denser material forms. If the excessive energy is absorbed, the polymer surface will be burnt and no porous structure forms, only peaks made of weak burnt material are left.

A trend can be seen that the laser track height increases when more energy is applied to the surface. It is a reasonable result, because when the surface absorbs more energy in a pulse, more material melts and expands its volume. Eventually more material is modified by the laser beam and a higher structure forms. The 2nd order polynomial trend line is used, to warn that the energy cannot be excessively high.

However the laser-machined area will not always go up, especially for some porous polymer or thermoset such as PTFE.

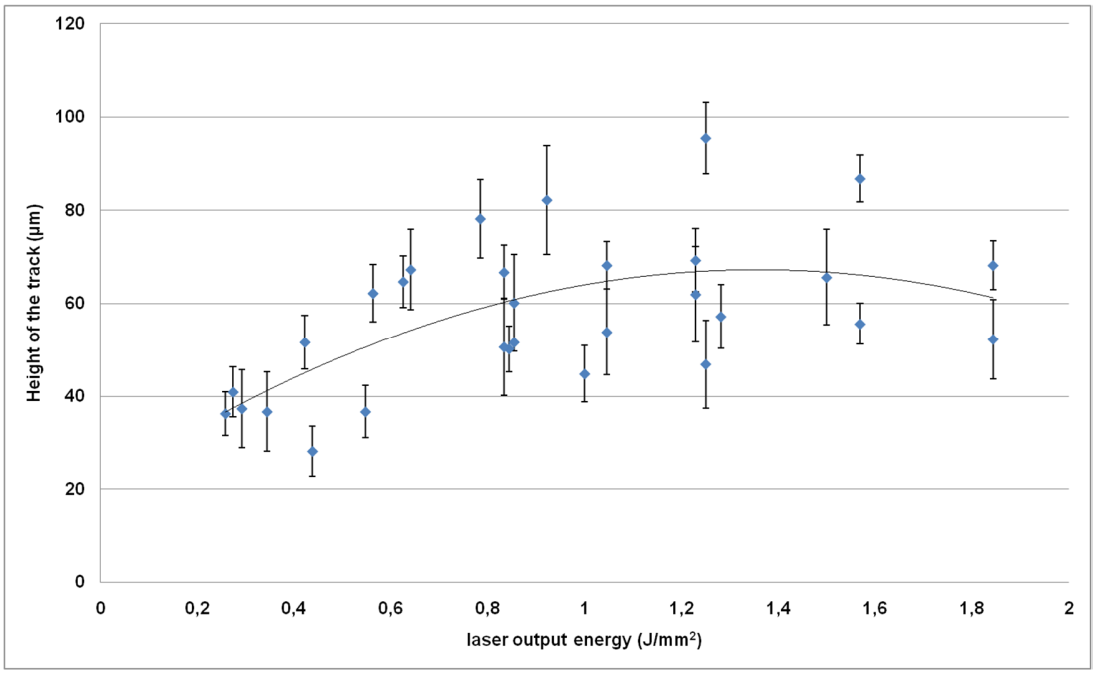

Figure 5.17 The laser beam energy density affects the laser track's height.

5.3 Other laser's result and comparison

5.3.1 UV laser

The UV laser is another laser source available for LISA. The substrates were sent to DPSS lasers Inc. and machined by their laser.

The wavelength of the utilized UV laser is 355 nm. When the Q-switch frequency is 30 KHz, the average power is 2W. The tested parameters are shown in Table 5.5. The pattern repetition number for all of the tested samples in this group is 5 passes. Besides, 6 passes at 30 KHz and 1000mm/s is also tried and the track appears similar as the one made by 5 passes when the other parameters are the same. Polycarbonate with 10% glass fibre was used as the substrate. The spot size is 40-45 µm in diameter. The laser parameters and pulse figure (Figure 5.18) were provided by DPSS lasers Inc.

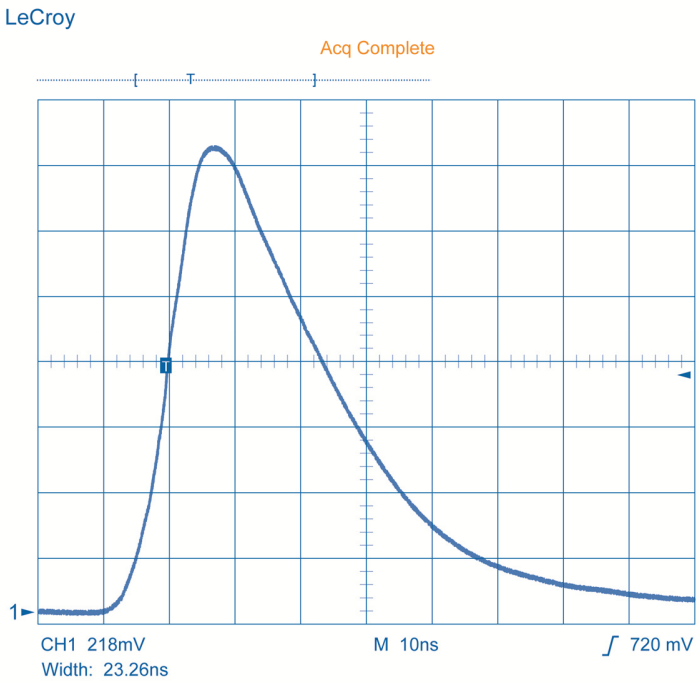

Figure 5.18 A pulse from the UV laser at 30Khz. The average output power of this pulse is approximately 3W.

Table 5.5 The used parameters for UV laser test

5 passes	Q-switch frequency (KHz)				
1000mm/s	30	40	50	60	70
2000mm/s	30	40	50	60	70

The surfaces shown in Figure 5.19 were made at 40 KHz and 70 KHz at the speed of 1000mm/s. When the frequency is 40 KHz, the whole machined surface has a spongy structure. A piece of fibre lies on the surface, because the sponge structure is not high enough to bury it, while on the surface machined by YAG laser most of the fibres are covered by the plastic structure. On the surface made at 70 KHz, separated holes are observed. One of the holes is shown in Figure 5.20. It can be seen that a porous structure actually exists, except the holes are not connected. However, plating can still occur except the plating velocity is almost half of the surface made by 40 KHz. The topography of pieces made at frequencies between 40 KHz and 70 KHz show a transition state and changes gradually. It was thought that at higher frequency, holes should be more connected than at a lower frequency, however, the observed phenomena is the opposite. One possible reason is that at 70 KHz, the peak power for each pulse is much lower than at 40 KHz, so that a single pulse does not have sufficient energy to melt a large amount of material, and only slight morphological change happens after one pulse. Once a hole is made on the

surface, the material underneath has more chance to be machined. That's why a porous structure exists in the holes underneath the surface. The tracks made at 2000mm/s were not studied by SEM, but in a microscope and from low frequency to high frequency, they have the same trend as those made by 1000mm/s, meanwhile, due to the higher speed, the distance between holes are larger on the pieces made by high frequencies.

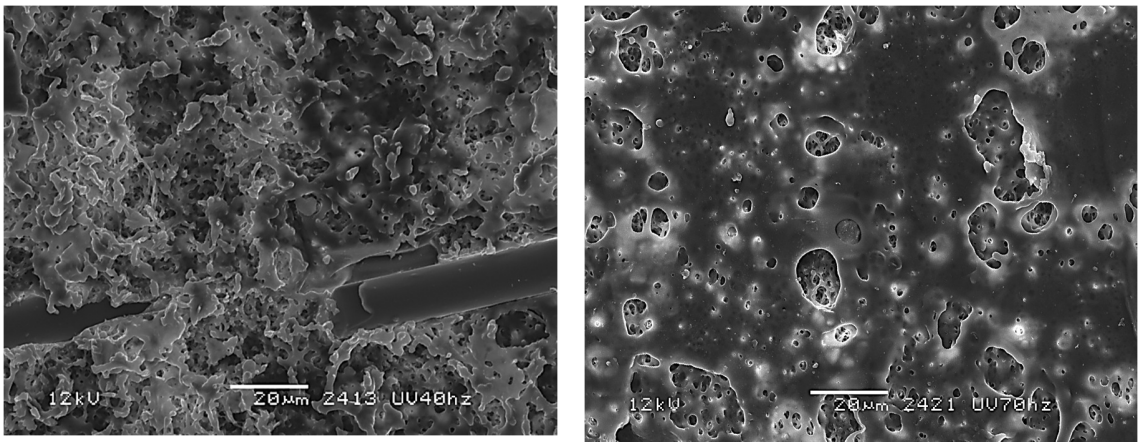

(a) When the UV laser is at 40KHz (b) When the UV laser is at 70KHz

Figure 5.19 Comparison of structure made by different Q-switch frequency of UV (a) 40 KHz, and the porous structure is continuous. (b) 70 KHz, separated holes were left on the surface.

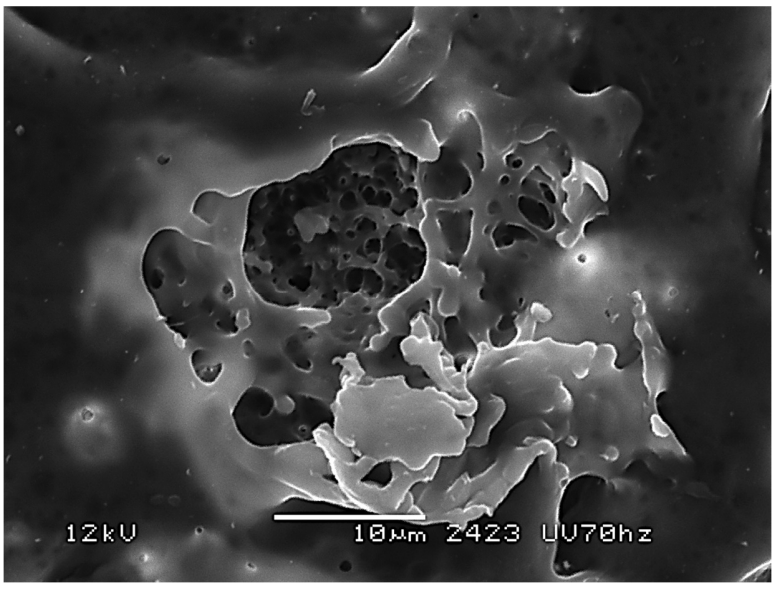

Figure 5.20 A single hole on the surface of the workpiece made at 70 KHz

It can be seen that the surface machined by a proper UV laser set-up shows a similar porous sponge-like structure as the surface made by Nd: YAG laser. Pictures (a) and (b) in Figure 5.21

are scanning electron microscope pictures exhibiting the difference between the YAG and UV laser's result.

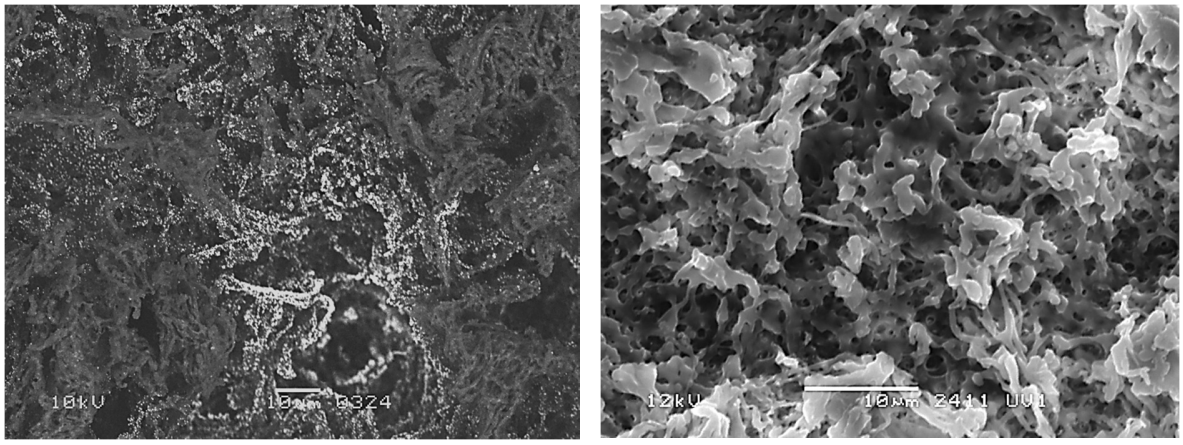

(a) surface made by YAG (b) surface made by UV

Figure 5.21 Comparison of surface made by YAG laser and UV laser. (a) SEM picture of a YAG laser machined PC surface when the lamp current is 18A, Q is1200Hz and speed is 40mm/s (b) SEM picture of a UV laser machined PC surface at 30 KHz and 1000mm/s

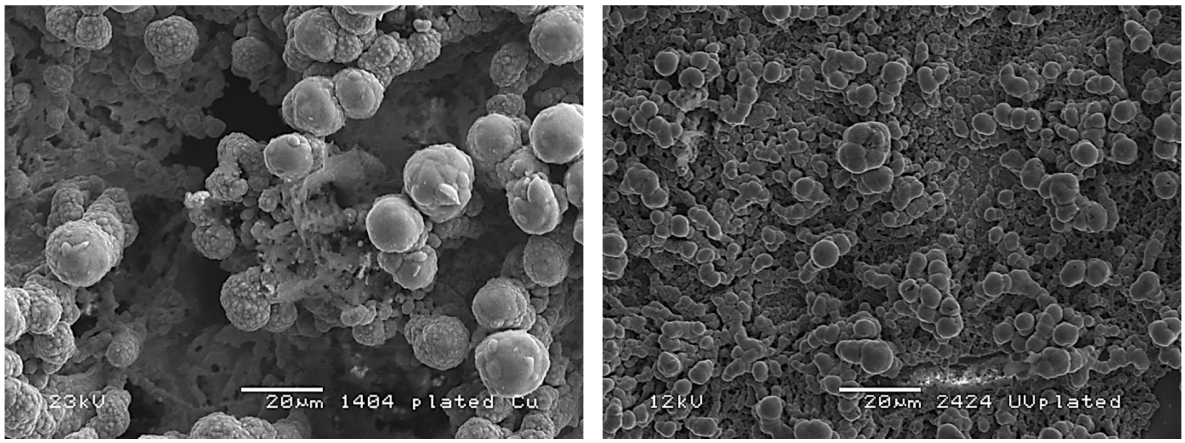

(a) copper plating for 45min on a YAG laser machined polycarbonate (b) copper plating for 10min on a UV laser machined polycarbonate

Figure 5.22 Comparison of plated laser track made by YAG and UV lasers. (a) is the surface made by YAG laser, the laser parameters are the same as the YAG piece in Figure 5.21 (b) is the surface made by UV laser (40KHZ, 1000mm/s).

Pictures in Figure 5.22 display the plated results. On the piece machined by the UV laser, copper plating was only carried out for 10 min, but a good trend is shown that the piece can be fully plated.

5.3.2 Fibre laser test

The experimental work described in this section was carried out by R. K. Fraser *et al*. [6].

Fibre lasers have some advantages, compared to other types of lasers. First of all, the laser head can easily be moved around without disrupting the internal beam as the beam flows through a flexible fibre cable. Traditionally, other laser types require a very delicate system of mirrors in order to get a proper beam, and movement of the system always requires recalibration of the laser.

Another advantage is that a fibre laser has a very high quality beam, as it is generated and confined inside the small core of the fibre. This means that the output beam can have a very small diameter, which results in a higher intensity of the energy supplied to the surface, compared to other lasers using the same effect.

The third advantage is that fibre lasers are very scalable, from as low as a few watts up to 100kW and therefore have many different practical applications. Last, but not least, fibre lasers are very efficient and can convert around 70-80% of the input power into the beam. This means that the energy waste is lower than the majority of lasers, which may only convert a few percentage of the input power into the beam. This also means that the system produces less waste heat so it is easier and cheaper to cool.

The fibre laser for study is built by Klaus Schütt Hansen [7]. It mainly consists of a moving x-y table, a lens group mounted on Z movable axis, and the fibre connected to the lens group. A glass beaker is used as the sample holder, and two metal blocks fix the sample in water.

A Q-switch is not available in the studied fibre laser. A sqare pulse was utilized, which is illustrated in Figure 5.23. The invovled laser parameters are the pulse length, pulse period, laser power and beam speed (realized in the XY table). The study of the fiber laser parameters aims to find out how the laser setup changes the topography of a laser track and the working window for the laser track to be plated.

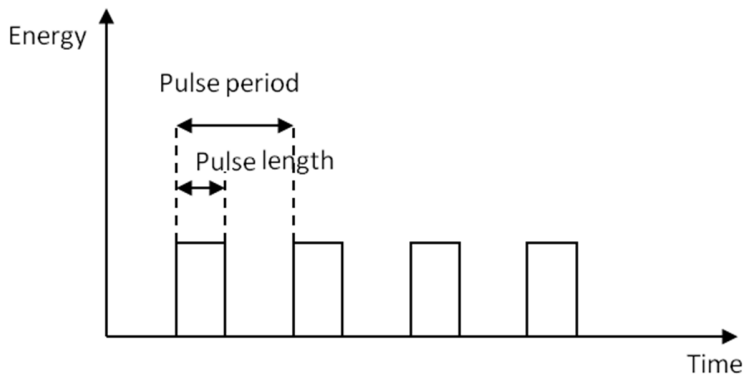

Figure 5.23 illustration of the fibre laser pulse mode

To have a general idea of the fiber laser track topography, firstly, the effect of the pulse length is studied by inspecting a single dot size, the measurements have been recorded from samples with a period of 0.1-0.5 seconds, thereby ensuring that no dots overlap. The measurement was carried on by an optical coorinate measuring machine DEMEET (the technical specification and calibration information are attatched in Appendix 2). Figure 5.24 shows the result. Second, when the effect from the pulse period is considered, the line width was measured and displayed in Figure 5.25. Obviously, both a single dot and a line (line is made of connected, partly overlapped dots) increase the size if the pulse length is increased. But for a long pulse period the line width is smaller, because the dots overlap is reduced, which means less heat is aborbed in the same place so less material melts.

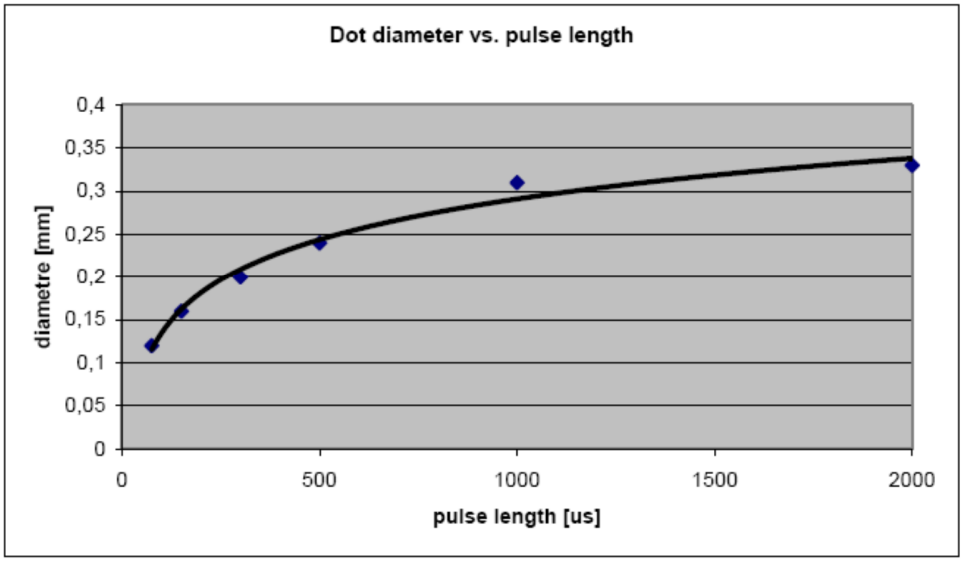

Figure 5.24 The dot made by Fiber laser increases diameter with pulse length.

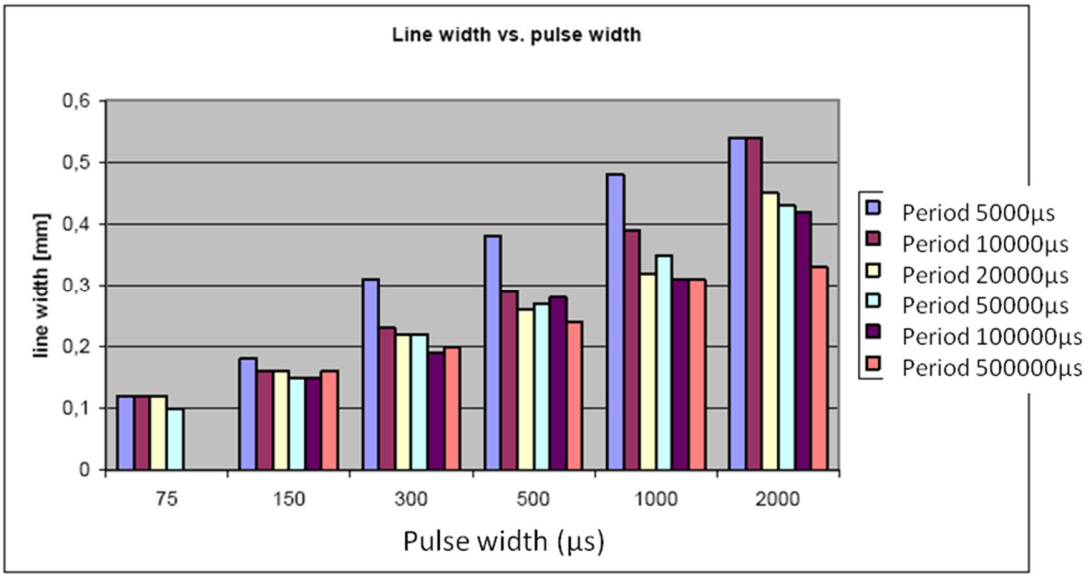

Figure 5.25 The lines made by fiber laser is effected by the pulse and period

The surface machined by the fibre laser was ignificantly different to the surface machined by the YAG laser or UV laser. However, similarly, if proper parameters are used, a porous structure can form and then the copper can deposit selectivly on those tracks. Figure 5.26 illustrates one laser track before and after plating. The plated track is conductive. Appearently, the obtained plated track is not as sharp as a YAG laser result. The reasons include

- The used protection glass to the lens has an imperfection in the center.
- The movement of the table leads to enormous vibration compared to the size of the track. (vibration of the XY table movement can be observed, no vibration data is available though)
- When the table moves, waves form on the surface of the water which is the machining media and re-direct the laser beam, so the area outside the designed pattern is also machined. Since all of the error sources mentioned above can be removed or improved, more research was conducted on the fibre laser.

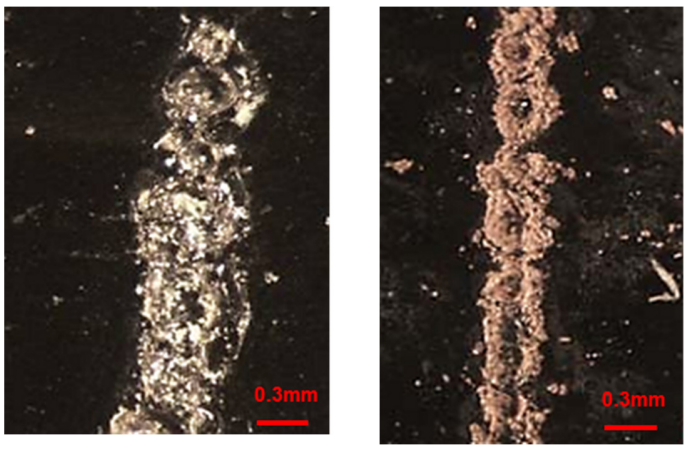

Before plating After plating

Figure 5.26 The fiber laser track made before and after plating it was made at pulse period 10000µs, pulse length300, the pattern repetition number is 2.

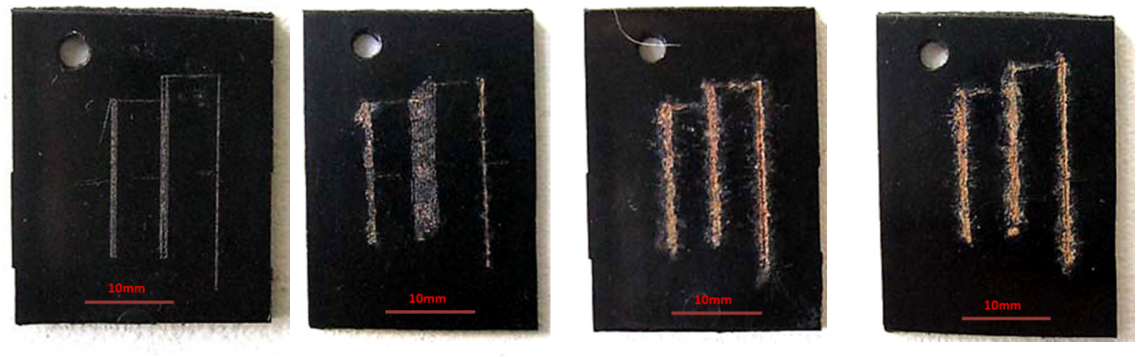

1/20: 10µs, 0.52W 1/10: 20µs, 1.48W 1/2: 100µs, 9.35W 3/4: 150µs, 14.02W

Figure 5.27 The fiber laser tracks made at the period 200µs . The ratio varies from 1/20 to 3/4. The average power output in the pulse is also listed. 30 passes were used as the repetition number.

To simplify the research, a constant velocity of the movement is used. Low speed is preferred to decrease the vibration and the waves in the water.

It was found that a determining factor for the platability is the pulse-period ratio. The definition of period and pulse length is illustrated in Figure 5.23. If the period-pulse ratio is kept, changing the period length has little effect. However the line consistency decreases in some cases. Figure 5.27 shows that high ratios such as 1/2 and 3/4 are in favor of plating. On the workpiece with low ratio, such as 1/20 and 1/10, copper particles can be found but they are not connected. A low pulse-period ratio has the risk that only separated dots can be obtained on the surface.

The repetition number has an effect mainly on the width of the track; Figure 5.28 displays how the width increases with the repetition numbers.

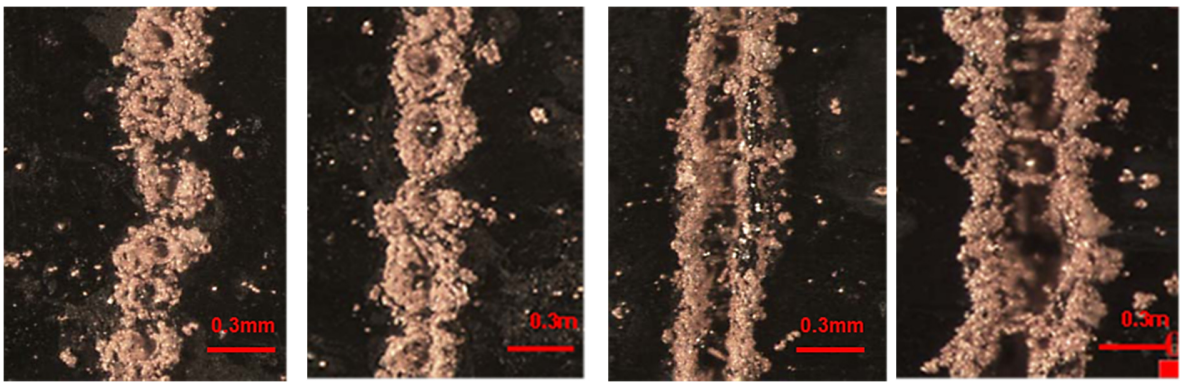

1 pass 2 passes 15 passes 30 passes

Figure 5.28 Pattern repetition number's effect for fiber laser. All the workpieces are made at pulse length 300μs and period 10000μs

5.4 The structure of LISA surface described by the bearing area curve

A quantitative characterization of the LISA surface is necessary for the laser process optimization, and in addition it provides the possibility of testing different materials. A bearing area curve and bearing area parameters are used to estimate the output. It is assumed that the bearing area curve can predict whether the surface can be used for LISA or not.

The bearing area curve or Abbott-Firestone curve, named after the author E.J. Abbott and F.A. Firestone in 1933 [8], describes the surface texture of an object, which is a plot of the material-air ratio at different heights above the object's general form. The surface is truncated successively from the top of the highest peak to the deepest bottom of the valley, and at each level of truncation, the ratio of material is plotted against the height [9]. The Abbott-Firestone curve initially describes only the profile of a surface, and in progress of related technology it is developed to cover a 3D scenario. In the 3D-region, the parameters associated with the curve are called S_{pk}, S_k, S_{vk}, S_{mr1} and S_{mr2}.

ISO standard [10] defines all the bearing parameters in 2D scenario, and the principles are the same for parameters in 3D region, as illustrated by Figure 5.29. In the figure, 1 and 5 are the maximum and minimum height of the curve. The blue line fits to the 40% segment of the curve (shown by 3 in the figure) with the lowest decline. From the intersection points of the blue line and the vertical axes for 0% and 100%, draw horizontal lines. The intersection points with the curve determine the parameters S_{mr1} and S_{mr2}; from these two points, draw a straight line which ends on the axis, so that the area of triangle 2 and triangle 4 have the same area as the one between the horizontal line and the bearing area curve, separately. In this way, S_{pk}, S_k, and S_{vk} are defined. All of these five parameters are explained in Table 5.6. Figure 5.30 illustrates the physical means of each parameter by an example of a profile [11]. Besides, from a volume point

of view, the curve is divided into peak, core and valley parts at 10% and 80% of the bearing area ratio, and there are related volume parameters, which are omitted [10].

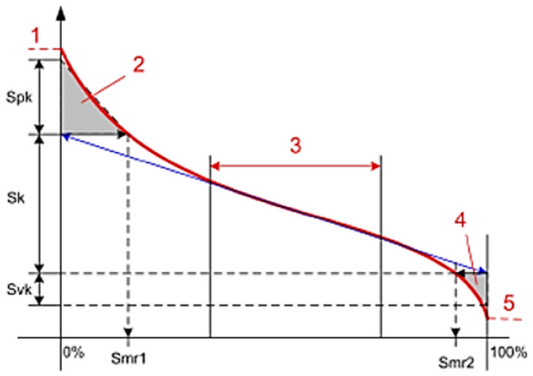

Figure 5.29 Definition of the bearing parameters on a bearing area curve [11]

Table 5.6 Bearing parameters and description based on Figure 5.29 [10][11]

Name	Description
S_k	Core roughness depth, Height of the core material
S_{pk}	Reduced peak height, mean height of the peaks above the core material
S_{vk}	Reduced valley height, mean depth of the valleys below the core material
S_{mr1}	Peak material component, the fraction of the surface which consists of peaks above the core material
S_{mr2}	Peak material component, the fraction of the surface which will carry the load

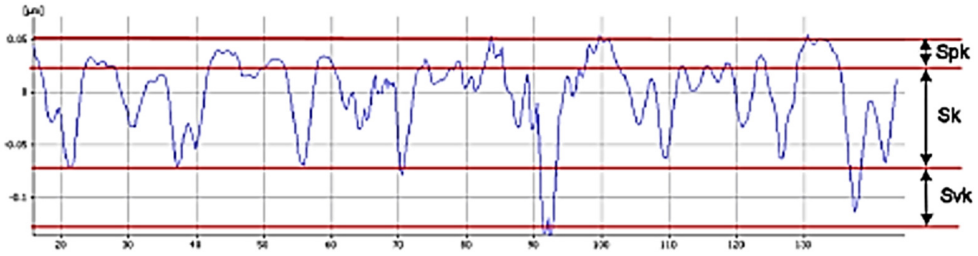

Figure 5.30 Example of the bearing parameters shown by a profile [10][11]

A good LISA surface which can be metalized tends to have these properties: 1.The laser track has a certain thickness, which has a porous and sponge-like structure, so the track can keep the palladium clusters during the rinsing step, and it means that S_k should be in a certain range. As

explained before, S_k indicates the thickness of the core part, which plays an important role to keep the activation seeds. 2. As mentioned before, the peak part should be low, so the copper will not need (a) long time to cover the entire surface, this is related to S_{pk}, and S_{pk} should be low. 3. The valley's depth, perhaps, does not influence the result because the plating may not reach the valleys.

Different laser type and material combinations lead to varieties of surface structure. In this work, the PC with 10% glass fibre is mainly studied as the substrate. Nd: YAG laser and UV lasers are both used as laser sources. All the measurements are performed by Alicona InfiniteFocus® optical microscope, and analyzed by its software IFM G4 3.5. The porosity curve analyzed in chapter 4 for diffusion behavior description is actually obtained from the bearing area curve, also measured by Alicona InfiniteFocus®.

Table 5.7 The laser parameters used for the five types of surfaces in the bearing area curve study

	Lamp current (A) for YAG /average power (w) for UV	Q-switch frequency (Hz)	Pattern repetition number	Beam speed (mm/s)
YAG good	18	1200	30	60(wobble 4)
YAG burnt	15	2400	30	60 (wobble 1)
YAG low energy	14	1800	30	80 (wobble 4)
UV good	2	40000	6	1000
UV high frequency	Lower than 2	60000	6	1000

The used laser parameters are listed in Table 5.7. Three cases from a YAG laser are analyzed here: The one named "YAG good", has the porous structure, which is suitable for plating; another is named "YAG burnt", and it is because of an excessively high laser power output. In this case, the plastic is burnt, which looks as if the delicate porous structure is removed; only holes are left. The third case is when the laser energy is very low which is not enough to modify the surface as much as for "YAG good". As a result the surface material melts partly but no porous structure forms. That case is named "YAG low energy". For the UV laser, there are two cases, one is a suitable result for plating, named "UV good", but the laser-affected layer is much thinner than the YAG's result. The last one is when the UV laser has a very high Q-switch frequency, named "UV high frequency", in this case, there are some porous structures left on the surface, but not in a continuous pattern. The original injection molded PC surface is also included as a reference, and the case is named, "PC original". It is the intention to investigate

whether the bearing area curve can help to categorize “UV good” and “YAG good” into the same group.

These five types of laser-machined surface mentioned above, as well as the original PC surface, are recorded by microscope measurements and the results are shown in Table 5.9. To obtain the bearing area curve, surface analysis was made by Alicona InfiniteFocus® microscope. When using the Alicona, a 3D model is first captured, and then the software IFM calculates the bearing area curve and related parameters. The 3D view for all the cases are also shown in Table 5.9. It is clear the “UV good” has a smaller thickness than “YAG good”. Moreover, the roughness information is also obtained from the 3D model.

The procedure for one bearing area curve measurement contains: 1. Set the microscopes light brightness and contrast, 2. Set the vertical resolution and lateral resolution, 3. Set the upper level and lower level, then scanning is started layer by layer from the lower to upper level and a 3D model is captured, 4. Edit the 3D model to remove artificial spikes as much as possible using the “3D editor”, 5. Make a surface analysis to get the bearing area curve and bearing area parameters.

Previous measurements show the selection of upper and lower level has a noticeable influence on the captured 3D model, especially on very porous surfaces or on surfaces with a high reflectivity. There are serious artificial spikes on the 3D model due to optical reflection during the scanning. The spikes change the bearing area ratio significantly. But on a relatively smooth surface such as the UV machined surface, the result is hardly to be influenced by the level set-up. In order to standardize the measurement and avoid the error induced from the upper and lower level set-up, for all of the measurements, the upper level is set close to the top of the surface, while the lower level is close to the bottom of the structure. For each type of laser-machined surface, this step is repeated 5 times to observe the operation uncertainty for the bearing area curve. Figure 5.31 shows an example on a piece of “YAG good”. 5 measurements were made on the same area, and for each one the lower and upper levels were reset. 5 curves and the related parameters were obtained, the parameters’ standard deviation were used as the error bars in the parameter analysis in the following contents. Table 5.8 presents the bearing area parameters averaged from the obtained 5 curves on “YAG good”. For the other cases (“YAG burnt”, *etc*.) investigated in Table 5.9, the same method was applied.

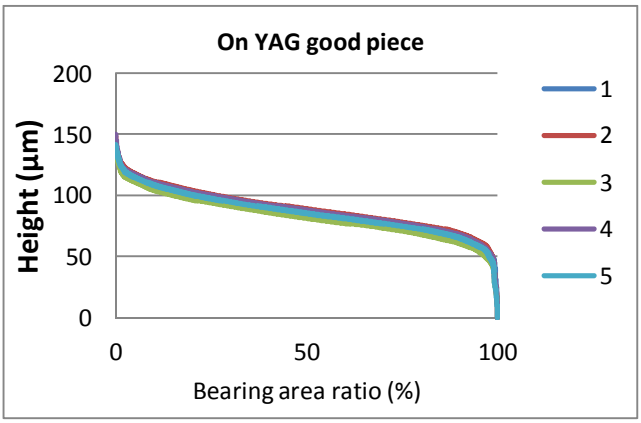

Figure 5.31 Repeatability of the 3D model capture on a piece of "YAG good". 5 repeated measurements on the same area were performed. The upper and lower levels were set close to the top or bottom of the surface (by operator's judgment), and then the level was reset for each measurement. 5 curves and parameters are used for the operation variance calculation.

Table 5.8 The obtained bearing area parameters for the repeatability measurement on the "YAG Good" piece. The 5 curves are shown in Figure 5.31.

	Average (µm)	Standared deviation (µm)	COV
S_k	43.43	0.42	0.96%
S_{pk}	16.51	0.55	3.32%
S_{vk}	20.49	1.25	6.12%
Normalized height at 10%	0.75	0.01	1.9%
Normalized height at 80%	0.51	0.01	2.4%
S_{pk}/S_k	0.38	0.01	2.9%

Table 5.9 Analysis of PC substrates machined by UV or YAG lasers. The specific laser parameters for each type of surface are listed in Table 5.7

	Microscope picture	Alicona 3-D model	Roughness
PC original	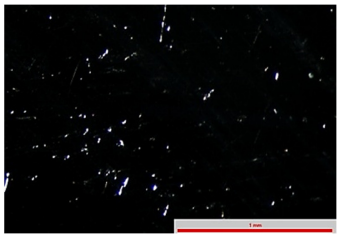	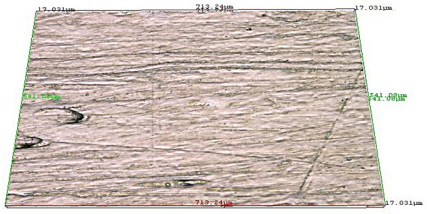	S_a 0.45µm S_p 3.10µm S_v 8.33µm S_z 11.44µm

YAG Good	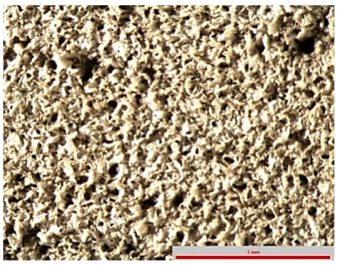	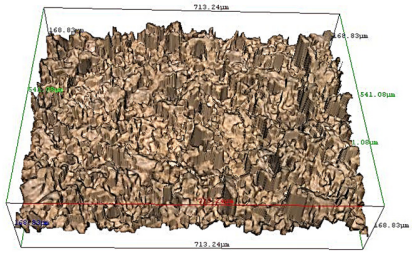	S_a 14.62µm S_p 78.61µm S_v 0.55µm S_z169.16µm
YAG low energy			S_a 4.04µm S_p 42.32µm S_v 16.80µm S_z 59.11µm
YAG burnt	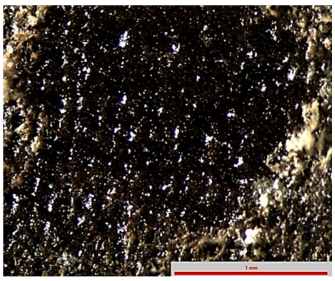	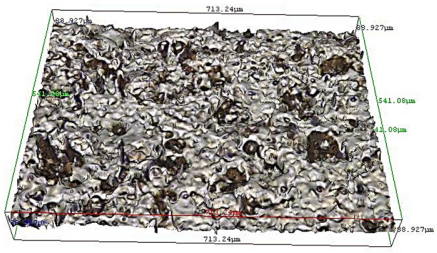	S_a 4.51µm S_p 34.84µm S_v 46.54µm S_z 81.38µm
UV good			S_a 1.19µm S_p 7.83µm S_v 9.21µm S_z 7.04µm
UV High frequency	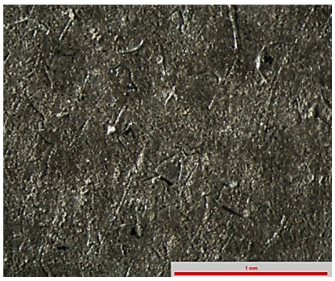		S_a 1.04µm S_p 5.86µm S_v 2.56µm S_z8.42µm
	Microscope picture	Alicona 3-D model	Roughness

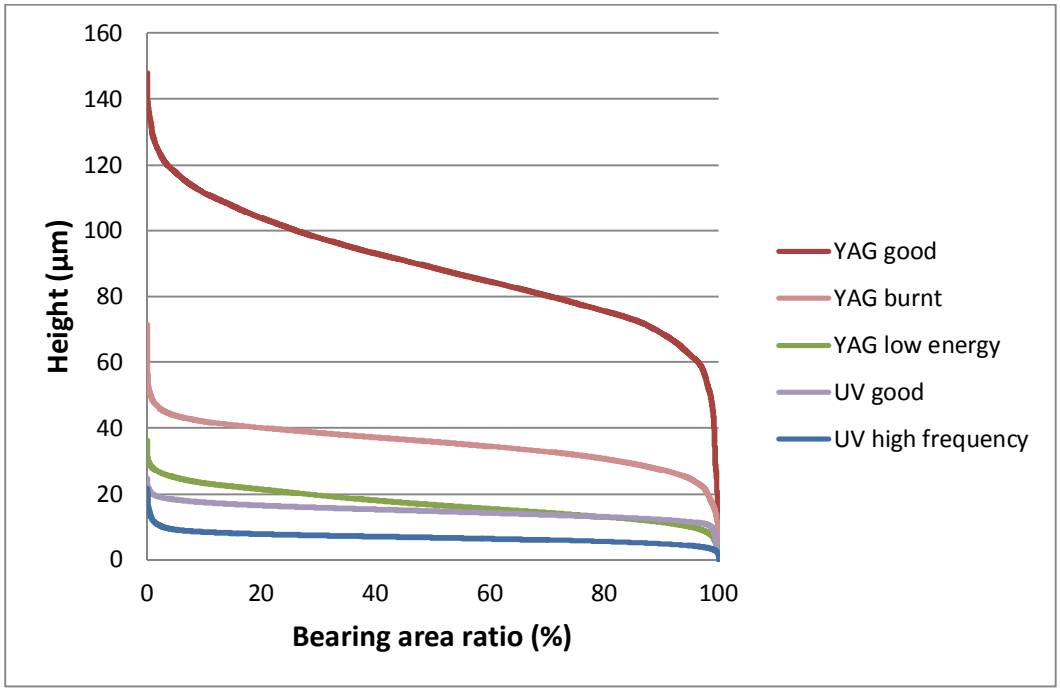

Figure 5.32 Bearing area curve for five types of laser machined surfaces. "YAG good" is from LISA surface made by YAG laser, "YAG burnt" is from surface made by excessively high energy using YAG laser, "YAG low energy" is from surface made by insufficient energy using YAG laser, "UV good" is from LISA surface made by UV laser, and "UV high frequency" is from surface made at 60Khz by UV laser

Figure 5.32 displays all the bearing area curves from the five cases mentioned above. Obviously, the curves "YAG good" and "UV good" have completely dissimilar appearance, though it's known they both present usable surface structures. One crucial reason is the structure height difference. The bearing area curve directly expresses the observed height, that's why the "YAG good" is much higher than the "UV good". The curves from the UV laser machined surfaces are both very low, and one of the bad cases, "YAG low energy" curve, is also in this region. It is hard to distinguish the good ones from the bad ones from this chart. To eliminate the effect of the height, all these curves are normalized by the structure's height, i.e. by dividing the Y-axis by the maximum height and make a plot to the bearing area ratio. In this method, for all of the investigated cases, the top of the structure is 1, and the bottom of the structure is 0. The Y-axis for the normalized curve is without unit.

All the normalized curves are displayed in Figure 5.33. In this figure, PC substrates machined by YAG and UV laser have almost the same shape curves. The "YAG burnt" has a similar slope but at a lower position in the core material section (10%-80% bearing area ratio). "UV high frequency" is the lowest, and the peak of this curve takes a large part of the whole curve, so the core material part is not thick enough to work. While the "YAG low energy" observably has a very steep curve, which means the structure has a relative wide opening, therefore it cannot keep the palladium clusters during the rinsing.

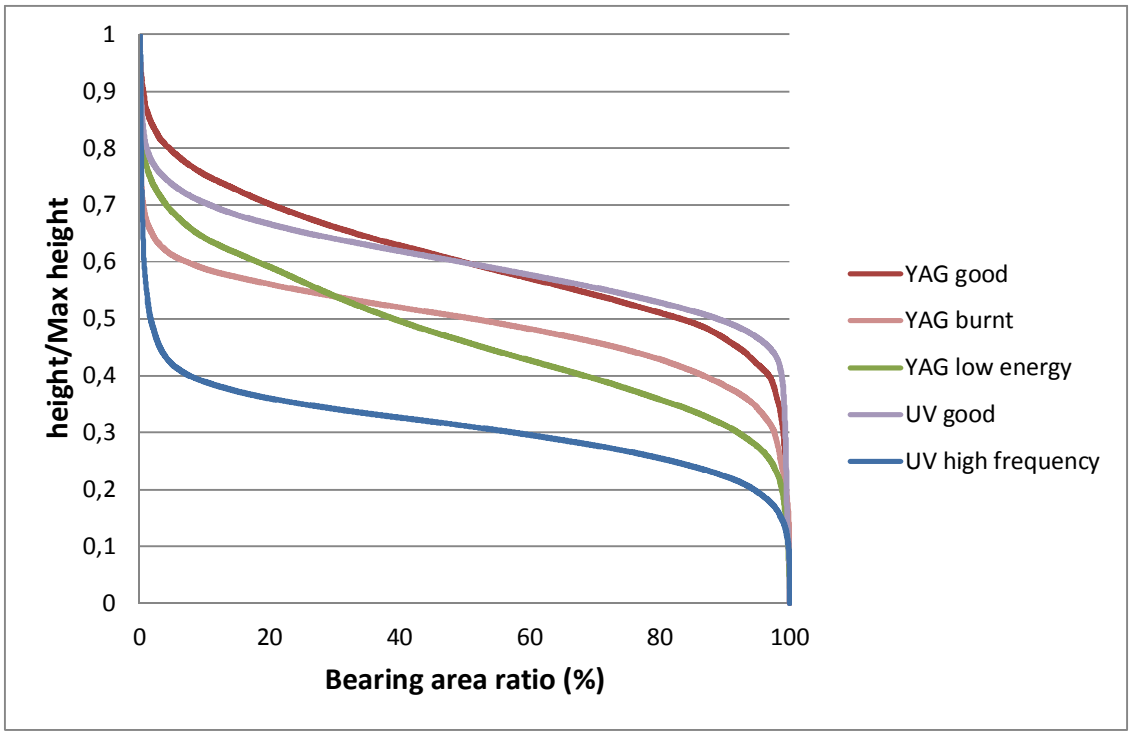

Figure 5.33 The curves in Figure 5.32 are normalized by their respective maximum height. The shape can be compared in this figure. The nomination of the curves is the same as in Figure 5.32.

Among all the bearing area parameters, S_k corresponds to the core material thickness, which is the key part for the plating process. On the other hand, S_k is defined by the height of the section of which the curve has the minimium 40% slope, and the unit is by length. Similar to the normalization of the curves, S_k is also normalized by the structure thickness. After normalization, it becomes a unitless value and indicates the minimium slope. Figure 5.34 shows the normalized S_k values (S_k/Max). The slope of the curve represents how fast the pores size shrink. Small S_k/max values indicate the structure narrows down from the top rapidly, which doesn't help when the palladium clusters try to diffuse inside the structure. But a very large S_k/max, perhaps, shows the structure has a large opening, so the rinsing can take the palladium clusters away easily. The sequence of all the cases corresponds to the slopes' order in Figure 5.32 well, which means the normalized S_k can be used to compare the slope. In Figure 5.34 "YAG good" and "UV good" lie in the intermediate range, "YAG low energy" has the largest value, and the other two are much lower. The figure can be easily explained based on the specific structure shown in Table 5.9. For example, the "YAG low energy" surface only has bumps but no porous structure in a smaller scale, the bearing area ratio changes a lot from the top to the bottom, that is the reason why the bearing area curve has a large slope.

The other criteron that can be used is the normalized height at 10% or 80% percent of bearing area ratio which helps to describe the vertical position of the normalized curve. As mentioned before, 10% and 80% at the bearing area ratio axis divide the whole curve into peak, core and valley volume. That's why these two specific ratios are used. In Figure 5.35 and Figure 5.36, the

height of the column is the curve's hight at 80% or 10% bearing area ratio and divided by the maximum, i.e, the value at the normalized curve.

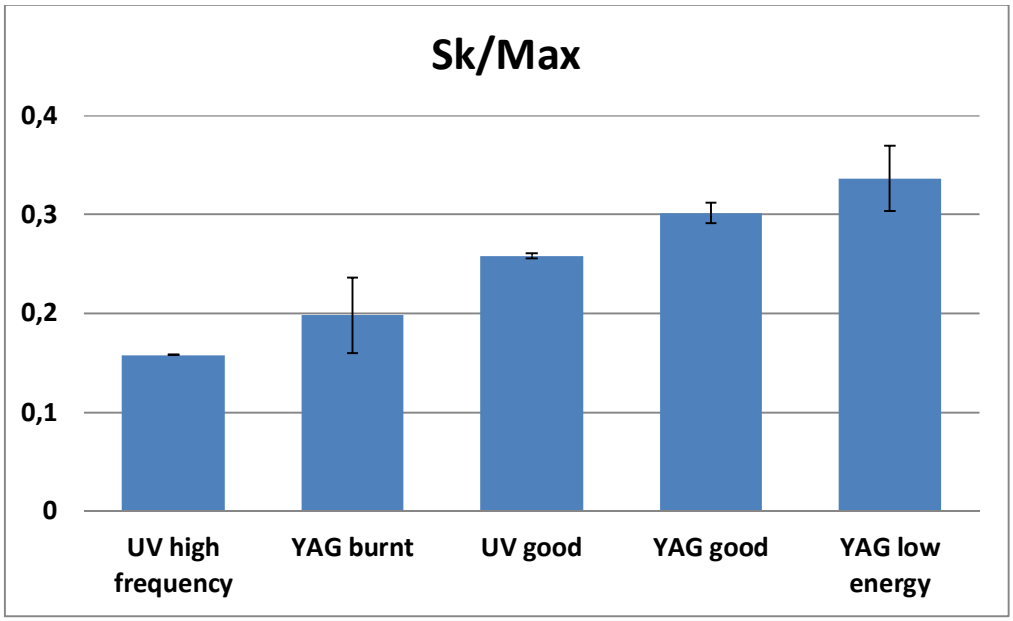

Figure 5.34 The bearing area parameter S_k is divided with the maximum height of each curve. S_k presents 40% segment of the curve with the minimum slope. The error bars are added according to the variance in the measurement process

Figure 5.35 is the comparison of the value at 80% (i.e. at which height the valley starts). The "UV high frequency" has the lowest value, and it means the structure has a wide opening to a very deep layer. The two good cases have higher values. But it does not mean the higher the better. Because if the value is too high, it means the valley part starts almost immediately at the top, which is not good for the plating.

At 10% (i.e. where the peaks ends) the curve "YAG low energy" lies inbetween "YAG good" and "UV good", which makes the comparison confusing. What is clear is that if this value is too low, it means that the peak takes a large part of the whole structure, that is not preferable for the plating process. A high value should be best, but it is important to look at the other parameters as well, since the peak part does not determine the plating outcome exclusively.

Another working parameter is the ratio of S_{pk} to S_k, shown in Figure 5.37. In this way the value should be as low as possible. Regarding the case of "YAG low energy", which lies inbetween the two good cases, it does not have too much peak part, but from the Sk/Max chart, it is clear that the curve has a large slope, which is also indicated from the 80% chart, the valley part starts quite near the top, which is not a good structure to keep the palladium clusters.

All these discussed parameters or normalized parameters can not be used seperately. They must be analyzed with each other and referenced to the substrate material type.

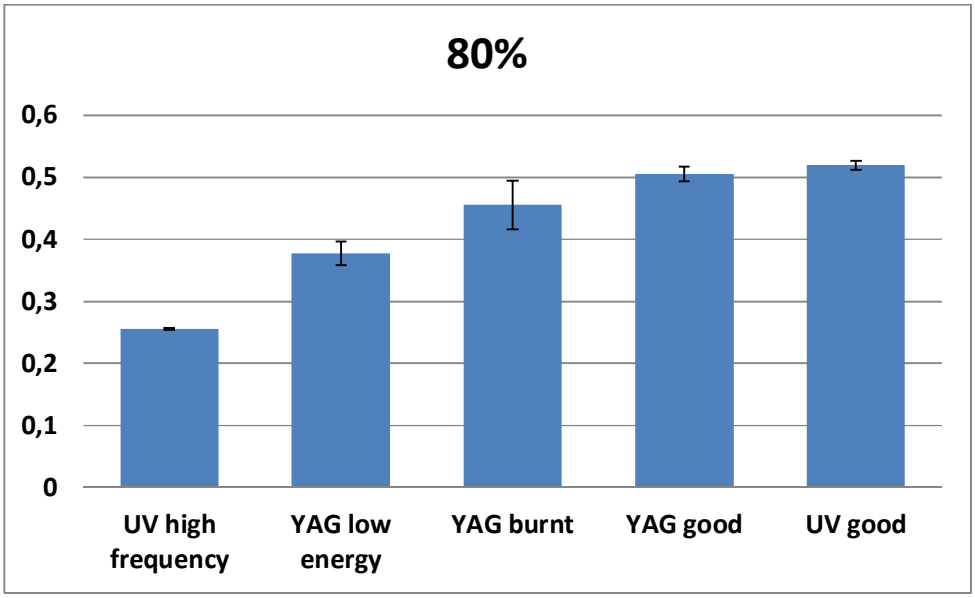

Figure 5.35 On the normalized curve, value of each curve at point 80% is compared. This helps to describe the curve's position. From 10% to 80% it is defined as core material volume and from 80% to 100% it is the valley volume for the volume parameters.

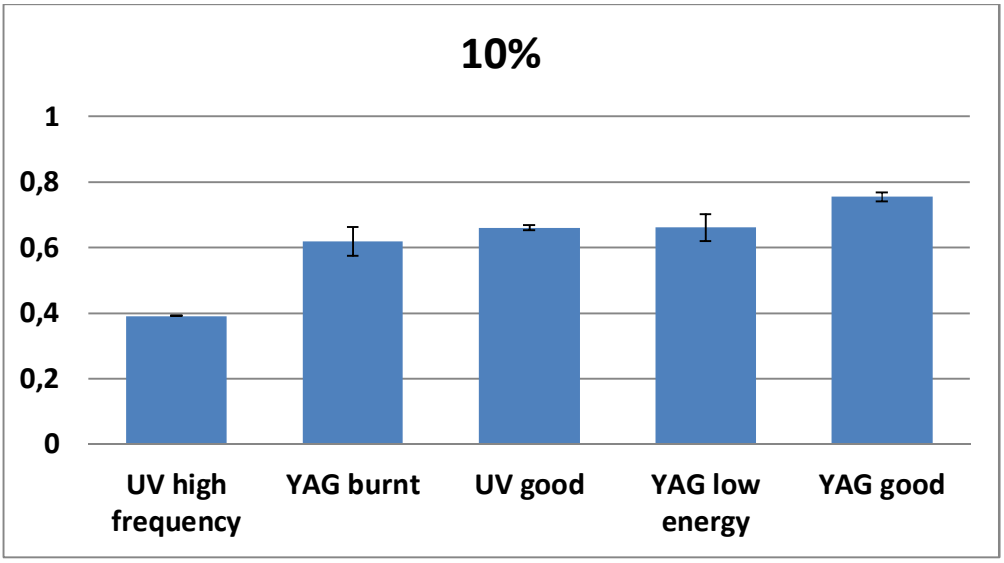

Figure 5.36 On the normalized curve, value of each curve at point 10% is compared. This helps to describe the curve's position. And by the volume parameter definition, from 0% to10% is accounted as peak volume, and from 10% to 80% it is defined as the core material volume.

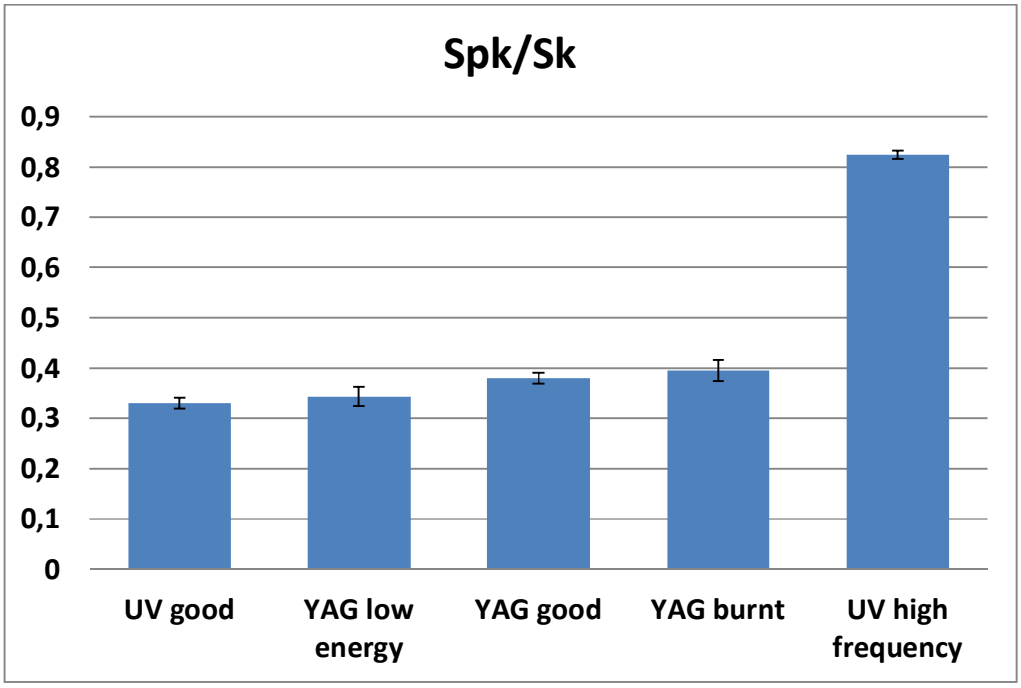

Figure 5.37 The ratio of S_{pk} to S_k is compared. This helps to describe the portion of the peak.

To conclude, bearing area curves are used to characterize the laser machined surface for subsequent plating in the LISA technique. Curves from successful and failed cases are compared, and bearing area curves are normalized by the structure height. By this means, the two successful cases, PC surface machined by a YAG laser and UV lasers, have similar shapes, while the others are obviously different. The core material section's height as well as slope is mainly investigated.

The normalized S_k is used to quantify the curve referring to the slope. The normalized height at 10% and 80% of the bearing area ratio is also compared among all the cases. The results show it is feasible to use the bearing area curve as a tool to tell whether a surface is suitable for plating or not.

If the bearing area parameters are chosen to be the criteron to tell whether a surface is suitable for plating, they should be normallized and combined with the materials type, laser type, as well as other conditions. Moreover the result cannot be determined from only one parameter, but other parameters need to be observed too.

5.5 Conclusion

In this chapter, the procedure of the laser machining process is explained. How the sponge structure forms was discussed hypothetically and then a thermal model is used to support the hypothesis.

Several types of industrial lasers are available to LISA, providing the laser beam's energy can be absorbed in the form of heat.

The effect of the YAG laser's parameters is studied. It is shown that the pass repetition number has the least influence on the laser track's structure; however, the pass has to be repeated sufficiently to make the laser track continuously porous. The structure of the laser track will not be influenced by the beam's incidence angle significantly within 14°. Pictures illustrate the laser tracks suitable and unsuitable for plating. The laser track's height increases with the laser power input. If a laser track with low roughness is desired, low laser energy should be applied, or a UV laser can be used instead.

Normalized bearing area curve and relevant parameters are proposed to characterize the LISA surface. The LISA surfaces made by a YAG laser and a UV laser have similar characters in the normalized bearing area curve. It is believed to be a feasible method to describe porous structure. It is also possible to be used as a method to quantify all types of laser tracks.

Reference

[1] Y. Zhang, J. S. Nielsen, P. T. Tang, H. N. Hansen, "Laser Induced Selective Activation Utilizing Autocatalytic Electroless Plating Polymer Surface", Proc. Int. CONF NOLAMP12, (12th Nordic Conference in Laser Processing of Materials) Copenhagen, Denmark, August, 2009.

[2] T. L. Cottrell, "The Strengths of Chemical Bonds", 2nd ed., Butterworths, Washington, DC, 1958.

[3] J. R. Fried, "Polymer Science and Technology", 2nd Ed. Pearson Education Inc. 2003.

[4] P. E. Nothnagle, W. Chambers, M. W. Davidson, "Introduction to Stereomicroscopy", Nikon Microscopy 2004, internet source: http://www.microscopyu.com/articles/stereomicroscopy/stereointro.html, accessed: 01-10-2010.

[5] Technical Brochure: "3-Dimensional Circuits, Laser Direct Structuring Technology (LPKF-LDSTM) for Moulded Interconnect Devices '', LPKF Laser & Electronics AG, 2009.

[6] R. K. Fraser, P. A. Jørgensen, P. Westergaard, "Selective activation induced by fiber laser", DTU course 42234 report, 2008.

[7] K. S. Hansen, "Setup for polymer welding with diode laser and welding in PC", IPL-015-06 L176 TM03-06.

[8] E.J. Abbott, F.A. Firestone, "Specifying surface quality: a method based on accurate measurement and comparison", Mechanical Engineering, Vol 55, pp. 569–572. 1933.

[9] E. Mainsah, J. A. Greenwood, D. G. Chetwynd, "Metrology and Properties of Engineering Surfaces", Springer – Verlag, 2001.

[10] ISO 13565-2, "Geometrical product specifications (GPS) – surface texture: profile method; surfaces having stratified functional properties – Part 2: Height characterization using the linear material ratio curve.

[11] Technical Brochure: "Alicona InfiniteFocus® Manual", IFM 3.1.1.2, En 26.02.2009.

Chapter 6. Optimization of the plating step

In this chapter, the plating process is studied. The purpose includes:

- Improvement of the plating velocity
- Finding out the influence of laser parameters on the plating velocity
- Improving the coating quality

Firstly, the plating procedure at laboratory condition will be explained in detail. Two activation methods will be introduced and compared from the aspect of plating velocity. Also, the plating velocity will be used to optimize the laser set up.

The copper coating's quality was characterized mainly by the conductivity, strength of adhesion to the substrate and the roughness. The measurement methods will be introduced before the experimental part.

6.1 Process procedure of activation and plating

The plating process includes two parts, activation and metal deposition. Two activation baths were developed, the so-called "old" one was used at the beginning of the research, and a "new" one was developed in the middle of the project. The new activation bath is believed to be able to provide more activation colloids than the old. Commercial copper baths are used in this project for metal deposition. Commercial activation baths are also available; however, the selectivity of the commercial activation baths is not satisfactory. Usually the commercial activation baths aim at full plating of the plastic surface, and as a result, when they are applied to a workpiece with laser tracks, metal deposition will occur all over the surface.

6.1.1 The so-called "old activation"

The composition of the so-called "old activation" is shown in the table below. The formula is inspired by an expired USA patent [1].

Table 6.1 Composition of the so-called "old activation" bath

0.77 g/L	Palladium chloride ($PdCl_2$)
9 g/L	Tin chloride ($SnCl_2$)
35 mL/L	Concentrated hydrochloric acid (HCl) 37% (v/v)
190 g/L	Sodium chloride (NaCl)

The procedure to prepare and use the "old activation" bath is explained below.

Step1: to make 1 L activation solution, add 190 g sodium chloride to approximately 800 mL of water, then add 35 mL concentrated hydrochloric acid, and stir until sodium chloride is completely dissolved. Then add 0.77 g palladium chloride to the solution and stir until dissolved completely ($PdCl_2$ can only dissolve in acid). Add water up to 1 L. The colour of the solution is light brown/orange. This solution can be stable for years if stored properly.

Step2: add $SnCl_2$ 9 g/L to the solution from step 1, the colour of the solution becomes dark green immediately after stirring. This solution has to be used freshly, because it will slowly lose its function after approximately 24 hours due to the oxidation of tin.

Step3: wash the workpiece with alcohol, to remove the organic dirt and also help the wetting. It is recommended that the workpiece should be either stored in water for 24 hours in advance, or rinse with alcohol, to make the laser track completely wetted by water. Then rinse the workpiece by distilled water.

Step 4: submerge the workpiece in the solution from step 2, for 5 minutes at room temperature.

Step 5: rinse the activated workpiece in three separated 1 L beaker of de-ionized water.

Now it is ready to be metallized in the copper bath. It is recommended that the activated workpiece should be plated as soon as Step 5 is finished.

6.1.2 The new activation

The so-called "new activation" is based on the results obtained in the Polymetal project, but is also inspired by an US patent [2]. The composition of the activation solution is:

Table 6.2 Composition of the so-called "new activation" bath

0.77 g/L	Palladium chloride ($PdCl_2$)
25 g/L	Tin chloride ($SnCl_2$)
120 g/L	Urea (H_2NCONH_2)
30 mL/L	Concentrated Hydrochloric acid (HCl) 37% (v/v)
100 g/L	Sodium chloride (NaCl)

The procedure to prepare and use the "new activation bath" is explained below:

Step 1: make solution part A. It will be stable for a long time if stored properly. For 1000 mL of stock, first add 40 mL of concentrated hydrochloric acid to approximately 300 mL of water, and then 100 g of sodium chloride is dissolved in this mixture. Add 1.54 g of palladium chloride and stir until everything is dissolved, then add water to a total volume of 1000 mL. The colour of this solution is light brown / orange.

Step 2: make solution part B; it will also be stable if stored properly. For 1000 mL of stock solution B, first add 20 mL of concentrated hydrochloric acid to approximately 800 mL of water, and then dissolve 100 g of sodium chloride in this mixture. Add 240 g of urea to the solution and stir until everything is dissolved. Add water to a total volume of 1000 mL. This solution has no colour.

Step 3: add 5 g of $SnCl_2$ to 100 mL of stock solution B; stir until $SnCl_2$ is completely dissolved.

Step 4: add 100 mL of stock solution A to the solution from step 3, the colour becomes dark green immediately. Leave the solution for at least 12 hours at room temperature, until the colour gradually changes to dark brown. This is the final activation solution. Its effect wears off after 24-48 hours, and precipitation may occur (The aging effect has not been studied in detail yet).

Step 5: rinse the workpiece in alcohol and water subsequently, or it is recommended the sample should preserved in water for 24 hours before use, to make the laser track completely wet for activation.

Step 6: submerge the workpiece in the activation solution for 1 minute at room temperature, and rinse with running water for 2 seconds (if it is rinsed for too long time, the activation solution may be totally washed away).

Step 7: submerge the workpiece in 10% HCl acid for 5 seconds, and rinse with running water for 2 seconds.

Now it is ready to be deposited in copper bath. It is recommended that the activated workpiece should be plated as soon as Step 7 is finished.

6.1.3 The method of re-activation

To decrease the plating time, a re-activation method was developed. When using the old activation bath, after several minutes in the copper bath, the workpieces were taken out and re-activated in the same activation bath for five additional minutes, and then returned to the copper bath after rinsing. The hypothesis is that in the reactivation step, ion-exchange plating takes place since Pd is nobler than copper, and when the workpiece is put back to the plating bath again, copper will grow on Pd. Since copper grows faster on palladium than on itself, the plating time will be shortened.

Table 6.3 shows the thickness difference using the standard method and the re-activation method for the old activation bath. The plating time for all the samples using reactivation method was 45 minutes, and the re-activation took 5 minutes, so the time for the whole process is approximately 50 minutes. To compare the whole process, the sample plated for 60 minutes using the standard method was analyzed. It can be seen that similar thickness of copper was obtained for both the standard method and the re-activation method. The thickness was measured by Fischerscope® X-ray XDVM®-W thickness measurement equipment, which is

introduced further in the section 6.2 and Appendix 2. The results show that the reactivation method is a good option to improve the velocity. However, the measurement uncertainties may not allow for a clear conclusion.

Table 6.3 The comparison of copper thickness using a reactivation method for the "old activation" bath. The thickness results were obtained by X-ray thickness measurement equipment.

Reactivation after	1min	2 min	3 min	No reactivation
Plating time in total (minute)	45	45	45	60
Copper thickness (µm)	5.1 ±0.2	4.7±0.3	4.8±0.9	4.8±0.6

Tests for the new activation bath and the results are shown in Table 6.4. Samples were reactivated after 1 minute, 20 minute and 30 minute of plating time, and then the workpieces were plated again. Compared to the standard method without reactivation, more copper was obtained. And reactivation after 1 minute is better than after a long time. This is because, after a 20 or 30 minute plating, the copper is already connected to a continuous layer; the area exposed to the solution is smaller. If the laser track was plated for 1 minute, the structure is still porous with a large surface area. So the reactivation after a short period is recommended.

Table 6.4 The comparison of copper thickness using reactivation method for the "new activation" bath. The thickness results were obtained by X-ray thickness measurement equipment.

Reactivation after	1min	20min	30min	No reactivation
Plating time in total (minute)	60	50	60	60
Copper thickness (µm)	5.6±0.5	4.9±0.4	5.4±0.4	4.6±0.5

6.1.4 Wetting, rinsing and cleaning

As mentioned before, it is recommended that the workpieces are stored in water after laser machining or kept in water for 24 hours before use, to make the surface completely wet using water. A dry workpiece can be submerged in alcohol or mixture of alcohol and water to improve the wettability, and then rinsed in water. An ultrasonic water bath is another option to wet and clean the surface.

The rinsing steps between the plating and activation are quite important. In the new activation, an extra step, rinsing by acid, is added, and there is a water rinse before and after this step. If the rinsing after the activation is not sufficient, parts of the surface outside the track, especially the area around the track may also be plated. Although this type of coating is weakly bonded to the surface and can be easily removed by tape, deposition to excessive area may cause the plating bath to collapse, which should be avoided. Also, production efficiency is decreased if an extra step is needed to remove the unwanted metal deposition. Figure 6.1 shows an example of

an overplated antenna pattern on a PBT/PET substrate. This is because activation drops remain on the surface, which are absorbed by the locally rough area or fillers such as glass fibre. The area surrounding the laser track has a stronger tendency to be plated because the metal deposition reaction, taking place, easily expands along the surface if there is a small amount of activation colloids. Nevertheless, if the rinsing is excessively strong, even the activation colloids on the laser track are also mostly removed, then the track will not be plated or only part of the track is plated.

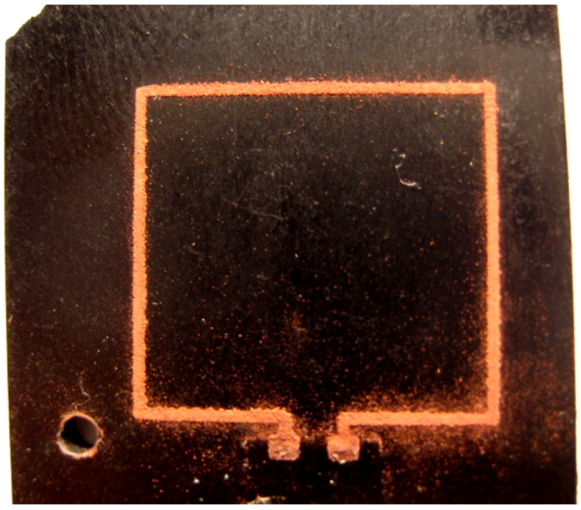

Figure 6.1 When the rinsing is not sufficient, copper may deposit outside the track. The substrate is PBT/PET with 40% glass fiber.

The available laboratory facilities for the wet steps (rinsing, activation, acceleration, and plating steps) are beakers and other small containers. Usually only 1 or 2 workpieces are rinsed at a time, meanwhile, the size of the workpiece is also limited to fit the beaker, otherwise there is a problem regarding the uniformity of the obtained coating. Running tap water is a suitable option for the rinsing process when the number of workpiece is small. Dipping and rocking the workpiece in a beaker of water also works. For both the methods the process time depends on the specific operator. Another possibility is to use an ultrasonic water bath, and both the power and rinsing time should be properly set.

For a mass production on an industrial scale or within an institute, air bubbling, water spray, or an ultrasonic bath can be used in the rinsing process.

6.2 Velocity of the plating for both activation methods

It is believed that the new activation bath is able to provide denser activation colloids than the old one. Also, as explained in chapter 4, after rinsing by acid (HCl), the $(SnCl_3)^-$ shell is removed from the activation colloids and the Pd-Sn core will be exposed to the plating bath [3], thus copper ions get direct contact to Pd; it is believed to improve the efficiency of the activation. Experiments show that, after 2 minutes of plating, the laser track activated by the new

activation bath is fully covered by copper. By contrast, the laser track activated by the old bath needs at least 5 minutes. In order to confirm that the new activation bath can lead to faster plating than the old one, the plating thickness is compared using those two baths.

The copper-plating bath used in this project is Circuposit 3350 from Rohm and Haas. The temperature can be allowed to vary in the range of 43-50°C, and the plating velocity will be affected. 45C or 46°C is believed to be the optimum. At 46°C, a copper thickness of 2.0 µm can be expected after 25 minutes plating time [4].

The thickness of the deposited metal layer was measured using a Fischerscope® X-ray XDVM®-W thickness measuring equipment (in Appendix 2 the technical specifications are attached). The working principle is that X-rays detect all the copper in the light path and add up the volume amount, and then the thickness is calculated by dividing the detected volume with the spot size and copper density. All the copper from the top to the bottom of the surface is calculated for the thickness result. The density of bulk copper (8.94 g/cm^3) is used in the system's calculation, although copper exists in the form of separated particles entangle with plastic. This means that the absolute value of the copper thickness may not be correct, but as an average value for the investigated volume it is believed to be a consistent and reproducible measuring method.

The plating thicknesses after several time periods for the two activation baths are displayed in Figure 6.2. It can be seen that at the first 30 minutes, the new activation bath leads to slightly faster plating than the expected number (2µm/25minutes) given by the plating bath datasheet, while the old activation bath is slower than it. Then in the following 90 minutes, for the new activation bath, the plating velocity slows down to approximately 2 µm /45 minute. For the old activation, after 40 minutes plating, the plating velocity increases significantly.

It is noticeable that the plating bath is designed for metallization of the PCB substrate. So the reported plating velocity should be obtained from a PCB substrate, which is always much less rough than a LISA surface. As explained before, the activation colloids tend to distribute all over the substrate independent of the surface topography [5]. A larger area exists on the type of LISA surface due to the porousness, so more copper deposition occurs. Pictures in Figure 6.3 illustrate copper deposition and the cross section of a laser track, and it can be seen that copper deposits all over the track, however broken sections exist. When the substrate structure is porous, copper deposition may happen in all directions until the copper particles meet each other. Meanwhile, as mentioned previously the X-ray equipment only detects the volume of copper; the thickness is obtained by dividing with the X-ray spot size. So on the plated laser track, there is actually more copper upon the same projected area than on a relatively flat substrate. As a result, the plating velocity in a porous structure is faster than on a flat surface. For the new activation bath, more activation colloids are provided, which means more copper deposition can occur simultaneously. And the copper particles size grows until they connect to each other. After 30 minutes, a continuous copper layer forms, and it can be considered as flat and compact. Therefore the plating velocity decreases when copper starts to deposit only on

copper, which is slower than copper on palladium. Regarding the plating using the old activation, the deposited copper particles are not as connected as using the new one, due to the fact that less colloid were provided and no acceleration is used; the high plating velocity after a 1-hour plating reveals that the copper layers structure is still porous.

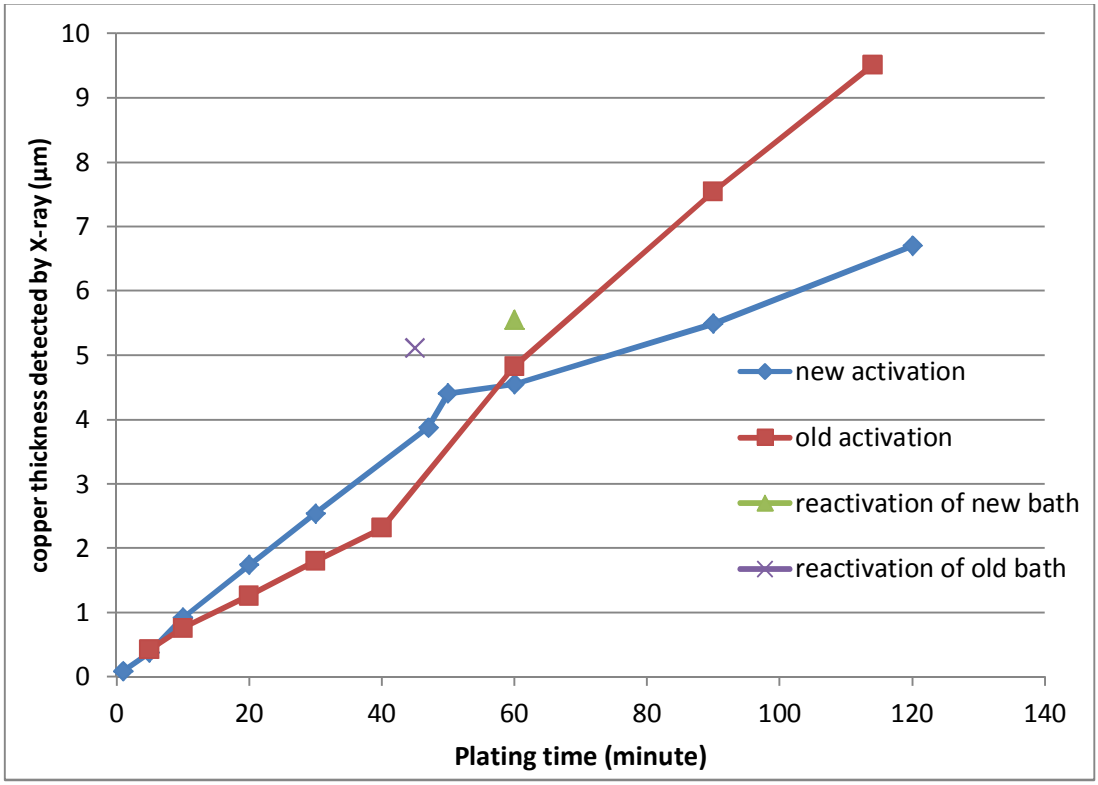

Figure 6.2 The plating velocity comparison for the "old activation" bath and the "new activation" bath

Although the two activation methods lead to comparable thickness after a 1-hour plating, the new activation bath is recommended. Firstly, the new activation step takes only less than 2 minutes while the old one takes 5 minutes. Secondly, when a thick metal layer (more than 10µm) is needed, electroplating is applied after half an hour of electroless plating; it is more effective than only using electroless plating. Thirdly, it is believed the new one can lead to a compact copper layer, though visual evidence is needed to prove this conclusion.

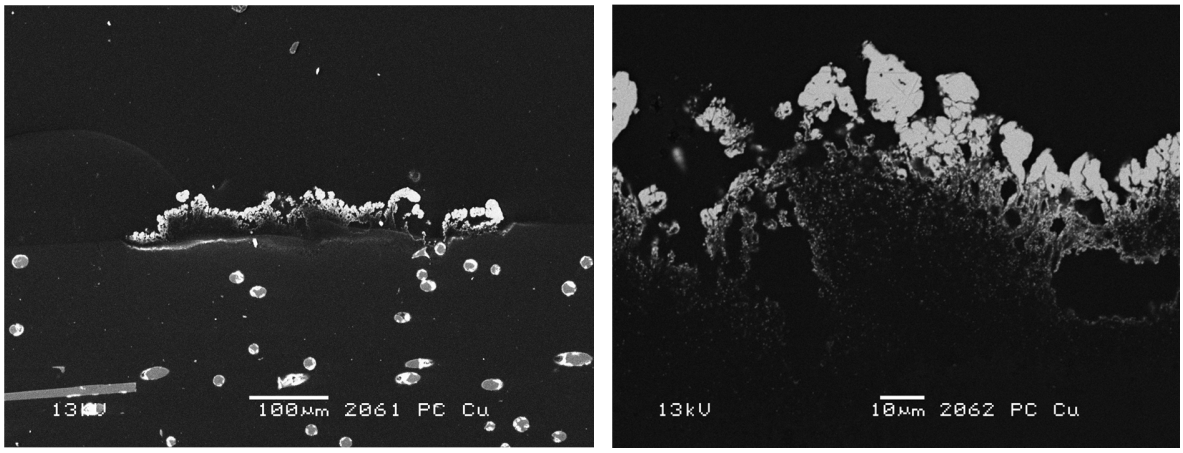

(a) (b)

Figure 6.3 Cross section of 1h plated polycarbonate (a) the whole cross section of a laser track (b) a part of the laser track

6.3 Coils experiment

To measure the conductivity and to examine the repeatability of the LISA process, 56 coils with the same length (more than 140 mm) were drawn on polycarbonate boards using the same laser parameters (the same as the so-called "YAG Good") and plated with copper for 1 hour. Then the resistance between the two ends of the coils was measured.

The reason why a coil shape was chosen is that a relatively long laser track can be achieved in a small area. The size of the workpiece is limited by both the laser equipment and the plating beaker. The machining window for the laser is 100 mm x 120 mm. In the plating, the stirring is made with a magnetic bar; if the workpiece is too large, part of the track will not be plated due to insufficient mass transport. Figure 6.4 shows one of the coil samples. The total length reaches more than 140mm and the width of the track is approximately 500µm. All of the samples were plated in the copper bath for 1 hour using the new activation bath, so the thickness of the deposited copper is approximately 5µm averagely according to experiments data showed in Figure 6.2.

Figure 6.4 One coil sample. The coil was made on polycarbonate (with 10% glass fibre) and plated by copper. The total length is approximately 148mm, and the width of the track is 500µm.

The conductivity is influenced by the uniformity of the copper layer. Ohm's law can be used to describe the factors related to the resistance of a copper wire, shown by Equation 6-1.

$$R = \frac{\rho L}{A}$$ **Equation 6-1**

Where R is the resistance, ρ is the resistivity, L is the length; A is the cross section area.

$$R = R_1 + R_2 + ... + R_n = \rho \times \Delta L \times (\frac{1}{A_1} + \frac{1}{A_2} + ... + \frac{1}{A_n})$$ **Equation 6-2**

If a copper wire has a similar size (length 148mm, cross section 500µm X 4.6µm), and the resistivity of copper at 20 °C is 1.68E-8 Ω·m [6], the resistance is 1.08 Ω theoretically. However, when a multimeter measures the resistance, the obtained value is actually larger due to the contact resistance existing when the probe touches the surface. The cross section is irregular as Figure 6.6 shows, and it also differs from one section to another, which means the cross section area is not the same when it is made at a different position. So the total resistance should be a complicated serial and parallel connection summation if we divide the line into small segments. Simplifying the question into a group of series connected resistors, calculated in Equation 6-2, the smallest cross sectional area effect, play a determining role due to the reciprocal relationship. As a result, if a small section of a long track is thin, the whole resistance increases sharply.

The histogram shown in Figure 6.5 displays the frequency of the obtained resistance. 60% of the coils are conductive between the two ends. And 30% of all has a resistance below 20 Ω.

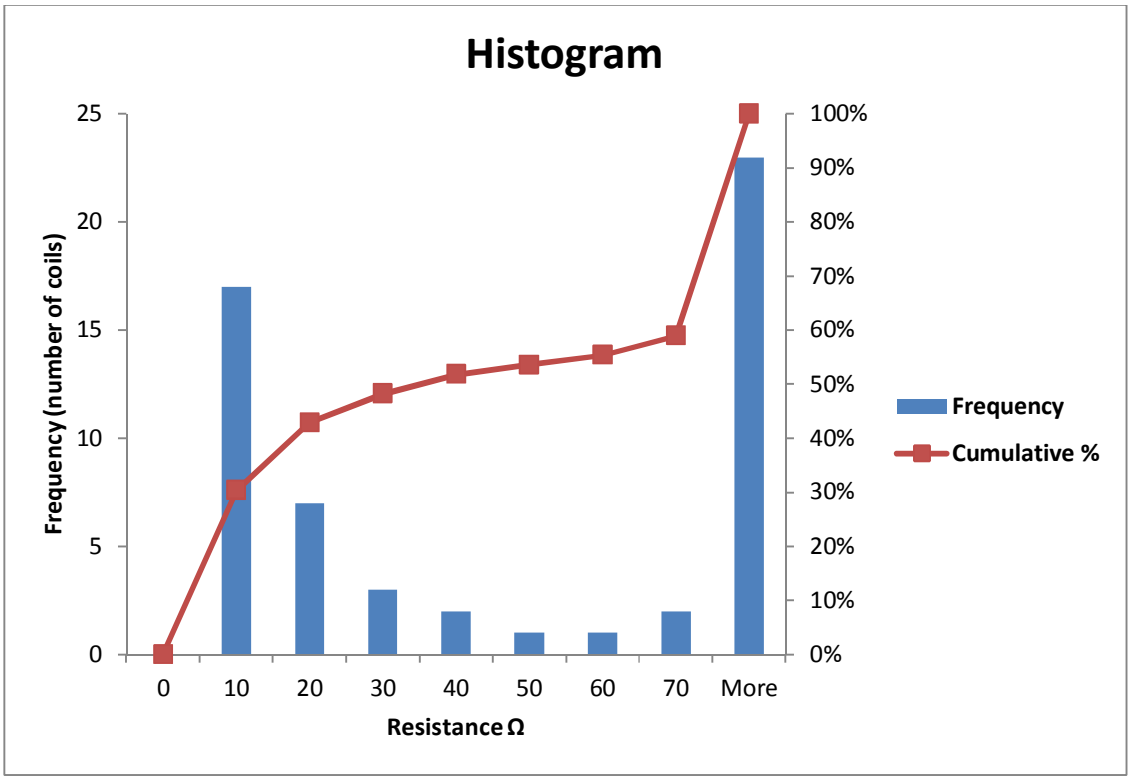

Figure 6.5 The frequency and cumulative percentage for the resistance of 56 coils are shown in histogram. The column "more" refers to all the failed samples, i.e. the coil is not conductive or only partly conductive.

Possible reasons for the samples which failed to be conductive are believed to be as following:

1. The copper layer is not uniform; it can be seen from Figure 6.3 or Figure 6.6 in the following section. As explained previously, the resistance increases sharply if there is one thin part of coating on the track.
2. The laser track is brittle, and scratches may happen easily during post-plating handling. Any scratch on the top may affect the conductivity.
3. Oxidation of the copper may happen after plating if not dried thoroughly due to the moisture and O_2 in the air. Adding nickel and gold on top of copper can prevent the oxidation. Also, after plating, an oven drying can prevent the workpiece from oxidation.

To be applied industrially, the repeatability should be improved. A thicker copper layer can be used to minimize the chance of broken track. Nickel and gold layers can be applied on top of copper to prevent corrosion or oxidation to happening. Also, if the pattern is shorter than the tested coil, chance of failure will also be less.

6.4 Characterization tools for the plating quality

The plated laser track is supposed to be utilized mainly in the electrical industry, including antennas, sensors and circuits boards for electronic devices. There are a series of industrial standards which describe the requirements for the coating to be applied in specific field, such as [7] and [8].

A cross section of a laser track is shown in Figure 6.6. It can be observed that a continuous coating forms on the laser track. However, the thickness is not consistent along the cross section. Additionally, the top view of a plated laser track is shown in Figure 6.7, where copper crystals appear as pillars. To investigate the feature of the coating further, characterization works were performed on the aspects of the adhesive property, and how the laser track structure affects the velocity of copper deposition.

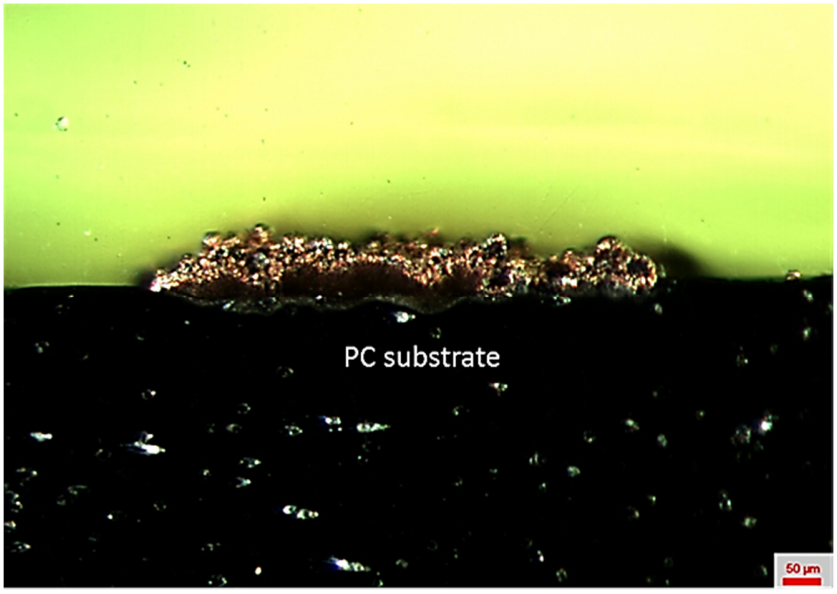

Figure 6.6 A cross section of a plated laser track on polycarbonate. The workpiece is molded in epoxy, which has a green color in the figure. And the black part is the substrate, polycarbonate with 10% glass fiber.

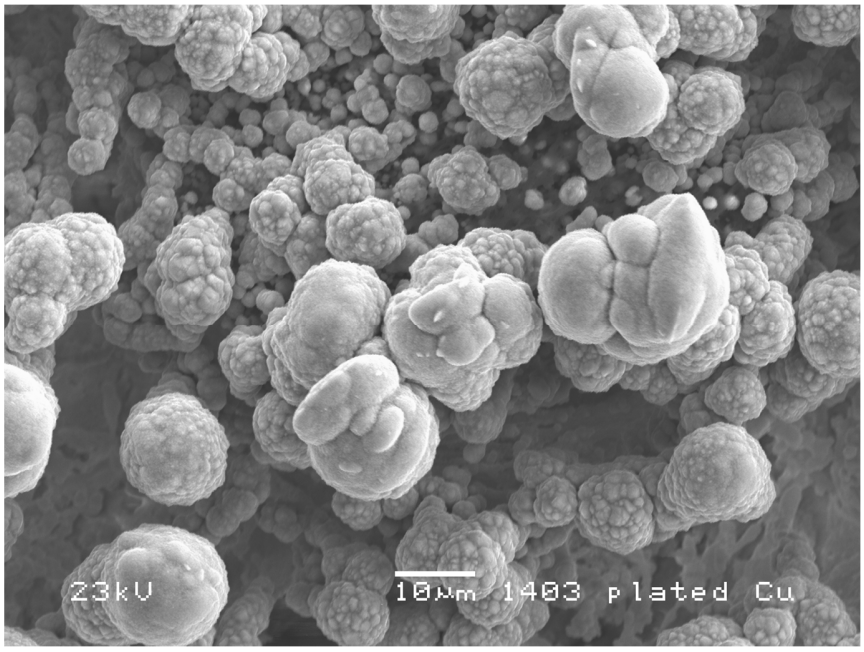

Figure 6.7 Top view of a copper plated laser track on polycarbonate (SEM picture).

6.4.1 Coating thickness measurement methods

The traditional method for the coating thickness is based on the weight difference (ΔW) before and after plating and the area (A) and the density (ρ) of the plated metal are available, then the thickness of the coating can be calculated by Equation 6-3.

$$\tau = \frac{\Delta W}{\rho A}$$ **Equation 6-3**

In Equation 6-3 τ is the thickness, ρ is the density of the plated metal, and A is the area. However a LISA surface is rough and irregular so that the area cannot be estimated correctly so far. Therefore this method was abandoned after some failures.

Another option to measure the thickness is using a Fischerscope® X-Ray system (XDVM®-W), which is introduced in the previous section, and more details about the equipment is attached in Appendix 2.

6.4.2 Adhesive property measurement methods

The adhesive strength of the deposited coating is an important quality. The metal coating needs a sufficient adhesion to the substrate to maintain the component function, when the component is under thermal and mechanical stress or different levels of load.

A wide range of testing methods can be used to characterize the adhesive property of a coating, for example, cross-cut test [9], scrape-adhesion test [10], pull-off test [11], peel-off test [12], *etc*.

Several industrial standards are available for the adhesive measurement. The preparation of the surface and the test procedure are described in the standards for specific uses. For instance, DIN EN 582 [13] is used to evaluate the adhesive strength of parent metal and spray deposit material; or DIN IEC 60326 [14] contains test methods and procedures for printed boards; or in MIL STD 883, [7] the testing method for adhesive strength of coating in microelectronic devices is mentioned. Commercial testers such as Dage® claim that they confirm to, or in some cases exceed some industrial standards [15].

The pull-off strength of a coating is an important performance property that has been used in specifications. In this project, two pull-off testers were used due to the availability of access. One of the testers is Dage® bond tester series 4000 [15] from HSG-IMAT, Stuttgart, Germany. The tester and how the tested substrate is fixed on the tester, is shown in Figure 6.8. A small metal bar is soldered on the tested surface, and then the pulling force is recorded until the metal bar breaks off from the substrate. According to experts with broad experience using this tester, usually for industrial use, the adhesion strength of a metal coating needs to achieve 3MPa.

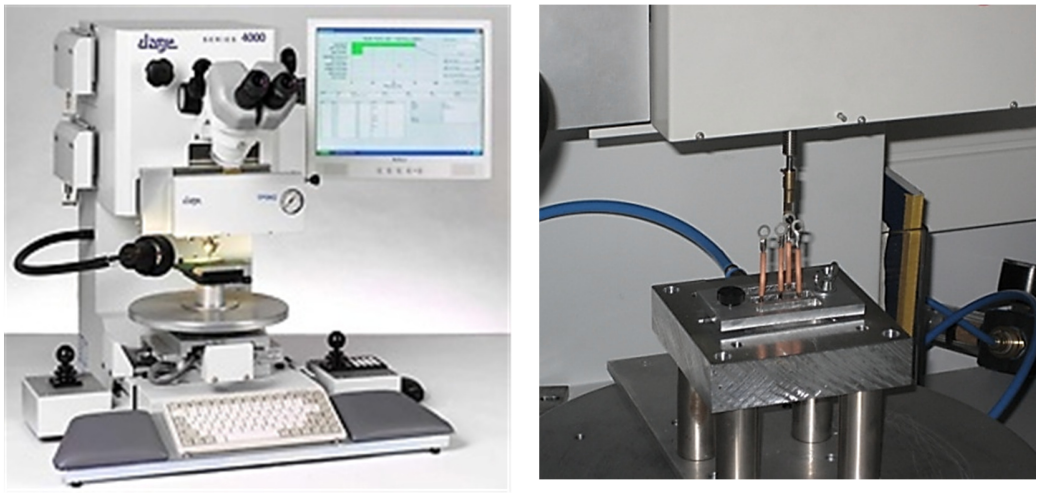

(a) (b)

Figure 6.8 (a) is the Dage bond tester series 4000 [15], which was located in HSG-IMAT, Stuttgart, Germany. (b) is how the equipment performs pulling force on the metal bar. The workpiece was fixed on the platform pressed by a metal board with two channels. The circular hole on top of the metal bar can be pinned by the machine, so the pulling force can be applied.

The other tester is a DFD® PAT model GM01-6.3kN manual hydraulic tensile adhesion tester [16] from DTU, shown in Figure 6.9. A dolly is glued on the tested surface, and then pulled off by hydraulic pressure provided by the manual pump. The calibration should have been applied to the diameter of the dolly and the force in the measurement, which has a reference to compare. But the calibration work has not been performed yet. Primer (Loctite® primer 7239) is applied with the glue (Loctite® glue 4062) to strengthen the adhesion between the surface

and dolly, so that the dolly won't break away from the surface before the copper layer does. The PC pieces used for the adhesion test are circular with a diameter of 65mm, as Figure 6.17 shows. The tested area (ca. 1mm x 1mm) was made in the center of the piece. There are four feet on the dolly's holder, and they can stand on the workpiece. The dolly used in the measurement is 0.8 mm in diameter.

Figure 6.9 The adhesion tester: DFD® PAT model GM01-6.3kN manual hydraulic tensile adhesion tester [16]

At HSG-IMAT, a novel instrument for peel-off test on MID part has been developed, where the coating is peeled off with a micro-chisel [17], the forces parallel and perpendicular to the conductor to be measured and evaluated. It will be involved in future work for LISA.

Furthermore, a scotch tape test is used as a primary examination. The method is to apply a piece of tape on the plated laser track, then peel off the tape, and check whether the coating is removed by the tape. If the coating is not removed or only several particles are gone with the tape, it is considered as “pass”. Standards are available for such type of test [18][19].

6.5 The influence of the laser parameters on plating velocity and quality

As mentioned in the previous chapter, laser parameters affect the structure of the laser track. In this section, the effect of the structure or the laser parameters on the plating velocity and the adhesive property is discussed. The coating thickness and the adhesion strength are measured using the methods described in section 6.4.

6.5.1 Experiment 1: samples made by YAG laser and plating at HSG-IMAT

The workpieces were machined by the Nd: YAG laser in DTU. Only one parameter was varied in the test, the lamp current. Table 6.5 lists the three laser parameter groups used in this test. The pass repetition number for all the samples is 30. 12 Φ2.75mm spots were made on one polycarbonate piece for each group. The “New activation” bath was prepared in DTU one day before it was used, then brought to Germany. The activation and plating process, as well as the

adhesive test, was carried out in the laboratory HSG-IMAT. Right before activation, the workpieces were rinsed in ultrasonic water bath, which was also used to wet the laser structure by water. Electroless copper plating bath Circuposit 4500 from Rohm and Haas was used for copper deposition. Figure 6.10 displays how the workpieces were fixed on the rack, as well as the copper bath tank. The bubbling in the tank provided sufficient stirring. It is believed that all the samples were plated in the same conditions.

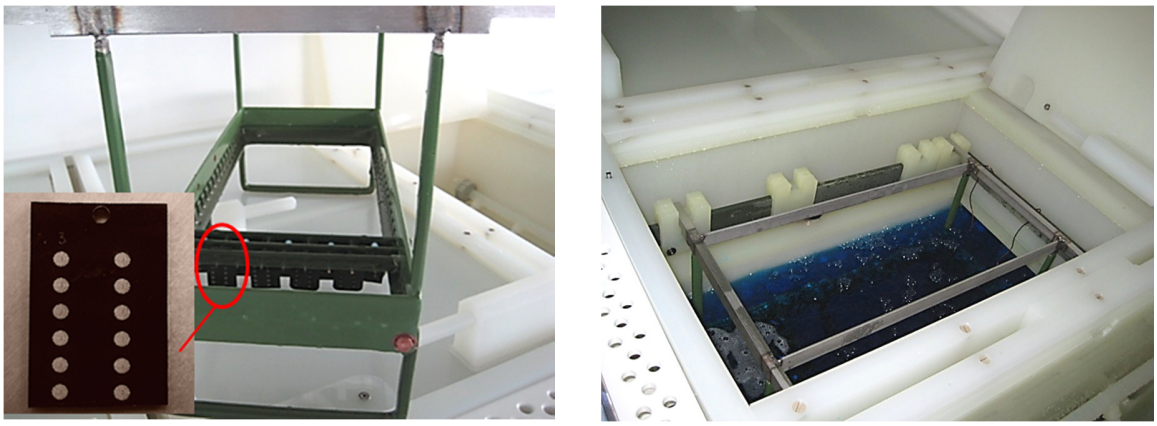

(a) (b)

Figure 6.10 Plating equpiment in HSG-IMAT. (a) is how the samples are fixed on the rack which fit the plating bath tank. (b) is tank for the copper plating bath.

The samples were plated for 0.5 hour at 52℃ and the thickness was measured by a Fischerscope® X-ray XDVM® - µ measurement system (the technical specification is attached in Appendix 2). 6 out of 12 spots were measured for each workpiece. The average results as well as the specific laser parameter are shown in Table 6.5. For the workpiece in group 2, the thickness for one spot was differently high due to an extra floating layer of copper, so this data was sorted.

Table 6.5 Average copper plating thickness for samples made by three laser parameter groups.

	Lamp current (A)	Q-switch (Hz)	Average power	Coating thickness (µm)
Group 1	22	1200	4.2W	4.2±0.3
Group 2	18	1200	2.7W	4.4±0.8
Group 3	14	1200	0.7W	4.3±0.3

Table 6.7displays the spot sample before and after plating in each group. It is believed that under higher laser energy, more material on the substrate surface melts, which leads to a denser sponge structure. The three laser set-ups lead to tracks with different height obviously.

In Group 3, the laser power is not sufficient that the melt materials are not enough to cover the whole spot. By contrast, spots in group 1 and group 2 are fully covered. So the spot in group 3 has a pattern of small circles due to the wobbling way of laser beam movement. But the thickness measurement shows that the coating thickness is not related to the laser power or the surface structure. It is concluded that same plating velocity was obtained for the listed three laser power set-ups.

The roughness on the plated spots was measured by Alicona InfiniteFocus® and analyzed using SPIP®. 20X lens was used. For the values of S series, five spots were measured and averaged. Since the coefficients of variance between spots are within 15%, so for the R series, 10 lines were measured on only one spot and averaged. R_a is in the range of approximately 6 µm to 12 µm. and S_a is in the range 7-14 µm. The results show that Group 3, which is made by the lowest laser energy, has the smallest roughness after plating. It is found that the roughness before and after plating is not significantly different. For example, the laser track made by Group 2, which uses the same laser parameter as the "YAG good" mentioned in section 5.4, has a S_a value approximately 14 µm, which is comparable with the value 12.3±1.7 for the surface after plating.

According to a report [20] from HSG-IMAT, the R_a of the metalized area on the substrate of PBT using the LDS® technology is in the order of 4µm and R_z 22µm.

The "e-Cu: Check" system [21] was used to measure the activity of the plating bath. In this way, the plating velocity on LISA surface can be compared with LDS®. The working principle of "e-Cu: Check" system is explained in Appendix 2. It measures the time that the plating bath needs for the testing bars to become conductive, and long time stands for low activity. Table 6.6 shows the comparison. LISA is obviously faster than LDS®. The Pd/Sn activation system is believed to be the reason.

Table 6.6 Comparison of plating velocity between LISA and LDS®

	LISA	**LDS®**
Plating time	0.5 hour	0.5 hour
Activity of the bath	1262 s	900 s-1200 s
Substrate material	Polycarbonate 10% glass fiber	LCP
Temperature	52°C	52°C
Average thickness	~4µm	~2µm

Table 6.7 The spots before and after copper plating. The roughness was measured on the plated spots. Group 1, 2, and 3 are same as in Table 6.5.

Group	The laser spot before plating	The laser spot after copper plating	Roughness after plating
1		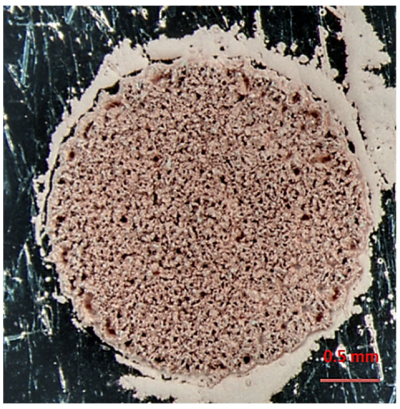	R_a11.7±1.3 R_z 68.2±9.9 S_a 13.9±1.3 S_z 126.3±13.3
2	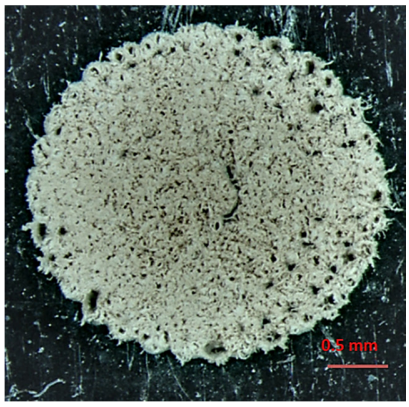		R_a 11.3±1.0 R_z 64.5±5.0 S_a 12.3±1.7 S_z 115.0±15.8
3		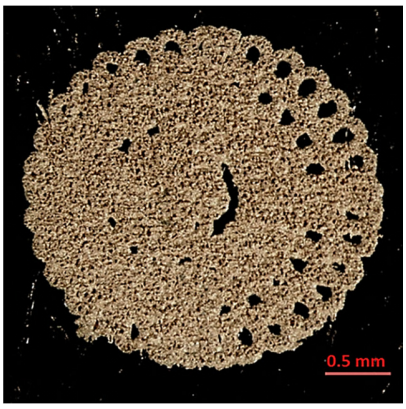	R_a 6.3±0.6 R_z 39.3±7.7 S_a 7.0±0.5 S_z 59.4±7.6

The tensile adhesion between the deposited metal layer and the polymer substrate is checked by the Scotch tape test and then measured using the Dage® tester in HSG-IMAT.

The samples used for the pull-off test were plated at 42℃ in the same bath, however the activity of the bath was lower (2051s). Approximately 5 µm copper was deposited after 1 hour. Electroless nickel immersion gold (ENIG) was used for subsequent nickel and gold plating. IPC 4552 specifies the metal layer thickness for quality test of ENIG [8]. As a result, approximately 5 µm nickel (10min in DODUCO® Durni-Coat 520/50, 88 ℃) and 0.1 µm gold (17min in DODUCO AUROL 20, 90 ℃) were plated on top of the copper. Then the samples were heated in an oven at 80℃ for 2 hours.

Figure 6.11 (a) shows a spot sample plated by copper, nickel and gold layers. Firstly, the Scotch tape test was applied to at least on spot on each workpiece. All workpieces passed the test.

For the pull-off test a small metal bar was soldered on the spot, as shown in (b) of Figure 6.11, and then it is pulled up at a constant speed. The average pull-off test results are presented in Table 6.8. For the calculation, at least 10 spots were measured and provide reasonable data for each parameter group; one or two data, which are much smaller than the others, was sorted out. The original data are presented in Figure 6.13. For the workpiece using laser parameter group 1, there were 3 spots for which the metal bars did not break even under the maximum load that the equipment could provide, so no specific values are available.

(a) (b)

Figure 6.11 (a) is sample of the spot plated by multiple metal layers: copper + nickel + gold. It is from group 3. (b) is the sample soldered with the metal bar for the adhesion test. There are 12 spots on one workpiece and 6 spots were soldered, to keep a distance among the metal bars.

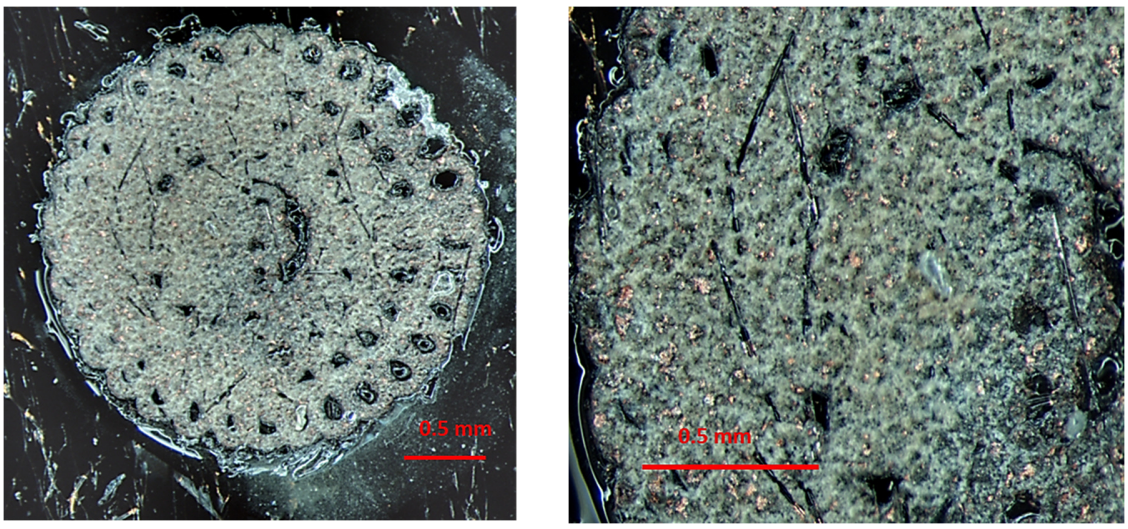

(a) (b)

Figure 6.12 the plated spot after the pull-off test. (a) shows one whole spot from group 3. And (b) shows the zoomed in section.

Most of the spots show strong adhesion (more than 10 MPa) between the deposited metal layers and the substrate. This can be explained by the entanglement of the copper particles and the porous plastic structure. The sample after the pull-off test is shown in Figure 6.12. It can be seen that most of the metal layers were removed except a few copper particles, and the plastic structure also broke in the middle area. This is believed to be the weakest point of the whole multiple layer system (substrate + porous plastic layer + copper + nickel +gold +solder material), due to insufficient copper to entangle with the plastic. According to HSG-IMAT's work [17], if using LDS® technology on the substrate of LCP, the adhesion strength measured by the same pulling-off test is approximately from 2.5 to 10 MPa depending on the laser set up.

Table 6.8 the average adhesion test results from the Dage bond tester series 4000, the equipment tolerance from is 0.25%.

Sample	Average adhesion strength (MPa)	COV
Group 1	13.2*	19.0%
Group 2	13.0	16.0%
Group 3	11.7	13.6%

** The spots, which are beyond the tester load limit, were sorted, because no specific value is available.*

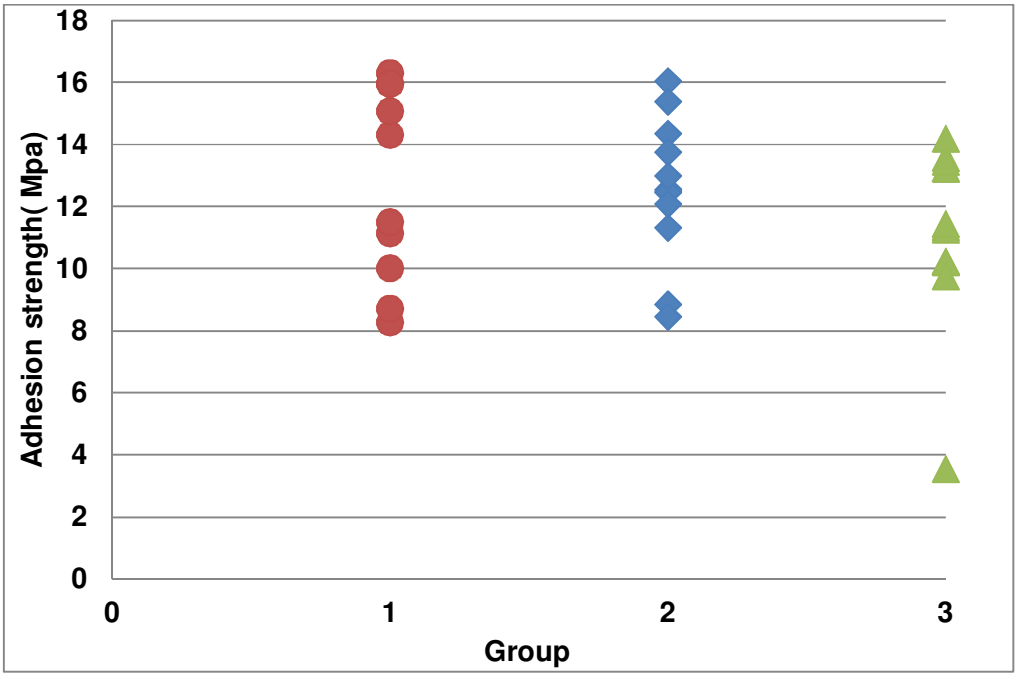

Figure 6.13 the adhesion strength distribution chart for 3 groups of laser parameters.

Both Table 6.8 and Figure 6.13 display a trend that high laser power is in favour of strong adhesion. As discussed in Table 6.7, higher laser energy will lead to more compact structure. The entanglement between the plastic structure and the metal particles is enhanced (providing the amount of the deposited metal for all the groups is similar). The adhesion of the metal layer will depend on how much the metal particles entangle with the substrate.However if the laser power is too high, the effect is the opposite, because when the surface is burnt by the laser beam, the remaining material may not be strong enough to support the copper.

6.5.2 Experiment 2: samples made by a YAG laser and plated in DTU

Extended experiments were carried out in DTU. Laser parameters were varied according to Table 6.9, thus 81 groups of laser parameters were used. The "old activation" bath and Circuposit 3350 were used for the activation and the plating.

Table 6.9 the laser parameters used for extended experiments to explore the relationship between the laser set-up and the plating velocity

Lamp current	Q-switch frequency	Speed	Wobble size
150	1200	40	1
180	1800	60	4
210	2400	80	7

After a microscope check to the laser track, only 36 groups out of 81 lead to the desired LISA surface, which has the possibility to be plated according to experiences. As a result, those 36 groups of laser parameter were studied further for the plating velocity and adhesion test.

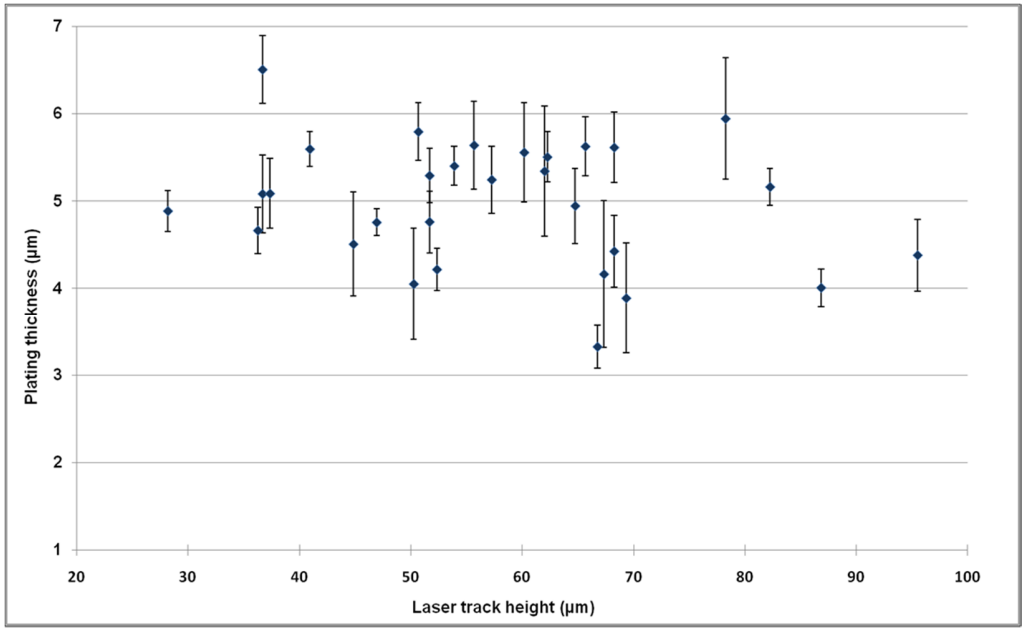

Figure 6.14 Plating thickness appears independent from the laser track's height

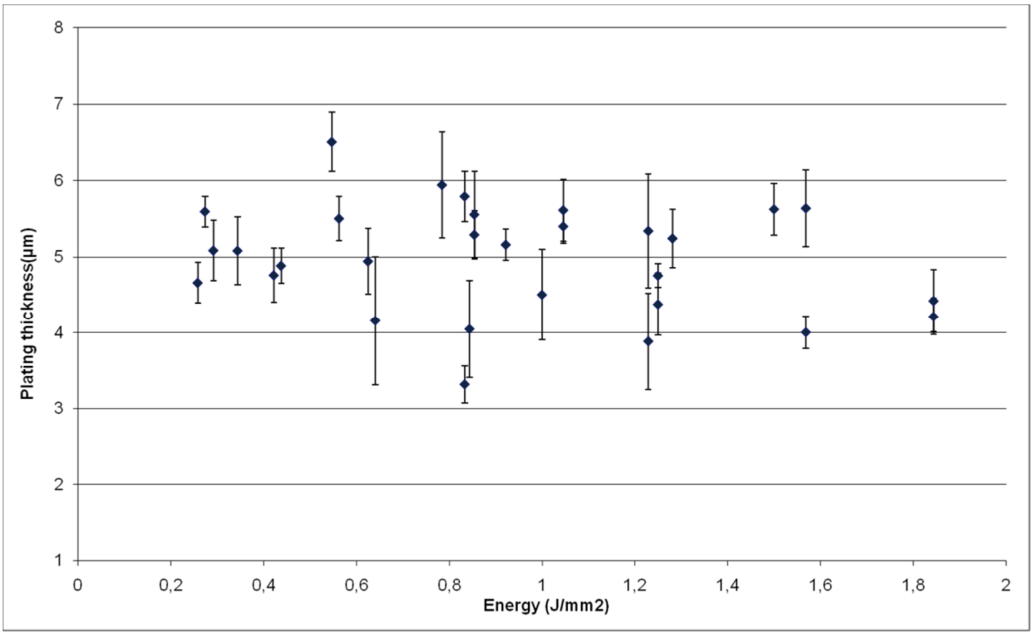

Figure 6.15 Plating thickness is independent on the laser energy input to the substrate.

For the plating velocity measurement, all the workpieces were plated for 1 hour. 2 laser tracks (5mm x 19mm) were made on polycarbonate pieces, with 3 or 4 thickness measurements

performed on each piece, and 2 or 3 such pieces were used for each laser group. The track's height was measured as mentioned in previous chapter.

The average copper thickness is plotted against the laser track height or the laser energy input in Figure 6.14 and Figure 6.15. Again, no obvious trend is displayed. The reasons include:

1. The plating process is influenced by a variety of factors, for instance the bath flow direction, the rinsing step and the piece's size. The thickness is in the 10µm range, even if a small uncertainty has a relative large effect on the final result. As a result, even on the same piece, the standard deviation is 0.53µm on average, and the coefficient of variation is 13%; if among different pieces made by the same laser parameters, the thickness standard deviation is 0.76µm, and the COV% is 17.6%. Table 6.10 shows the standard deviation of the thickness measurement by X-ray instrument.

Table 6.10 The standard deviation and COV% in the plating thickness

	On the same piece	In the same laser group (2 or 3 pieces)
STD	0.53µm	0.76µm
COV	13%	17.6%

2. It is known from the previous chapter that the laser tracks height changes with laser energy input. It was also expected that a high track may lead to more copper deposition during the same period. However the results show that the plating velocity is not related to the laser track's height. It supports the result from the plating in HSG-IMAT, Stuttgart. According to the study to those short-time-plated samples, Cu particles start to deposit from the middle layer of the laser track but not from the bottom, so it's reasonable that the height of the track won't affect the Cu thickness, only (the) upper part of the laser track is plated, which is shown in Figure 6.3 and Figure 6.16.

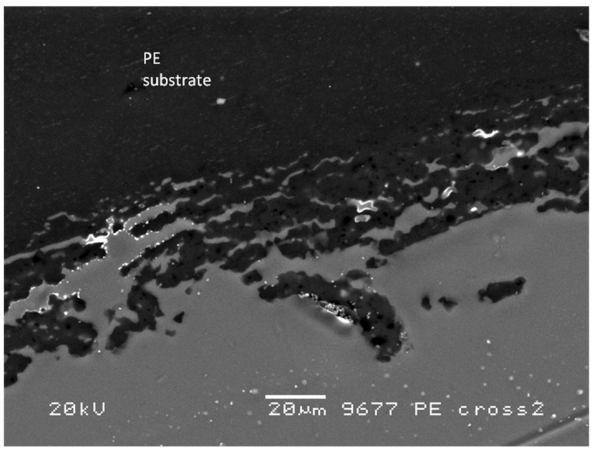

Figure 6.16 A cross section from PE piece plated for only 1 minute. The bright spots are copper particles.

For all the samples the same plating bath was used, and it's reasonable during a certain period that the same amount of copper deposit is found. Especially after a certain period, when the copper particles connect to each other and form a copper layer, the deposition velocity is much larger than the beginning. From these points of view, the copper thickness is independent of laser parameters as long as the structure can be plated.

Figure 6.17 the substrate piece for adhesion test use

The adhesion test was performed by DFD® PAT model GM01-6.3kN manual hydraulic tensile adhesion tester.

Almost all the obtained results are above 3MPa, which is a very high value according to an expert's experience using this tester. Figure 6.18 and Figure 6.19 show the dolly and the tested surface after the pulling off test, and on both sides there are entangled copper particles and plastic. This was used to make sure that during the test, the dolly breaks from the copper layer but not from glue side.

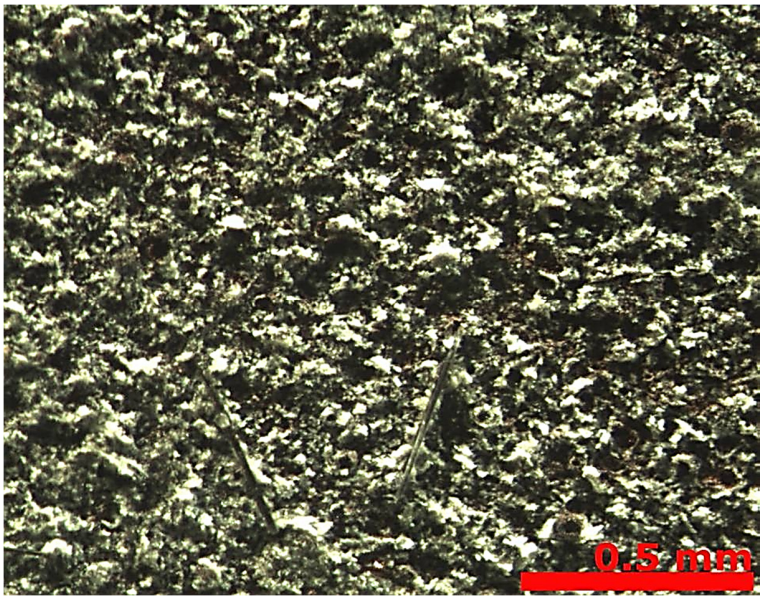

Figure 6.18 The dolly surface after pull-off

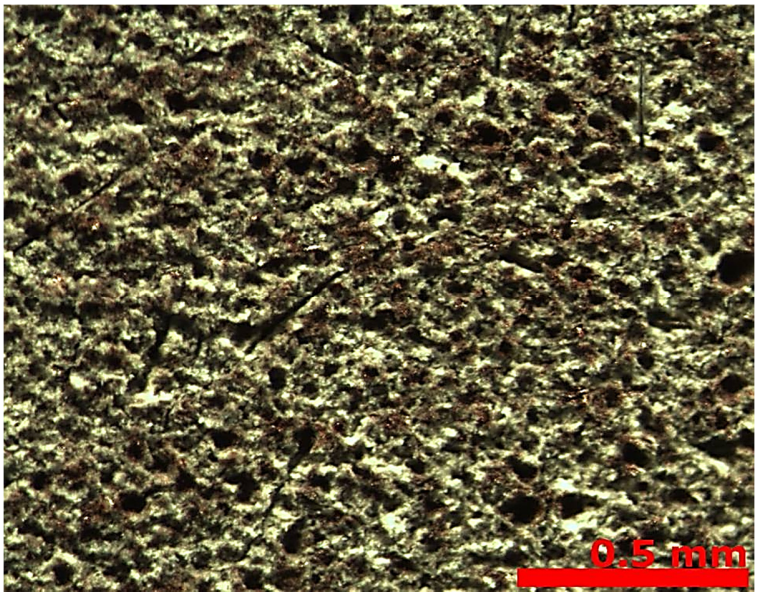

Figure 6.19 the substrate after pull-off

The adhesion strength is plotted as a function of laser input energy, as shown in Figure 6.20. Apparently no expected relation is displayed. The standard deviation in the measurement is about 1 MPa, which may eliminate the trend. As mentioned in the previous chapter, it is expected to have a high uncertainty when using the tester DFD® PAT model. Besides the surface condition, the speed of force loading is another factor, which gives uncertainty. Additionally, it was glue that is used to bond the dolly to the coating, and glue is easy to dry in the air, but this is not easy to control, so the uncertainty is increased. The obtained adhesion value by this tester

is smaller than by the one from Dage®, because it is believed that the heat during the soldering process increases the adhesion.

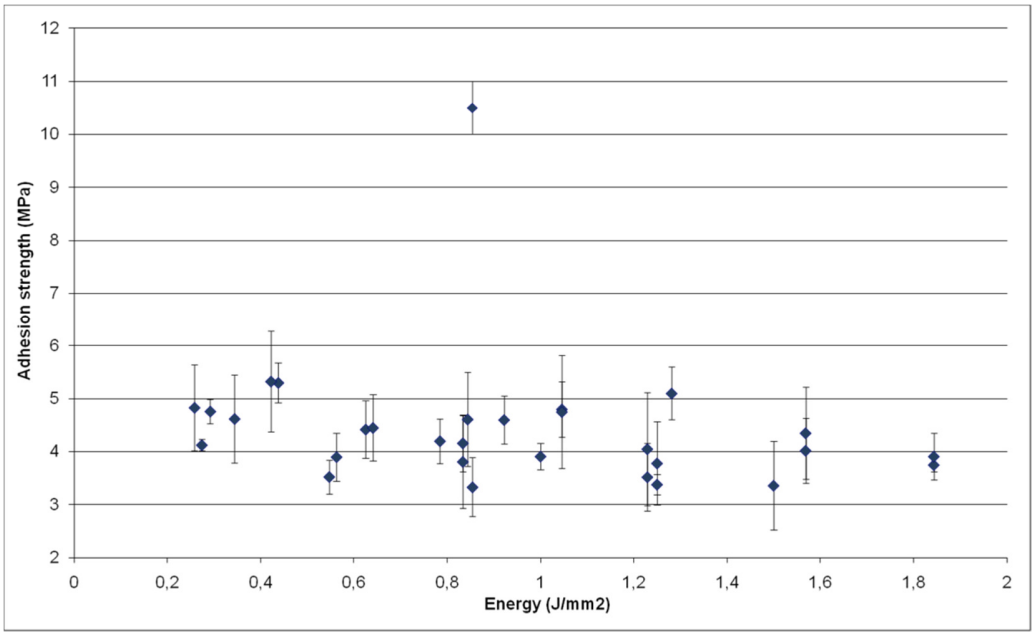

Figure 6.20 Adhesion strength is plotted against laser energy input.

6.5.3 Experiment 3: sample made by UV laser and plated in DTU

Regarding the samples made by a UV laser, only the Q switch frequency was changed (the parameters were shown in Chapter 4).

As mentioned before, a sponge-like structure is observed on the laser tracks. Under high frequency (above 50 KHz) only non-continuous holes were left on the surface, however, below the surface the structure is porous.

Figure 6.21 displays the copper thickness on each track after 1 hour plating activated by the "new activation" bath. On the tracks made at 30 and 40 KHz, the copper thickness is 4 µm approximately, similar to the results obtained on YAG laser tracks. Again, it proves that the copper deposition velocity is not affected by the structure as long as it is porous and continuous. By contrast, the tracks made at 50-70 KHz only got approximately 1.5 µm thick copper. Figure 6.22 shows the plated laser tracks made by (a) different Q-switch frequency. Obviously, when the frequency is larger than 50 KHz, there are spots on the plated laser track, due to the thinner copper coating locally.

Regarding the adhesive property, all of the plated tracks passed the Scotch tape test. In future work, the adhesion strength of the copper coating on the UV laser track should be checked by (a) Dage® tester and compared with the YAG laser track.

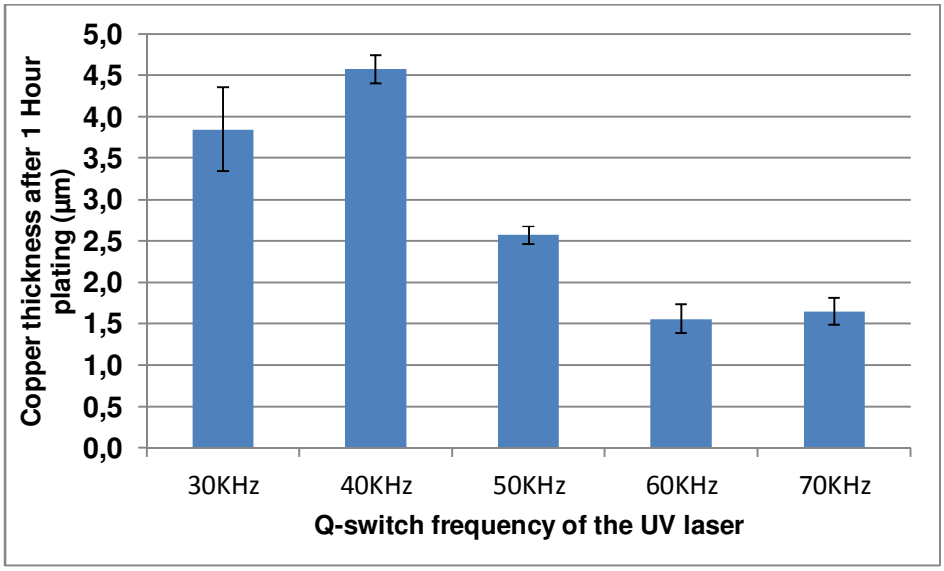

Figure 6.21 Copper thickness on the tracks made by UV laser after a 1 hour plating

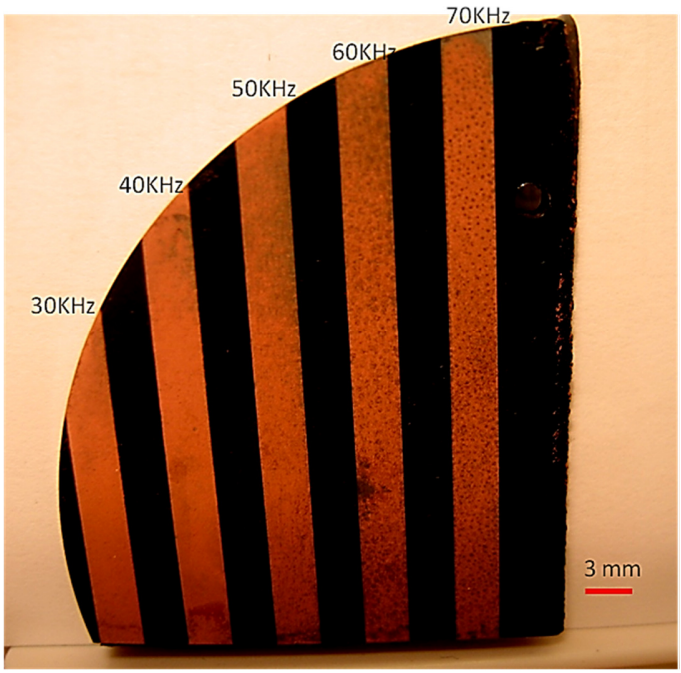

Figure 6.22 the workpiece with laser tracks made by a UV laser. The used Q-switch frequency is marked above each track.

The roughness on the plated track made at 40 KHz was measured using Alicona and SPIP®. Five measurements were made for the S series and 10 lines were measured on one of them. The results are shown in Table 6.11. The roughness of the track made by the UV laser is much smaller than the YAG laser's.

Table 6.11 The roughness values obtained from the plated UV laser track (made at 40 KHz)

	R_a	R_z	S_a	S_z
µm	1.8±0.2	11.3±2.1	1.6±0.1	27.2±6.3

6.6 Conclusion

In this chapter, two activation methods are explained and compared via the velocity in the subsequent plating. The new activation bath is recommended because the resulting copper plating is faster and the copper layer is believed to be more compact though more visual evident is needed to support this conclusion.

It is also shown that the plating velocity is independent of the height of the laser track, as long as the structure is sponge-like and continuous. In Chapter 4, typical LISA surfaces made by (the) YAG laser and (the) UV laser were described using normalized bearing area curves. It means common ground can be found though the height of the laser track is quite different. In the future, work, effort will be put on the description of the laser track structure using a mathematical way based on the bearing area curve or porosity measurement. The purpose will be to predict the plating velocity or even the plating quality.

The adhesive strength of the copper coating is related to the laser structure. High laser energy input will lead to high laser tracks, on which the copper coating has a stronger adhesion than on the track made by lower energy (even they have similar thickness). In the future work, the plated UV laser track will be checked using a Dage® tester, and the strength will be compared with the quality of laser track made by a YAG laser.

Using a YAG laser, R_a of surface after plating is in the range of 6-12µm. Lower laser energy leads to a smoother surface. R_a of LISA surface made by a UV laser is only around 2µm. So a UV laser is recommended if a surface with low roughness is desired.

The rinsing steps are important to the whole process. In mass production, it is recommended that these two steps should be quantitatively controlled using special equipment such as an ultrasonic bath.

In future work, the roughness of the copper coating will be studied and the task will be to decrease the roughness. The feature of the copper coating will be further observed using SEM and other techniques.

Reference

[1] D. A. Arcilesi, R. K. Klein, D. Magda (OMI), “Sensitizing nonconductive substrates prior to electroless plating”, GB patent 2 154 251 A, 1985.

[2] Shipley company, “Catalyst solution for electroless deposition of metal on a substrate”, U.S. patent 1482758, 1977.

[3] T. Osaka, H. Takematsu, "A Study on Activation and Acceleration by Mixed PdCl2/SnCl2 Catalysts for electroless Metal Deposition", Transactions of the Society for Advancement of Electrochemical Science and Technology, Vol.127, No. 5, pp.1021-1029, 1980.

[4] Technical data sheet: Circuposit Electroless Copper 3350, Shipley, Rohm and Haas.

[5] J. Kim, S. H. Wen, D. Y. Jung, R. W. Johnson, "Microstructure evolution during electroless copper deposition", IBM Journal of Research and Development archive, Vol. 28, No. 6, November 1984.

[6] D. Griffiths, "Introduction to Electrodynamics" 3rd ed. Upper Saddle River, New Jersey: Prentice Hall. 1999.

[7] MIL STD 883, " Test method Standard – Microcircuits", 2010.

[8] IPC 4552, "SPECIFICATION FOR ELECTROLESS NICKEL/IMMERSION GOLD (ENIG) PLATING FOR PRINTED CIRCUIT BOARDS", 2002.

[9] ASTM D3359-07, "Standard Test Methods for Measuring Adhesion by Tape Test."

[10] ASTM D2197-98, "Standard Test Method for Adhesion of Organic Coatings by Scrape Adhesion."

[11] ASTM D4541 - 09e1, "Standard Test Method for Pull-Off Strength of Coatings Using Portable Adhesion Testers."

[12] ASTM D903 - 98 "Standard Test Method for Peel or Stripping Strength of Adhesive Bonds", 2004.

[13] DIN EN 582, "Thermal Spraying - Determination of Tensile Adhesive Strength", 1994.

[14] DIN IEC 60326-2, "Printed Boards; Part 2: Test", 1992.

[15] Technical brochure, "Dage 4000: Advanced bond test solutions", Internet source: http://www.dage.de/download/bondtest/ser4000.pdf, accessed: 01-10-2010.

[16] Internet source: http://www.dfdinstruments.co.uk/GM01-6.3kN.htm, accessed: 01-10-2010.

[17] H. Willeck, W. Eberhardt and H. Kück, "A New Measuring Tool for Determining the Adhesive Strength of Micro Structured Metal Layers and Conductors Directly on Polymer Micro Devices", Conference proceeding, 7th international symposium polymer surface modification-relevance to adhesion, Orono, 2009.

[18] ASTM D3359 - 09e2 "Standard Test Methods for Measuring Adhesion by Tape Test."

[19] IPC TM 650, "TEST METHODS MANUAL."

[20] Internet source: http://www.imat.hsg-imit.de/fileadmin/hsg-imat/pdfs/aif12417.pdf, in German, accessed: 01-10-2010.

[21] Technical Brochure, "e-Cu: Check: Monitoring of electroless copper electrolyte of LPKF LDS® technology", Internet source: http://www.imat.hsg-imit.de/fileadmin/hsg-imat/pdfs/Flyer_eCuCheck.pdf, accessed: 01-10-2010.

Chapter 7. Demonstrators

This chapter explores some possible applications of LISA. Different patterns were printed on different substrates to demonstrate LISA's flexibility. Then, high frequency electrical components, e.g. antenna, waveguide, were manufactured by LISA and tested for their characteristics.

7.1 Patterns on several types of substrates

Obviously lasers can make patterns on a flat substrate, such as on a plate as shown in Figure 7.1. Using the existing YAG laser, a single track's width could be set from 0.2 mm to more than 1mm. The easiest way to make a wide area is to combine two or more single tracks together. The space between the closest tracks is approximately 50μm if using the existing Nd: YAG laser, as illustrated by picture (b) in Figure 7.1. The track pattern was set by software and several basic shapes as well as sizes were created, such as a helix, circle, ellipse, square, *etc*. Picture (a) in Figure 7.1 shows a coil shape.

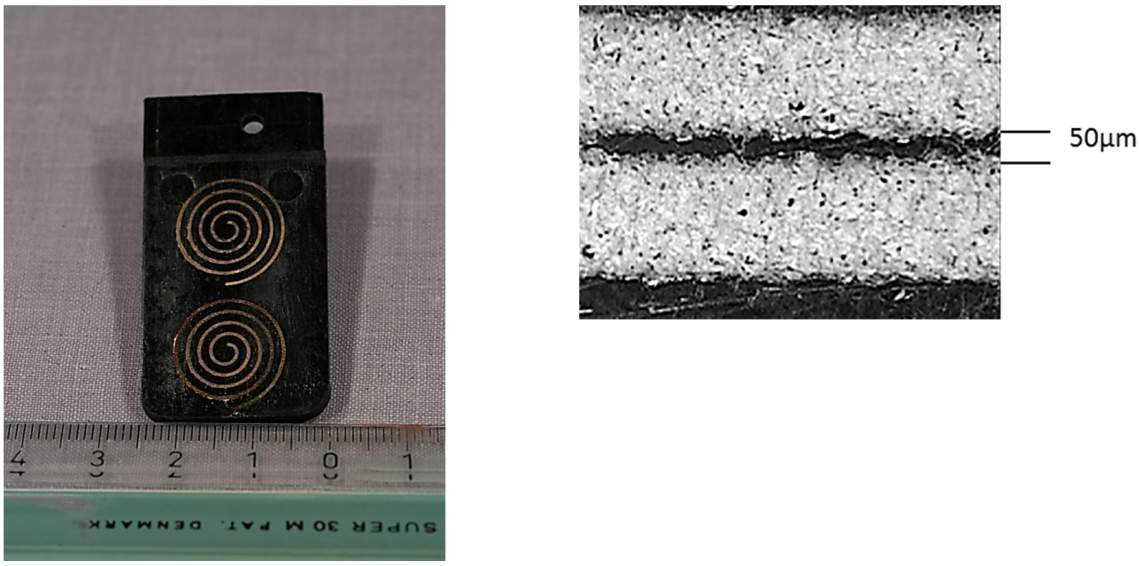

(a) (b)

Figure 7.1 Two samples made by LISA technology. The used YAG laser parameters are lamp current 18A, Q 1200 Hz, speed 60mm/s and wobble size 4. (a): a coil after plating on a flat injection molding PC substrate. The total length of the coil is approximately 130mm (b): two strait lines before plating on PC substrate. The space between the two tracks is approximately 50μm.

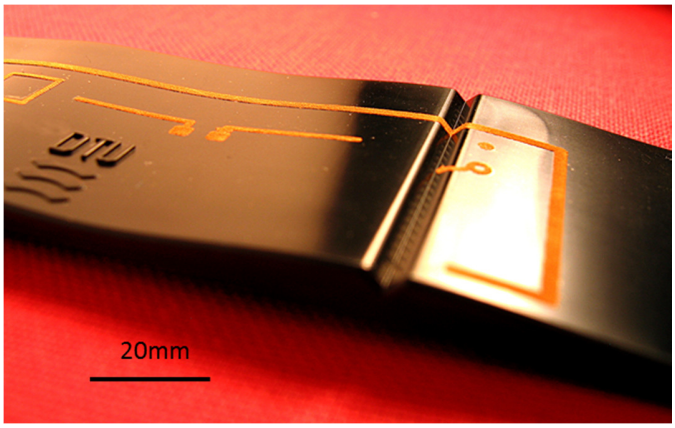

Figure 7.2 2.5D ABS substrate with plated laser tracks. They are plated by copper and gold layers.

For a substrate with height difference on the surface, e.g. a 2.5D substrate, LISA can also be applied. Figure 7.2 is from a demonstration sample with a 2.5 dimensional surface, plated by Cu, Ni and Au. A pattern can be made in a 120° V groove. When the height difference is within the focus length of the laser beam, or even slightly more than the focus length, the pattern can be drawn in one shot. If the height difference is a lot more than the focus range, or the workpiece shape is more than 2.5 dimensional, several shots are needed to accomplish the pattern; meanwhile high accuracy is required for the alignment system. Figure 7.3 shows a sample made by 2k injection molding, and the white and black color present two types of ABS. Three "v" shape laser patterns were drawn separately; for each of them the workpiece has to be tilted so that the wall of the white cylinder can be machined in one shot. However, the laser tracks on the wall are not plated well. A movable laser head or sample holder system is required to machine such a type of workpiece or a real 3D workpiece in one shot.

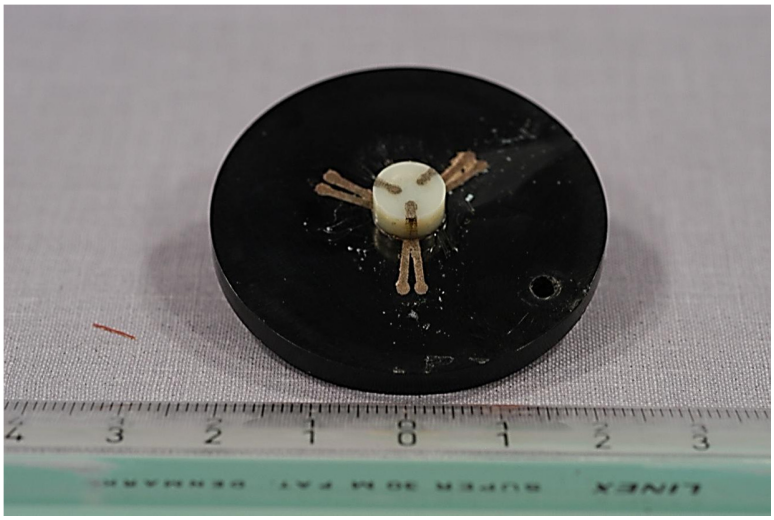

Figure 7.3 A workpiece made by 2 shot injection moulding. The three V shape patterns were made seperately. The workpiece was tilted when making each pattern. Each pattern was made by one shot laser patterning. After plating, the laser track on the wall is not fully plated.

7.2 Analysis of antenna prototypes

Antennas were chosen to be studied as an application case. Antennas transform guided waves into propagating waves and vice versa, therefore making them vital components in any wireless system.

The investigation can be broken down into the following stages:

- Is LISA a suitable technique for making antennas?
- What limitations does LISA impose on an antenna design?
- What are the differences between using LISA and commercial available techniques?

This section will first introduce a brief overview of network analyzer measurement techniques. Two prototypes of antenna made by LISA will be compared with theoretical calculation or alternative techniques. This work is collaborated with the Department of Electrical Engineering, DTU. All the measurement and relative analysis to the antenna prototypes was performed by Mater student F. Cheng as part of his special course work [1].

7.2.1 Simulation of the influence from roughness

When comparing the various techniques that are currently used, such as PCB or 2-shot-injection molding, there is one difference between the final product of LISA and the final product of all other techniques, namely the roughness of the metallic tracks. To see whether the roughness of the tracks have significant influence on the high frequency behavior of the products, a series of simulations were carried out.

The simulations were carried out with an Arbitrary Transmission Line Calculator available for free online. For the simulations, a microstrip was designed with the following specifications

- Line width: 3 mm.
- Substrate height: 1 mm.
- Substrate ε_r: 2.5.

Using formulas from [1] with width/height > 1,

- ε_{eff}: 2.09
- Z_o: 48.5Ω

To simulate line roughness, a sine-shaped approximation is applied to the surface, where the mean of the oscillation is taken at the top of the smooth line, and the amplitude of the oscillation is the height of the smooth line.

When setting up the simulation, the program only considers relative size, therefore the line (red) width was set to 400px and the substrate (yellow) height was 133px. The entire structure is 1600x1000 pixels across, with the green line representing the ground. Simulation results can be seen in Table 7.1.

The simulation program is able to calculate the characteristic impedance, Z_o (Ohm), capacitance, C (pF/m), and inductance, L (nH/m) of the microstrip line. Also, it is able to calculate the electric field intensity of the given structure. From the results, it can be seen that both impedance results agree quite well with the predicted result, but, more importantly, they agree with each other. Also, looking at the capacitance and inductance of the lines, there is almost no difference between the smooth and rough lines.

Table 7.1 simulation of the effect from roughness

Smooth	Rough
Z_o = 46.20 Ω; C = 103.6 pF/m; L = 221.1 nH/m	Zo = 45.63 Ω; C = 104.9 pF/m; L = 218.3 nH/m
Electric Field – x component 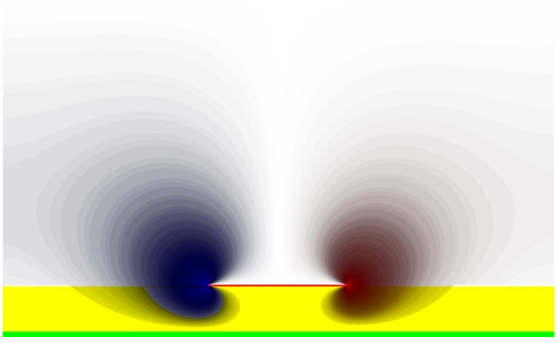	Electric Field – x component 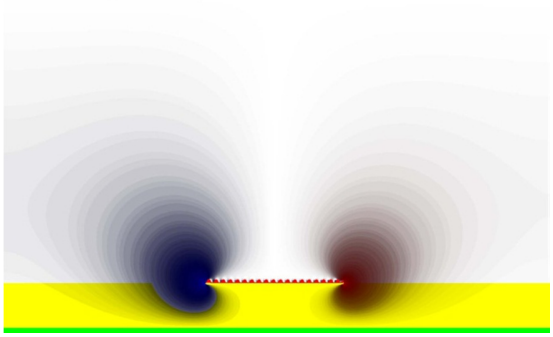
Electric Field – y component 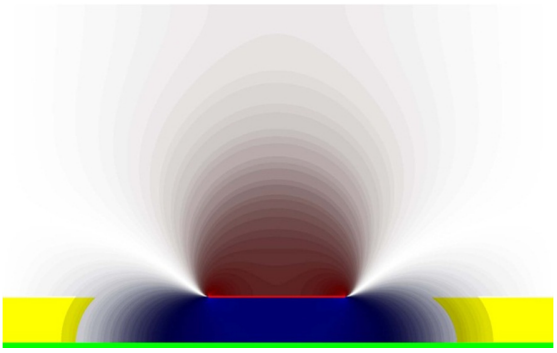	Electric Field – y component 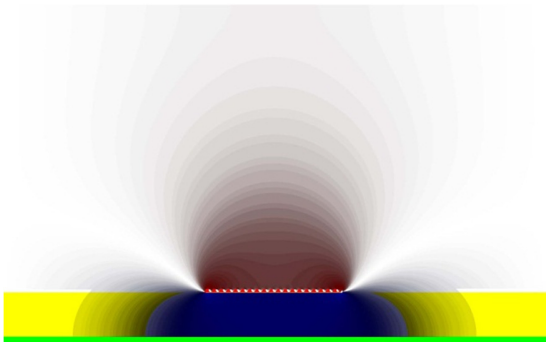

When studying the field lines, with the red and blue lines representing positive and negative voltages respectively, the field distributions also agree quite well with each other, although the smooth line's fields seem to be slightly stronger than the rough line's fields. The simulation suggests that surface roughness has no significant influence on the device's performance.

7.2.2 Measurement Techniques

This section gives an introduction to the measurement techniques used in the investigation. Single-ended and differential measurements are compared, a measurement technique to obtain the quality factor of the antenna is discussed, and a pseudo-differential measurement technique is presented.

7.2.2.1 Single-Ended and Differential Measurements

Single-ended measurements are a form of single-ended signaling, which is the simplest, and most commonly used method of transmitting electrical signals over wires. In such a system, one wire will carry the information, normally in the form of an electrical voltage, and the other wire is connected to a reference voltage, usually the ground. This is a very simple system, and also one that requires few wires. If there are n signals, only (n+1) wires are required – one for each signal and another one for the ground.

A different technique is differential signaling, which requires a pair of wires for each signal transmission. The two wires have equal impedances to the ground, and the signal carried is interpreted differentially, meaning the information lies within the differences between the two signals [3]. This method has the advantage of high noise rejection, as any unwanted influence will likely affect the two wires equally and the difference remains the same, as illustrated by Figure 7.4. Note that this does not reduce the effect of noises that affect the two wires differently, e.g. thermal noise.

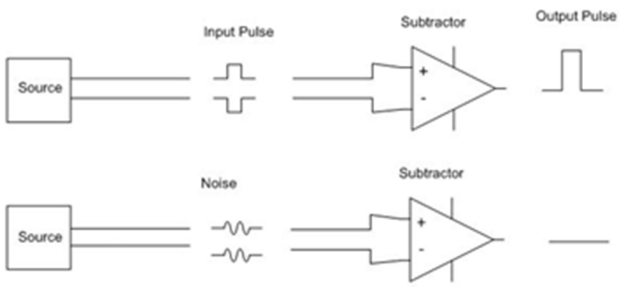

Figure 7.4 the common noise cancelling effect of differential measurement

7.2.2.2 Quality Factor Measurements

To obtain the quality factor, a single-ended probe with a wire structured similar to the antenna is connected to the vector network analyzer, and the reflection coefficient is monitored. By bringing the antenna close to the structure and varying its position, the coupling between the two loops is varied, and this has an effect on the antenna resistance's magnitude when referred to the probe's side. Eventually, this referred resistance will form a good match to the vector network analyzer's input impedance, and by recording the match frequency and the frequencies at which the reflection coefficient is at -7dB, the quality factor may be calculated as Equation 7-1 [4]:

$$Q = \frac{f_{match}}{f_{-7dB\_upper} - f_{-7dB\_lower}}$$

Equation 7-1

7.2.3 Prototyping I – Planar Antennas

To put theory into practice, two types of antennas were manufactured with LISA: a planar dipole and a planar square loop. These two structures were selected due to the simplicity of their design. This section will present the design and manufacturing process of these two types of antennas, followed by a look at its measurement results and a discussion of these results. Some failed manufacturing attempts will also be outlined.

7.2.3.1 Design and Manufacturing

The dimensions of the design were limited by factors such as substrate size and availability. For this series of prototypes, a PBT/PET substrate (Pocan® TP 500-002, 40% glass fiber) with a height of 2mm was used. Note that the electrical data of this polymer grade was unavailable, but based on the other grades in the same series; a good estimate of its relative permittivity is 3.5. This material was chosen mainly as it has a high melting point, thus allowing soldering to take place with relative ease.

Nd: YAG laser was used to draw the desired pattern. Soldering pads were also printed at the end of arms to ease the measurement process. Activated by the new activation bath, it was first plated by electroless copper bath for 0.5 hour and then by electroplating the copper bath to a thickness of approximately 35µm.

The finished dipole and loop are shown in (a) and (b) of Figure 7.5 respectively. The dimensions are marked on the pictures.

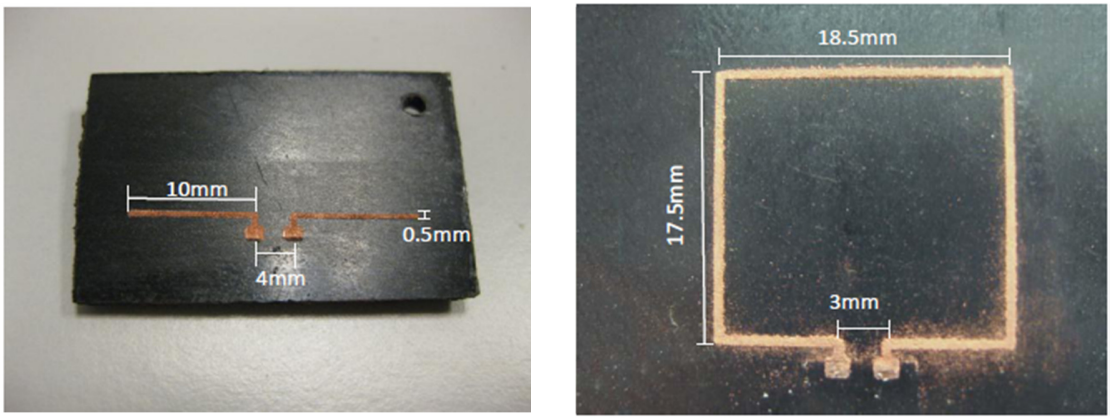

(a) (b)

Figure 7.5 Antanna manufactured using LISA, on PBT/PET (a) Dipole antenna (b) Loop antenna

It can be seen in Figure 7.5 (b) that there are speckles of copper spread around the antenna line, and those are copper deposited due to the insufficient rinsing.

Lastly, a printed dipole was manufactured on FR4 PCB using PCB etching (Figure 7.6) to compare the LISA dipole to a more mature technique. Note that the dimensions are same as that made from LISA and the material FR4 PCB has a relative permittivity of 3.7, which is quite close to the estimate of PBT/PET.

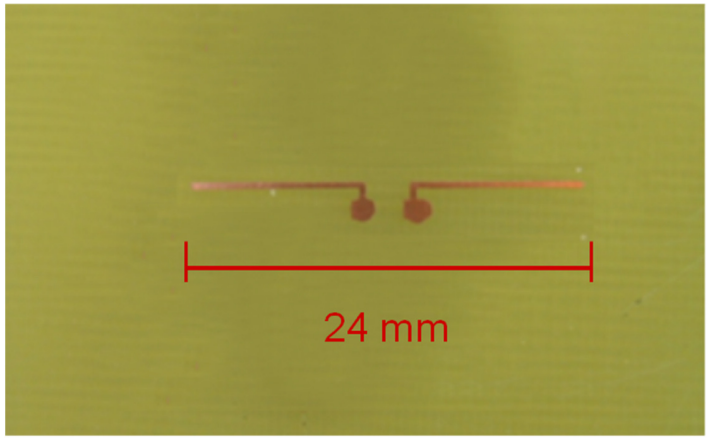

Figure 7.6 Dipole antenna manufactured using PCB etching technology, on substrate of FR4

7.2.3.2 Frequency theoretical prediction

To predict the resonance frequencies of the antennas manufactured, the antenna resonance frequency in free space would be predicted first. Then, because the antennas are being heavily loaded by the substrate, the frequency will be down-scaled according to the relative permittivity of the material.

The dipole has a total length of 24mm, which means its half wave resonance would occur at

$$\frac{3\times10^{8}\,m/s}{2\times24\times10^{-3}\,m}=6.25GHz$$

With a relative permittivity of 3.5, the resonance frequency of the manufactured dipole is expected at

$$\frac{6.25\times10^{9}\,GHz}{\sqrt{3.5}}=3.34GHz$$

The free space resonance of the loop is slightly more difficult to predict with a simple formula, therefore it was simulated in WIPL-D.

The calculated input impedances are plotted in Figure 7.7 and Figure 7.8, with the latter figure having a smaller impedance range. Ignoring the anti-resonance just beyond 2GHz, the first resonance is spotted at 4.8GHz. Taking dielectric loading into account, the expected loop resonance is

$$\frac{4.8\times10^{9}\,GHz}{\sqrt{3.5}} = 2.57GHz$$

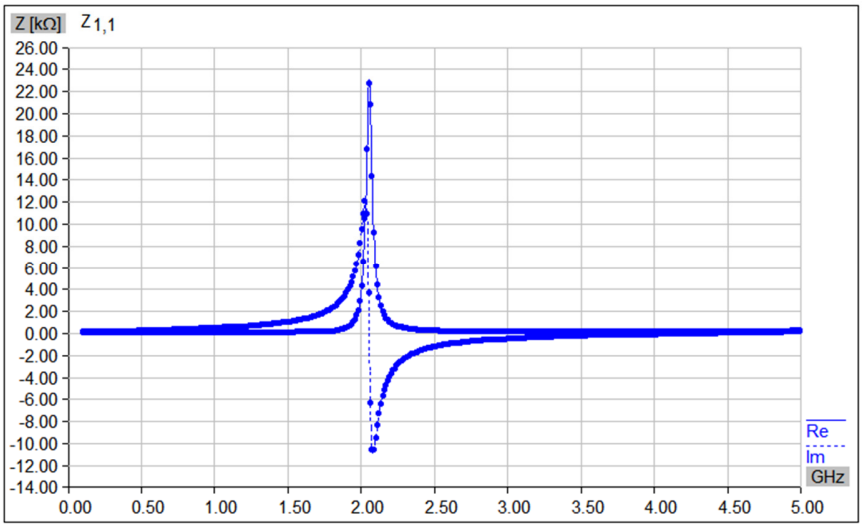

Figure 7.7 Simulated input impedance of loop antenna in free space

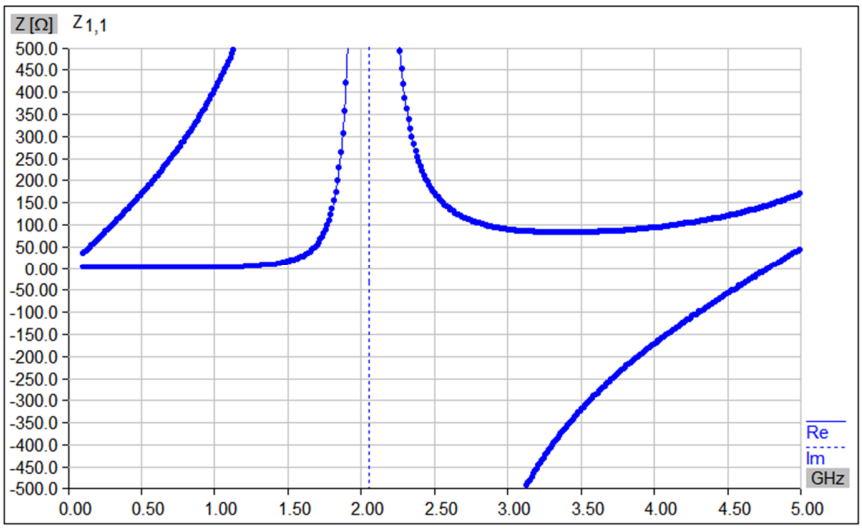

Figure 7.8 Simulated input impedance of loop antenna in free space (zoomed in)

7.2.3.3 Imepedance measurement of LISA Dipole

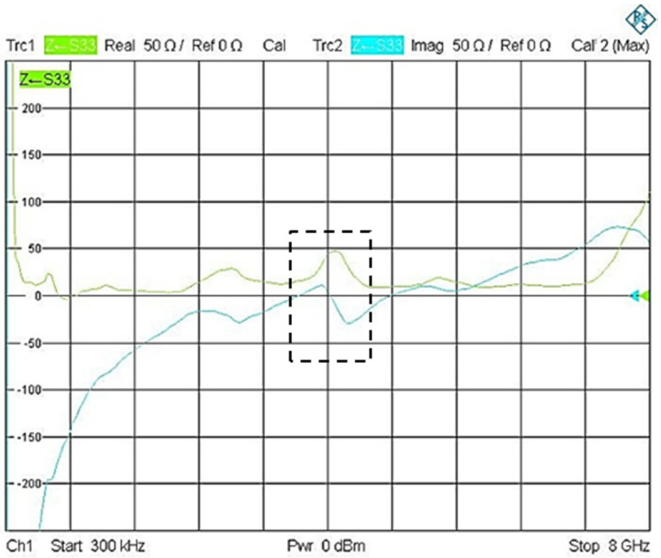

Figure 7.9 Measured input impedance (Real and Imaginary) of LISA dipole antenna (300 kHz – 8GHz), the highlight part is zoomed in in Figure 7.10 to show characteristic values.

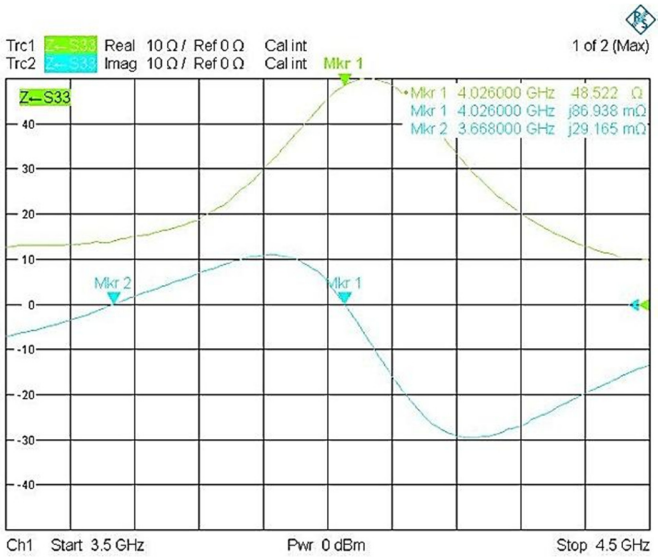

Figure 7.10 Measured input impedance (real and Imaginary) of LISA dipole antenna (3.5GHz-4.5GHz).

The dipoles were measured differentially using a differential probe, and the impedances measured were converted from S parameter measurements.

The full frequency range dipole input impedance shown in Figure 7.9 shows many characteristics expected from a dipole. At DC, the real part (green) is infinite, and at lower frequencies, the imaginary part (blue) indicates the dipole is capacitive. The half wave frequency is noted in Figure 7.10 as 3.68 GHz, which is quite close to the predicted 3.34 GHz. At the following anti-resonance, the real part is measured to be at 48.5 Ohm, which can act as a very good match.

7.2.3.4 Impedance measurement of PCB Dipole

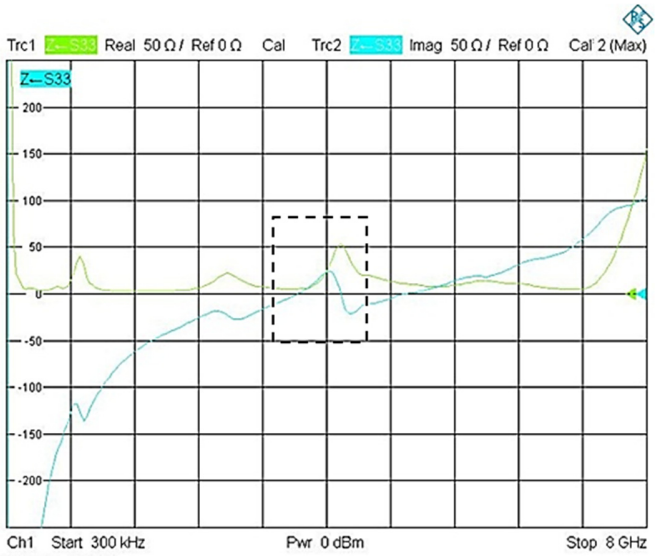

Figure 7.11 Measured input impedance (Real and Imaginary) of PCB dipole antenna (300 kHz – 8GHz), the highlight part is zoomed in in Figure 7.12 to show characteristic values.

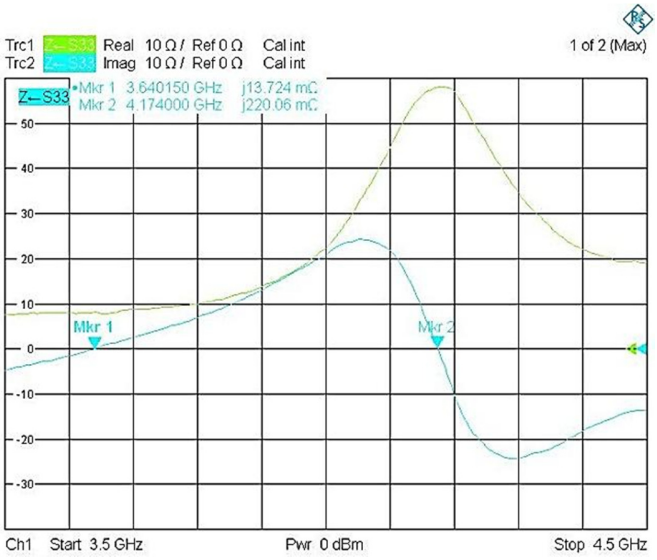

Figure 7.12 Measured input impedance (Real and Imaginary) of PCB dipole antenna (3.5 GHz – 4.5 GHz)

The full frequency impedance shown in Figure 7.11 is very similar to that of the LISA dipole. This indicates LISA is a very feasible antenna manufacturing technique. The half-wave resonance is read off Figure 7.12 to be 3.64 GHz, which is very close to the LISA dipole. If it is assumed that the relative permittivity of the PBT/PET used is 3.7, then antennas made by LISA and PCB etching, display almost no difference. However, it may also be concluded that there is a certain difference between the antennas made by LISA and PCB etching, but that difference was negated by the difference in the substrate relative permittivity.

7.2.3.5 Measurement of LISA loop

The loop was measured via a loose coupling. A copper wire was bent into a shape that resembles the loop antenna and soldered onto a single ended probe. Then the probe's loop is brought close to the loop antenna. The reflection coefficient would dip at the resonance frequency of the loop antenna when the coupling matches the real impedances of the two loops. There may also be some de-tuning due to the probe loop, but that will not be investigated in this project.

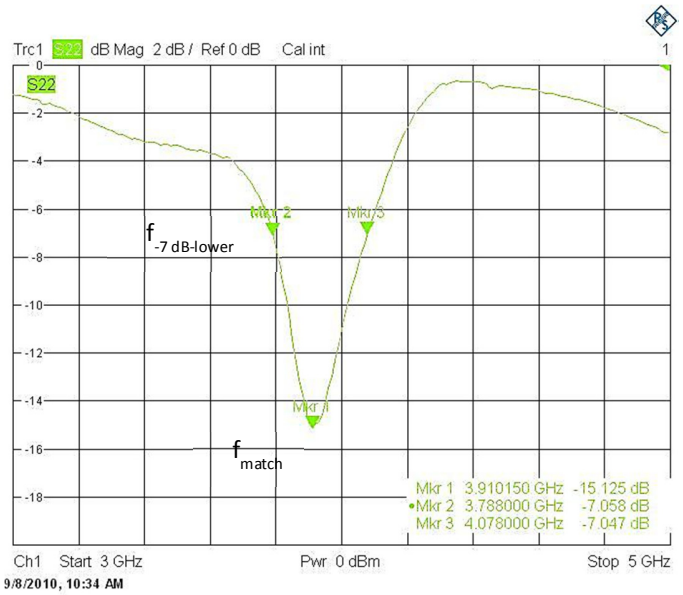

Figure 7.13 Measured reflection coefficient of the LISA loop via proximity coupling

From the measurement result displayed in Figure 7.13, the resonance of the loop antenna is determined to be at 3.91 GHz. This indicates the substrate does not load the loop as heavily as it loaded the dipole. From the -7dB measurements, according to Equation 7-1, the Q of the loop is determined to be

$$\frac{3.910GHz}{4.078GHz - 3.788GHz} = 13.5$$

7.2.4 Prototype II – Co-Planar Stripline

Previous prototypes demonstrated that LISA was well suited to manufacture planar antennas. This section describes another type of prototype, namely a co-planar stripline.

7.2.4.1 Design and Manufacturing

In a same manner as the design and manufacturing process of the first set of prototypes, the dimensions are only confirmed once the prototype has been manufactured. In this case, the manufactured co-planar stripline is shown in Figure 7.14. PC (Lexan 500R, 10% glass fiber) is used as substrate, and the relative permittivity is 2.8.

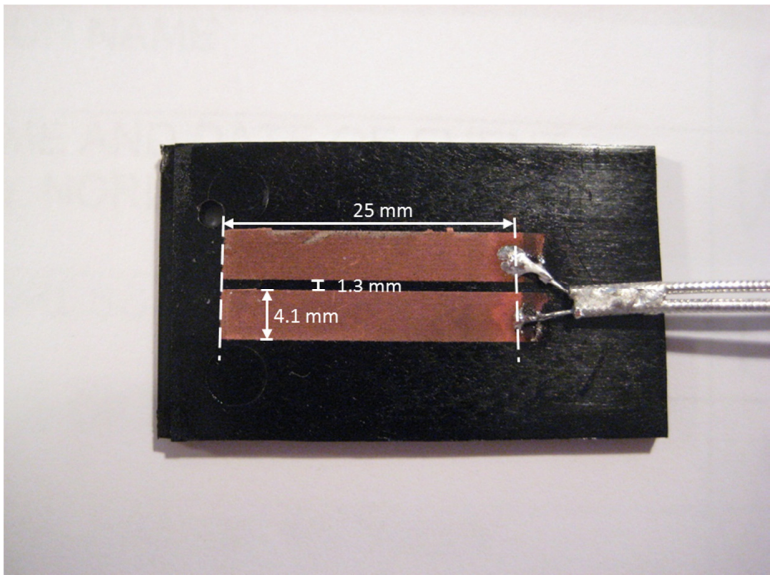

Figure 7.14 LISA co-planar stripline with differential probe

7.2.4.2 Theoretical prediction of the frequency

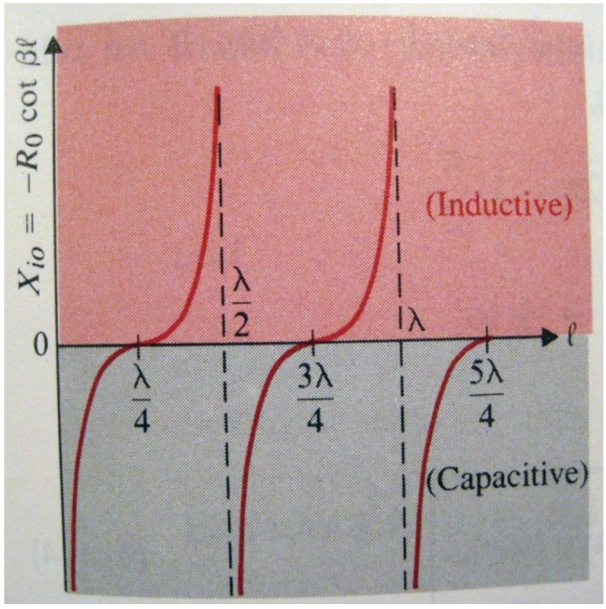

Figure 7.15 Input reactance of ideal transmission line [5]

With an open transmission line, the reactance is expected to follow a co-tangent curve with increasing length, as demonstrated in Figure 7.15[5]. The first zero crossing occurs at quarter wavelength, and given the current line length of 25mm, the frequency of the first crossing is

$$\frac{3\times10^{8}\,m/s}{4\times25\times10^{-3}\,m}=3GHz$$

Taking substrate loading into consideration again, the frequency becomes

$$\frac{3.0\times10^{9}\,GHz}{\sqrt{2.8}}=1.79GHz$$

7.2.4.3 Measurements

Because the line is inherently balanced, a balanced probe is used to measure the line with a differential measurement. The probe is calibrated to the reference plane at the tip of the inner conductors, therefore the length measurement started from there also.

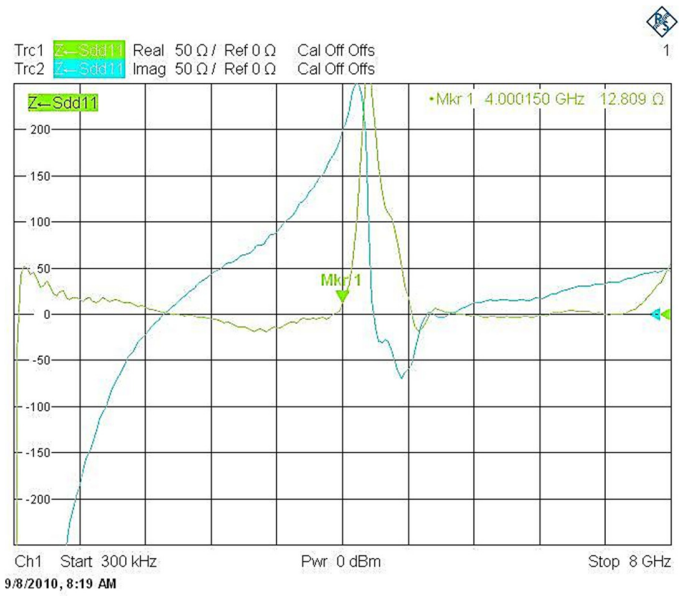

Figure 7.16 Measured input impedance of LISA co-planar stripline (300 KHz – 8 GHz)

The measurement displayed in Figure 7.16 shows that the line exhibits the pattern expected of a transmission line from DC to the frequency at which the line is about half wavelength. The quarter wavelength can be read off the measurement file, and it is 1.84 GHz. This is quite close to the predicted 1.79 GHz.

However, note that the measurement is far from precise, as the real part of the impedance displayed negative values at places. Beyond the point where the line is half wavelength, the measurement is incomprehensible. Also, it was because of measurement difficulties that the input impedance of the line while shorted could not be obtained. Had that been possible, the characteristic impedance of the line could be calculated.

7.2.4.4 Conclusion

This chapter shows demonstrators using LISA technology.

Firstly LISA was proved to be able to make patterns on 2D, and 2.5D substrate. The dimensions of the substrate are limited by the laser head or sample holder system.

The following content documented the study of using LISA to manufacture antennas and transmission lines. Prototypes of antennas and transmission lines were manufactured and measured. Two simple antenna shapes, the planar dipole and (the) planar loop were studied, and a co-planar stripline was also studied. It can be concluded that the antennas made by LISA exhibited impedance characteristics expected from the respective antenna shapes. Also, the frequency of operation of the dipole agreed with the predicted frequency, and matched that of a dipole manufactured with traditional PCB etching techniques. The Q of the loop antenna was also measured to demonstrate that the loop antenna constructed by LISA could be probed using traditional techniques.

The co-planar transmission line exhibited good input reactance characteristic from DC to the frequency at which it is roughly half wavelength. The quarter wavelength resonance point was also quite close to prediction.

7.2.4.5 Future Work

There are many areas that desire improvement, for example a better substrate could be selected for the LISA manufacturing process, and the differential measurement carried out to characterize the co-planar stripline could be improved.

Also, additional high frequency components could be studied in the future. Fractal shapes for antennas could be manufactured to take advantage of LISA's flexibility, and baluns can be printed onto the substrate with the component. Co-planar waveguides, microstrips, slot transmission lines are also examples of what can be investigated in the future.

Reference

[1] F. Cheng, special course report (to be filed), "synthesis of antenna - a comparison between laser induced selective activation and current techniques", Department of Electrical Engineering, DTU 2010.

[2] D. M. Pozar, "Microwave Engineering", 3rd Ed. Wiley, 2005.

[3] A. R. Hambley, "Electrical Engineering", 3rd Ed. Pearson, 2005.

[4] F. Cheng, "Efficiency Analysis of Miniaturized Antenna", Bachelor Thesis, DTU, 2009.

[5] D. Cheng, "Field and Wave Electromagnetics", 2nd Ed. 1989.

[6] Product datasheet, X-Pocan, Product range with reference data, LANXESS DEUTSCHLAND GMBH.

Chapter 8. Summary and Outlook

This thesis presents the experimental work and analysis for the PhD project "laser induced selective activation (LISA) for subsequent autocatalytic electroless plating".

In the beginning of the thesis, LISA is introduced briefly. LISA is a new MID technology for selective plating on polymer substrates. Lasers (Nd: YAG laser, UV laser, fiber laser, *etc.*) are used to draw the desired patterns on a polymer substrate in the medium of distilled water, then after $PdCl_2/SnCl_2$ activation and water rinsing, autocatalytic electroless plating will only take place on the laser machined area. Compared with some leading technologies in MID fields, LISA has economic and environmental advantages. Then the main laboratory set-up for the project is described.

The following chapters study LISA from three aspects:

1. The activation mechanism

A $PdCl_2/SnCl_2$ activation system is used to activate the laser track. The working principle and the structure of the activation colloids are explored by literature study. Then three hypotheses were proposed to discuss how the activation colloids are retained by the laser track. The conclusion is that there are multiple mechanisms. Firstly the laser track has a stronger attraction to the activation solution than to water, which explains why after rinsing by water, activation solution can still be leaft on the laser track. Secondly a model using diffusion theory is built, and it is proven that the porous structure prevents the activation colloids rinsing away. So when the rinsing time is not excessively long, there are still colloids left in the porous structure. Thirdly, chemical bonding between the activation colloids and the laser track is not excluded though no evidence is found so far.

In future work, the mechanism can be explored further. For example, more polymers should be tested for the attraction strength using surface tension components. Also for the diffusion behavior analysis, an improved structure description is needed, so more parameters for the effective diffusivity can be obtained.

2. Optimization work on the laser machining process

First, the laser set up which can lead to LISA surface is introduced, for Nd: YAG, UV and fiber lasers. The LISA surface is compared with failed surfaces by using microscope pictures. Secondly, the formation reasoning of the structure is discussed. YAG laser's parameters are studied. It is concluded that the repetition number of the pattern has the least influence on the laser track's structure; however, the pass has to be repeated sufficiently to make the laser track continuously porous. The structure of the laser track will not be influenced by the beam's incidence angle significantly within 14°. Pictures illustrate the laser tracks suitable and unsuitable for plating. The laser track's height increases with the laser power input. Finaly the

bearing area curve and its parameters are proposed to describe porous structure and it is proved to be feasible.

Two hypotheses are proposed for future work. The first one is that the porous structure formed in the laser process is due to the rapid solidification of the melt polymer when the surface absorb laser energy and gets cooled down by surrounding water. It is described in chapter 3 and a thermal effect model is used to simulate the temperature distribution for a single point. More simulation work using finite element analysis based on polymer fluid mechanics theory is required. The movement of the laser beam will be considered, and finally the deformation of the substrate will be integrated. The other hypothesis is that the structure can be described mathematically. To accomplish this, the focus will be put on how the porosity and pore size change when it goes deeper into the laser machined area.

3. Optimization work on the plating process

In the beginning the preparation of the two activation baths are introduced, and they are compared to the plating velocity. It is believed that the so-called “new activation” can lead to faster plating and the resulted coating is continuous and compact. Also, the plating quality on the laser track is presented by conductivity, roughness, and adhesive property. It is concluded that the porous and continuous laser structure is the key factor for fast plating and strong adhesion. The plating velocity is independent of the height of the laser track, as long as the structure is sponge-like and continuous. More laser energy input favors stronger adhesion but it should not be excessive.

In future work, effort should be made on the standardization of the activation and plating process, for example, the rinsing time should be specified. In the lab condition, using beakers, a rack can be built to carry 3-5 pieces of samples, and tunable ultrasonic bath equipment may be an option for the rinsing step.

At the end of the thesis, demonstrators using LISA are displayed. Firstly LISA is shown to be able to make patterns on a 2.5D workpiece. Then LISA was used to manufacture antennas. The main conclusions drawn from the measurement and analysis are:

- LISA can be used to manufacture antennas and other high frequency electrical devices, e.g. a co-planar stripline.
- Simulations have shown that surface roughness have little influence on microstrips.
- Antenna made by LISA had very similar characteristics compared to that of an antenna made by PCB etching
- In future work, more applications should be found out. Cooperation with industrial companies is an option. Meanwhile, some simple electrical devices made in the lab are also feasible and necessary to display LISA.

Appendix 1. Material grades and main polymers datasheets

The grades of all the polymers used in experiments are shown in the table of material list, followed by PC and PBT/PET's datasheets.

Materials list

PE (good)	Unknown	
PE (bad)	Lupolen 5031	
PS	Basf Kr2795	
PC	Lexan 500R,	10% glass fibre
PC	Lexan 920a	
ABS	Terluran GP35	
Green ABS	Unknown	From Lego®
PBT/PET	Pocan TP550	40% glass fibre
PMMA	Unknown	
SAN	Luran 378p	
PEI	Ultem1000	Amber colour, then mixed with carbon black to have the black colour
PEEK	Victrex 150GL30	30% glass fibre
Polyphenyleneether blend	GFN1520V	20% glass fibre

PC Lexan 500R Polycarbonate, 10% glass fiber.

Physical Properties	Metric	English	Comments
Specific Gravity	1.27 g/cc	1.27 g/cc	ASTM D 792
Density	1.245 g/cc	0.04498 lb/in³	ASTM D 792
Water Absorption	0.120 %	0.120 %	24 hrs; ASTM D 570
Water Absorption at Saturation	0.310 %	0.310 %	ASTM D 570
Linear Mold Shrinkage, Flow	0.00200 - 0.00400 cm/cm	0.00200 - 0.00400 in/in	SABIC Method
	@Thickness 3.20 mm	@Thickness 0.126 in	

Melt Flow	7.50 g/10 min	7.50 g/10 min	ASTM D 1238
	@Load 1.20 kg,	@Load 2.65 lb,	
	Temperature 300 °C	Temperature 572 °F	
Mechanical Properties	**Metric**	**English**	**Comments**
Hardness, Rockwell M	85.0	85.0	ASTM D 785
Hardness, Rockwell R	124	124	ASTM D 785
Tensile Strength at Break	55.0 MPa	7980 psi	Type I, 5 mm/min; ASTM D 638
Tensile Strength, Yield	66.0 MPa	9570 psi	Type I, 5 mm/min; ASTM D 638
Elongation at Break	15.0 %	15.0 %	Type I, 5 mm/min; ASTM D 638
Elongation at Yield	8.00 %	8.00 %	Type I, 5 mm/min; ASTM D 638
Flexural Modulus	3.44 GPa	499 ksi	1.3 mm/min, 50 mm span; ASTM D 790
Flexural Yield Strength	103 MPa	14900 psi	1.3 mm/min, 50 mm span; ASTM D 790
Izod Impact, Unnotched	21.36 J/cm	40.02 ft-lb/in	ASTM D 4812
	@Temperature 23.0 °C	@Temperature 73.4 °F	
Tensile Impact Strength	157 kJ/m²	74.7 ft-lb/in²	Type S; ASTM D 1822
Falling Dart Impact	101 J	74.5 ft-lb	ASTM D 3029
Taber Abrasion, mg/1000 Cycles	11.0	11.0	CS-17, 1 kg; ASTM D 1044
Izod Impact,	1.06 J/cm	1.99 ft-lb/in	ASTM D 256

Notched	@Temperature 23.0 °C	@Temperature 73.4 °F	
Electrical Properties	**Metric**	**English**	**Comments**
Volume Resistivity	>= 1.00e+17 ohm-cm	>= 1.00e+17 ohm-cm	ASTM D 257
Dielectric Constant	3.05	3.05	ASTM D 150
	@Frequency 1.00e+6 Hz	@Frequency 1.00e+6 Hz	
	3.10	3.10	ASTM D 150
	@Frequency 50.0 - 60.0 Hz	@Frequency 50.0 - 60.0 Hz	
Dielectric Strength	17.7 kV/mm	450 kV/in	In air; ASTM D 149
	@Thickness 3.20 mm	@Thickness 0.126 in	
Dissipation Factor	0.000800	0.000800	ASTM D 150
	@Frequency 50.0 - 60.0 Hz	@Frequency 50.0 - 60.0 Hz	
	0.00750	0.00750	ASTM D 150
	@Frequency 1.00e+6 Hz	@Frequency 1.00e+6 Hz	
Arc Resistance	<= 60.0 sec	<= 60.0 sec	Tungsten; PLC Code 7; ASTM D 495
Comparative Tracking Index	175 - 250 V	175 - 250 V	UL 746A
Hot Wire Ignition, HWI	60.0 - 120 sec	60.0 - 120 sec	PLC 1; UL 746A
High Amp Arc Ignition, HAI	<= 15.0 arcs	<= 15.0 arcs	Surface; UL 746A
High Voltage Arc-Tracking Rate, HVTR	>= 150 mm/min	>= 5.91 in/min	PLC 4; UL 746A
Thermal Properties	**Metric**	**English**	**Comments**
CTE, linear	32.4 µm/m-°C	18.0 µin/in-°F	Flow; ASTM E 831

	@Temperature -40.0 - 95.0 °C	@Temperature -40.0 - 203 °F	
Specific Heat Capacity	1.21 J/g-°C	0.289 BTU/lb-°F	ASTM C 351
Thermal Conductivity	0.200 W/m-K	1.39 BTU-in/hr-ft²-°F	ASTM C 177
Deflection Temperature at 0.46 MPa (66 psi)	146 °C	295 °F	Unannealed; ASTM D 648
	@Thickness 6.40 mm	@Thickness 0.252 in	
Deflection Temperature at 1.8 MPa (264 psi)	142 °C	288 °F	Unannealed; ASTM D 648
	@Thickness 6.40 mm	@Thickness 0.252 in	
Vicat Softening Point	154 °C	309 °F	Rate B/50; ASTM D 1525
UL RTI, Electrical	130 °C	266 °F	UL 746B
UL RTI, Mechanical with Impact	130 °C	266 °F	UL 746B
UL RTI, Mechanical without Impact	130 °C	266 °F	UL 746B
Flammability, UL94	V-0	V-0	UL 94
	@Thickness 1.52 mm	@Thickness 0.0598 in	
	5VA	5VA	UL 94
	@Thickness 3.04 mm	@Thickness 0.120 in	
Oxygen Index	36.0 %	36.0 %	ASTM D 2863
Descriptive Properties			
CSA File Number	LS88480		CSA LISTED
Radiant Panel Listing	YES		UL Tested
UV-light, water exposure/immersion	F2		UL 746C

PBT/PET LanXess Pocan TP550-002

	Test Condition	Unit	Standard	Value
Rheological property				
Melt volume-flow rate, (MVR)	280℃; 2.16kg	Cm^3/(10min)	ISO 1133	10
Molding shrinkage, parallel	60x60x2; 280℃/WZ 80°C; 600bar	%	ISO 294-4	0.1
Molding shrinkage, perpendicular	60x60x2; 280℃/WZ 80°C; 600bar	%	ISO 294-4	0.6
Shrinkage, parallel	60x60x2; 150℃; 1h	%	ISO 294-4	0.1
Shrinkage, perpendicular	60x60x2; 150℃; 1h	%	ISO 294-4	0.1
Mechanical property (23℃/50%r.F.)				
Zug module	1mm/min	MPa	ISO 527-1,-2	10600
Tensile Stress at break	5mm/min	MPa	ISO 527-1,-2	108
Tensile Strain at break	5mm/min	%	ISO 527-1,-2	1.6
Izod impact strength	23℃	kJ/m^2	ISO 180-1U	32
Bending module	2mm/min	MPa	ISO 178	10500
Bending strength	2mm/min	MPa	ISO 178	160
Flexural strain	2mm/min	%	ISO 178	2.0
Thermal Features				
Melting temperature	10 ℃/min	℃	ISO 11357-1,-3	255
Distortion temperature	1.80 MPa	℃	ISO 75-1,-2	210
Distortion temperature	0.45 MPa	℃	ISO 75-1,-2	250
Vicat softening temperature	50N, 120℃/h	℃	ISO 306	220

Linear Thermal expansion coefficient, parallel	23 -55℃	10-4/K	ISO 11359-1,-2	0.15
Linear Thermal expansion coefficient, perpendicular	23 -55℃	10-4/K	ISO 11359-1,-2	0.55
Other Features (23℃)				
Density		kg / m³	ISO1183	1700
Glass fiber		%	ISO 3451-1	40

Appendix 2. Equipment list

Hot press machine

To make thin plastic foils, a small piece of injection-molded plastic is put between 2 steel plates. Then the plastic piece is pressed under certain pressure and temperature. The temperature should be set lower than the melting temperature of the tested polymer. To obtain foils with uniform thickness, it is recommended that the pressure should be increased step by step (e.g. 100 bars for each step) until 400-500 bars, and kept for 30-45 minutes. Since the thickness of the desired foils is not a crucial condition for the study, no technical datasheet of the equipment is attached here.

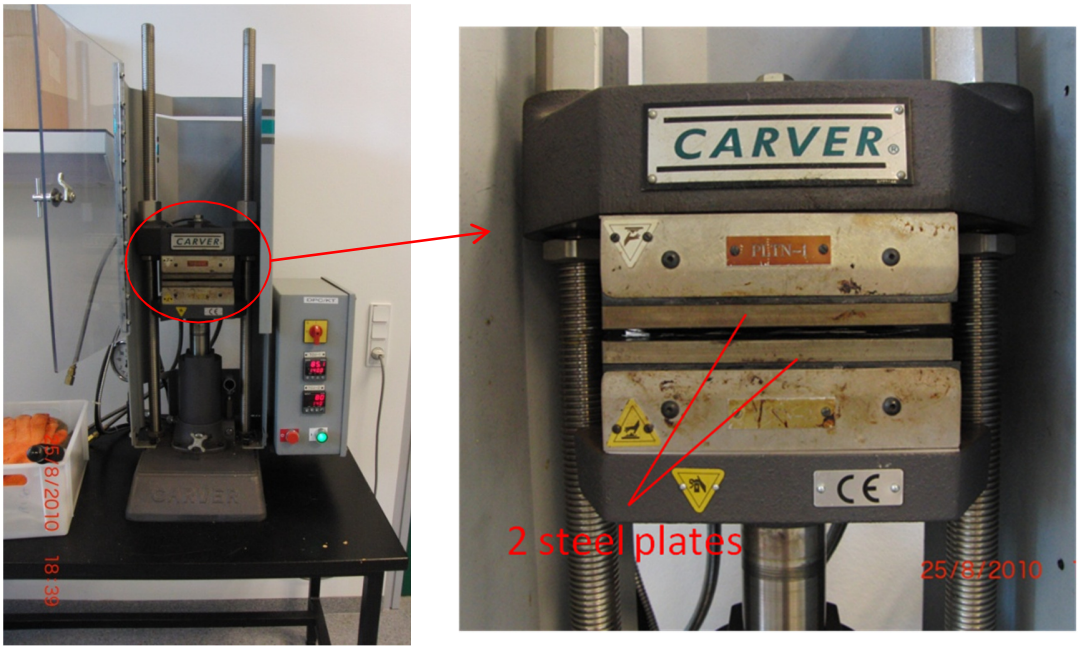

Figure 2.1 (left) the hot embossing equipment; (right) the steel plates

XPS spectroscopy

X-ray photoelectron spectroscopy (XPS) spectra are obtained by using a beam of X-rays to irradiate a substrate surface, simultaneously the kinetic energy and number of electrons that escape from the top 1 to 10 nm of the material is analyzed [1]. Figure 2.2 shows the appearance of the equipment and the general working principle.

The Thermo Scientific K-Alpha from has calibration standards built into the sample stage, including copper, silver and gold, which are used to calibrate the energy scale [2]. The calibration method is described in ISO standard [3]. However the specific calibration information for the utilized instrument is not available.

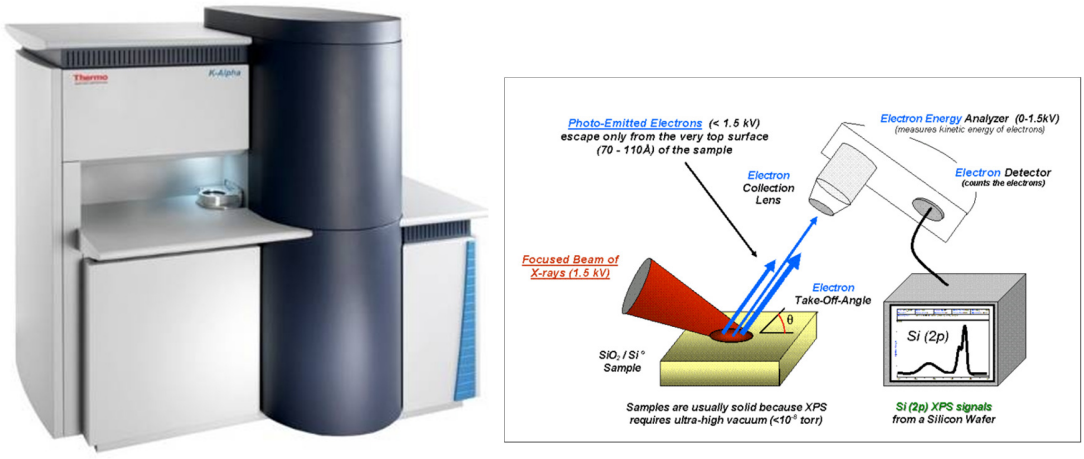

(a) (b)

Figure 2.2 (a) K-Alpha Thermo Scientific X-ray Photoelectron Spectrometer (XPS) system Error! Reference source not found. **(b) Work principle for general XPS instrument [4]**

Alicona InfinteFocus®

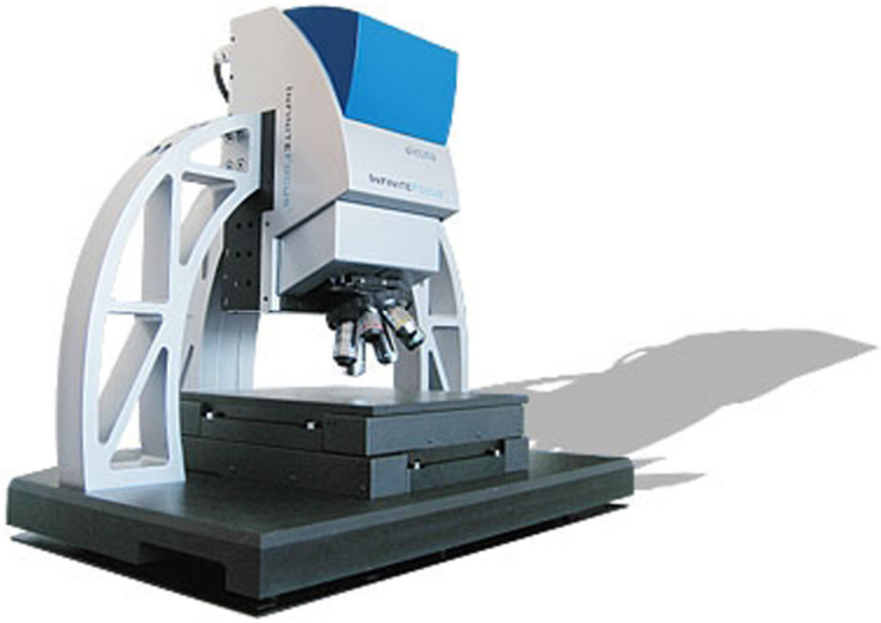

Figure 2.3 Alicona InfiniteFocus®

The principle of the InfiniteFocus® measuring is based on the technology Focus-Variance developed by Alicona, as illustrated by Picture (a) in Figure 2.4. The Focus-Variance method has been added to upcoming ISO standards.

The measuring system is composed of a sensor head with light source, optic, nosepiece and z-stage, a motorized XY stage and a passive variance absorption system. Picture (b) in Figure 2.4 illustrates those elements. The specimen is placed onto the XY stage and is illuminated with coaxial white light provided by the light source on the sensor head. The light passes through a beam splitter to a series of objectives, which can be selected in a six-place turret. The specimen's reflected light is projected through the beam splitter onto a colour digital sensor. As the distance between the object and objective is varied images are continuously captured. The vertical and lateral resolutions can be selected based on the used objectives. For each position in depth the object sharpness is calculated. The variation of sharpness is utilized for extracting depth information. The harmonized interaction between modulated illumination, vertical scanning and sensor capturing is crucial for the image capturing process. A 3D model, which is representative to the measured object, can be obtained for further analysis. With the IFM software, analysis can be made to the profile, the surface texture and the 3D form.

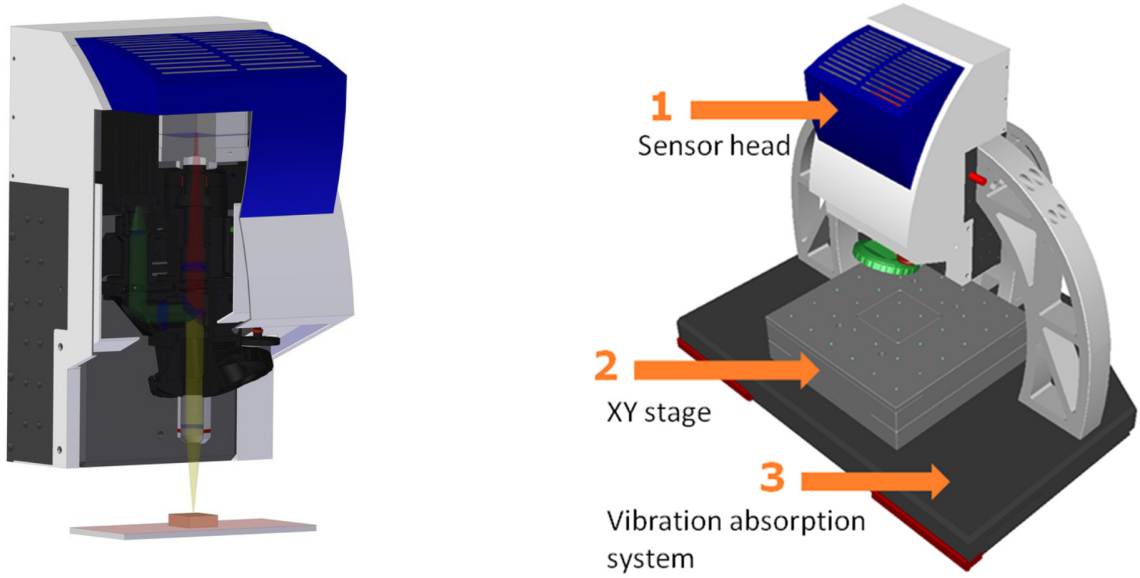

(a) (b)

Figure 2.4 The principle of Alicona InfiniteFocus® measurement.[5] (a) Illustration of focus-variance (b) Elements of the measuring system.

In this PhD project, Alicona InfiniteFocus® was mainly used to study the roughness of the surface, to observe the topography and to obtain the bearing area curve.

Table 2.1 indicates the technical specification of the instrument [6]. Table 2.2 shows the resolution and limits for each lens [6]. In this project, the most used lenses are the 20X and 10X.

The calibration tool is provided by Alicona. The calibration work on the height and lateral step was performed by M. Sc S. Gasparin.

Table 2.1 Technical data for the Alicona InfiniteFocus® instrument [6]

Objectives	2,5x	5x	10x	20x	50x	100x
Sampling Distance µm	3.52	1.76	0.88	0.44	0.18	0.09
Optical lateral resolution µm	5.6	2.2	1.1	0.8	0.6	0.4
Vertical resolution (low speed)[#] nm	2300	410	100	50	20	10
Vertical resolution (high speed)[#] nm	47100	8200	2000	1000	400	200
Scan speed (low) µm/s	112	20	5.0	2.5	1.0	0.5
Scan speed (high)[##] µm/s	2300	400	100	50	20	10
Vertical dynamic	3400	52000	160000	250000	430000	380000
Working distance mm	8.8	23.5	17.3	13	10.1	3.5
Field of view X µm	5716	2858	1429	715	286	143
Field of view Y µm	4351	2175	1088	544	218	109

Note: # Vertical resolution can be adjusted depending on the application; this also influences the scan. ## The maximum scan speed is not achieved by every application

Table 2.2 Resolution and application limits for the Alicona InfiniteFocus® [6]

Objectives	2,5x	5x	10x	20x	50x	100x
Min. measurable height nm	2300	410	100	50	20	10
Max. measurable height mm	8	22	16	12	9	3.2
Max. measurable area mm²	10000	10000	10000	4500	700	150
Max. measurable profile length mm	100	100	100	100	100	100
Min. repeatability nm	800	120	30	15	8	3
Min. measurable roughness (Ra)[#]nm	7000	1200	300	150	60	30
Min. measurable roughness (Sa)[#]nm	3500	600	150	75	30	15

Min. measurable radius µm	20	10	8	5	2	1
Min. measurable vertical angle °	20	20	20	20	20	20

Note: # The minimum measurable values are dependent on the structure of the specimen

Table 2.3 shows the nominal values of the height step and lateral grids on the calibration tool, as well as the calibration results.

Table 2.3 Calibration results for Alicona Infinite Focus® in DTU, by S. Gasparin on 12-01-2010

Purpose and optic (IFM G4)	Nominal value (µm)	Calibrated value (µm)	Measured value (µm)	Deviation (nm)
Height step 10x	1000	1.0019 (mm)	1.0017 (mm)	139
Lateral step 2.5x	120	119.86	119.87	12
Lateral step 5x	50	49.94	49.962	23
Lateral step 10x	24	23.963	23.994	31
Lateral step 20x #	24	23.963	23.988	25
Lateral step 50x	24	23.963	23.963	2
Lateral step 100x	24	23.963	23.972	10

Note: # The result was obtained on 08-07-2010

ATR-FTIR

Almost all the compounds containing covalent bonds absorb electromagnetic radiation in the infrared region [7]. Fourier-Transform infrared (FTIR) spectroscopy is a spectroscopy that records absorptions of infrared light by chemical bonds in all molecules incl. polymers. Wavenumbers are used in the spectrum because they are directly proportional to energy. And the vibrational portion (4000 cm^{-1} to 400 cm^{-1}) of the infrared region is the studied region.

Like other energy absorption systems, molecules are excited to a higher energy state when they absorb infrared radiation. The absorption of radiation leads to an energy change on the order of 8 to 40 KJ/Mole. The stretching and vibrational frequencies of the bonds in most covalent compounds lie in the same range. When absorbing energy, the vibration motion of the bonds is increased. However, not all bonds in a molecule are capable of absorbing infrared energy. Only the bonds with a dipole moment can absorb infrared radiation. Symmetric bonds such as those

of H_2 and Cl_2 do not absorb infrared energy. A bond must present an electrical dipole that is changing at the same frequency as the incoming radiation in order for transferring energy. A symmetric bond with identical or nearly identical groups at each end does not absorb infrared radiation. Figure 2.5 shows samples of those types of bonds.

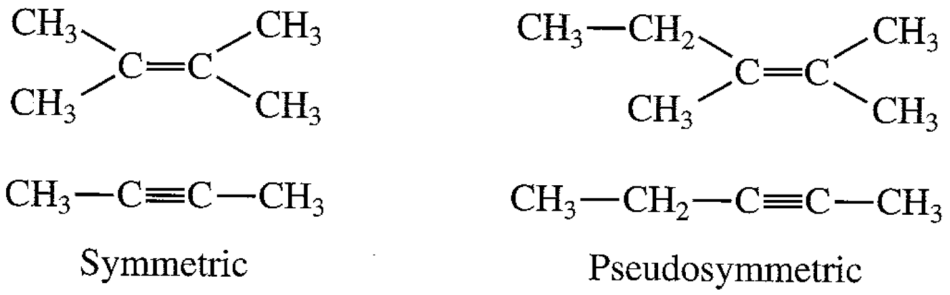

Figure 2.5 Symmetric bonds with identical (symmetric) or nearly identical (pseudo symmetric) groups at each end [7]

Since all the bonds have identical vibration frequency, and the environment of (the) two same bonds in two different molecules is slightly different, no molecules of different structure have the same infrared absorption pattern, or infrared spectrum.

There are several types of modes of vibrational motion that are infrared active, such as bending, stretching, twisting, wagging *etc*. And there are symmetric and asymmetric stretching motions. For example, the methyl group has a symmetric stretching at 2872 cm^{-1} and an asymmetric stretching at 2962 cm^{-1}. The wavenumber for a specific bond usually can be found in a handbook.

The instrument to determine the infrared spectrum is called an infrared spectrometer. There are two types: dispersive and Fourier transform (FT). They can provide nearly identical spectrums for a given compound. FTIR can get a spectrum much faster than the dispersive instrument.

Since light transmittance through a sample is necessary, the measurement requires very thin film material or a sample finely dispersed in a non-absorbing matrix. Nevertheless, with Attenuated Total Reflectance (ATR), measurement by reflecting is realized [8]. So the sample is forced in close contact with a reflecting surface. In this way polymer and non-dissolvable films can be analyzed directly without complicated sample preparation. Figure 2.6 shows the ATR-FTIR instrument is located in the Department of Chemical Engineering, DTU.

Figure 2.6 The ATR-FTIR instrument in Department of Chemical Engineering, DTU [8]

PicoScope 3000 series

A PC oscilloscope from Pico is used to measure the output laser pulse [10]. The PicoScope computer oscilloscope connects to the USB port on a computer and the laser signal output port. Oscilloscope and spectrum analyzer software works together with the equipment.

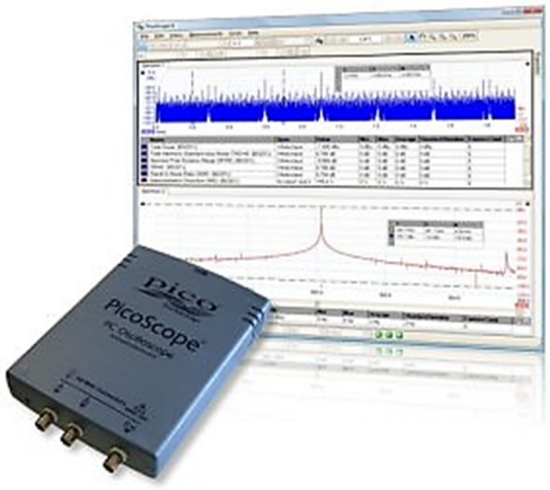

Figure 2.7 PicoScope 3000 series [9]

Scientech® Vector D200

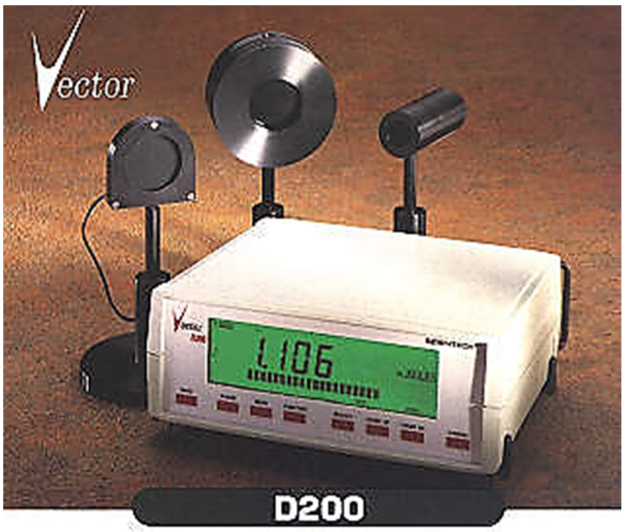

Figure 2.8 Scientech Vector D200 [10]

This equipment was used to measure the average power given by the Nd: YAG laser.

A pyroelectric detector is used to receive laser energy and the calorimeter transfers the data. However, the used detector in the project is specifically for the CO_2 laser, which means the wavelength is 10 times more than Nd: YAG's. So the measured data can only be used as an indication or for comparison between data obtained in the same method.

UBM Microfocus

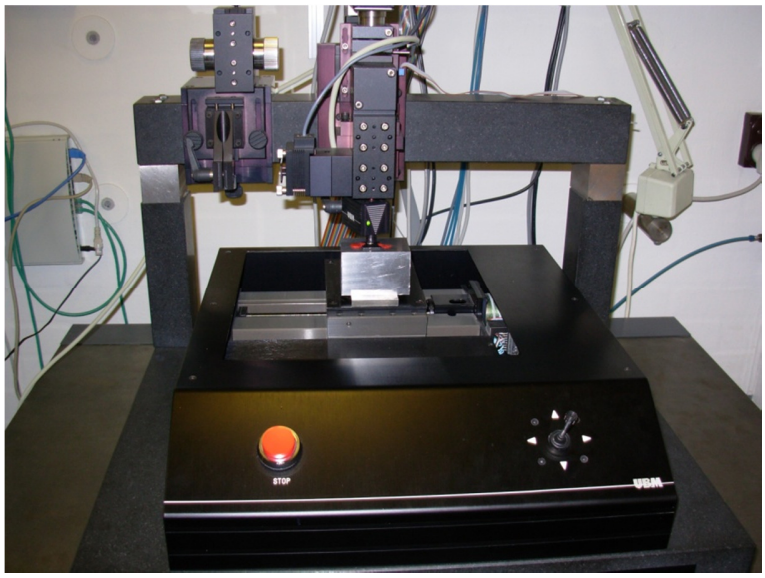

Figure 2.9 The UBM Microfocus in the Department of Mechanical Engineering, DTU

UBM Microfocus is a type of laser focus detection instrument [11]. It is possible to perform non-contact and non-destructive measurements on solid surface. The optical probe is used to scan in the lateral plane, and during the scan the laser beam of the scanning probe is brought into focus on the workpiece surface. Vertical movement of the lens helps to achieve focus.

As an optical instrument it is sensitive to the surface optical properties. The reflectivity of the material and the topographical slopes has crucial influence on the measurement.

The instrument has a lateral range of several millimeters and a lateral resolution of 0.5 µm. Two modes are available for the vertical range and resolution: 1mm range with a resolution of 50nm and 100 µm with a resolution of 5 nm. The maximum possible sampling frequency is between 200 and 1200 Hz depending on lateral resolution. The measurement time can be calculated based on the selected resolution and sampling frequency.

DeMeet 220

Figure 2.10 DeMeet 220, an optical coordinate measuring machine

DeMeet was used for the dimension measurements of laser spots or lines. It is an optical coordinate measuring machine, as shown by Figure 2.10. Table 2.4 indicates the technical data for the used instrument. Calibration work was carried out using the CGM optomechanical hole plate, by J. Rasmussen on 22-10-2009. Figure 2.11 is used to illustrate the calibration results. Figure 2.12 to Figure 2.14 indicate the length measurement uncertainties. Figure 2.15 shows the

difference in X and Y coordinates for each hole. The calibration method and measurement procedures are described in [12].

Table 2.4 Technical data of the utilized DeMeet equipment from the verification report

Machine type	DeMeet-220 Combo Model
Range of X-axis	220mm
Range of Y-axis	150mm
Range of Z-axis	100mm
Accuracy U1 at (20.0±0.5 ℃)	(4.0 + L/150) µm
Accuracy U2/U3 at (20.0±0.5 ℃)	(5.0 +L/150) µm

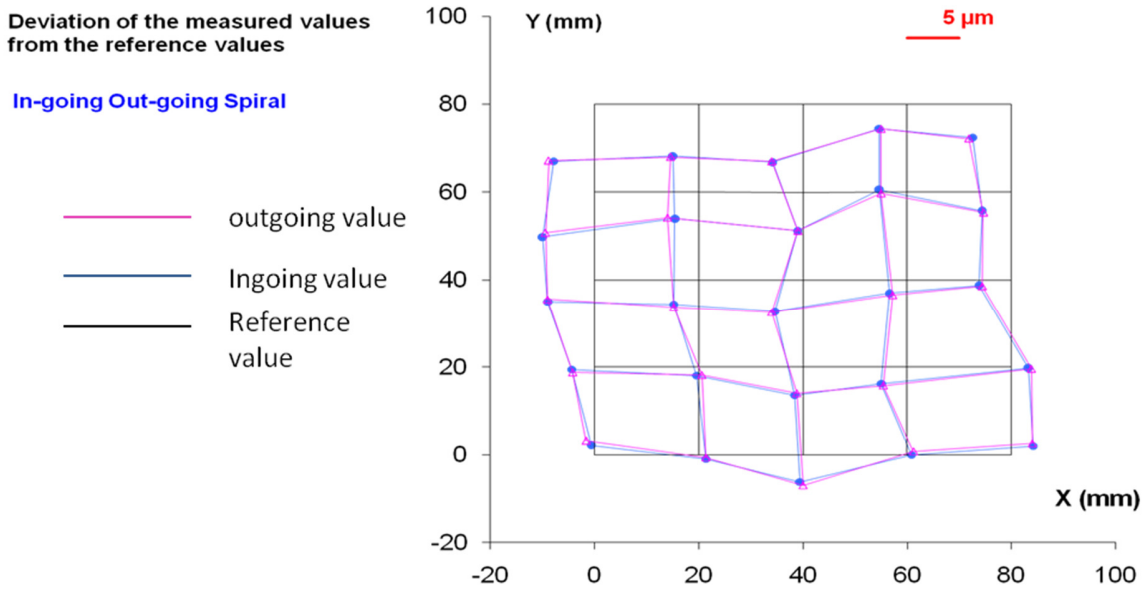

Figure 2.11 Calibration work of the used DeMeet: visualization of deviation of the measured coordinate values from the reference values during the ingoing and outgoing spiral measurement, using hole plate Temperature: 22.5 °C.

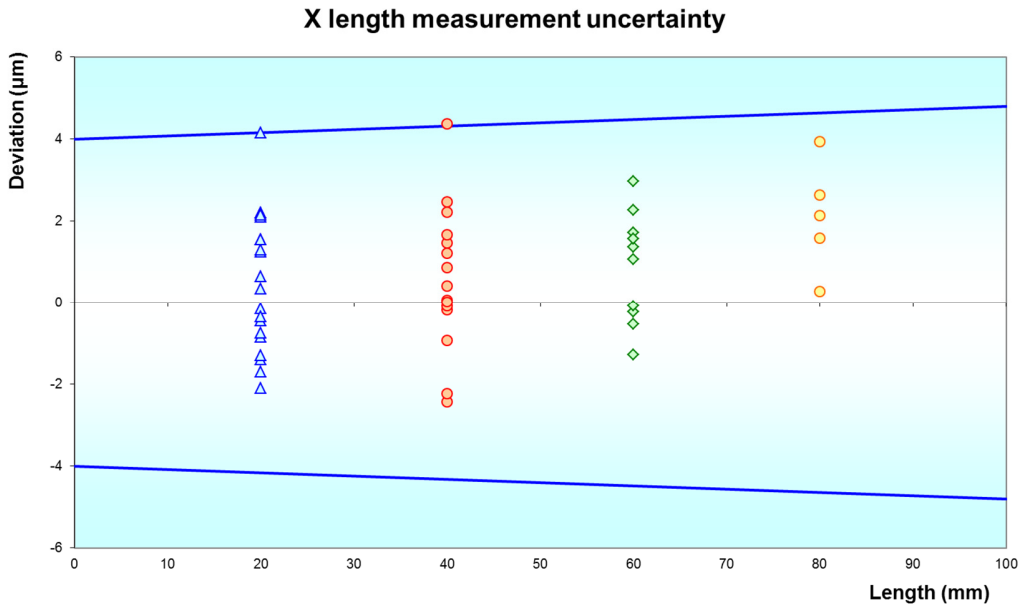

Figure 2.12 Calibration work of the used DeMeet: 1D length measurement uncertainty diagram for X axis, using hole plate Temperature: 22.5 °C

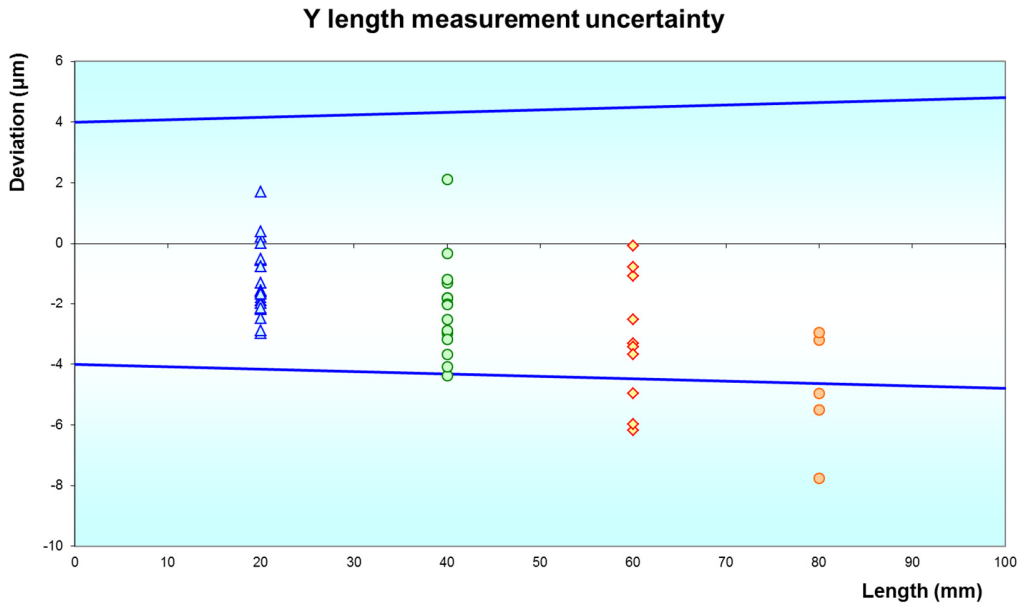

Figure 2.13 Calibration work of the used DeMeet: 1D length measurement uncertainty diagram for Y axis, using hole plate Temperature: 22.5 °C

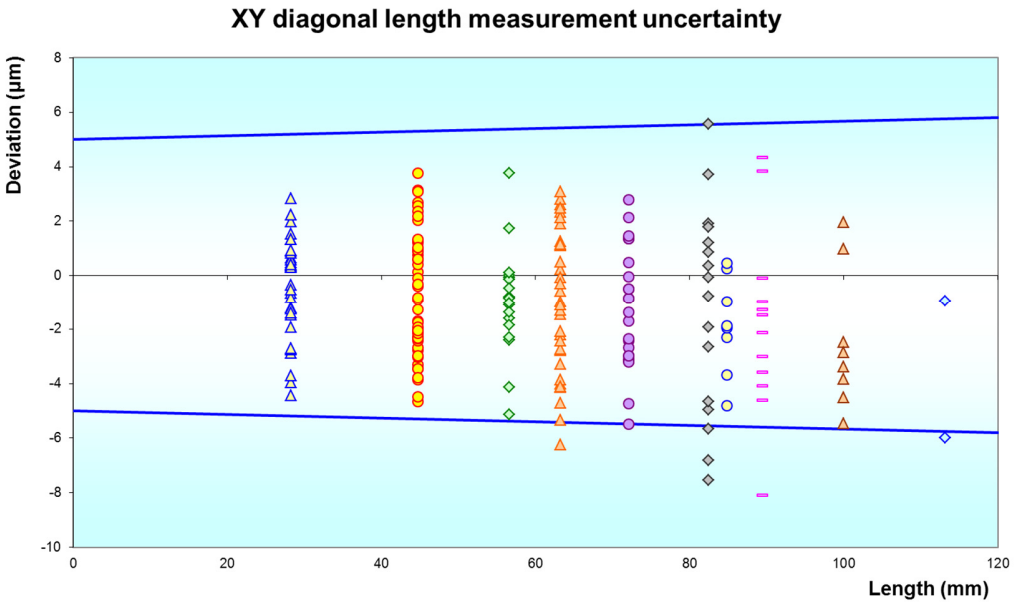

Figure 2.14 Calibration work of the used DeMeet: 2D length measurement uncertainty diagram for XY axis, using hole plate Temperature: 22.5 °C

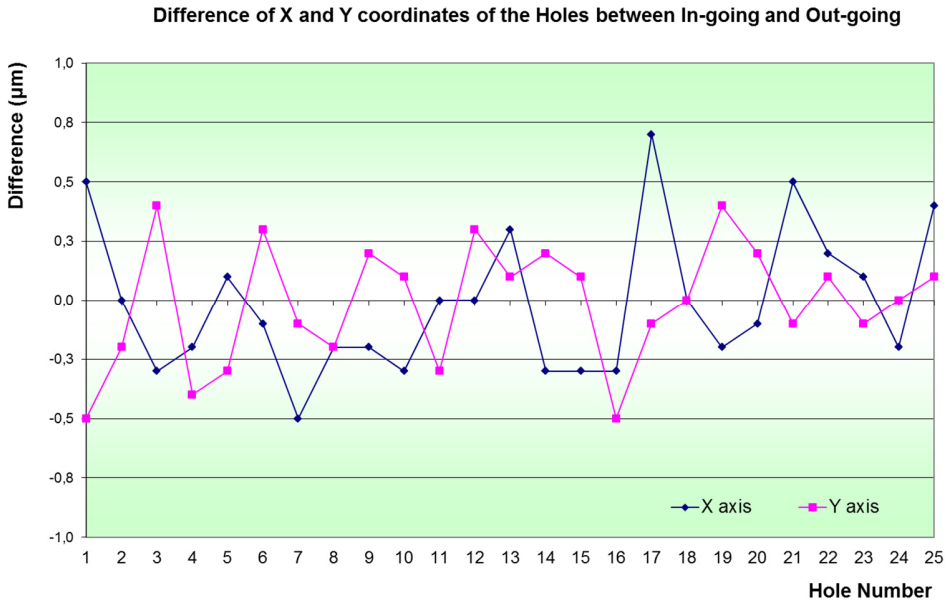

Figure 2.15 Calibration work of the used DeMeet: differences in X and Y coordinates for each hole between ingoing and outgoing spiral measurement, using hole plate. Temperature: 22.5 °C

Fischerscope® X-Ray system (SDVM®-W)

Two types of Fischerscope® X-Ray fluorescence measuring system were used in the study, SDVM®-W and SDVM®-µ. In both instruments the technology EDXRF (Energy Dispersive X-Ray Fluorescence) is utilized for quick, non-destructive and quantitative multi-elements analysis and

coating thickness measurement [13]. The functional principle for the instruments is that the tested sample is excited by the radiation from an X-ray tube, and then emits X-ray fluorescence radiation that is characteristic for each element. The energy spectrum is registered by a detector. The elements contained in the sample can be identified through the characteristic energies of the peaks of the spectrum. The concentrations of the elements are determined by the intensity of their radiation.

No preparation of the sample is needed. Table 2.5 indicates the technical specifications for both types of instruments [13].

There are reference specimens with calibrated thickness, and the X-Ray equipment in DTU was calibrated by the reference specimens. If using perfect homogeneous surface, and calibrated by the substrate for each thickness, the uncertainty of the system is supposed to be in the order of 10%. It is believed that this method provides stable and convincing results.

(a) (b)

Figure 2.16 The equipment Fischerscope® X-ray system used for coating thickness measurement [13] (a) XDVM®-μ which was used in HSG-IMAT (b) XDVM®-W which was used in DTU

Table 2.5 Technical specifications of the used X-Ray thickness measuring instruments

	XDVM®-μ	**XDVM®-W**
Instrument type (XRF = X-Ray fluorescence)	XRF coating thickness analyzer with innovative micro-focus x-ray optics for very small measurement spots.	Universal XRF coating thickness analyzer with a programmable precision stage. The top instrument for users with the highest demands.
Primary fields of application	Coating thickness measurement and materials analysis in the element range Z = 17 (Cl) to Z = 92 (U). Pc board testing, lead frames with extremely small structures, raster scans (area profiles) e. g., of hard disk coatings, fine wires	Coating thickness measurement and materials analysis in the element range Z = 17 (Cl) to Z = 92 (U). Connector contacts, pc-boards, for raster scans (area profiles) or coatings with very small measurement spots, fine wires.
Product highlights	Ultra high precision, programmable XYZ-stage with large travel range.	Ultra high precision, programmable XYZ-stage with large travel range. Very

	Revolutionary x-ray optics with very small measurement spot for high count rates.	small measurement spot, greatly enlarging optics, large measurement chamber, very fast stage loading.
Standard software[(1)]	WinFTM® V.6; PDM standard.	WinFTM® V.3; PDM optional
Measurement direction	Primary beam top to bottom.	Primary beam top to bottom
X-ray tube	Micro-focus tungsten tube with Be window.1 additional primary filter (Ni) can be added.	Micro-focus tungsten tube with Be window.1 additional primary filter (Ni) can be added.
Collimators	……	Four collimator positions, exchangeable sizes from 0.03 mm to 0.2 mm.
Minimum size of measuring spot	Ca. 0.1 mm x 0.1 mm	0.07 mm x 0.27 mm
Detector	2.5 mm	5; 29; 61; 93 mm
Eff. Focusing range[(2)]	Xenon-filled proportional counter tube for high count rates.	Xenon-filled proportional counter tube for high count rates.
Measuring stage	Motor-driven in X- and Y-direction with joystick, left or right mouse button; moveable and programmable sample support. Laser light spot as positioning aid.	Motor-driven in X- and Y-direction with joystick, left or right mouse button; moveable and programmable sample support. Laser light spot as positioning aid.
Stage loading and sample positioning	Measuring stage automatically moves out when opening the cover (tongue function). Fine positioning using joystick or mouse (Point &Shoot).	Tongue function – additional fast Y-axis for stage delivery; ideal for frequent sample loading. Fine positioning using joystick or mouse (Point & Shoot).
Programmable XY-travel	250 mm x 220 mm V max. = 25 mm/s Precision = 0.005 mm	250 mm x 250 mm; v maxes. = 25 mm/s Additional axis for 4x stage travel velocity (rapid loading!). Precision = 0.005 mm
Z-axis	Motorized moveable and programmable detector unit.	Motorized moveable and programmable detector unit.
Interior dimensions [mm]	W = 560; D = 530; H = 130	W = 560; D = 530; H = 145.
Measuring chamber	Slotted design for large flat specimens that would otherwise not fit in the measurement space.	Slotted design for large flat specimens that would otherwise not fit in the measurement space
Focusing on meas. Spot	Autofocus or visual focusing.	Autofocus or visual focusing.
Magnification (In reference to a 19“ Monitor)[(3)]	Optical: 30 / 92 / 277x Digitally: in steps 1, 2, 3 and 4x Total: 30-1108x	Optical: 40-142x Digitally: in steps 1, 2, 3 and 4x Total: 40-568x

Note: (1) Systems using WinFTM V.3 can be upgraded to V.6 inclusive PDM Software for extended product administration and result documentation. (2) For parts with a measurement point positioned behind; measured beginning at specimen support (Z = 0). (3) Depending on the measuring distance.

e-Cu: Check system

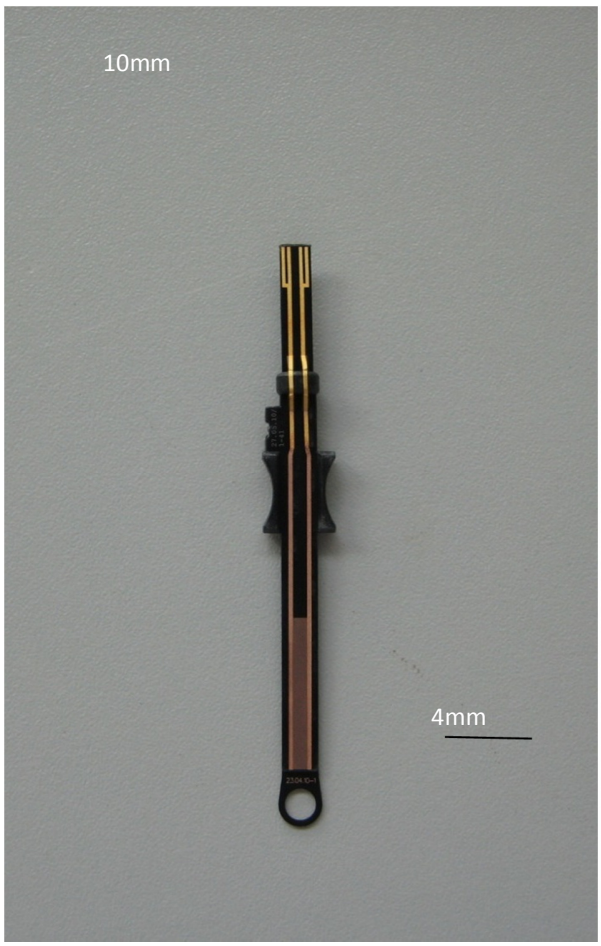

Figure 2.17 "e-Cu: Check" system for monitoring activity of copper plating bath

The plating velocity using an autocatalytic electroless copper bath is affected by several factors, e.g. temperature, flow rate of the air bubbling and concentration of the components. The "e-Cu: Check" system is invented by HSG-IMAT and used to monitor the auto-catalytic electroless copper electrolytes [14]. It is a probe with electrodes patterns and a laser activated sensor area using LDS® technology. To monitor the electrolyte activity the probe is plugged in a special holder. Then the holder is submerged in the electrolyte, where copper is deposited on the activated area. The impedance between the electrodes on the probe is measured. When the activated area becomes conductive, a strong phase shift between current and voltage can be detected. The time needed for the phase shift is recorded as the rate of electrolyte activity. The time for phase shift decreases when the electrolyte activity increases. It is claimed that the system is able to detect the activity in a short time, even when the electrolytes are very active.

Reference

[1] http://www.thermoscientific.com/wps/portal/ts/products/detail?navigationId=L11007&categoryId=80481&productId=11962357, accessed 06-10-10.

[2] https://fscimage.fishersci.com/images/D16121~. Pdf accessed 06-10-10.

[3] International Standard ISO 15472, "Surface chemical analysis - X-ray photoelectron spectrometers - Calibration of energy scales", 2001.

[4] http://en.wikipedia.org/wiki/X-ray_photoelectron_spectroscopy accessed 01-10-10.

[5] Technical Brochure: "Alicona InfiniteFocus® Manual", IFM 3.1.1.2, En 26.02.2009.

[6] http://www.alicona.com/home/products/InfiniteFocus/TechnicalSpecification.en.php accessed 06-10-2010.

[7] D. L. Pavia, G. M. Lampman, G. S. Kriz, "Introduction to spectroscopy", 3rd Ed. Thomson Learning, 2001.

[8] http://www.dpc.kt.dtu.dk/Research/Instrumentation/FTIR.aspx, accessed, 01-10-10.

[9] http://www.picotech.com/computer-oscilloscope.html, accessed, 01-10-10.

[10] http://www.scientech-inc.com/vectord200.phtml, accessed, 01-10-10.

[11] U. R. A. Theilade, PHD Thesis " Surface micro topography replication in injection moulding", Manufacturing Engineering and Management, DTU, 2004.

[12] E. Larsen, "Measurement procedure for optomechanical hole plate", Department of Manufacturing Engineering and Management, DTU, Lyngby, 2003.

[13] Technical brochure, "The Measure of Experience, X-Ray Fluorescence Measuring Instruments for Coating Thickness Measurement and Materials Analysis http://www.helmut-fischer.com/globalfiles/DE_X-RAY_EN_0103.pdf, accessed, 01-10-10.

[14] Technical brochure, "e-Cu: Check system, Monitoring of electroless copper electrolytes for LPKF-LDS® technology", HGS-IMAT.

Appendix 3. List of pulications

Patent

- P. T. Tang, P. C. Nielsen, J. S. Nielsen, H. N. Hansen & Y. Zhang, PREPARATION OF A POLYMER ARTICLE FOR SELECTIVE METALLIZTION, Application filled March 30, 2007, published as WO2008/119359 A1.

Referred Scientific Journal

- Y. Zhang; P. T. Tang; H. N. Hansen; J. S. Nielsen, "Electroless Plating on Plastic Induced by Selective Laser Activation", Plating and Surface Finishing Vol: 97, issue: 2, pages: 43-47, 2010, American Electroplaters and Surface Finishers Society, Inc. (AESF)
- Y. Zhang; G. M. Kontogeorgis; H. N. Hansen, "An explanation of the selective plating of laser machined surfaces using surface tension components", Journal of adhesion science and technology, accepted, 2010.
- Y. Zhang; H.N. Hansen; A. De Grave; P. T. Tang; J. S. Nielsen, "Laser Machined Polymer Surface for Future Plating and Characterization Using Bearing Area Curve Parameters", e-published, International Journal of Advanced Manufacturing Technology , 2010

Referred Proceeding

- Y. Zhang, P. T. Tang, J. S. Nielsen; H. N. Hansen, "Laser Induced Selective Activation and Electroless Metallization of Standard grade polymer", Abstract, 9th International Congress on Molded Interconnect Devices, Fuerth Germany, (expected), September, 2010.
- Y. Zhang; H.N. Hansen; A. De Grave; P. T. Tang, J. S. Nielsen "Characterization of Laser Machined Polymer Surface Using Bearing Area Curve Parameters for Future Plating", Proceeding, ICOMM/4M 2010, Madison, WI, US.
- Y. Zhang; P. T. Tang; H.N. Hansen; J. S. Nielsen "Electroless Plating on Plastic Induced by Selective Laser Activation", Proceeding, Sur/Fin 2009, Madison, US, 2009.
- Y. Zhang; J. S. Nielsen; P. T. Tang; H.N. Hansen; "Laser Induced Selective Activation Utilizing Auto-catalytic Electroless Plating on Polymer Surface", Proceeding, NOLAMP 12th, Copenhagen 2009.
- Y. Zhang, P. T. Tang, J. S. Nielsen; H. N. Hansen, "Laser induced selective activation utilizing auto-catalytic electroless plating on polymer surfaces", Proceeding abstract, 8th International Congress on Molded Interconnect Devices, Fuerth, Germany, 2008.